IntechOpen

Recent Advances and Applications in Remote Sensing

Edited by Ming-Chih Hung and Yi-Hwa Wu

RECENT ADVANCES AND APPLICATIONS IN REMOTE SENSING

Edited by **Ming-Chih Hung** and **Yi-Hwa Wu**

Recent Advances and Applications in Remote Sensing
http://dx.doi.org/10.5772/67959
Edited by Ming-Chih Hung and Yi-Hwa Wu

Contributors

Hakim Saibi, Nouredine Saadi, Mohand Bersi, M. Bodruddoza Mia, Khalid Mohamed Saleh Al Bloushi, Yuanzhi Zhang, Jiang Tingchen, Yu Li, Guido Staub, Vladimir Lukin, Oleksii Rubel, Ruslan Kozhemiakin, Sergey Abramov, Andrii Shelestov, Mykola Lavreniuk, Benoit Vozel, Kacem Chehdi, Mykola Meretsky, Linglin Zeng, Daxiang Xiang, Junhao Xie, Guowei Yao, Hamid Hamraz, Marco Contreras, Yan Jia, Yuekun Pei, Ming Chih Hung, Yi-Hwa Wu, Jeff Thomas, Maureen Gallagher

Notice

Statements and opinions expressed in the chapters are these of the individual contributors and not necessarily those of the editors or publisher. No responsibility is accepted for the accuracy of information contained in the published chapters. The publisher assumes no responsibility for any damage or injury to persons or property arising out of the use of any materials, instructions, methods or ideas contained in the book.

First published in London, United Kingdom, 2018 by IntechOpen
eBook (PDF) Published by IntechOpen, 2019
IntechOpen is the global imprint of INTECHOPEN LIMITED, registered in England and Wales, registration number: 11086078, The Shard, 25th floor, 32 London Bridge Street
London, SE19SG – United Kingdom
Printed in Croatia

British Library Cataloguing-in-Publication Data
A catalogue record for this book is available from the British Library

Additional hard and PDF copies can be obtained from orders@intechopen.com

Recent Advances and Applications in Remote Sensing
Edited by Ming-Chih Hung and Yi-Hwa Wu

p. cm.

Print ISBN 978-1-78923-536-4

Online ISBN 978-1-78923-537-1

eBook (PDF) ISBN 978-1-83881-271-3

Meet the editors

Dr. Ming-Chih Hung is a Professor of Geography/GIScience at Northwest Missouri State University. He earned his bachelor's degree from National Taiwan University focusing on digital elevation model applications, his MS from the University of Utah focusing on the vegetation-impervious surface-soil model and soft classification of Thematic Mapper images, and his Ph.D. also from the University of Utah focusing on remote sensing and geographic information systems (GIS) in urban areas. His research emphasizes the use of GIScience in urban areas. In addition to urban areas, he is also interested in precision agriculture and environmental issues. At Northwest Missouri State University, he teaches courses on remote sensing, GIS, Global Positioning System, and cartography.

Dr. Yi-Hwa Wu is a Professor of Geography/GIScience at Northwest Missouri State University. She earned her bachelor's degree and MS from National Taiwan University, both focusing on the geographic information system (GIS) modeling process. She earned her Ph.D. from the University of Utah focusing on modeling the dynamic nature of urban transportation systems. Her research emphasizes the GIS database and design, GIS models, and modeling processes in various environments, such as transportation models, predictive models, etc. At Northwest Missouri State University, she teaches courses on GIS, cartography, and GIS programming.

Contents

Preface

Since the first environmental monitoring satellite launched back in 1972, remote sensing has been the primary data source, collecting environmental data faithfully and unbiasedly. In the past five decades or so, the broader geospatial community has witnessed a rapid growth in satellite remote sensing, evolving from the one and only legendary Landsat 1, offering 4-band spectral resolution, 80-meter spatial resolution, 18-day temporal resolution, and a 6-bit radiometric resolution multispectral scanner satellite image, to various satellite images that nowadays offer a hundred bands in spectral resolution, submeter in spatial resolution, daily revisit capacity in temporal resolution, and 10 or 12 bits in radiometric resolution in comparison. The evolution was impressive, yet the advance in data collection still continues, not only with satellite remote sensing, but also other forms of remote sensing. In recent years, light detection and ranging has become popular in terms of collecting surface model data. In even more recent years, drones or unmanned aerial systems have caught our attention with their ability to capture environmental data with unprecedented spatial detail and the mobility to launch and collect data on demand.

Along with the wealth of data come the methodologies to process the data as well as applications that utilize the data on real-world issues. Much cutting-edge research on new theories and/or understanding of remote sensing technology has been published in journals or scholarly outlets. Relatively little attention has been given to the applications of remote sensing.

Through years of teaching remote sensing and digital image processing, we have heard many cases of the use of remote sensing and geospatial technologies in different environments. Most of our students are working professionals. They work in different fields of the geospatial industry or environmental sciences. Though the principles are similar, results can vary dramatically, depending on the environment to which remote sensing was applied. We are always amazed at how remote sensing with simple methodology or processing can provide remarkable results. Besides being wowed, it is always a little unsettling to hear people saying "Oh, that is a good idea; maybe my company should do that." People may well know how remote sensing was used in their field, but often don't know how remote sensing was used in other disciplines.

Sharing results and experience is an important part of our teaching and learning. This inspired us to have this book dedicated to sharing experience, either by advancing our theory and understanding of remote sensing technology or by solving real-world issues with existing remote sensing technology. It is our hope that scientists, scholars, and working professionals all over the world can share their remote sensing experience. If it solves your problem, it may solve others' problems. Contrarily, if it solves others' problems, it may solve my problem. Every project is a learning experience and worthy of sharing.

Many people deserve a hearty thanks for bringing this book to reality. We wish to extend our great appreciation to all of the authors and reviewers who contributed to this book. We also want to extend our sincere gratitude to the staff at InTechOpen. They certainly put in a lot of effort in helping and guiding us through this book project. Without their help and guidance, this book would not be possible. Finally, we thank our families for their continued support and encouragement.

Ming-Chih Hung and Yi-Hwa Wu
Northwest Missouri State University
Maryville, Missouri, USA

Section 1

Advances in Theory and Understanding

Chapter 1

A Study on Phenology Detection of Corn in Northeastern China with Fused Remote Sensing Data

Linglin Zeng and Daxiang Xiang

Additional information is available at the end of the chapter

http://dx.doi.org/10.5772/intechopen.73096

Abstract

Accurate phenology information detection is the basis for other remote-sensing based agriculture applications. So far, there have been a lot of phenology estimation models based on remote-sensing data, but little attention was paid to microscopic mechanism of crops and the environmental factors. The main purpose of this chapter is to apply a new phenology detection model, which combined physical mechanism-based crop models with remote-sensing data to detect the critical phenological stages of corn in Northeast China (Jilin and Liaoning Provinces). Compared to the phenology observations from the agriculture meteorological stations, the corn phenology estimation accuracy in Northeast China using only MODIS data is much lower than that in the US field sites. The main reason might be the small size of single piece of cropland in northeastern China, which led to the mixed MODIS pixels. Accordingly, Landsat and MODIS data fusion methods were applied to get time-series images with Landsat-like spatial resolution and MODIS-like temporal resolution, and quantitative and qualitative validation was conducted to evaluate and verify the accuracy of the data fusion. The results show that data fusion of Landsat and MODIS improved the spatial resolution and decreased the influence of mixed pixels.

Keywords: air temperature, data fusion, land surface temperature, remote sensing, crop phenology

1. Introduction

Accurate measurements of regional-to-global-scale vegetation dynamics and phenology information improve our understanding of inter-annual vegetation change in terrestrial ecosystems, as well as climatic and other environmental variations from year to year [1–7]. The phenological stages of crops provide essential information for agricultural activities such as irrigation scheduling and fertilizer management [26]. In addition, accurate detection

of key crop growth stages is a key input for crop yield estimation based on remote-sensed vegetation index (VI) data and crop model applications integrated with remote sensing data [8–11].

The traditional approaches to estimating crop phenology have been through ground observations and the use of crop models (e.g., Simple and Universal CROp growth Simulator (SUCROS) [12], Hybrid-Corn [14], WOrld FOod STudies (WOFOST) [13–15]). The crop models can estimate crop growth dates with a high level of accuracy [root mean square error (RMSE): 0–4 days], but they require a number of detailed information inputs such as crop (e.g., cultivar used and plant population), weather (e.g., temperature, rainfall, solar radiation and wind speed) conditions [14, 16] and soil (e.g., initial soil moisture). On the one hand, the use of these crop models is usually limited by the availability of the required data inputs; on the other hand, the models need to be calibrated for particular species and site-specific conditions based on ground data [11, 16], and the ground observations collected by observers are not cost-efficient. Accordingly, the traditional methods are site-specific and typically cannot monitor crop phenology beyond the field scale over larger areas [11].

Satellite remote sensing observations from global imaging sensors offer considerable potential to provide the information of regional spatio-temporal patterns of the key crop growth stages of cash crops in a consistent, time- and cost-efficient manner [11]. The commonly used remote-sensing based phenology detection methods can be divided into four groups [11]: (1) threshold methods that estimate phenological stages by using either a fixed or dynamic threshold [17–20]; (2) moving window methods that determine the phenology dates by vegetation index (VI) changes of a time-series VI curve in a defined moving temporal window (e.g., 20 days) [21–23]; (3) function fitting methods that apply mathematical functions (e.g., logistic [24], Fourier transformation, wavelet [25]) to fit the time-series VI curves to a given function and extract phenological stages through the detection of defined feature points (e.g., second derivative equals 0) on the function curves; and (4) the shape model method [two-step filtering (TSF) approach developed by Sakamoto et al. [26]] that applies a novel shape-model fitting concept to times-series VI curves for date identification and by Zeng et al. [11] who proposed a hybrid method with environmental factors taken into consideration by integrating crop models.

The first three remote-sensing-based phenology detection methods summarized above are generally based on mathematical methods that directly detect the feature points as the transition dates of vegetation [24, 27, 28]. Usually, these dates represent general vegetation growth stages (e.g., greenup onset, peak greenness and dormancy onset [24]) but have little association with the specific agronomic stages of a specific kind of crops (e.g., corn, soybeans) [11]. Some key crop growth stages (e.g., R1 (beginning bloom), R3 (beginning pod) stages of soybeans) are challenging or impossible to be detected by finding feature points of the VI time-series curve. In addition, these methods are often sensitive to observation errors and noise caused by cloud coverage, atmospheric constituents (e.g., water vapor), bi-directional reflectance distribution function (BRDF) effect and the mixed-pixel effect in time-series VI data products [11, 26].

The TSF approach is potential for the specific agronomic stages detection of specific crops with a high estimation accuracy [root mean square error (RMSE) ranging from 2.9 to 7.0 days and from 3.2 to 6.9 days for corn and soybeans, respectively] [26]. However, this method was based on an assumption that the shape model is linearly scalable to fit the time-series VI curve through geometrical scaling, regardless of all the factors that would influence the crop's growth pattern expressed in the VI data [11, 26]. For example, air temperature is generally one of the decisive factors that affect the growth rate of all crops. Photoperiod is even a more important factor for some photosensitive crops, as longer daylength may decrease the development rate by delaying reproductive development (e.g., soybeans). As a result, the time-series VI profile of a crop's growth pattern under different environmental conditions can vary from year to year [11].

Zeng et al. [11] proposed a hybrid phenology detection approach that incorporates the "shape-model fitting" concept of the TSF method [26] and simulation concept of traditional crop model that incorporates other environmental factors that influence crop development [11]. The approach is designed to detect the critical vegetative stages (V1 and V6) and reproductive stages (R1–R6) of corn from the MODIS 250-m Wide Dynamic Range Vegetation Index (WDRVI) time-series data. This method was tested over a 10-year period (2003–2012) for three experimental field sites to calibrate and quantitatively assess its performance with ground-based crop phenology observations for each site. It was also tested regionally over eastern Nebraska and the state of Iowa to evaluate its ability to characterize spatio-temporal variation of the targeted corn and soybean phenology stage dates across a larger major crop-producing region.

In this chapter, this method was tested in northeastern China where the environment is different with that in the US. As the piece of farmland is smaller than that in the US, the results were affected by mixed pixels from the MODIS observations. Then data fusing method was used to generate time-series VI data with high spatial and temporal resolution data, based on which phenological information of corn was estimated.

2. Study area

Northeast China, an important agricultural production base, plays a significant role in the national food security. In addition, it is a major corn producing area and named as one of the world's three golden Corn Belts. Jilin and Liaoning province were selected as the study area to further study the phenology estimation in nonirrigated region with small plots of cropland.

The ground-based data are from 30 agricultural meteorological stations (**Figure 1**). It mainly includes crop species, growth stage, soil moisture and air temperature. The ground-based crop growth stage observations were conducted by agronomists once every 1–10 days during the growing seasons and recorded in every 10 days. The recorded stages include VE, VT, R1, R4, R6 stages if they were match to general stage system (vegetation (V)-stage or reproductive (R)-stage) according to their growth stage names.

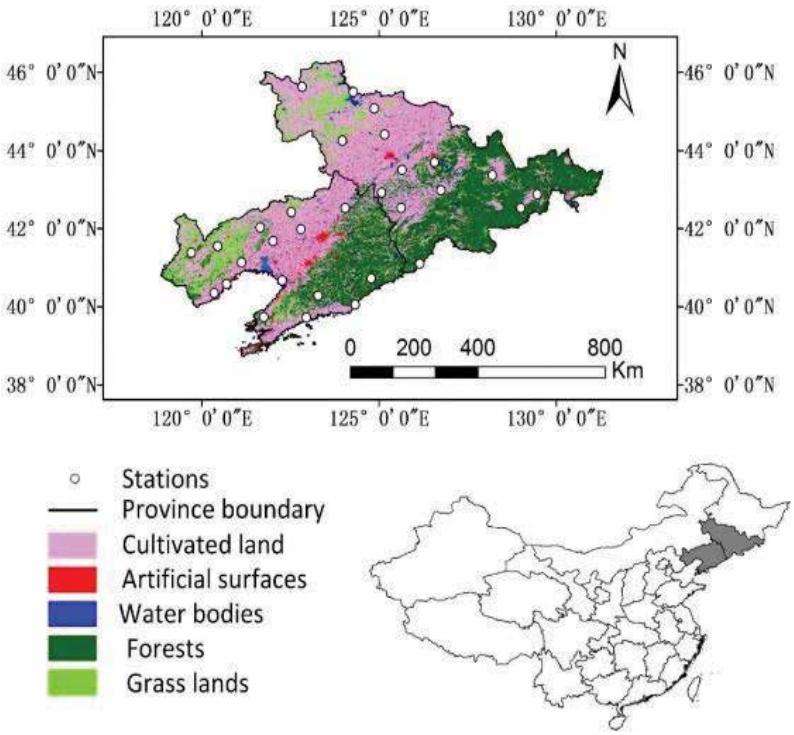

Figure 1. The study area in northeastern China.

3. Data description and preprocessing

3.1. WDRVI data

The original source data for the WDRVI time-series data set used in this study include the MODIS 8-day composite, 250 m surface reflectance data (MOD09Q1, Collection 5) and 30 m Landsat Surface Reflectance Climate Data Records (CDRs). The WDRVI developed by Gitelson [29] offers valuable alternative VI to monitor crops because its sensitivity is at least three times greater than that of NDVI at moderate-to-high LAI values and maintains a linear relationship across the range of LAI values for both corn and soybeans [11, 26, 29, 30].

3.2. Average air temperature data calculated from MODIS land surface temperature products

Average air temperature is a critical input for crop models in this chapter. It is estimated by both daily daytime and nighttime 1-km land surface temperature (LST) data (MOD11A1, Collection 5) by a linear regression model [11, 31], and the calibration and validation were based on the observations from the meteorological stations in the study areas of China. The daily averaged air temperature (Tavg) was calculated by averaging the daily maximum and

minimum air temperatures [11]. The 8-day composite air temperature was then calculated by averaging daily Tavg of cloud-free days during the 8 day composite period [11].

3.3. Land use data layer

GlobeLand30 datasets were selected as the regional land use classification data of China, which was developed under the "Global Land Cover Mapping at Finer Resolution" project led by National Geomatics Center of China (NGCC) China [32]. An area-ratio threshold of 75% was adopted to select all MODIS 250 m pixels across the region that was covered predominately by corn [11, 26].

3.4. Using spatial and temporal adaptive reflectance fusion model algorithm to blend Landsat and MODIS surface reflectance

Before data fusion, preprocessing of Landsat and MODIS data was conducted, including format conversion, atmospheric correction, geometrical correction, resampling, reprojection, registration, mosaicking and cropping. Using more than one pair of reference images, particularly those observed in different stages of the growing season, can reduce the impact of the cloud and improve the estimation accuracy [33]. Using the reference images in different stages of the growing season may avoid some mistakes caused by harvest and fallow. In addition, using the reference images that were observed closer to the time of the Landsat images to be estimated can improve the estimation accuracy [34]. In this chapter, three cloud-free Landsat images observed in the beginning, middle and end of growing season respectively were selected as the reference images as possible to be blended with 250 m 8-day MODIS reflectance image using spatial and temporal adaptive reflectance fusion model (STARFM) method. The two reference images observed in the beginning and middle of the growing season were used to estimate time-series high spatial resolution images of the beginning and middle of the growing season. Correspondingly, the two reference images observed in the middle and end of the growing season were used to estimate time-series high spatial resolution images of the middle and end of the growing season. The quality flag data and cloud mask of both MODIS and Landsat were used to identify the pixels with cloud or low quality.

4. Methodology

4.1. Crop models for corn

Plant growth processes are mainly influenced by interactions among genotype, environment conditions and crop management [35, 36]. In this chapter, we assumed that the influence of genotype and crop management (i.e., proper management of pests and diseases and fertilizer applications was implemented) was minimal as compared to environmental factors [11]. For this chapter, the developmental stages of corn were assumed to be most closely related to air temperature [37–39].

The models that describe the relationship between crop development and environment factors include linear and nonlinear models. Nonlinear approaches have been shown to provide better predictions of plant development stages than linear models for a number of different crops including corn [40], soybeans [15], wheat [41], potato [42], rice [43], as nonlinear models often describe the biological processes underlying crop growth in more detail [44, 45].

The Wang-Engel (WE) model [45], nonlinear models, simulates crop development with response functions that range from 0 to 1. The temperature response function in the WE model is described by a beta function with three parameters (i.e., minimum, optimum and maximum air temperatures). When the temperature is below the minimum or above the maximum temperature, crop development stops and the temperature response function equals zero. When the temperature is at optimum, which is a value between minimum and maximum temperature (e.g., 28°C for corn), development takes place at the maximum rate and temperature response function equals one [45]. The WE model was originally developed for winter wheat [45] but has also been used to simulate the development of other annual crops including corn [44] and soybeans [15] with positive results. Accordingly, the WE model was used in this study to describe the development of corn responding to air temperature Eqs. (1)–(4).

$$r_{corn} = r_{\max} f(T) \tag{1}$$

$$f(T) = 0, \ if\ T \geq Tup\ or\ T \leq Tbase \tag{2}$$

$$f(T) = \left[2\,(T - Tbase)^{\alpha}(Topt - Tbase)^{\alpha} - (T - Tbase)^{2\alpha}\right] / \left[(Topt - Tbase)^{2\alpha}\right],\ Tbase \leq T \leq Tup \tag{3}$$

$$\alpha = \ln(2) / \ln\left[(Tup - Tbase)/(Topt - Tbase)\right] \tag{4}$$

where r_{max} is the maximum development rate (per day). T is the average near surface air temperature estimated from MODIS data. *f(T)* is a temperature response function, which varies from 0 to 1.T_{up}, T_{base} and T_{opt} are the abovementioned three parameters (maximum, minimum, and optimum air temperature, respectively).

4.2. Combining crop models with time-series WDRVI data

Photothermal time which combined both temperature and photoperiod information was used to describe leaf appearance rate and phenological response of various plant species [46–48]. To combine the crop model and time-series MODIS WDRVI data, photothermal time (accumulated photothermal time, APTT) was used instead of calendar time [Day of Year (DOY)] on the time axis in this chapter. It was defined as the accumulated development rate ($\sum r$) calculated by temperature and photoperiod response function (Eq. 5). Usually, the planting date varied from year to year to ensure that APTT value was calculated from the same onset

of growth, a starting point of APTT was set as the beginning of greenness of the crops (S_0) derived by the Zhang's method [24].

$$\text{APTT} = \sum_{onset} r\max f(T) \times f(P) \tag{5}$$

where onset is when corn reaches the beginning of greenness detected by the Zhang's method [24]. *f(T)* and *f(P)* are temperature and photoperiod response functions, respectively. While as the growth of corn is insensitive to photoperiod to some extent, *f(P)* equals constant 1. In order to combine APTT time and time-series WDRVI data, the APTT was calculated at the same eight-day interval with the eight-day composite periods of the MODIS WDRVI data [11].

4.3. Building a shape model

Before building the shape model, the Savitzky–Golay Filter method [49] was used to de-noise and rebuild the time-series VI data. In order to generate the shape model from an idealized temporal VI for both crops, the shape model in this study built under APTT with higher peak WDRVI value (>80). In order to generate the shape model from an idealized temporal VI for corn, the smoothed WDRVI time series data were stretched in the Y direction to make sure that the peak WDRVI value equals the median peak value and shifted in the X direction by detecting the beginning of the growing season with the Zhang's method to make sure that the time-series curves have the same onset. After the preliminary Y-scale and X-shift, the discrete points of smoothed WDRVI data were used to build the shape models for corn. They were fitted by the sum of three sine functions [11]. The predefined APTT X_0 for each phenological stage was calculated by averaging the APTT of each phenological stage' transition dates of all the observations used to build the shape model [11].

4.4. Fitting the smoothed WDRVI data on the shape model

The smoothed WDRVI time series data for each year were stretched by a Y-scale to make sure that the peak value was equal to the median peak value. Then, the shape model is fitted on the smoothed WDRVI time-series data. The optimum scaling parameters (X-scale, Y-scale) that approximate the fit of the smoothed WDRVI data to the shape model were calculated based on the smallest root mean square error (RMSE) between the shape model and the scaled smoothed WDRVI data [11], see Eqs. (6) and (7).

$$RMSE = \sqrt{\sum_{S0}^{Xe} \left(f(x) - g(x)\right)^2} \tag{6}$$

$$g(x) = yscale \times h\left(xscale \times \left(x - xshift\right)\right) \tag{7}$$

The function *h(x)* refers to the smoothed WDRVI data, *f(x)* is the shape model and *g(x)* is transformed from the smoothed WDRVI data for a given site or year, where x is the APTT value.

5. Results and discussion

5.1. Results in northeastern China using MODIS only

5.1.1. Shape model

The smoothed WDRVI curve with peak larger than 80 was selected to establish the corn shape model in the study area to reduce the impact of mixed pixels, noises, environmental stress on crop growth and phenology (**Figure 2**).

5.1.2. Phenology estimation results

Due to the lack of regional-scale crop phenological observations in Northeast China, phenology estimation accuracy was only validated in a field scale by comparing with the observations from agricultural meteorological stations and the estimated phenological stages derived from the time-series WDRVI data of the corn field in the stations. The RMSE of the estimated five corn growth stages varies from 3.78 to 8.41 days with little system bias (**Figure 3** and **Table 1**). The estimation accuracy was higher in the field sites of University of Nebraska (with RMSE varied from 1.99 to 4.30 days) [11]. The RMSE of the estimated five phenological stages is within 15 days, which indicates that the phenology estimation model is also effective in northeastern China.

Similar to the results in the field sites of the University of Nebraska Lincoln, lower estimation accuracy was observed at the beginning and end of the growing season (such as V1, R6) than that at the middle stage of the growing season when vegetation cover reaches the peak, such as R1 stage (**Table 1**). As in the beginning and end of the growing season, the vegetation index is more sensitive to noise and susceptible to weeds and other noncrop plants [50, 51].

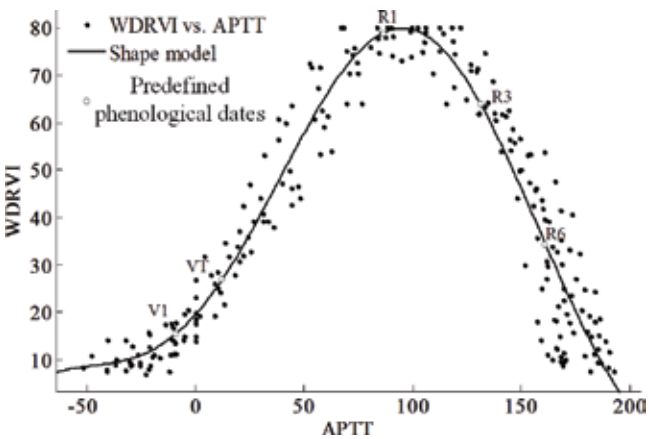

Figure 2. The shape model of corn from the stations in northeastern China derived by curve fitting with characteristic points indicating the start of the specific phenological stages.

Stages	RMSE (days)	R
V1	8.41	0.70
VT	6.59	0.64
R1	3.78	0.53
R4	5.60	0.53
R6	6.33	0.61
V1-R1	8.43	0.45
R1-R6	5.56	0.66
V1-R6	7.39	0.74

Table 1. Accuracy assessment of the estimated phenological date and period against the ground-based observations by calculating RMSE and R for corn in northeastern China.

5.1.3. The comparison between the model from northeastern China and the field sites from Nebraska

The shape models of corn which were built on the data from the field sites of University of Nebraska-Lincoln and the agricultural meteorological stations in northeastern China were compared and shown in **Figure 4**. The needed APTT time of corn in two study areas was about the same, while there were some differences between the derived time-series VI curves from the study areas in the USA and China [11]. The time-series VI curves from the field sites of University of Nebraska-Lincoln and the Corn Belt in the USA were generally in agreement with each other: the curves reach the peak and then drop quickly after a slow decline, while the curves derived from corn field in northeastern China drop rapidly after reaching the peak [11].

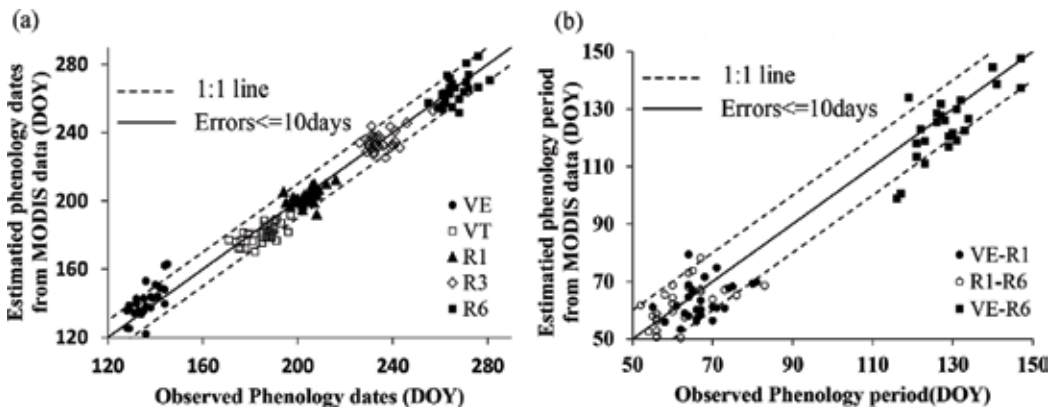

Figure 3. Comparison of phenological dates of corn in the stations of northeastern China between ground-based observation data and MODIS-derived estimation.

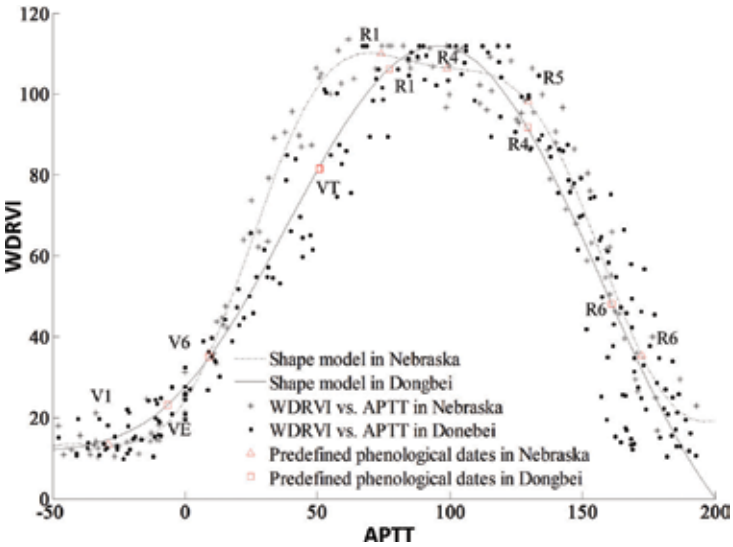

Figure 4. Comparison of shape model of corn from the stations of northeastern China and field sites in Nebraska.

The diameters of the farmland in the Corn Belt of USA are usually greater than 250 m, the size of MODIS pixels in red and near-infrared bands, and the VI observations from MODIS were less influenced by mixed pixels. Therefore, the time-series VI curves from this area may be closer to reality, which decrease rapidly after a slow decline following the peak. While in northeastern China, the size of the cropland is usually smaller than 250 m, the mixed pixels may cause error to time-series VI curves. Although the shape of the time-series VI curves in some stations of northeastern China is to some extent consistent with those in the Corn Belt of USA, the shape model from northeastern China was built by fitting the data with mixed pixels and pure pixels, which results in the loss of some characteristic details of the time-series VI curves.

The predefined APTT time required for some phenological stages in the field of the USA and China is about the same, such as the R1 and R6 stages, while there are obvious differences at some stage. The needed APTT time for the corn from the Corn Belt of USA reached V1 stage even less than the needed APTT time for VE stage of corn from the agricultural meteorological stations in northeastern China. One reason may be the description of phenology for corn in the two regions is different. In addition, the differences in the corn varieties and genotype may also contribute to difference of the need APTT.

5.2. Results in northeastern China with data fusion of MODIS and Landsat images

5.2.1. Shape model

As in northeastern China, the size of the cropland is usually smaller than 250 m, the mixed pixels may cause error in time-series VI curves. Data fusing of 8-day composition MODIS images and Landsat images was conducted with the StarFM method to get the 8-day composition data with the spatial resolution like Landsat and with the temporal resolution like MODIS.

The smoothed WDRVI curve of corn field in each meteorological station was calculated from time-series fused data and MODIS data, respectively. The smoothed WDRVI curves with peak larger than 80 in 2013 were selected to establish the corn shape model in the study area to reduce the impact of mixed pixels, noises, environmental stress on crop growth and phenology (**Figure 5**).

5.2.2. Phenology estimation results

The error of five corn growth stages estimated from fused data is basically within 10 days (**Figure 6**). The RMSE of the results varies from 2.63 to 6.23. The estimation accuracy is higher than that derived from MODIS data only (3.78–8.41 days) (**Table 2**). Similar to the results in the field sites of the University of Nebraska Lincoln [11], lower estimation accuracy was observed at the beginning and end of the growing season (such as V1, R6) than that at the middle stage of the growing season when vegetation cover reaches the peak, such as R1 stage (**Table 2**).

5.2.3. The comparison between the model from the MODIS only data and the data fusion of Landsat and MODIS

The estimation accuracy of five corn growth stages from MODIS data only is lower than that derived from MODIS and Landsat fused data. As the mixed pixels in MODIS data may include artificial surface, water bodies, fallow land, etc. around the cropland, which may result in a decrease in the WDRVI data of the entire MODIS pixel where the station locates and influence the phenology estimation accuracy. Similarly, the forests area around the cropland might increase the WDRVI value in the early and late stages of crop growth. By sampling 9 × 9 window of the 30 m pixels (270 × 270 m) centered on the farmland of the station, **Figure 7** shows the time-series WDRVI curves derived from MODIS data only and the fused data in 2013. The trend of the fused time-series WDRVI data is the same with that of MODIS derived data, as cloud and other noise affect the MODIS data as well as the fused result with MODIS

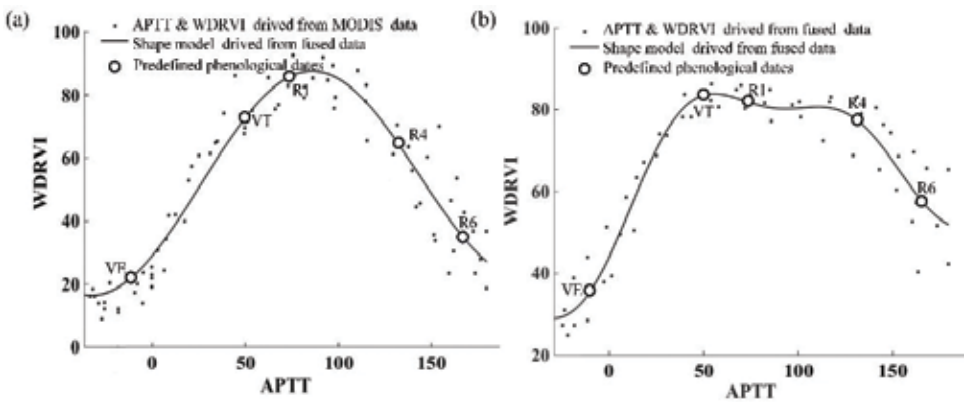

Figure 5. The shape model of corn derived from (a) MODIS data only and (b) fused data with MODIS and Landsat data in 2013 by curve fitting with characteristic points indicating the specific phenological stages.

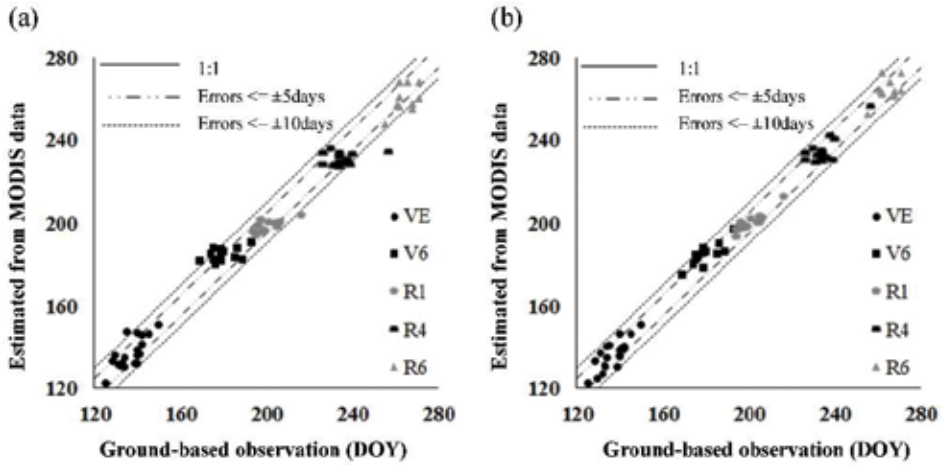

Figure 6. Comparison of phenological dates of corn in the stations of northeastern China between ground-based observation data and MODIS-derived estimation.

Stages	Fused data RMSE(days)	MODIS only RMSE(days)
V1	6.07	7.91
VT	6.23	7.18
R1	2.63	4.77
R4	4.30	6.40
R6	5.54	8.39

Table 2. Accuracy assessment of the estimated phenological date against the ground-based observations by calculating RMSE for corn in 2013.

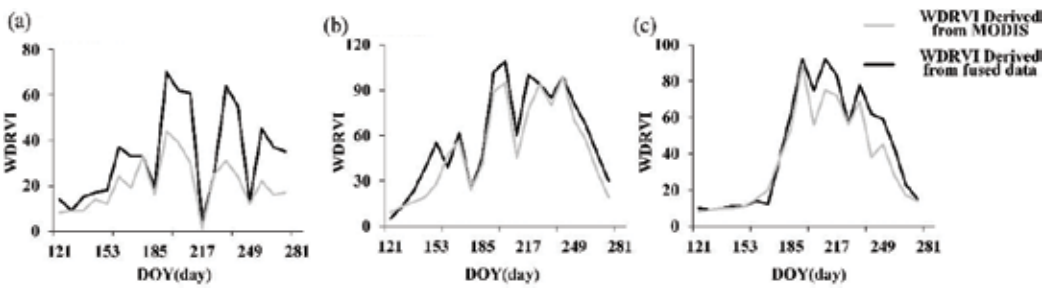

Figure 7. The time-series WDRVI curves of three stations derived from MODIS data only and fused data in 2013.

data and Landsat data. However, the fusion of MODIS and Landsat data can reduce the influence of mixed pixels to a certain extent. For example, station 1 is mixed with cultivated land and artificial surface, in which the proportion of artificial surface in the two sites 9 × 9 windows was 50.6%. The fused data of this site are higher than the observed values of MODIS images.

Station 2 and station 3 are mixed with cultivated land and fallow land. The fused data of these two sites are higher than that obtained from MODIS images, especially in the middle of growing stage when WDRVI value is high in cropland, but low in fallow land.

6. Conclusion

This chapter applied a hybrid remote sensing-based crop phenology estimation method for corn that incorporated the simulation concept of crop growth models with the shape-model fitting concept of the TSF method developed by Sakamoto et al. [26], in Northeast China (Jilin and Liaoning Provinces), which is an important grain production base in China. Compared to the field phenology observations from the agriculture meteorological stations, the corn phenology estimation accuracy in Northeast China using only MODIS data is much lower than that in the US field sites (RMSE of corn phenology estimate in Northeast China ranges from 3.78 to 8.41 days). The main reason might be the small size of single piece of cropland in northeastern China, which led to the mixed MODIS pixels. Accordingly, Landsat and MODIS data fusion methods were applied to get time-series images with Landsat-like spatial resolution and MODIS-like temporal resolution, and quantitative and qualitative validation was conducted to evaluate and verify the accuracy of the data fusion. The results show that data fusion of Landsat and MODIS ensured the temporal resolution of time-series images, to some extent, improved the spatial resolution and decreased the influence of mixed pixels.

Acknowledgments

The study was supported by the National Key Research and Development Program of China (Grant No. 2017YFC1502406-03), the National Natural Science Foundation of China (Grant No. 41401487) and Excellent Agricultural Scientist Fund & Open Research Fund Program of Key Laboratory of Agricultural Remote Sensing, Ministry of Agriculture (Grant No. 2016007).

Author details

Linglin Zeng[1,2]* and Daxiang Xiang[3]

*Address all correspondence to: zenglinglin@whu.edu.cn

1 School of Resource and Environmental Science, Wuhan University, Wuhan, China

2 Collaborative Innovation Center of Geospatial Technology, Wuhan, China

3 Changjiang River Scientific Research Institute, Changjiang River Water Resources Commission, Wuhan, China

References

[1] Brown ME, de Beurs KM, Marshall M. Global phenological response to climate change in crop areas using satellite remote sensing of vegetation, humidity and temperature over 26 years. Remote Sensing Environment. 2012;**126**:174

[2] Brown JF, Wardlow BD, Tadesse T, Hayes MJ, Reed BC. The vegetation drought response index (VegDRI): A new integrated approach for monitoring drought stress in vegetation. GISCI Remote Sensing. 2008;**45**:16

[3] Peña-Barragán JM, Ngugi MK, Plant RE, Six J. Object-based crop identification using multiple vegetation indices, textural features and crop phenology. Remote Sensing Environment. 2011;**115**:1301

[4] Schwartz MD. Green-wave phenology. Nature. 1998;**394**:839

[5] Cleland EE, Chuine I, Menzel A, Mooney HA, Schwartz MD. Shifting plant phenology in response to global change. Trends in Ecology & Evolution. 2007;**22**:357

[6] Pettorelli N, Vik JO, Mysterud A, Gaillard J, Tucker CJ, Stenseth NC. Using the satellite-derived NDVI to assess ecological responses to environmental change. Trends in Ecology & Evolution. 2005;**20**:503

[7] Cong N, Wang T, Nan H, Ma Y, Wang X, Myneni RB, Piao S. Changes in satellite-derived spring vegetation green-up date and its linkage to climate in China from 1982 to 2010: A multimethod analysis. Global Change Biology. 2013;**19**:881

[8] Sakamoto T, Gitelson AA, Arkebauer TJ. MODIS-based corn grain yield estimation model incorporating crop phenology information. Remote Sensing Environment. 2013;**131**:215

[9] Funk C, Budde ME. Phenologically-tuned MODIS NDVI-based production anomaly estimates for Zimbabwe. Remote Sensing Environment. 2009;**113**:115

[10] Bolton DK, Friedl MA. Forecasting crop yield using remotely sensed vegetation indices and crop phenology metrics. Agricultural and Forest Meteorology. 2013;**173**:74

[11] Zeng L, Wardlow BD, Wang R, Shan J, Tadesse T, Hayes MJ, Li D. A hybrid approach for detecting corn and soybean phenology with time-series MODIS data. Remote Sensing Environment. 2016;**181**:237

[12] Spitters CJT, van Keulen H, van Kraalingen DWG. A simple and universal crop growth simulator: SUCROS87. In: Rabbinge R, Ward SA, van Laar HH, editors. Simulation and Systems Management in Crop Protection. Wageningen: Centre for Agricultural Publishing and Documentation; 1989

[13] Diepen CV, Wolf J, Keulen HV, Rappoldt C. WOFOST: A simulation model of crop production. Soil Use and Management. 1989;**5**:16

[14] Yang HS, Dobermann A, Lindquist JL, Walters DT, Arkebauer TJ, Cassman KG. Hybrid-maize—A maize simulation model that combines two crop modeling approaches. Field Crop Research. 2004;**87**:131

[15] Setiyono TD, Weiss A, Specht J, Bastidas AM, Cassman KG, Dobermann A. Understanding and modeling the effect of temperature and daylength on soybean phenology under high-yield conditions. Field Crop Research. 2007;**100**:257

[16] Bhatia AK. Crop growth simulation modeling. In: Basu SKKN, editor. Modelling and Simulation of Diffusive Processes. Cham, Switzerland: Springer International Publishing; 2014. p. 315

[17] White MA, Nemani RR. Real-time monitoring and short-term forecasting of land surface phenology. Remote Sensing Environment. 2006;**104**:43

[18] Delbart N, Le Toan T, Kergoat L, Fedotova V. Remote sensing of spring phenology in boreal regions: A free of snow-effect method using NOAA-AVHRR and SPOT-VGT data (1982-2004). Remote Sensing Environment. 2006;**101**:52

[19] Fischer A. A model for the seasonal variations of vegetation indices in coarse resolution data and its inversion to extract crop parameters. Remote Sensing Environment. 1994;**48**:220

[20] Lloyd D. A phenological classification of terrestrial vegetation cover using shortwave vegetation index imagery. International Journal of Remote Sensing. 1990;**11**:2269

[21] Balzter H, Gerard F, George C, Weedon G, Grey W, Combal B, Bartholom EE, Bartalev S, Los S. Coupling of vegetation growing season anomalies and fire activity with hemispheric and regional-scale climate patterns in central and east Siberia. Journal of Climate. 2007;**20**:3713

[22] Tateishi R, Ebata M. Analysis of phenological change patterns using 1982-2000 advanced very high resolution radiometer (AVHRR) data. International Journal of Remote Sensing. 2004;**25**:2287

[23] Reed BC, Brown JF, VanderZee D, Loveland TR, Merchant JW, Ohlen DO. Measuring phenological variability from satellite imagery. Journal of Vegetation Science. 1994;**5**:703

[24] Zhang X, Friedl MA, Schaaf CB, Strahler AH, Hodges JCF, Gao F, Reed BC, Huete A. Monitoring vegetation phenology using MODIS. Remote Sensing Environment. 2003;**84**:471

[25] Sakamoto T, Yokozawa M, Toritani H, Shibayama M, Ishitsuka N, Ohno H. A crop phenology detection method using time-series MODIS data. Remote Sensing Environment. 2005;**96**:366

[26] Sakamoto T, Wardlow BD, Gitelson AA, Verma SB, Suyker AE, Arkebauer TJ. A two-step filtering approach for detecting maize and soybean phenology with time-series MODIS data. Remote Sensing Environment. 2010;**114**:2146

[27] Xu H, Twine T, Yang X. Evaluating remotely sensed phenological metrics in a dynamic ecosystem model. Remote Sensing-Basel. 2014;**6**:4660

[28] Wardlow BD, Kastens JH, Egbert SL. Using USDA crop progress data for the evaluation of greenup onset date calculated from MODIS 250-meter data. Photogrammetric Engineering & Remote Sensing. 2006;**11**:1225

[29] Gitelson AA. Wide dynamic range vegetation index for remote quantification of biophysical characteristics of vegetation. Journal of Plant Physiology. 2004;**161**:165

[30] Gitelson AA, Wardlow BD, Keydan GP, Leavitt B. An evaluation of MODIS 250-m data for green LAI estimation in crops. Geophysical Research Letters. 2007;**34**:L20403

[31] Zeng L, Wardlow BD, Tadesse T, Shan J, Hayes MJ, Li D, Xiang D. Estimation of daily air temperature based on MODIS land surface temperature products over the corn belt in the US. Remote Sensing-Basel. 2015;**7**:951

[32] Chen J, Chen J, Liao A, Cao X, Chen L, Chen X, He C, Han G, Peng S, Lu M. Global land cover mapping at 30 m resolution: A POK-based operational approach. ISPRS Journal of Photogrammetry & Remote Sensing. 2015;**103**:7

[33] Gao F, Masek J, Schwaller M, Hall F. On the blending of the Landsat and MODIS surface reflectance: Predicting daily Landsat surface reflectance. IEEE Transactions on Geoscience and Remote Sensing. 2006;**44**:2207

[34] Walker JJ, De Beurs KM, Wynne RH, Gao F. Evaluation of Landsat and MODIS data fusion products for analysis of dryland forest phenology. Remote Sensing Environment. 2012;**117**:381

[35] Asseng S, Turner NC. Modelling genotype environment management interactions to improve yield, water use efficiency and grain protein in wheat. In: Spiertz JHJ, Struik PC, van Laar HH, editors. Scale and Complexity in Plant Systems Research: Gene-Plant-Crop Relations. Dordrecht, The Netherlands: Springer; 2007. p. 93

[36] Soltani A, Maddah V, Sinclair TR. SSM-wheat: A simulation model for wheat development, growth and yield. International Journal of Plant Production. 2013;**7**:711

[37] Tollenaar M, Daynard TB, Hunter RB. Effect of Temperature on Rate of Leaf Appearance and Flowering Date in Maize. Crop Science; 1979;**19**:363

[38] Abendroth LJ, Elmore RW, Boyer MJ, Marlay SK. Corn Growth and Development. Ames: Iowa State University, University Extension; 2011

[39] Bannayan M, Hoogenboom G, Crout NMJ. Photothermal impact on maize performance: A simulation approach. Ecological Modelling. 2004;**180**:277

[40] Cutforth S. A temperature response function for corn development. Agricultural Forest Meteorology. 1990;**50**:159

[41] Schr Der U, Sondgerath D. The concept of biological time for computing the switching points of a growth model for winter wheat. Ecological Modelling. 1996;**88**:1

[42] Fleisher DH, Shillito RM, Timlin DJ, Kim SH, Reddy VR. Approaches to modeling potato leaf appearance rate. Agronomy Journal. 2006;**98**:522

[43] Yin X, Kropff MJ, McLaren G, Visperas RM. A nonlinear model for crop development as a function of temperature. Agricultural Forest Meteorology. 1995;**77**:1

[44] Streck NA, Lago I, Gabriel LF, Samboranha FK. Simulating maize phenology as a function of air temperature with a linear and a nonlinear model. Pesquisa Agropecuária Brasileira. 2008;**43**:449

[45] Wang E, Engel T. Simulation of phenological development of wheat crops. Agricultural Systems. 1998;**58**:1

[46] Masle J, Doussinault G, Farquhar GD, Sun B. Foliar stage in wheat correlates better to photothermal time than to thermal time. Plant, Cell & Environment. 1989;**12**:235

[47] Deen W, Hunt LA, Swanton CJ. Photothermal time describes common ragweed (*Ambrosia artemisiifolia L.*) phenological development and growth. Weed Science. 1998;**46**:561

[48] Ellis RH, Roberts EH, Summerfield RJ. Photothermal time for flowering in faba bean (*Vicia faba*) and the analysis of potential vernalization responses. Annals of Botany-London. 1988;**61**:73

[49] Chen J, Jönsson P, Tamura M, Gu Z, Matsushita B, Eklundh L. A simple method for reconstructing a high-quality NDVI time-series data set based on the Savitzky-Golay filter. Remote Sensing Environment;**91**:332-344

[50] Wardlow BD, Egbert SL. Large-area crop mapping using time-series MODIS 250 m NDVI data: An assessment for the U.S. Central Great Plains. Remote Sensing Environment. 2008;**112**:1096

[51] Wardlow BD, Egbert SL, Kastens JH. Analysis of time-series MODIS 250 m vegetation index data for crop classification in the U.S. Central Great Plains. Remote Sensing Environment. 2007;**108**:290

Chapter 2

Despeckling of Multitemporal Sentinel SAR Images and Its Impact on Agricultural Area Classification

Vladimir Lukin, Oleksii Rubel, Ruslan Kozhemiakin,
Sergey Abramov, Andrii Shelestov,
Mykola Lavreniuk, Mykola Meretsky,
Benoit Vozel and Kacem Chehdi

Additional information is available at the end of the chapter

http://dx.doi.org/10.5772/intechopen.72577

Abstract

This chapter addresses an important practical task of classification of multichannel remote sensing data with application to multitemporal dual-polarization Sentinel radar images acquired for agricultural regions in Ukraine. We first consider characteristics of dual-polarization Sentinel radar images and discuss what kind of filters can be applied to such data. Several examples of denoising are presented with analysis of what properties of filters are desired and what can be provided in practice. It is also demonstrated that the use of preliminary denoising produces improvement of classification accuracy where despeckling that is more efficient in terms of standard filtering criteria results in better classification.

Keywords: Sentinel, dual polarization, radar image, classification, agricultural area

1. Introduction

Remote sensing (RS) systems have become tools of intensive everyday use for numerous applications in ecology, forestry, oceanology, agriculture, and disaster monitoring [1–5]. This is due to significant advances and achievements in science and technology. Firstly, imagers' characteristics such as spatial resolution, swath width, receiver input signal-to-noise ratio, bandwidth and throughput, and near real-time data delivery have improved considerably. Secondly, it has become possible to process more data both onboard and on-land in real time

or quickly enough. Thirdly, many existing spaceborne RS systems provide data with frequency needed (convenient) for performing monitoring for scenes under interest.

In particular, such monitoring is possible using RS data by Sentinel-1 A/B two-polarization synthetic aperture radar (SAR) that has been put into operation recently [6]. There are several positive features of data (images) provided by this SAR. Firstly, radars are known to be able to operate well (to acquire images) during day and night in almost all weather conditions [7, 8]. Secondly, polarization radars (Sentinel SAR produces VV and VH polarization images) offer more opportunities for effectively solving different classification tasks than single-channel radars [8, 9]. Thirdly, Sentinel SAR is characterized by spatial resolution about 10 m, and data are available free of charge for noncommercial use. Finally, Sentinel satellites carry out global coverage with 6-day revisit frequency.

All together, these facilities of Sentinel SAR provide excellent prerequisites for solving tasks of agricultural monitoring where multitemporal radar images can be employed either separately or jointly with other types of images including optical and infrared ones [10–12]. However, radar images also have certain drawbacks. One of them is the presence of noise-like phenomenon called speckle [7, 13]. Although speckle intensity and probability density function (PDF) can be different depending upon the number of looks and other factors [7, 14, 15], speckle is the main factor that deteriorates radar image quality and prevents their efficient processing [16, 17] and classification [18].

Taking this into account, speckle noise has to be reduced. Speckle removal (despeckling) is not an easy task. There are several known peculiarities of speckle. Firstly, it is supposed to be pure multiplicative noise [7, 13]. Secondly, it has PDF that is usually non-Gaussian [7, 16]. Thirdly, speckle often possesses spatial correlation [19] that has to be taken into account.

There are many existing image processing software packages, which allow performing radar image pre-filtering such as ESA SNAP toolbox, ENVI, etc. In particular, they provide such good filters as Frost, Lee, refined Lee, etc. [6, 13]. However, there are three aspects worth taking into consideration. Firstly, selection of a proper filter and its parameters (scanning window size, thresholds, etc.) should be done based on careful analysis of speckle properties for SAR data supposed to be used (Sentinel SAR data in our case). Secondly, there are good despeckling filters that have not been yet implemented in toolboxes including filters based on discrete cosine transform (DCT) and/or that belong to a new family of nonlocal filters [20, 21]. Thirdly, efficiency of filtering should be assessed with respect to a final task as crop or agricultural area classification in our case where type of data, methodology of classifier learning, and other factors have essential impact on final classification [9].

The goal of this chapter is threefold. Analysis of speckle characteristics has to be carried out, and the obtained data can be considered as a prerequisite for choosing a proper technique (or several possible methods) of radar image processing. Performance of different despeckling methods has to be evaluated and compared where emphasis should be done on modern techniques. Besides, our intention is to assess the impact of filtering techniques on crop classification accuracy and provide practical recommendations.

2. Image and noise model and its parameters

In this book chapter, we focus on processing Sentinel SAR images. It is known from the literature that the dominant factor degrading SAR image quality is speckle which is supposed to be a specific type of pure multiplicative noise [7, 14], i.e.:

$$I^n_{k\,ij} = I^{true}_{k\,ij}\,\mu_{k\,ij},\ i = 1, \ldots, I, j = 1, \ldots, J, k = 1, \ldots, K, \tag{1}$$

where $I^n_{k\,ij}$ denotes the *ij*th sample of the *k*th component for a considered multichannel image, $\mu_{k\,ij}$ is the *ij*th value of the multiplicative noise in the *k*th component image, I^{true}_{kij} is the true value for the *kij*th pixel, *I* and *J* define the data size, and *K* denotes the number of components ($K = 2$ for two-polarization data that are mainly considered below). Random variable $\mu_{k\,ij}$ is supposed to have unity mean and variance $\sigma^2_{\mu k}$ that, in general, can be different for different component images.

To the best of our knowledge, the assumption on pure multiplicative nature of speckle in Sentinel images has not been tested. Other properties of speckle such as spatial correlation have not been thoroughly analyzed yet as well. Thus, we have performed a preliminary analysis. First, our study has been performed for manually selected image fragments. Examples of such fragments (all of rectangular shape) are shown by frames for vertical-vertical (VV) and vertical-horizontal (VH) polarization components of SAR image fragments presented in **Figure 1**. Analysis has confirmed the assumption that speckle is pure multiplicative. The estimated value of its relative variance $\sigma^2_{\mu k}$ is about 0.05 for both components ($k = 1$ and 2), i.e., we deal with multi-look data. Automatic blind estimation [19] has resulted in almost the same estimates of $\sigma^2_{\mu k}$ that varied only slightly (no more than 10–15% for 19 analyzed VV and 19 studied VH images) (**Figure 2**).

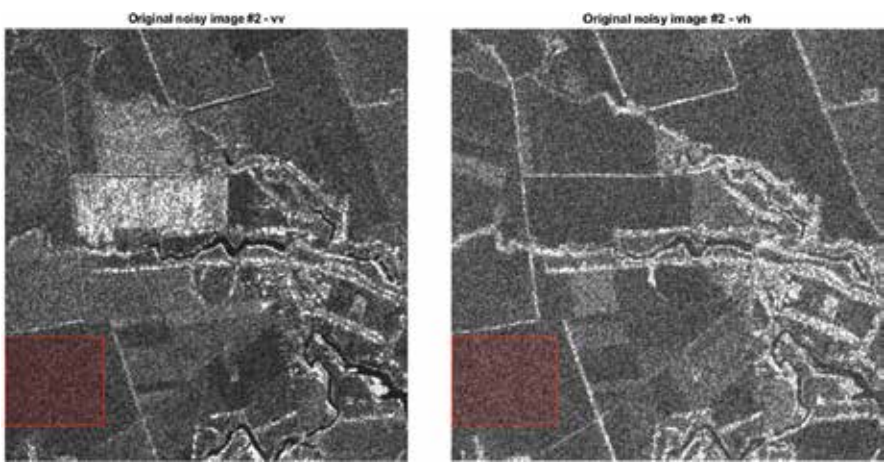

Figure 1. An example of Sentinel SAR images in Kiev region of Ukraine with marked homogeneous regions.

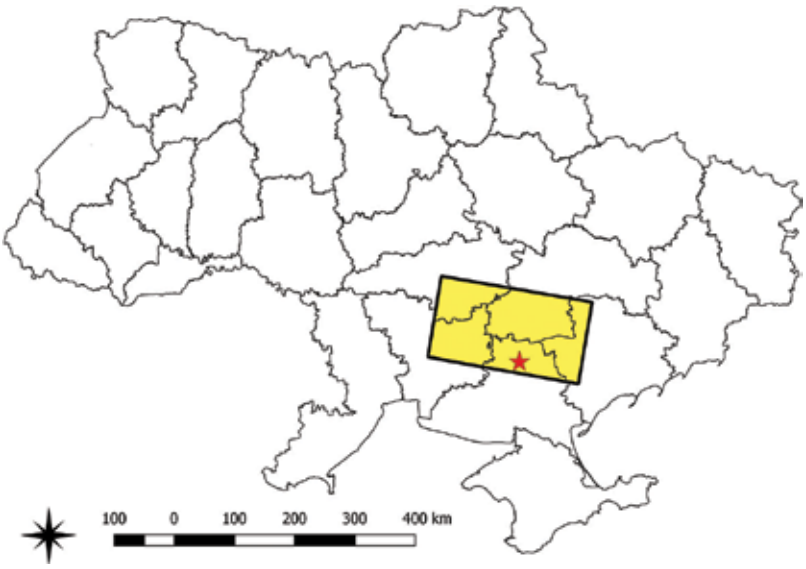

Figure 2. The sensed region (**Figure 1**) in Ukraine to south from Kiev marked in map.

Visual inspection of images in **Figure 1** also shows that they are similar and different simultaneously. The objects might have different contrasts with respect to background or neighbor objects. Some objects can be present in image with one polarization and be absent in image of other polarizations. For example, there is a rectangular shape high-intensity object in the central part of VV image (**Figure 1**, left) that is not observed in VH image (**Figure 1**, right).

Cross-correlation factor values for VV and VH polarizations (under condition that they are jointly registered or superimposed with high accuracy) are about 0.8. Speckle has been found practically uncorrelated between component images. These properties will be taken into account in consideration of filters to be applied.

Another important property of speckle is its spatial correlation. There are different approaches to describe and analyze it. One approach is to obtain 2D autocorrelation functions in homogeneous image areas [7, 22]. Under condition of *a priori* known $\sigma^2_{\mu k}$, such areas can be detected by comparing relative variance $\sigma^2_{k\,r\,loc}$ (calculated by Eq. 2) to $Th \times \sigma^2_{\mu k}$. Here, it is supposed that the considered area is of rectangular shape defined by indices $i_{\min}; i_{\max}$ in one direction and $j_{\min}; j_{\max}$ in the other direction; Th is threshold that can be set approximately equal to 1.2; $\bar{I}_{kloc}$ is the local mean (calculated by Eq. 3):

$$\sigma^2_{k\,r\,loc} = \sum_{i=i_{\min}}^{i_{\max}} \sum_{j=j_{\min}}^{j_{\max}} \left(I^n_{k\,ij} - \bar{I}_{kloc}\right)^2 / \left((i_{\max} - i_{\min} + 1)(j_{\max} - j_{\min} + 1)\bar{I}^2_{kloc}\right), \tag{2}$$

$$\bar{I}_{kloc} = \sum_{i=i_{\min}}^{i_{\max}} \sum_{j=j_{\min}}^{j_{\max}} I^n_{k\,ij} / \left((i_{\max} - i_{\min} + 1)(j_{\max} - j_{\min} + 1)\right). \tag{3}$$

http://dx.doi.org/10.5772/intechopen.72577

Below we characterize speckle correlation in another manner, using spectrum in DCT domain. The reasons for this will become clear later, in Section 3. Suppose that we have found N homogeneous image blocks of size 8×8 pixels, i.e., blocks for which

$$\sigma_{k\,n}^2 = \sum_{i=i_{\min}}^{i_{\min}+7} \sum_{j=j_{\min}}^{j_{\min}+7} \left(I_{k\,ij}^n - \bar{I}_{kn}\right)^2 / \left(64\bar{I}_{kn}^2\right) \le Th \times \sigma_{\mu k}^2, \tag{4}$$

where $\bar{I}_{kn}$ is the local mean for the nth block. 2D DCT is then calculated for each nth block with obtaining $D_n(l,m), l = 1, \ldots, 8; m = 1, \ldots, 8$ where lm are indices of spatial frequencies, l = 1 and m = 1 relate to DC (direct current) term proportional to the block mean, and alternating current (AC) DCT components with larger l and m relate to higher spatial frequencies. Power spectrum shape estimate is obtained through Eq. 5. Then, the normalized DCT spectrum is obtained through Eq. 6:

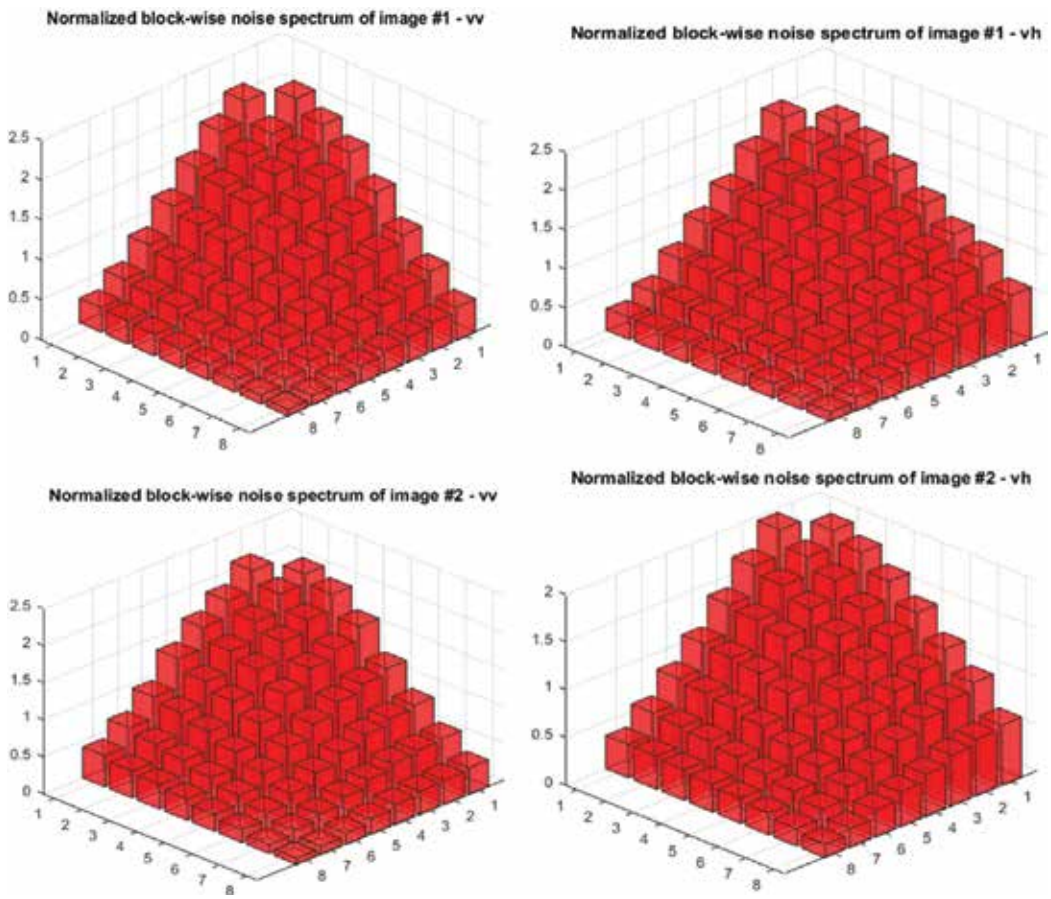

Figure 3. Examples of estimated normalized DCT spectra in 8×8 blocks.

$$\widehat{D}_p(l,m) = \sum_{n=1}^{N} \left(D_m^2(l,m)/D_n^2(1,1)\right)/n, l = 1, \ldots, 8; m = 1, \ldots, 8, \tag{5}$$

$$\widehat{D}_{norm}(l,m) = 63\widehat{D}_p(l,m)/\left(\sum_{l=1}^{8}\sum_{m=1}^{8}\left(\widehat{D}_p(l,m)\right) - \widehat{D}_{p}(1,1)\right), l = 1, \ldots, 8; m = 1, \ldots, 8, \tag{6}$$

where, in fact, $\widehat{D}_{norm}(l,m)$ is not of interest for us since it is not taken into account in denoising (see the details in Section 3). There exist also other methods of estimation [23] including blind methods [24, 25].

The obtained estimates are presented in **Figure 3** for both polarization components. Bin heights that reflect spectrum values clearly demonstrate that speckle is spatially correlated (spectrum values are considerably smaller for higher spatial frequencies). These correlation properties are quite similar for VV and VH polarizations as well as for different images analyzed.

Thus, it is possible to state that speckle in Sentinel SAR images is practically pure multiplicative with $\sigma_{\mu k}^2 \approx 0.05, k = 1, 2$. Its distribution is not Gaussian—this has been shown by Gaussianity tests. Speckle is spatially correlated and practically independent for different polarizations. All these properties should be taken into consideration at image processing stage.

3. Filters and their impacts on images

First of all, let us recall requirements to filters applied to radar image processing. The main requirement is, certainly, effective suppression of speckle noise. However, edge/detail/texture preservation is important as well. Additional requirement is to retain mean level in homogeneous image regions (some filters do not perform this automatically, without specific correction [26]). This is important since mean in homogeneous regions is strictly connected with calibration [7]. Finally, computational efficiency is important, especially in the considered application since standard size of Sentinel SAR images we deal with is large, ~25k × 16k pixels. Note that some requirements are contradictory [27]. In particular, it is difficult to provide a trade-off between speckle suppression and edge/detail/texture preservation.

If we deal with multichannel images (multispectral, hyperspectral, multipolarization ones), there are two main approaches to their filtering [28]. The first is component-wise processing, i.e., if each component image is processed as single-channel image [13]. This approach is, in general, simpler. There exist more methods. It is easier to take into account speckle properties including its spatial spectrum. Processing of multichannel images can be done in parallel.

The second approach is 3D (vectorial) processing [20, 29]. This group of filters is able to take correlation of image components into account. This, under certain conditions, allows improving the efficiency of noise suppression. However, these methods can run into problems of different properties of noise (noise variance can be not the same, spectrum can be not identical, etc.). Then, either special methods of component image preprocessing are needed [30], or the use of 3D processing benefits in full extent becomes impossible.

Below we consider representatives of both groups of methods. All studied filters are based on DCT. The reasons for this are the following. Firstly, DCT is one of the best data decorrelating transforms approaching Karhunen-Loeve transform. This property is important in denoising and data representation. Secondly, DCT denoising is carried out in sliding blocks [31]. Due to this, it is easily adapted to signal-dependent noise [32] and its spatial correlation [28]. Thirdly, 2D DCT is a standard operation in image processing (in particular, in compression), and its efficient software and hardware implementations exist.

Thus, in addition to known despeckling techniques available in ESA SNAP toolbox, we also study filtering techniques based on DCT. For all modifications considered below, the main principles of processing are the same. Denoising is carried out in blocks of square shape, usually of size 8×8 pixels although other variants are possible. In each block, direct 2D DCT is performed. Then, amplitudes of obtained DCT coefficients are compared to thresholds, and one or another type of threshold operation is accomplished (the coefficient with indices (1,1) is remained unchanged in any case). Then, inverse 2D DCT is done, and as the result, filtered values are obtained for all pixels that belong to a given block.

There are different modifications of DCT-based denoising that concern block overlapping and threshold type. Denoising can be done with nonoverlapping, partly overlapping, and fully overlapping blocks. In the latter case, neighbor blocks are shifted by only one pixel with respect to each other in horizontal or vertical direction. Processing with full overlapping of blocks takes more time compared to processing with partly overlapping or nonoverlapping blocks. But the use of fully overlapping blocks provides the best efficiency of filtering in terms of standard quantitative criteria as peak signal-to-noise ratio (PSNR) and visual quality metrics. So, we will further employ this variant of DCT-based denoising. Note that for most image pixels, one has 64 filtered values coming from different block positions. They are averaged (although other methods of aggregation are possible).

There are hard, soft, and combined types of threshold. Below we employ the former type since hard thresholding is the most simple and efficient. This means that if a DCT coefficient is larger than a corresponding threshold, then it is remained unchanged. Otherwise, a zero value is assigned.

Multiplicative nature of speckle and its spatial correlation can be taken into consideration in different manners. Consider possible variants more in detail. If processing is component-wise, signal-dependent (locally adaptive) and frequency-dependent thresholds can be used. The local thresholds in an nth block are determined as

$$T(n,l,m) = \beta\sigma(n)D^{0.5}_{norm}(l,m), l = 1,\ldots,8; m = 1,\ldots,8, \tag{7}$$

where $\sigma(n)$ is local noise standard deviation for the nth block that can be approximately calculated as $\sigma(n) = \sigma_\mu \bar{I}_n$ (index k is omitted for simplicity) and β is the filter parameter usually set equal to 2.7 for hard thresholding [32]. This approach to filtering will be further referred as **Filter 1**.

Another way of component-wise processing mentioned earlier is based on utilizing homomorphic or variance-stabilizing transforms. A general form of logarithmic-type homomorphic transform (HT) is $I^h_{ij} = c\log_d\left(I^n_{ij}\right)$ [7, 33] where c and d are transform parameters that are both

larger than unity. These parameters can be chosen in different ways depending upon certain conditions. The main aspect here is that in multilook SAR images subject to such a HT, speckle converts to pure additive noise with non-Gaussian PDF. Its variance can be calculated as $\sigma_h^2 \approx c^2\sigma_\mu^2/(\ln(\mathrm{d}))^2$.

After this direct HT, a DCT-based filter version for additive noise is applied. Since additive noise is spatially correlated as well and its normalized DCT spectrum is practically the same as for original data, frequency-dependent thresholds are determined as

$$T(n,l,m) = \beta\sigma_h D_{norm}^{0.5}(l,m), l = 1,\ldots,8; m = 1,\ldots,8, \tag{8}$$

where the recommended β is the same as earlier. After filtering, inverse HT is performed, and it is desired to carry out mean level correction [26]. This variant of filtering will be further referred as **Filter 2**. According to our studies, it performs slightly worse compared to **Filter 1**. One reason is that additional distortions are introduced by direct and inverse HTs.

Joint processing of two component images that we plan to perform for the considered application can be carried out in two ways. The first one [20] is to use one component as basic one and to perform data correction for the second component image with providing equal mean values for each block of these images. Then, 3D DCT is performed in each block, and $\sigma(n)$ is set according to (4) where $\overline{I}_n$ from the basic image is used for its calculation.

Another, practically equivalent, variant is to carry out variance-stabilizing transforms separately for each component images in such a manner that $\sigma_{h1}^2 = \sigma_{h2}^2$. If $\sigma_{\mu 1}^2 \approx \sigma_{\mu 2}^2$ as we have in our case, parameters of logarithmic transform c and d can be the same. After this, 3D is done in each block, then thresholding follows, after this inverse 3D DCT is carried out. Due to separability of 3D transform into two-element 1D DCT and 2D DCT, obtaining of sum and difference images is possible. Then, their separate processing is applied with further inverse two-element DCT for each pixel. Threshold (8) is used in this case. The described denoising method is further called **Filter 3**.

There is one condition that should be satisfied for both presented 3D filtering techniques. Normalized spectra for component images should be the same or, at least, almost identical. Preliminary analysis carried out in Section 2 has demonstrated that this condition is satisfied. So, we have averaged estimates of normalized spectra obtained for all analyzed fragments of 19 VV and 19 VH radar images.

It is worth recalling that methods for predicting noise suppression efficiency have been proposed previously [27, 34]. Equivalent noise variance can be determined for original image with speckle as

$$\widehat{\sigma}_{eq\,k}^2 = \left(\sum_{i=1}^{I}\sum_{j=1}^{J}\sigma_{\mu\,k}^2 I_{kij}^{true}\right)/(IJ) \approx \left(\sum_{i=1}^{I}\sum_{j=1}^{J}\sigma_{\mu\,k}^2\left(I_{kij}^{n}\right)^2\right)/(IJ). \tag{9}$$

Then, the proposed methods of efficiency prediction are able to either predict the ratio $MSE_k^{out}/\sigma_{eq\,k}^2$ where

$$MSE_k^{out} = \sum_{i=1}^{I}\sum_{j=1}^{J}\left(I_{k\,ij}^{f} - I_{kij}^{true}\right)^2/(IJ), k = 1, \ldots, K \tag{10}$$

and $I_{k\,ij}^{f}, i = 1, \ldots, I; j = 1, \ldots, J; k = 1, \ldots, K$ is the kth component image after despeckling or improvement of PSNR (IPSNR) equal to $10\log_{10}\left(\sigma_{eq\,k}^2/MSE_k^{out}\right)$ [35, 36]. Experiments carried out with 512×512 pixel fragments of Sentinel SAR images have shown that IPSNR for **Filter 1** varies within the limits from 5 to 12 dB, i.e., images enhance sufficiently.

Let us prove this by two examples. **Figure 4a** presents original image with VV polarization. The output of Filter 1 is shown in **Figure 4b**. In turn, **Figure 4c** represents the output of Filter 2. Finally, **Figure 4d** shows the output of the modification [30] applied within the scheme [26] instead of standard BM3D (block matching three-dimensional) filter. Note that this is only an example for the latter filter applied to image fragment of limited size. We have not applied it to processing large-size Sentinel data further subject to classification since this filter requires too much time for image denoising.

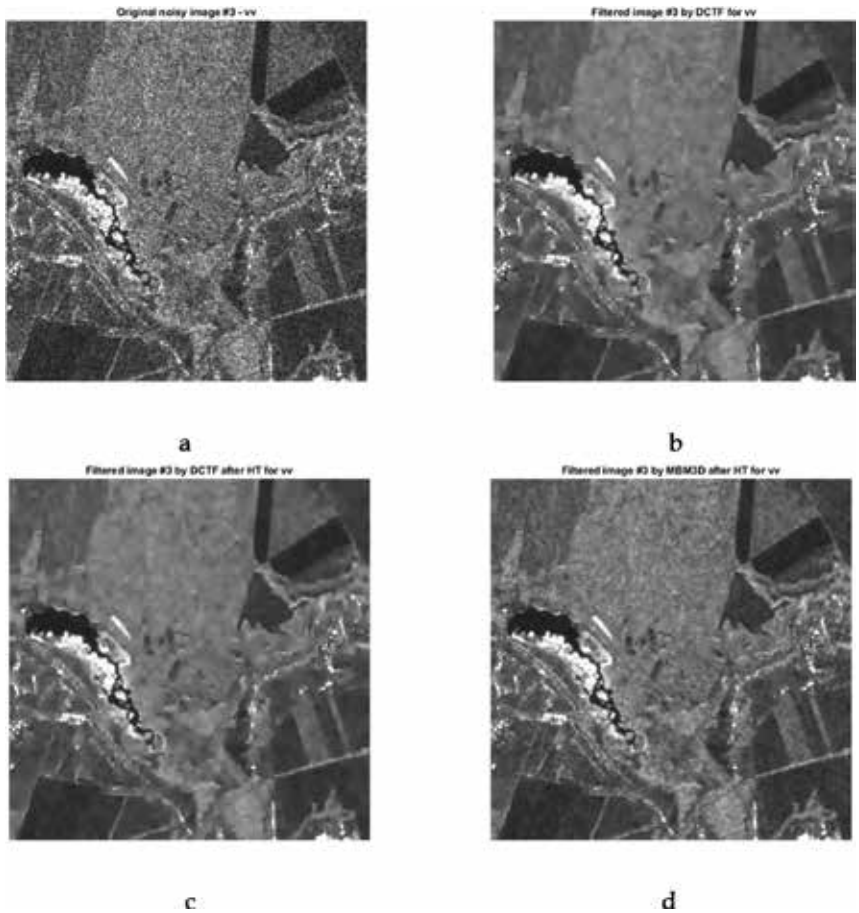

Figure 4. Original SAR image (a) and outputs of three denoisers: Filters 1 (b), Filter 2 (c), and nonlocal filter with HT (d).

The filtering results represented in **Figure 4** look quite similarly. Efficient speckle suppression is provided, while edge/detail preservation is good enough. Visual inspection carried by us and quantitative data in [30] show that the output of Filter 2 is the most smeared and some artifacts are present. Due to linearity nature of the main used computational procedures (DCT) of the considered filters, all computational costs can be easily reduced using parallel-wised algorithms or hardware. On the following computer configuration—Intel Core i7, 16 GB RAM—the entire calculation time for one image (recall that average size of images is ~25k $\times$ 16k pixels) is about 17 min. We also note that such time can be reduced by realizing the considered denoising methods in low-level programming language due to filter simplicity.

We have also analyzed filter outputs for 3D despeckling methods. One example is given in **Figure 5**. Original image of VV polarization is presented in **Figure 5a**. Again, a good compromise between speckle suppression and edge/detail preservation is provided.

However, visual analysis is not able to draw conclusions what filter will suit the final goal of reaching high classification accuracy in the best way. Thus, three denoising techniques (Filters 1, 2, and 3) described above have been used to improve SAR image quality before classification. Note that for multitemporal SAR data, more sophisticated 3D filtering methods can be

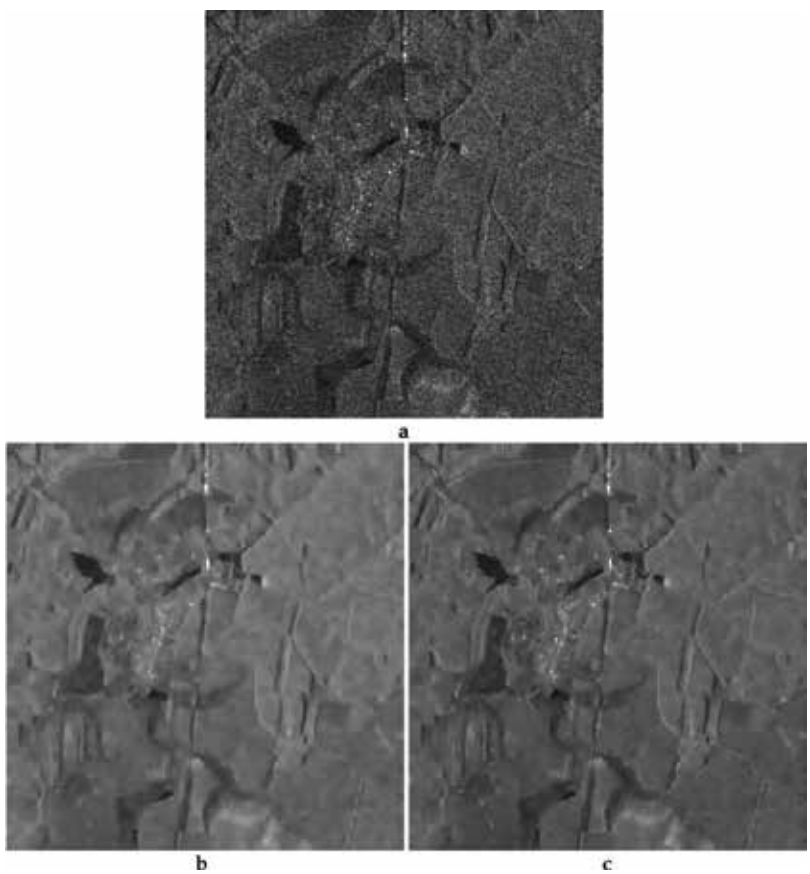

Figure 5. Original (noisy) image (a) and outputs of Filter 3 (b) and filters in [20].

applied, but our task here is to establish connection between filtering efficiency and classification accuracy. We expect that the use of Filter 2 and Filter 3 will produce comparable or better classification than Filter 1 and other filters available in known toolboxes.

4. Classification of multichannel radar images

There are many classifiers that can be applied. Popular ones such as support vector machine (SVM), decision tree (DT), and random forest (RF) classifiers were often employed for remote sensing image classification in the recent years. Many papers have demonstrated comparable or better performance of neural networks (NN) [37–40]. Although the NN training can be resource- and time-consuming, the corresponding classifiers have several positive features compared to SVM and DT. In particular, NNs are usually fast at processing new data that is important in processing of large volumes of radar data. Besides, they are able to produce probabilistic outputs, which can be employed for characterizing reliability (quality) of the final results (classification map). Hence, for classification, we have used a specific type of NN—an ensemble of feedforward neural networks, namely, multilayer perceptrons (MLPs). This type of classifiers was validated earlier for five Joint Experiment of Crop Assessment and Monitoring (JECAM) test sites in several countries, and it outperformed other considered techniques [41, 42]. The architecture of the used approach is represented in **Figure 6**. A committee (ensemble) of MLPs was used to improve performance of individual classifiers [9, 10]. The committee was obtained using a variant of the bagging technique [43] where MLPs with different parameters were trained using the same training data. This approach has several advantages. It is rather simple, non-computationally intensive and proved to be efficient for various applications. Outputs from the used MLPs were integrated using the method of average committee. According to this technique, the average class probability over all elementary classifiers is calculated, and the class that has the highest average posterior probability for the given input sample is chosen [9]. The following equation describes this procedure:

$$c_r^e = \frac{1}{Q}\sum_{q=1}^{Q} p_r^q, \qquad c^* = \arg\max_{c=1,\,C} p_c^e, \tag{11}$$

where c^* is the class to which the input sample is assigned by the committee of classifiers, p_r^e denotes the resulting posterior probability of the committee, p_c^e is posterior probability for each of MLPs, Q is the total number of classifiers in the committee, and C denotes the number of classes. There are two differences between average committee procedure and a majority voting technique: (i) the former approach gives probabilistic output, which can be employed as an indicator of reliability for classifying a particular pixel or area; (ii) there is no ambiguity when two or more classes have got the same number of "votes."

Let us give some details. Our MLP classifier used hyperbolic tangent activation function for neurons in the hidden layer and logistic activation function in the output layer. We utilized a cross-entropy (CE) error function for training our neural network. This provided better performance in terms of speed of training and classification accuracy [9, 44]:

$$E(\mathbf{w}) = -\ln p(\mathbf{T}|\mathbf{w}) = -\sum_{s=1}^{S}\sum_{c=1}^{C} t_{sc} \ln y_{sc}, \tag{12}$$

where $E(\mathbf{w})$ denotes the CE error function that is dependent on the neurons' weight coefficients $\mathbf{w}$, $\mathbf{T}$ is the set of vectors of target outputs in the training set that is composed of S samples, and t_{sc} and y_{sc} denote the target and MLP outputs, respectively. In the target output for class c, all components of vector t_s are set to 0, except for the cth component, which is set to 1. The CE error $E(\mathbf{w})$ had to be minimized. This was done by the scaled conjugate gradient algorithm by varying

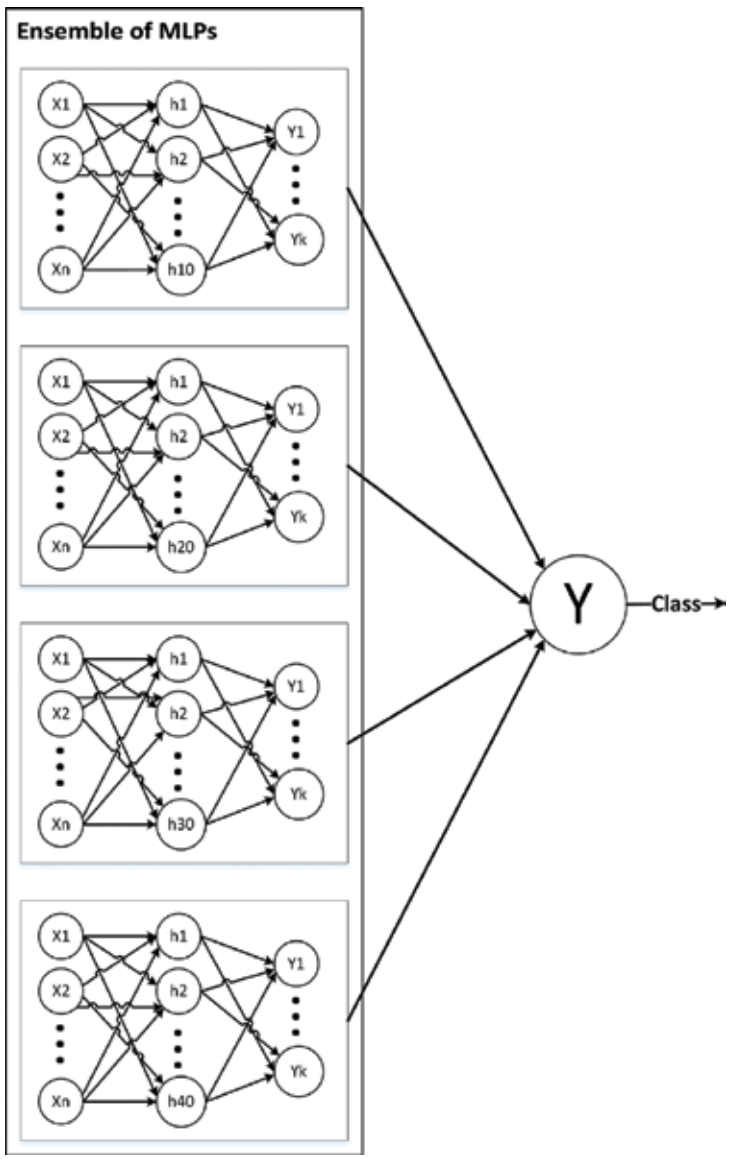

Figure 6. Architecture of an ensemble of feed forward NNs based on multilayer perceptrons (MLPs).

weight coefficients **w**. Backpropagation method was utilized for NN training. To prevent NN overfitting, we used early stopping and weight decay (L_2 regularization) techniques.

Classification of multitemporal radar images was performed on a per-pixel basis [45]. We have considered all SAR images available during the crop growth period. Note that the use of multitemporal images allows more accurate classification of crops than a single-date image.

5. Classification results

Filtering approaches for Sentinel-1 images were verified in the south part of Ukraine (yellow rectangle in **Figure 2**). Zoomed results after different filters are shown for fragment (marked by star) in **Figure 2** that has coordinates (33.73052, 47.18544). Such a territory is an intensive agricultural area; it corresponds to different climatic zones (humid continental) and has many different land cover types (forest on the north and agricultural crop in the southern part). The crop calendar is September–July for winter crops and April–October for spring and summer crops. A typical field size is 30–250 ha.

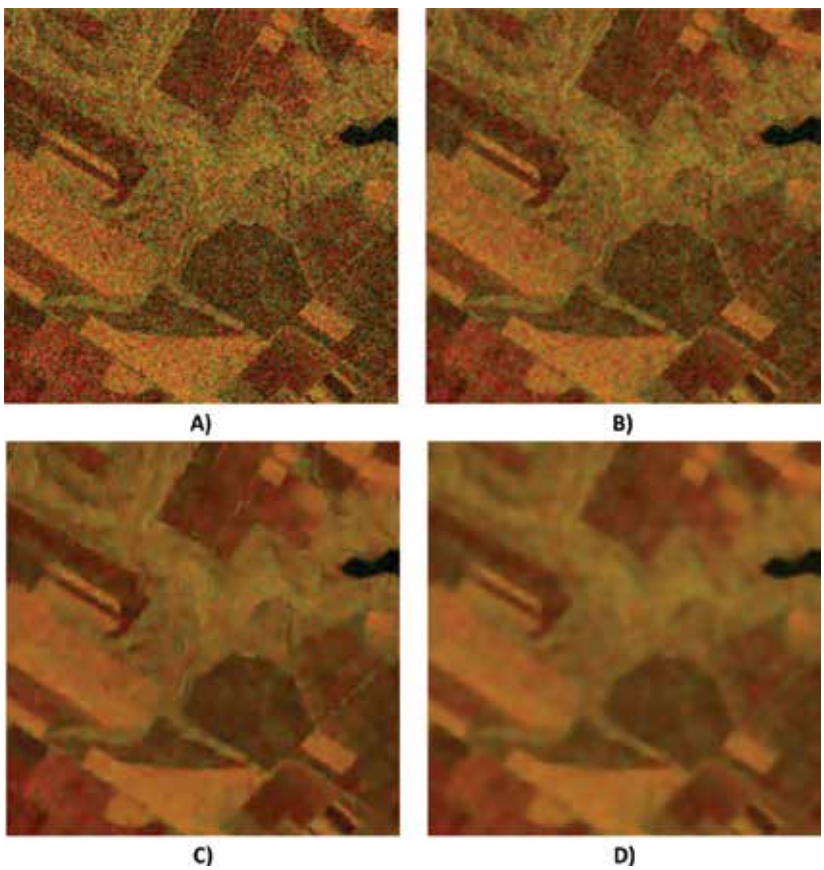

Figure 7. Example of using different filters applied to Sentinel-1A images (R channel, VV polarization; G channel, VH polarization): (A) image without filtering, (B) refined Lee filter, (C) Filter 1, and (D) Filter 3.

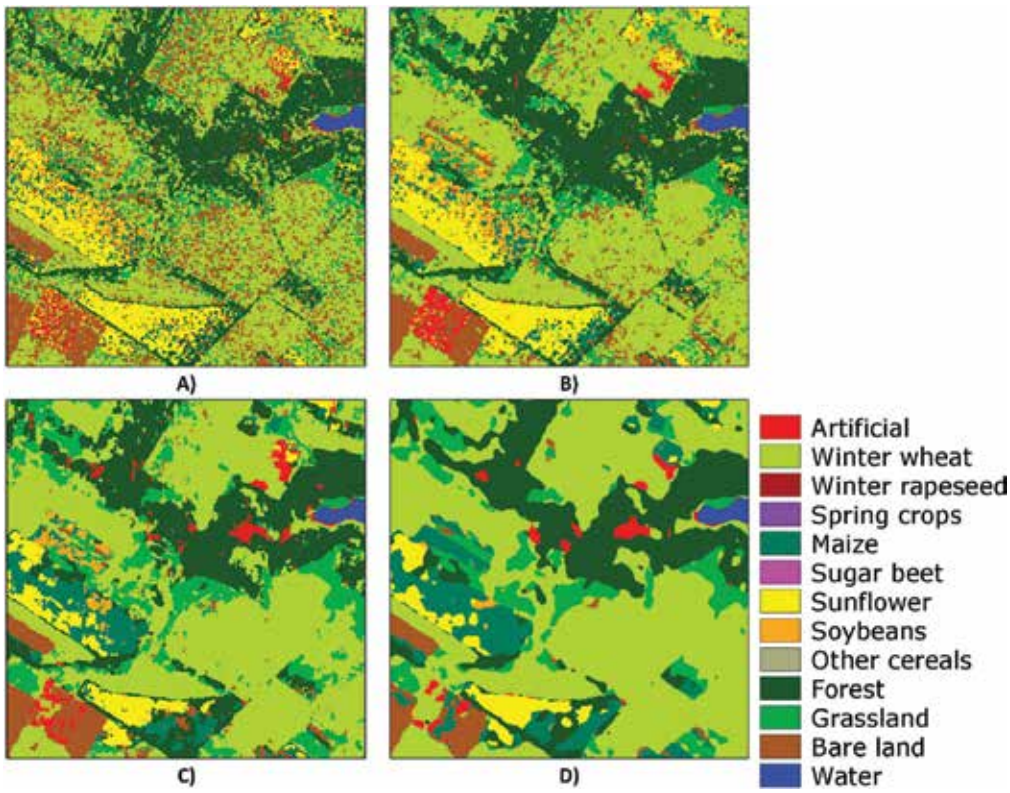

Figure 8. Example of crop classification maps based on different filters for Sentinel-1A images: (A) without filtering, (B) refined Lee filter, (C) Filter 1, and (D) Filter 3.

We preprocessed time series of 10 Sentinel-1A images with different filters available in ESA SNAP toolbox and Filter 1, Filter 2, and Filter 3. The comparison of those filters with non-filtered image for July 7, 2016, is shown in **Figure 7**. It is not easy to evaluate quality of filtering visually (user's opinions can be subjective). Therefore, we provide crop classification maps based on the same in situ data for time series of images obtained by each filter. For each time series of images, we independently trained an ensemble of neural networks. For this, we collected 153 data samples for nine classes, and all the accuracies were evaluated on independent set, which consisted of 146 samples for nine classes. Under the term "sample," we assume one polygon that consists of homogeneous pixels and all of them relate to the same class.

For ground-truth data collecting, we have used the along the roads approach. During these trips, we have collected georeferenced type of crops for definite fields. After that, collected data were divided into two independent datasets: one was used for training and another one for validation (as ground-truth data). So, for training and validation, we have used independent datasets with 153 and 146 samples, respectively.

The obtained crop classification maps after applying different filters are shown in **Figure 8**. In **Tables 1** and **2**, we present the comparison of user accuracy (UA), producer accuracy (PA), overall accuracy (OA), and Kappa coefficient for all classes [46] from crop classification map using different filters for SAR data in 2016.

Class	No filter		Boxcar		Frost		Gamma map		IDAN		Lee	
	UA, %	PA, %	UA, %	PA, %	UA, %	PA, %	UA, %	PA, %	UA, %	PA, %	UA, %	PA, %
Artificial	4.6	42.1	10.8	43.1	15.7	42.1	7.1	43.1	5.9	56	10.2	43.5
Winter wheat	65.5	73.5	79.7	76.3	78.4	76.9	79.6	76	71.9	67.3	79.5	76.6
Maize	62.7	49.8	79.6	54.5	78.1	55.4	78.7	55.8	93.2	62.5	79.8	56.2
Sunflower	96.5	90.2	96.6	92.9	96.5	92.9	96.7	92.4	96.5	94.7	96.7	92.9
Soybeans	37	61.3	41.9	65.6	42.6	65.1	39.6	65.2	51.5	69.2	41.3	65.4
Forest	52.9	88.3	55.4	92.1	56.4	92.9	61.5	91.9	23.9	42	54.9	92.5
Grassland	38.5	83.6	44.3	92.1	44.9	92	44.3	85.5	48	93.3	47.1	92.1
Bare land	49.8	23.2	68	51	67.4	52.4	71.3	46.6	36.9	22.4	60.8	47.4
Water	98.1	99.9	97.6	100	98.7	99.9	93.2	100	99.5	100	99.1	100
OA, %/kappa	82.6/0.7		86.4/0.76		86.7/0.77		86/0.75		86.2/0.76		86.5/0.76	

Table 1. Comparison of user accuracy (UA), producer accuracy (PA), overall accuracy (OA), and kappa coefficient (in the lowest raw) for different filters for SAR data in 2016.

Class	Lee sigma		Median		Refined Lee		DCTF		DCTF HT		3D DCTF	
	UA, %	PA, %	UA, %	PA, %	UA, %	PA, %	UA, %	PA, %	UA, %	PA, %	UA, %	PA, %
Artificial	9.4	43.5	7.8	38.9	6.8	45.4	3.7	52.3	8.9	81.9	8.4	65.3
Winter wheat	69.5	71.8	75.8	76	80.3	77.6	78.1	76.1	85.3	75.1	86.1	70.5
Maize	92.6	61.3	78.5	55	82.1	57.9	92.7	73.5	95	78.7	94.9	82.6
Sunflower	96.7	94.9	96.5	92.3	96.7	93.8	97.2	95.1	96.8	95.3	96.6	95.2
Soybeans	51.6	69.9	40.5	63.7	45.5	66.8	58.1	71.1	56.6	72.5	59.5	72.3
Forest	45.5	79.2	55.3	93.3	66.5	91.9	48.2	58.7	9.5	19.9	29.1	48.4
Grassland	53.9	89.6	45.8	91.3	46.3	92.8	44.6	94.2	48.8	90.9	48.6	91.1
Bare land	36.9	26.6	63.5	44	62.6	47.9	32.1	14.9	23.4	9.3	48.6	29.8
Water	95.3	100	96	100	99.3	100	99.7	100	99.8	100	99.7	100
OA, %/kappa	87.0/0.77		85.8/0.75		87.4/0.78		87.7/0.78		87.5/0.78		88.7/0.80	

Table 2. Comparison of user accuracy (UA), producer accuracy (PA), overall accuracy (OA), and kappa coefficient (in the lowest raw) for different filters for SAR data in 2016.

The overall accuracy of the crop classification map without applying any filtering is 82.6%. The lowest accuracy among all the available filters is provided by Median filter; classification accuracy is higher by +3.2% than classification of original (non-filtered) data. The proposed Filter 1 and Filter 2 have similar results with a nonsignificant gain of +0.3 and +0.1% compared to refined Lee, respectively. The most accurate crop map was obtained based on images preprocessed by the Filter 3. The gain of using this method is +6.1% compared to classification of original data and +1.3% compared to the refined Lee filter. It is worth noting that Filter 3

positive gains were observed not only for overall accuracy but also for PA and UA for each class, excluding forest and bare land.

6. Conclusions

One aim of this study was to analyze properties of Sentinel SAR images. It has been shown that speckle is quite intensive and spatially correlated. These peculiarities have been taken into account in choosing proper filters for data preprocessing.

Another aim was to compare the impact of different filters for SAR imagery denoising on crop classification accuracy. Ten SAR images with VV and VH polarization acquired by Sentinel-1A satellite for the Ukraine territory were explored. For speckle suppression, all available filters from the ESA SNAP toolbox were evaluated along with those based on DCT, namely, DCTF, DCTF HT, and 3D DCTF. Filter quality estimation has been performed in terms of overall crop classification accuracy. An ensemble of feed forward neural networks, in particular MLPs, was used as this method was validated for multiple JECAM test sites and proved to be efficient for multitemporal image classification.

The best performance using available filters in SNAP toolbox in terms of overall accuracy was achieved by the refined Lee filter. At the same time, all proposed DCT-based filters outperformed common filters from the SNAP toolbox. 3D DCTF provided the most accurate crop classification map after removing the speckle, and that is essential for crop area estimation and for solving other applied problems. It should be noted that 3D DCTF improved not only overall accuracy but also PA and UA for each class (especially for summer crops), excluding forest and bare land.

Author details

Vladimir Lukin[1]*, Oleksii Rubel[1], Ruslan Kozhemiakin[1], Sergey Abramov[1], Andrii Shelestov[2], Mykola Lavreniuk[2], Mykola Meretsky[2], Benoit Vozel[3] and Kacem Chehdi[3]

*Address all correspondence to: lukin@ai.kharkov.com

1 National Aerospace University, Kharkov, Ukraine

2 National Technical University of Ukraine, Ukraine

3 University of Rennes 1, France

References

[1] Schowengerdt R. Remote Sensing: Models and Methods for Image Processing. 3rd ed. Cambridge: Academic Press; 2006. 560 p. DOI: 10.978.00804/80589

[2] Blanes I, Magli E, Serra-Sagrista JA. Tutorial on image compression for optical space imaging systems. IEEE Geoscience and Remote Sensing Magazine. 2014;**2**(3):8-26. DOI: 10.1109/MGRS.2014.2352465

[3] Kravchenko A, Kussul N, Lupian E, Savorsky V, Hluchy L, Shelestov A. Water resource quality monitoring using heterogeneous data and high-performance computations. Cybernetics and Systems Analysis. 2008;**44**(4):616-624. DOI: 10.1007/s10559-008-9032-x

[4] Kogan F, Kussul N, Adamenko T, Skakun S, Kravchenko A, Krivobok A, Shelestov A, Kolotii A, Kussul O, Lavrenyuk A. Winter wheat yield forecasting: A comparative analysis of results of regression and biophysical models. Journal of Automation and Information Sciences. 2013;**45**(6):68-81. DOI: 10.1615/JAutomatInfScien.v45.i6.70

[5] Skakun S, Kussul N, Shelestov A, Kussul O. The use of satellite data for agriculture drought risk quantification in Ukraine. Geomatics, Natural Hazards and Risk. 2015;**7**(3):901-917. DOI: 10.1080/19475705.2015.1016555

[6] European Space Agency. Earth Online [Internet]. 2006. Available from: https://earth.esa.int/documents/653194/656796/Speckle_Filtering.pdf [Accessed: 2017-06-07]

[7] Oliver C, Quegan S. Understanding Synthetic Aperture Radar Images. USA: SciTech Publishing; 2004. 486 p. DOI: 10.978.18911/21319

[8] Lee JS, Pottier E. Polarimetric Radar Imaging: From Basics to Applications. USA: CRC Press; 2009. 438 p. DOI: 10.1080/01431161.2010.535193

[9] Skakun S, Kussul N, Shelestov A, Lavreniuk M, Kussul O. Efficiency assessment of multitemporal C-band Radarsat-2 intensity and Landsat-8 surface reflectance satellite imagery for crop classification in Ukraine. IEEE Journal of Selected Topics in Applied Earth Observation and Remote Sensing. 2016;**9**(8):3712-3719. DOI: 10.1109/JSTARS.2015.2454297

[10] Kussul N, Skakun S, Shelestov A, Lavreniuk M, Yailymov B, Kussul O. Regional scale crop mapping using multi-temporal satellite imagery. International Archives of the Photogrammetry, Remote Sensing and Spatial Information Sciences. 2015;**XL-7/W3**:45-52. DOI: 10.5194/isprsarchives-XL-7-W3-45-2015

[11] Kolotii A, Kussul N, Shelestov A, Skakun S, Yailymov B, Basarab R, Lavreniuk M, Oliinyk T, Ostapenko V. Comparison of biophysical and satellite predictors for wheat yield forecasting in Ukraine. International Archives of the. 2015;**XL-7/W3**:39-44. DOI: 10.5194/isprsarchives-XL-7-W3-39-2015

[12] Kussul N, Lemoine G, Gallego F, Skakun S, Lavreniuk M, Shelestov A. Parcel-based crop classification in Ukraine using Landsat-8 data and sentinel-1A data. IEEE Journal of Selected Topics in Applied Earth Observations and Remote Sensing. 2016;**9**(6):2500-2508. DOI: 10.1109/JSTARS.2016.2560141

[13] Touzi R. Review of speckle filtering in the context of estimation theory. IEEE Transactions on Geoscience and Remote Sensing. 2002;**40**(11):2392-2404. DOI: 10.1109/TGRS.2002.803727

[14] Anfinsen S, Doulgeris A, Eltoft T. Estimation of the equivalent number of looks in polarimetric synthetic aperture radar imagery. IEEE Transactions on Geoscience and Remote Sensing. 2009;**47**(11):3795-3809. DOI: 10.1109/TGRS.2009.2019269

[15] Lukin V, Ponomarenko N, Abramov S, Vozel B, Chehdi K, Astola J. Filtering of radar images based on blind evaluation of noise characteristics. In: Proceedings of Image and Signal Processing for Remote Sensing XIV (SPIE RS'08); 10 October 2008; Cardiff. SPIE; 2008. p. 12. DOI: 10.1117/12.799396

[16] Kang X, Han C, Yang Y, Tao T. SAR image edge detection by ratio-based Harris method. In: Proceedings of the International Conference of Acoustics, Speech and Signal Processing (ICASSP'06); 14-19 May 2006; Toulouse. IEEE; 2006. pp. 837-840. DOI: 10.1109/ICASSP.2006.1660473

[17] Marques R, Medeiros F, Ushizima D. Target detection in SAR images based on a level set approach. IEEE Transactions on Systems, Man and Cybernetics. 2009;**39**(2):214-222. DOI: 10.1109/TSMCC.2008.2006685

[18] Lukin V, Ponomarenko N, Fevralev D, Vozel B, Chehdi K, Kurekin A. Classification of pre-filtered multichannel remote sensing images. In: Escalante-Ramirez B, editor. Remote Sensing—Advanced Techniques and Platforms. Austria: InTech; 2012. pp. 75-98. DOI: 10.5772/36046.ch4

[19] Abramov S, Abramova V, Lukin V, Ponomarenko N, Vozel B, Chehdi K, Egiazarian K, Astola J. Methods for blind estimation of speckle variance in SAR images: Simulation results and verification for real-life data. In: Awrejcewicz J, editor. Computational and Numerical Simulations. Austria: InTech; 2014. pp. 303-327. DOI: 10.5772/57035.ch14

[20] Kozhemiakin R, Lukin V, Vozel B, Chehdi K. Filtering of dual-polarization radar images based on discrete cosine transform. In: Proceedings of 15th international radar symposium (IRS'14); 16-18 june 2014; gdansk. IEEE. 2014:1-4. DOI: 10.1109/IRS.2014.6869301

[21] Deledalle CA, Denis L, Poggi G, Tupin F, Verdoliva L. Exploiting patch similarity for SAR image processing: The nonlocal paradigm. IEEE Signal Processing Magazine, Recent Advances in Synthetic Aperture Radar Imaging. 2014;**31**(4):69-78. DOI: 10.1109/MSP.2014.2311305

[22] Lukin V, Abramov S, Ponomarenko N, Uss M, Zriakhov M, Vozel B, Chehdi K, Astola J. Methods and automatic procedures for processing images based on blind evaluation of noise type and characteristics. SPIE Journal on Advances in Remote Sensing. 2011;**5**(1):1-27. DOI: 10.1117/1.3539768

[23] Ponomarenko N, Lukin V, Egiazarian K, Astola J. A Method for blind estimation of spatially correlated noise characteristics. In: Proceedings of SPIE Conference Image Processing: Algorithms and Systems VII (SPIE EI'10); 8 February 2010; San Jose. SPIE; 2010. p. 12. DOI: 10.1117/12.847986

[24] Colom M, Buades A, Morel JM. Nonparametric noise estimation method for raw images. Journal of the Optical Society of America. 2014;**31**(4):863-871. DOI: 10.1364/JOSAA.31.000863

[25] Uss M, Vozel B, Lukin V, Chehdi K. Maximum likelihood estimation of spatially correlated signal-dependent noise in hyperspectral images. Optical Engineering. 2012;**51**(11):1-12. DOI: 10.1117/1.OE.51.11.111712

[26] Makitalo M, Foi A, Fevralev D, Lukin V. Denoising of single-look SAR images based on variance stabilization and non-local filters. In: Proceedings of International Conference of Mathematical Methods in Electromagnetic Theory (MMET'10); 6-8 September 2010; Kyiv. IEEE; 2010. p. 4. DOI: 10.1109/MMET.2010.5611418

[27] Lukin V, Melnik V, Pogrebniak A, Zelensky A, Saarinen K, Astola J. Digital adaptive robust algorithms for radar image filtering. Journal of Electronic Imaging. 1996;**5**(3):410-421. DOI: 10.1117/12.240715

[28] Fevralev D, Lukin V, Ponomarenko N, Abramov S, Egiazarian K, Astola J. Efficiency analysis of color image filtering. EURASIP Journal on Advances in Signal Processing. 2011;**2011**:41. DOI: 10.1186/1687-6180-2011-41

[29] Deledalle CA, Denis L, Tabti S, Tupin F. MuLoG, or how to apply Gaussian denoisers to multi-channel SAR speckle reduction? IEEE Transactions on Image Processing. Forthcoming. DOI: 10.1109/TIP.2017.2713946

[30] Rubel A, Lukin V, Egiazarian K. Block matching and 3D collaborative filtering adapted to additive spatially correlated noise. In: Proceedings of 9th International Workshop on Video Processing and Quality Metrics (VPQM'2015); 26 February 2015; Chandler. 2015. p. 6

[31] Pogrebnyak O, Lukin V. Wiener DCT based image filtering. Journal of Electronic Imaging. 2012;**4**:1-14. DOI: 10.1117/1.JEI.21.4.043020

[32] Oktem R, Egiazarian K, Lukin V, Ponomarenko N, Tsymbal O. Locally adaptive DCT filtering for signal-dependent noise removal. EURASIP Journal on Advances in Signal Processing. 2007;**2007**:1-10. DOI: 10.1155/2007/42472

[33] Tsymbal O, Lukin V, Ponomarenko N, Zelensky A, Egiazarian K, Astola J. Three-state locally adaptive texture preserving filter for radar and optical image processing. EURASIP Journal on Applied Signal Processing. 2005;(8):1185-1204. DOI: 10.1155/ASP.2005.1185

[34] Abramov S, Krivenko S, Roenko A, Lukin V, Djurovic I, Chobanu M. Prediction of filtering efficiency for DCT-based image denoising. In: Proceedings of 2nd Mediterranean Conference on Embedded Computing (MECO'2013); 15-20 June 2013; Budva. IEEE; 2013. pp. 97-100. DOI: 10.1109/MECO.2013.6601327

[35] Rubel O, Kozhemiakin R, Abramov S, Lukin V, Vozel B, Chehdi K. Performance prediction for 3D filtering of multichannel images. In: Proceedings of SPIE: Image and Signal Processing for Remote Sensing XXI (SPIE RS'15); 15 October 2015; Toulouse. SPIE; 2015. p. 11. DOI: 10.1117/12.2193976

[36] Rubel O, Lukin V, de Medeiros FS. Prediction of despeckling efficiency of DCT-based filters applied to SAR images. In: Proceedings of International Conference on Distributed Computing in Sensor Systems (DCOSS'15); 10-12 June 2015; Fortaleza. IEEE; 2015. pp. 159-168. DOI: 10.1109/DCOSS.2015.16

[37] Huang FJ, LeCun Y. Large-scale learning with SVM and convolutional NETWORK for generic object recognition. In: Proceedings of the IEEE Computer Society Conference on Computer Vision and Pattern Recognition (CVPR'06); 17-22 June 2006; New York. IEEE; 2006. pp. 284-291. DOI: 10.1109/CVPR.2006.164

[38] Ding J, Chen B, Liu H, Huang M. Convolutional neural network with data augmentation for SAR target recognition. IEEE Geoscience and Remote Sensing Letters. 2016;**13**(3):364-368. DOI: 10.1109/LGRS.2015.2513754

[39] Kussul N, Lavreniuk M, Skakun S, Shelestov A. Deep learning classification of land cover and crop types using remote sensing data. IEEE Geoscience and Remote Sensing Letters. 2017;**14**(5):778-782. DOI: 10.1109/LGRS.2017.2681128

[40] Shelestov A, Lavreniuk M, Kussul N, Novikov A, Skakun S. Exploring Google earth engine platform for big data processing: Classification of multi-temporal satellite imagery for crop mapping. Frontiers in Earth Science. 2017;**5**(17):1-10. DOI: 10.3389/feart.2017.00017

[41] Waldner F, De Abelleyra D, Veron S, Zhang M, Wu B, Plotnikov D, Bartalev S, Lavrenyuk M, Skakun S, Kussul N, Le Marie G, Dupuy S, Jarvis I, Defourny P. Towards a set of agrosystem-specific cropland mapping methods to address the global cropland diversity. International Journal of Remote Sensing. 2016;**37**(14):3196-3231. DOI: 10.1080/01431161.2016.1194545

[42] Lavreniuk M, Kussul N, Skakun S, Shelestov A, Yailymov B. Regional retrospective high resolution land cover for Ukraine: Methodology and results. In: Proceedings of the IEEE International Geoscience and Remote Sensing Symposium (IGARSS'15); 26-31 July 2015; Milan. IEEE; 2015. pp. 3965-3968. DOI: 10.1109/IGARSS.2015.7326693

[43] Bishop C. Pattern Recognition and Machine Learning. New York, USA: Springer; 2006. 758 p. DOI: 10.978.03873/10732

[44] Lavreniuk M, Skakun S, Shelestov A, Yalimov B, Yanchevskii S, Yaschuk D, Kosteckiy A. Large-scale classification of land cover using retrospective satellite data. Cybernetics and Systems Analysis. 2016;**52**(1):127-138. DOI: 10.1007/s10559-016-9807-4

[45] Kussul N, Skakun S, Shelestov A, Kussul O. The use of satellite SAR imagery to crop classification in Ukraine within JECAM project. In: Proceedings of the IEEE International Geoscience and Remote Sensing Symposium (IGARSS'14); 13-18 July 2014; Quebec City. IEEE; 2014. pp. 1497-1500. DOI: 10.1109/IGARSS.2014.6946721

[46] Congalton R. A review of assessing the accuracy of classifications of remotely sensed data. Remote Sensing of Environment. 1991;**37**(1):35-46. DOI: 10.1016/0034-4257(91)90048-B

Chapter 3

Remote Sensing of Forests using Discrete Return Airborne LiDAR

Hamid Hamraz and Marco A. Contreras

Additional information is available at the end of the chapter

http://dx.doi.org/10.5772/intechopen.71777

Abstract

Airborne discrete return light detection and ranging (LiDAR) point clouds covering forested areas can be processed to segment individual trees and retrieve their morphological attributes. Segmenting individual trees in natural deciduous forests, however, remained a challenge because of the complex and multi-layered canopy. In this chapter, we present (i) a robust segmentation method that avoids a priori assumptions about the canopy structure, (ii) a vertical canopy stratification procedure that improves segmentation of understory trees, (iii) an occlusion model for estimating the point density of each canopy stratum, and (iv) a distributed computing approach for efficient processing at the forest level. When applied to the University of Kentucky Robinson Forest, the segmentation method detected about 90% of overstory and 47% of understory trees with over-segmentation rates of 14 and 2%. Stratifying the canopy improved the detection rate of understory trees to 68% at the cost of increasing their over-segmentations to 16%. According to our occlusion model, a point density of ~170 pt/m^2 is needed to segment understory trees as accurately as overstory trees. Lastly, using the distributed approach, we segmented about two million trees in the 7440-ha forest in 2.5 hours using 192 processors, which is 167 times faster than using a single processor.

Keywords: individual tree segmentation, multi-layered stand, vertical canopy stratification, segmentation evaluation, point density, canopy occlusion effect, big data, distributed computing

1. Introduction

Global forests cover about 30% of the land surface of the earth, include 80% of plant biomass, and account for 75% of primary productivity of biosphere, providing essential and unreplaceable ecosystem services to humans and the life on the planet [1]. Forest management has traditionally been based on stand (forested area with similar vegetation characteristics) attributes collected

using field sampling and interpretation of aerial photography [2]. Field sampling is inevitably limited to a small percentage because of the large acquisition costs, which results in rough estimates of stand attributes while ignoring large variability in terrain and vegetation within stands [3]. Recent advances in remote sensing, geographic information systems, and information science have the potential to bring dramatic changes to forest data acquisition and management by providing inventory information at unprecedented spatial and temporal resolutions. Specifically, discrete return airborne light detection and ranging (LiDAR) technology has extensively been used in the past two decades in forestry [4, 5]. Due to its ability to penetrate vegetation canopy, LiDAR data captured in the shape of 3D point clouds contain vertical information from which vegetation structural characteristics can be retrieved, even from understory canopy layers. Airborne point clouds has successfully been used to derive digital surface models representing top surface of objects above the ground, as well as digital elevation models (DEMs) representing bare ground surface excluding the above ground objects [6]. Earlier studies built relationships between the LiDAR-derived variables and vegetation attributes using field sampling and extrapolated those relationships to the LiDAR coverage area and/or to the entire forest [7]. Although such methods can remarkably reduce field work and increase precision, they are insufficient for detailed forest management at the individual tree level [8].

Detailed tree-level forest management requires individual trees to be segmented from the LiDAR point clouds. Although numerous tree segmentation methods have been developed, they have major focus on conifer forests or forests with relatively open canopy where assumptions about size and shape of tree crowns are made [9]. Deciduous forests present considerably more complex vegetation conditions due to large variation in tree shapes and sizes, larger number of species, and denser canopy where individual trees are considerably more challenging to segment [8]. In addition, retrieval of understory trees using airborne LiDAR is much harder because of the reduced amount of LiDAR points penetrating below the main cohort formed by overstory trees [10]. Typically, the detection rate of overstory (dominant and co-dominant) trees is around 90% while the detection rate of understory (intermediate and overtopped) trees is below 50%. Trivially, a minimum point density is the basic requirement for a reasonable segmentation of trees, which is typically not satisfied for understory trees in a dense forest [11, 12]. Furthermore, LiDAR data covering an entire forest is much more voluminous than the memory of a workstation and may also take an unreasonable time to be sequentially processed using an external memory algorithm. Because large-scale LiDAR data is typically arranged in several tiles for efficient management and delivery, distributed processing of different tiles is straightforward. However, the data representing tree crowns located across tile boundaries are split into two or more pieces that need to be processed by different computing units. Only few studies have considered distributed processing of large geospatial data addressing the boundary problem [13]—specifically there are no studies considering forest data. This is increasingly important when obtaining tree-level information for areas other than small plots, which is often the ideal objective. Moreover, continuous advancements of sensor technology and platforms [14] is resulting in point clouds to be acquired with greater resolutions, increasing the need for more efficient and scalable processing schemes.

To address these limitations, in this chapter we present: (i) a robust tree segmentation method, which is designed to be applied in closed-canopy deciduous forests, (ii) a vertical canopy

stratification procedure that separates the canopy into an overstory layer and multiple understory canopy layers, (iii) a LiDAR pulse occlusion model in terms of point density to further investigate the inferior segmentation quality of understory trees, and (iv) a distributed computing approach that addresses the tile boundary problem to efficiently and accurately process the data at the forest level.

2. Methodology

2.1. Robust tree segmentation

The main inputs of the tree segmentation method [15] are the LiDAR point cloud and the LiDAR-derived DEM. A pre-processing step bins the point cloud to a horizontal grid with cell width equals to the average footprint (AFP) of the point cloud (equals to the reciprocal of square root of the point density) and selects the highest point within each grid cell as a LiDAR surface point (LSP). Using the DEM, heights above ground are calculated for all LSPs and ground and lower vegetation (below 4 m) points in the LSPs are removed from further analysis. Based on the vegetation structure, this yields some gaps with no vegetation in the remaining LSP dataset, which are utilized later for segmentation. The next pre-processing step smoothens LSPs to reduce small variation in vegetation elevation within tree crowns while maintaining important vegetation patterns. We used a Gaussian smoothing filter with standard deviation of 2 × AFP.

After pre-processing, the segmentation method includes the following routines: (1) locate the global maximum (GMX) among LSPs, assumed to represent the apex of the tallest tree, (2) generate vertical profiles originating from the GMX location and stretching outwards, (3) identify the individual LSP along each profile that represents the crown boundary via between-tree gap detection and local minimum (LM) inspection, (4) create a convex hull of boundary points delineating the tree crown, and (5) cluster all LSPs encompassed within the convex hull as the current tallest tree crown. These routines iterate until all LSPs have been clustered into tree crowns. Clusters representing crowns with diameter below a minimum detectable crown width (MDCW), set here as 1.5 m, are considered noise. **Figure 1a** shows the flowchart of the tree segmentation method and **Figure 1b** illustrates an iteration of a tree clustering.

2.1.1. Profile generation

After identifying the GMX, eight uniformly spaced vertical profiles (every 45°) originating from it and stretching a maximum horizontal distance of 20 m are generated. The width of each profile was set to 2 × AFP to ensure a sufficient number of LSPs representing vegetation characteristics. After the crown boundary is determined for each profile (explained below), the maximum crown radius (r) is used to determine the chord height (x) between two maximum crown radii profiles separated by the angular spacing (φ) (**Figure 2**) using the following equation:

$$x = r(1 - \cos(\varphi/2)) \tag{1}$$

If the chord height is greater than the AFP, the angular spacing is decreased to half and the number of profiles is doubled. The new chord height is calculated again based on the updated maximum crown radius and the new profile angular spacing. Doubling the number of profiles iterates until the chord height becomes smaller than the AFP. In this way, the number of profiles adapts incrementally according to the maximum LiDAR-derived crown radius to smoothly delineate the tree crowns.

2.1.2. Crown boundary identification

To identify the crown boundary along a profile, inter-tree crown gaps are firstly detected. These gaps are assumed to correspond to relatively large horizontal distance between two consecutive LSPs along the profile, which are identified using a statistical outlier detection method. Horizontal distances between consecutive points along the profile follow a Poisson distribution. When transformed to their square root or to their logarithm, the resulting distribution reasonably

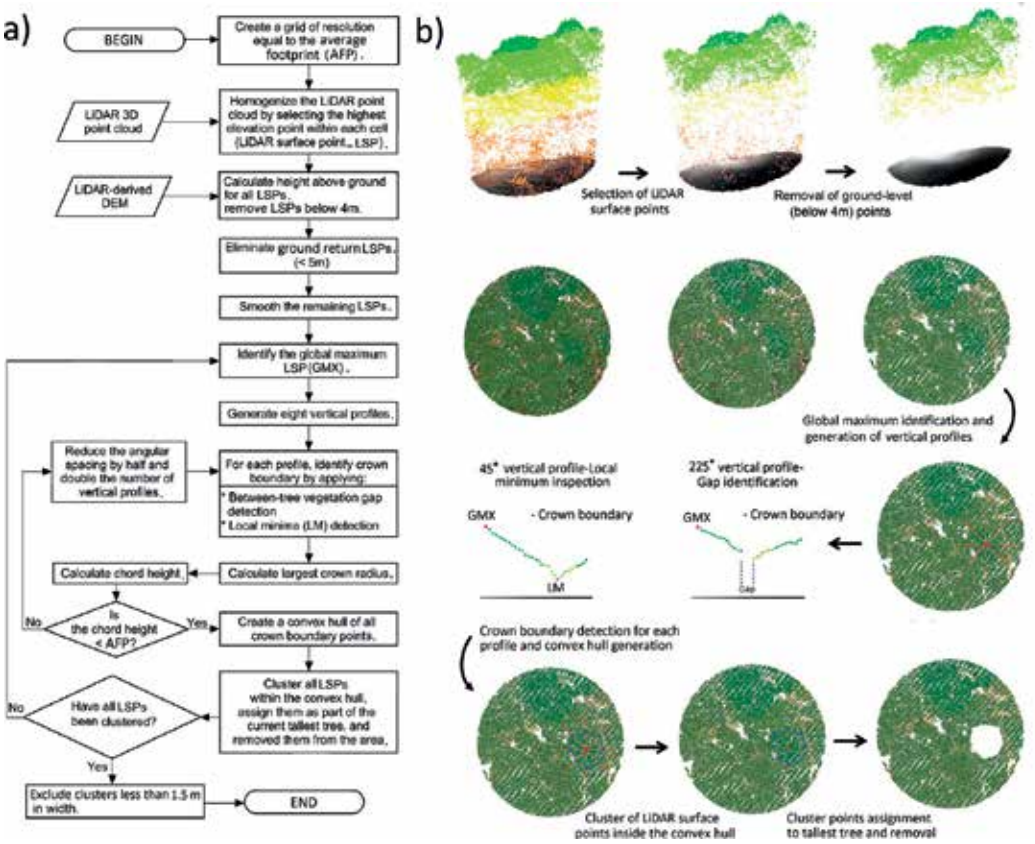

Figure 1. (a) Flowchart of the tree segmentation method used to identify tree locations and delineate tree crowns and (b) illustration of the process of clustering the tallest tree crown.

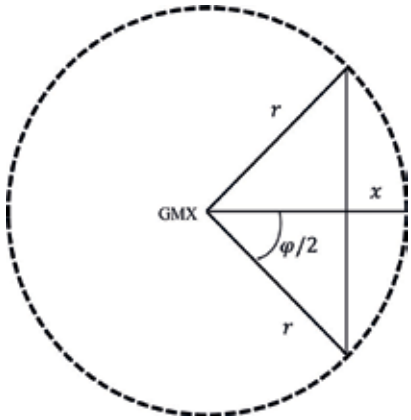

Figure 2. Diagram illustrating the calculation of the chord height (x) formed by two profiles of maximum crown radius (r) separated by the angular spacing (ϕ).

approximates a normal distribution, which is more appropriate for the outlier detection method. To be conservative, transformed distance values larger than six times the interquartile range from the third quartile are considered inter-tree gaps. After gaps are detected, only the LSPs between the GMX and the first gap remain for further analysis and the LSPs located beyond the first gap are removed from the profile. At this point, the profile is assumed to represent either the crown of the current tallest tree or the crowns of multiple adjacent trees, growing close together with overlapping crowns.

In the next step, the remaining LSPs are inspected starting from the GMX to locate an LM, which is defined as an LSP with elevation lower than its two adjacent LSP neighbors. Once an LM is located, two windows on both sides of it are considered to determine if the LM represents the crown boundary. The left window expands from the LM to the GMX. The size of the right window is estimated based on the steepness of the crown (S_{right}), which is calculated as the median of the absolute slopes between consecutive points (i, $i+1$) located within a distance of MDCW to the right of the LM ($MDCW_{right}$):

$$S_{right} = tan^{-1}\left(median\left[|slope_{i,i+1}|i, i+1 \in MDCW_{right}\right]\right) \tag{2}$$

If the LM represents the crown boundary, the LSPs within $MDCW_{right}$ partially represent the crown of an overlapping and shorter tree with a steepness that is approximated by S_{right}. We bound the value of S_{right} between the steepness of two distinct crown shapes: a sphere-shaped crown and a narrow cone-shaped crown (two ends of the spectrum). As the height of the adjacent tree (h_{ad}) is between the heights of the GMX and the LM point, we approximate it by the average of the GMX and the LM heights. The steepness of a narrow cone-shaped crown is expressed as $90^\circ - \varepsilon$, where ε (set here as 5°) indicates a small deviation from nadir. The cone-shaped crown radius (cr_c) can then be calculated as follows:

$$cr_c = \frac{h_{ad} \times CL_c}{tan\left(90^\circ - \varepsilon\right)} \times O_c \tag{3}$$

where CL_c is the ratio of the crown height to the total height and O_c indicates the crown radius reduction due to the overlap assuming the cone-shaped tree is situated in a dense stand. On the other hand, the slope of a sphere-shaped crown ranges from 0° to 90° with the expected value of 32.7° (see [15]). Its crown radius (cr_s) can be calculated as follows:

$$cr_s = \frac{h_{ad} \times CL_s}{2} \times O_s \tag{4}$$

where CL_s and O_s indicate the crown to total height ratio and the crown radius reduction due to the overlap within a dense stand for the sphere-shaped tree.

The size of the right window (w_{right}) is then calculated by interpolating cr_c and cr_s with respect to S_{right}, which is bounded between 32.7° and 90° − ε, as follows:

$$w_{right} = cr_c \left(\frac{(90^\circ - \varepsilon) - S_{right}}{(90^\circ - \varepsilon) - 32.7^\circ} \right) + cr_s \left(1 - \frac{(90^\circ - \varepsilon) - S_{right}}{(90^\circ - \varepsilon) - 32.7^\circ} \right) \tag{5}$$

Lastly, after determining both windows on both sides of the LM, the median of slopes between consecutive LSPs of each window is calculated. If the median slope of the left window is negative (downwards from the apex to the crown boundary) and the median slope of the right window is positive (upwards from the crown boundary toward the apex of the adjacent tree), the LM is identified as a boundary point. Otherwise, the current LM is considered to represent natural height variation within the current tallest tree crown and the next LM farther from the GMX along the profile is inspected. If no LM along the profile satisfies the crown boundary criterion, the last LSP is identified as the crown boundary.

The crown height to total height ratio is highly variable among individual trees and species with values typically varying between 0.4 and 0.8 [16]. The crown ratio of a narrow cone-shaped tree tends to be larger than that of a sphere-shaped tree. Hence, for demonstrating the application of our method, here we used 0.8 and 0.7 for CLc and CLs, respectively. Similarly, crown radius reduction due to overlap is highly variable with a value of even less than one half for a very dense stand. The radius of a narrow cone-shaped tree is reduced less than that of a sphere-shaped tree because the crown of a narrow cone-shaped tree is compacted from the sides. Thus, we used two-thirds for Oc and one-third for Os. Although these values can affect the size of the right window (Eq. (5)), the sign of the median slope would remain the same as long as the size is within a reasonable range. Also, considering the multiple profiles generated for each GMX, the effect of a single potentially mislocated boundary point on the ability to delineate tree crown is reduced.

Both routines for generation of a sufficient number of profiles and for identifying the crown boundary of each profile are completely based on the information extracted on-the-fly from the 3D locations of the LSPs. This avoids a priori assumptions of tree crown shapes, dimensions, and inter-crown spacing, which yields a robust tree segmentation method that can be applied to different vegetation types.

2.2. Vertical canopy stratification

The canopy stratification procedure [17] uses all LiDAR vegetation points binned into the horizontal grid. It then analyzes the height histogram of all points within a circular locale around each individual grid cell. The locale should include a sufficient number of points for building an empirical multi-modal distribution but not extend too far to preserve locality. We fixed the locale radius to $6 \times$ AFP (containing about $\pi \times 62$ points), which is lower bounded at 1.5 m to prohibit too small locales capturing insufficient spatial structure. To analyze the height histogram of each locale, the histogram is smoothed using a Gaussian kernel with standard deviation of 5 m to remove variability pertaining to vertical structure of a single crown. The salient curves in the smoothed histogram (height ranges throughout which the second derivative of the smoothed histogram are negative) represent the canopy layers. The midpoint of the top canopy layer and the canopy layer below it are regarded as the height threshold for stratifying the top layer in that cell location (**Figure 3**). Using the height thresholds determined for all grid cells, the top canopy layer is stratified and removed from the point cloud and the AFP is updated according to the density of the remainder of the point cloud. The stratification procedure iterates binning the remainder of the point cloud into a horizontal grid with the cell size equal to the updated AFP, analyzing locales of individual grid cells, and removing layers until the point cloud is emptied.

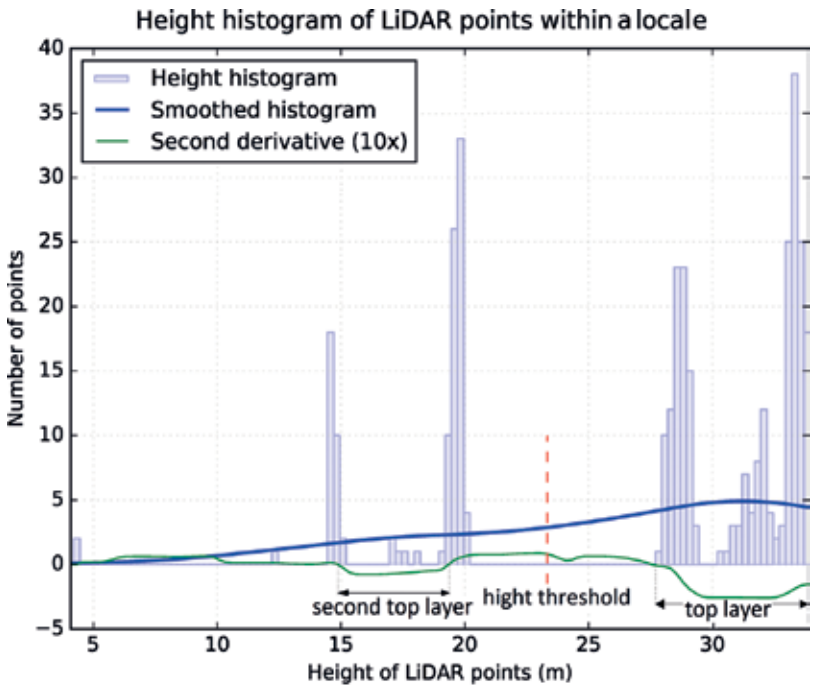

Figure 3. Height histogram of LiDAR points within a locale including over 100 points used for determining the height threshold for stratifying the top canopy layer in a cell location.

As the height thresholds to stratify the top canopy layer are determined using overlapping locales, the canopy layer smoothly adjusts to incorporate the vertical variability of vegetation height to minimize under/over-segmenting tree crowns across layers. To improve segmentation of understory trees within a point cloud representing a multi-story stand, the method presented in the previous section can be applied independently to each canopy layer (**Figure 4**).

2.3. Canopy occlusion model

Using the canopy stratification procedure, we model the occlusion effect of higher canopy layers on the lower layers in terms of point density [18], which is defined as the number of points divided by the horizontal area covered by them. Point density of the entire LiDAR point cloud (PCD) is dependent upon different flight and sensor parameters such as flight altitude and speed, pulse repetition rate, field of view, and swath overlap [12, 19]. These parameters

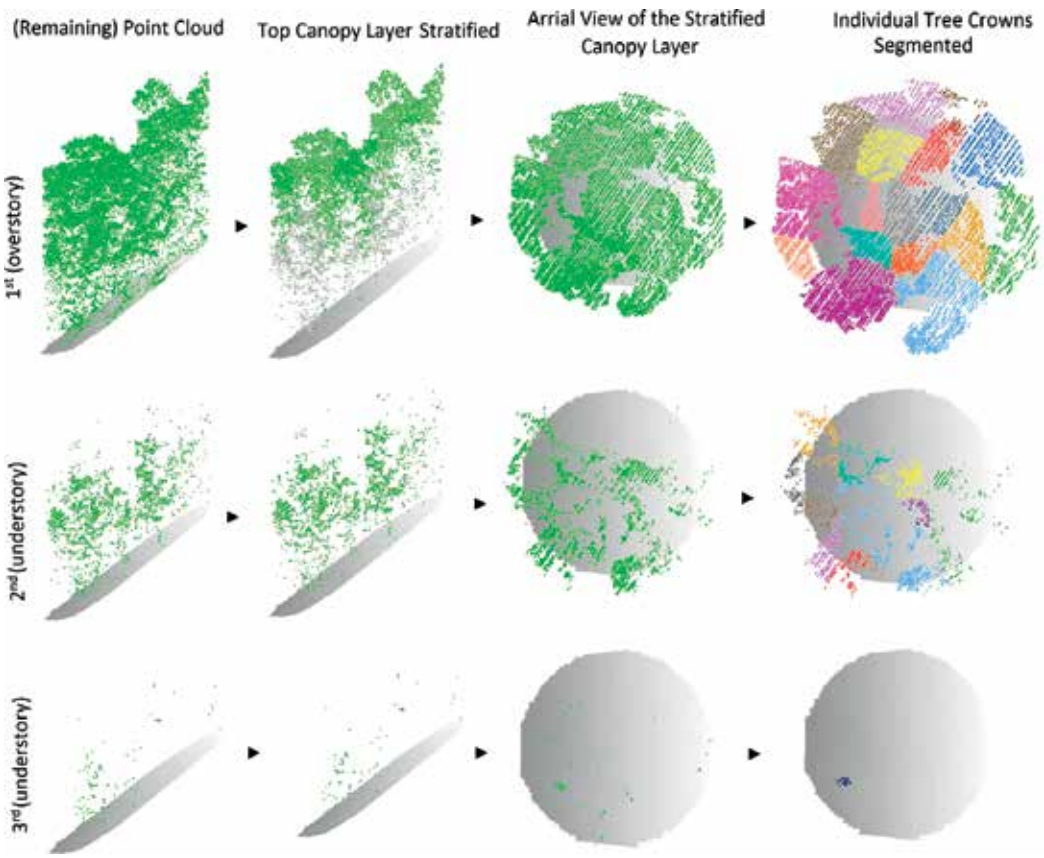

Figure 4. Illustration of the tree segmentation process in a multi-story stand by stratifying one canopy layer at a time, removing it from the point cloud, and segmenting crowns within it. A number of understory trees seem to be missed within the third canopy layer, which is likely due to the much lower point density compared to the first and second layers.

also affect the fractions of points recorded for over/understory canopy layers, yet point density of individual layers decreases with proximity to ground.

Assuming all canopy layers cover the same area as the entire point cloud, PCD equals the total of point densities of constituting canopy layers of the point cloud plus the density of the DEM. Because the ground is different from a canopy layer in returning LiDAR pulses, necessitating a different density model for the DEM, we assume an infinite number of canopy layers were placed instead of the ground to simplify the analysis. The point density of DEM approximately equals the total of point densities of the canopy layers in place of the ground. Thus, PCD can be calculated as the sum of point densities of an infinite number of canopy layers (the actual ones plus those in place of the ground):

$$PCD = d_1 + d_2 + d_3 + \ldots + d_n \qquad n \in \mathbb{N} \tag{6}$$

where d_n denotes the point density of the nth top canopy layer and converges to zero as n increases. To normalize point densities, we divide both sides of Eq. (6) by PCD:

$$1 = p_1 + p_2 + p_3 + \ldots + p_n \qquad n \in \mathbb{N} \tag{7}$$

where p_n denotes the fraction of LiDAR points at the nth top layer and can be estimated using a logarithmic series distribution that has a discrete domain decreasing function supporting natural numbers [20].

We denote the required PCD of a point cloud for reasonable segmentation of trees forming the top canopy layer of the point cloud by PCD_{min}. The required PCD of a point cloud for a reasonable segmentation of trees forming the nth top canopy layer can then be calculated using Eq. (7). We hypothetically remove the $n - 1$ top canopy layers of the point cloud. The remaining point cloud has a density fraction of $1 - (p_1 + p_2 + \ldots + p_{n-1})$ of the original point cloud. Given this density fraction should yield a density of PCD_{min} for the remaining point cloud, the point density of the original point cloud for reasonable segmentation of trees forming its nth top canopy layer ($pcd_{min}(n)$) by proportionality becomes:

$$pcd_{min}(n) = \frac{PCD_{min}}{1 - (p_1 + p_2 + \ldots + p_{n-1})} \tag{8}$$

2.4. Distributed processing of large-scale forest LiDAR data

The distributed approach for tree segmentation [21] uses a master-slave scheme, where the master is in charge of maintaining the global tile map and coordinating how to process individual tiles and their boundary data while the slaves perform the actual tree segmentation. Tile boundary data (solid/striped colored regions in **Figure 5**) are tree crowns located across two adjacent tiles (light-colored)—hereafter referred to as edge data—or across three or four neighboring tiles (dark-colored)—hereafter referred to as corner data. After segmenting a tile, all segmented crowns that are within a horizontal distance of 2 × AFP from a tile edge form part of the boundary data. Crowns adjacent to only one edge (solid light-colored) are regarded

Figure 5. A schematic of a tile with the two types of boundary data. The solid-colored tree crown pieces inside the tile should be unified with the corresponding stripe-colored parts outside in a distributed computing environment.

as part of the associated edge data and those adjacent to exactly two edges (solid dark-colored) are regarded as part of the associated corner data.

Figure 6 shows the flowcharts of the master and the slave processes, where it is assumed that all processes can independently input tiles data and output results. Such an assumption can be fulfilled by using a supercomputing with a unified file system, or by maintaining the tiles and the results on a specialized distributed spatial data organization/retrieval system [22, 23]. The master initializes the work by loading the tile map and assigning each slave to process a unique tile via a process tile (PT) message. Upon receiving a PT message, a slave loads and segments the tile and identifies the boundary data inside the tile including eight disjoint sets (four edges and four corners). The slave outputs the segmented non-boundary trees, notifies the master via a tile complete (TC) message conveying the boundary sets, and waits for a new assignment. The master then updates the tile map and examines all eight boundary sets it received from the slave to determine if any of the associated edge/corner data are ready to be unified. Edge data are ready when both tiles sharing the edge are segmented and corner data are ready when all four tiles sharing the corner are segmented. The master then unifies all edge/corner data that are ready and re-assigns the waiting slave to re-segment the unified boundary data, which is conveyed by a process boundary (PB) message. The slave process, upon receiving the PB message, segments the boundary data, outputs the result trees, and notifies the master via a boundary complete (BC) message. The master then re-assigns a new tile via a PT message to the slave. If the master cannot locate any ready boundary data when it receives the TC message, it proceeds with re-assigning the waiting slave to segment a new tile

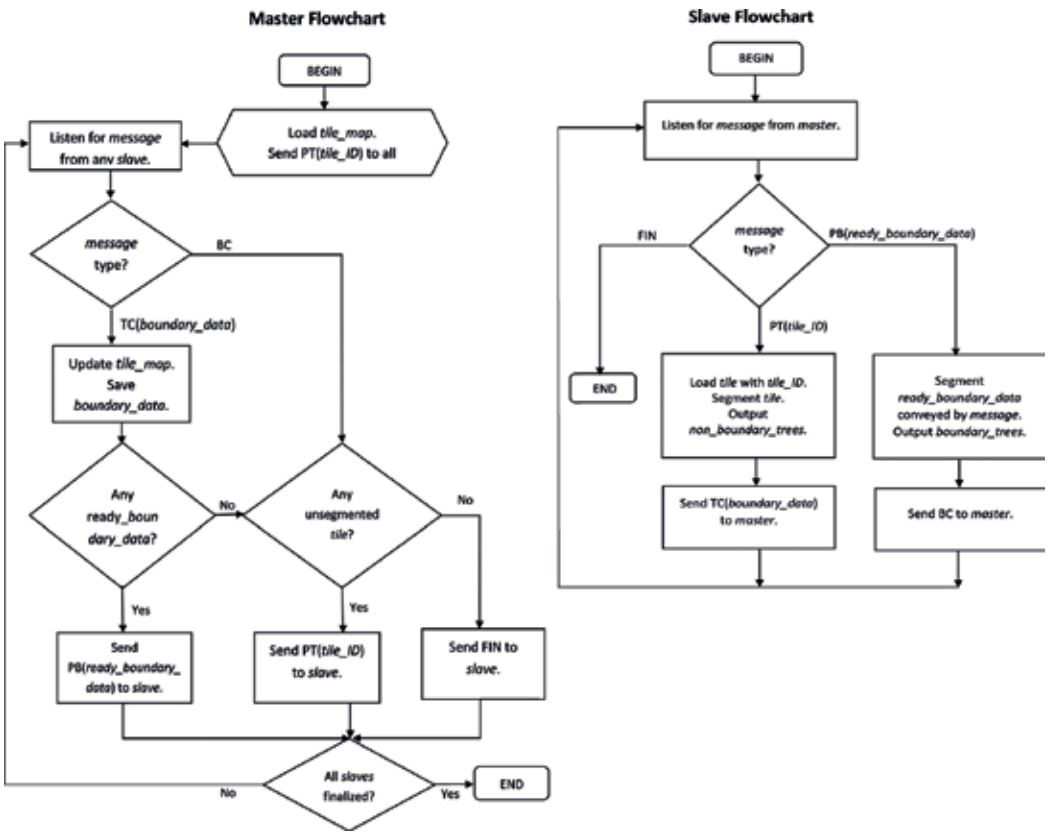

Figure 6. Flowcharts of the master and the slave. The master is responsible for maintaining the tile map globally and coordinating the slaves while a slave segments tiles and boundary data as directed by the master.

via a PT message. If all tiles are segmented, the master terminates the slave process by sending a final (FIN) message. The master process continues until all slaves are finalized, implying that all tiles and their boundary data were processed.

In the presented distributed approach, once all tiles sharing each specific edge or corner are segmented, the edge/corner data are assigned to be processed by the slave that completed the last tile. Assuming the master remains responsive, the slaves keep working all the time resulting in an efficient distributed processing scheme (see [21] for a theoretical analysis of the runtime and scalability).

2.5. Study site and LiDAR campaign

The study site is the University of Kentucky's Robinson Forest (RF, Lat. 37.4611, Long. −83.1555) located in the rugged eastern section of the Cumberland Plateau region of southeastern Kentucky in Breathitt, Perry, and Knott counties (**Figure 7a**). RF features a variable dissected topography with moderately steep slopes ranging from 10 to over 100% facing predominately northwest to southeast, and with elevations ranging from 252 to 503 m above sea level [24]. Vegetation consists of a diverse contiguous mixed mesophytic forest made up of

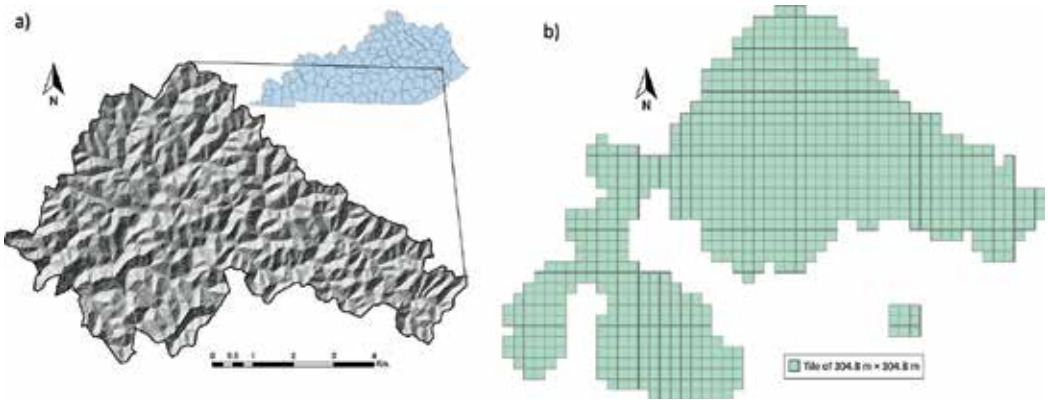

Figure 7. (a) Terrain relief map of the University of Kentucky Robinson Forest and its general location within Kentucky, USA and (b) LiDAR tile map of Robinson Forest consisting of 801 9.3-ha tiles.

approximately 80 tree species. Overstory species include northern red oak (*Quercus rubra*), white oak (*Quercus alba*), yellow-poplar (*Liriodendron tulipifera*), American beech (*Fagus grandifolia*), eastern hemlock (*Tsuga canadensis*), and sugar maple (*Acer saccharum*). Understory species include eastern redbud (*Cercis canadensis*), flowering dogwood (*Cornus florida*), spicebush (*Lindera benzoin*), pawpaw (*Asimina triloba*), umbrella magnolia (*Magnolia tripetala*), and bigleaf magnolia (*Magnolia macrophylla*) [24, 25]. Average canopy cover of RF is about 93% and it includes small opening scattered throughout. Most areas have a canopy cover of greater than 97% and recently harvested areas have an average cover as low as 63%. Because of being extensively logged in the 1920s, RF is considered second growth forest with the trees 80–100 years old, and is now protected from commercial logging and mining.

The LiDAR acquisition campaign over RF was performed in the summer of 2013 during leaf-on season (May 28–30) using a Leica ALS60 sensor, which was set at 40° field of view and 200 KHz pulse repetition rate. The sensor was flown at the average altitude of 214 m above ground at the speed of 105 knots with 50% swath overlap. Up to four returns were captured per pulse. Using the 95% middle portion of each swath, the resulting LiDAR dataset given the swath overlap has an average density of 50 pt/m^2. The provider processed the raw LiDAR dataset using the TerraScan software to classify LiDAR points into ground and non-ground points. The ground points were then used to create a 1-m resolution DEM using the natural neighbor as the fill void method and the average as the interpolation method. The LiDAR dataset was delivered in 801 square (304.8 m side ~9.3 ha area) tiles (**Figure 7b**), each containing about 5 million LiDAR points on average and occupying about 400 MB of disk space.

2.6. Evaluation

2.6.1. Field data

Throughout the entire RF, 270 regularly distributed circular plots of 0.04 ha in size spaced every 384 m were surveyed during the summer of 2013. Plot centers were georeferenced with 5 m accuracy. Within each plot, DBH (cm), tree height (m), species, crown class (dominant, co-dominant, intermediate, overtopped), tree status (live, dead), and stem class (single,

Plot-level metric		Min	Max	Avg.	Total	Percent of total
Slope	(%)	0	93	50		
Aspect		2	360	179		
Tree count		2	41	14.7	3971	
Dominant		0	3	0.5	130	3.3
Co-dominant		0	10	3.5	954	24.0
Intermediate		0	34	5.5	1481	37.3
Overtopped		0	19	4.3	1152	29.0
Dead		0	7	0.9	254	6.4
Species count		1	12	6.0	43	
Shannon diversity index		0.0	2.25	1.50		
Average tree height	(m)	13.9	28.8	19.5		
Standard deviation of tree heights	(m)	1.2	12.4	5.5		

Table 1. Summary of plot-level data collected from the 270 plots in Robinson Forest.

multiple) were recorded for all trees with DBH > 12.5 cm. In addition, horizontal distance and azimuth from plot center to the face of each tree at breast height were collected to create a stem map. Site variables including slope, aspect, and slope position were also recorded for each plot. **Table 1** shows a summary of the plot-level data. LiDAR data corresponding to each plot include a 4.7-m buffer to capture complete crowns of border trees.

2.6.2. Tree segmentation evaluation

To evaluate the performance of the tree segmentation method, a score to each pair of LiDAR-derived tree location, assumed to be the apex of the segmented crown, and stem location measured in the field is assigned. The score is based on the tree height difference, which should be less than 30%, and the leaning angle between the crown apex and the stem location, which should also be less than 15° from nadir. The set of pairs with the maximum total score where each crown or stem location appears not more than once is selected using the Hungarian assignment algorithm and is regarded as the matched trees [15]. The number of matched trees (MT) is an indication of the tree segmentation quality. The number of unmatched stem map locations (omission errors—OE) and unmatched LiDAR-derived crown apexes that are not in the plot buffer area (commission errors—CE) indicate under- and over-segmentation, respectively. The segmentation accuracy is calculated in terms of recall (Re—measure of tree detection rate), precision (Pr—measure of correctness of detected trees), and F-score (F—combined measure) using the following equations [26]:

$$Re = \frac{MT}{MT + OE} \tag{9}$$

$$Pr = \frac{MT}{MT + CE} \tag{10}$$

$$F = \frac{2 \times Re \times Pr}{Re + Pr} \tag{11}$$

3. Results and discussion

3.1. Tree segmentation evaluation

On average for the 270 plots in RF, recall of the tree segmentation method was 60%, precision was 91%, and F-score was 70% (**Figure 8**). Recall values ranged from 16 to 100% and precision values ranged from 36 to 100%. In dense plots with a relatively large number of understory trees, several trees were missed resulting in relatively low recall values (**Figure 9**). However, more than 90% of overstory trees were detected in those plots. As expected, the overall three segmentation accuracy metrics were higher for overstory trees compared with understory trees (**Figure 8**). Recall, precision, and F-score for overstory trees were 91, 85, and 86%, respectively, while for understory trees they were 48, 97, and 62%. When considering all crown classes, the tree segmentation method was able to detect 95% of dominant, 90% of co-dominant, 62% of intermediate, and 30% of overtopped trees in the 270 plots. In addition, the method was able to detect 20% of dead trees.

By stratifying the canopy to layers and independently segmenting each layer, the average precisions over the 270 plots decreased for all crown classes while average recalls increased (**Figures 8** and **9**). When comparing performance measures with and without stratification using two-tailed paired T-tests, all metrics except F-score for overstory trees showed significant ($P < .0001$) changes, which is also evidenced by the non-overlapping 95% confidence intervals in **Figure 8**. Recall and precision for understory trees showed the most remarkable changes: an increase from 46 to 68% (MSE = 10.04) and a decrease from 99 to 84% (MSE = 3.97), respectively. Overall, vertical stratification of canopy improved the F-scores for understory (from 61 to 73%, MSE = 1.70) as well as for all trees (from 70 to 77%, MSE = 0.66), while it barely affected

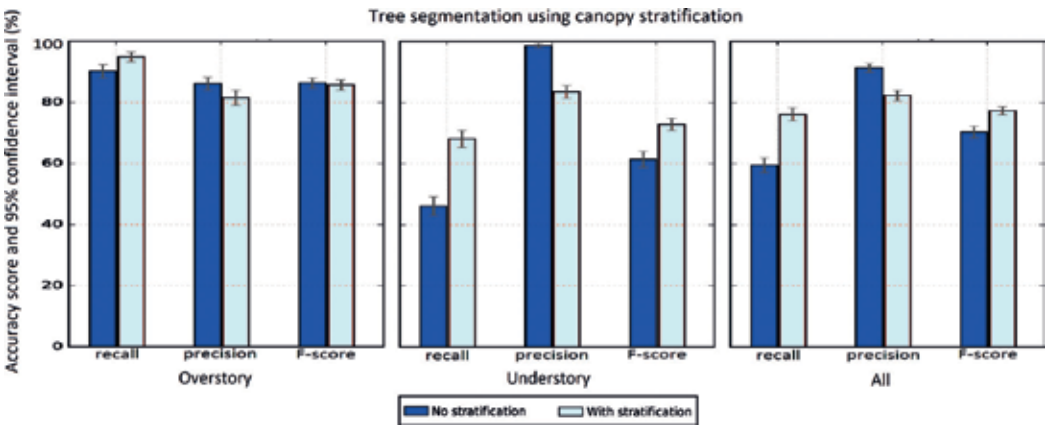

Figure 8. Average segmentation accuracies over 270 sample plots grouped by crown class.

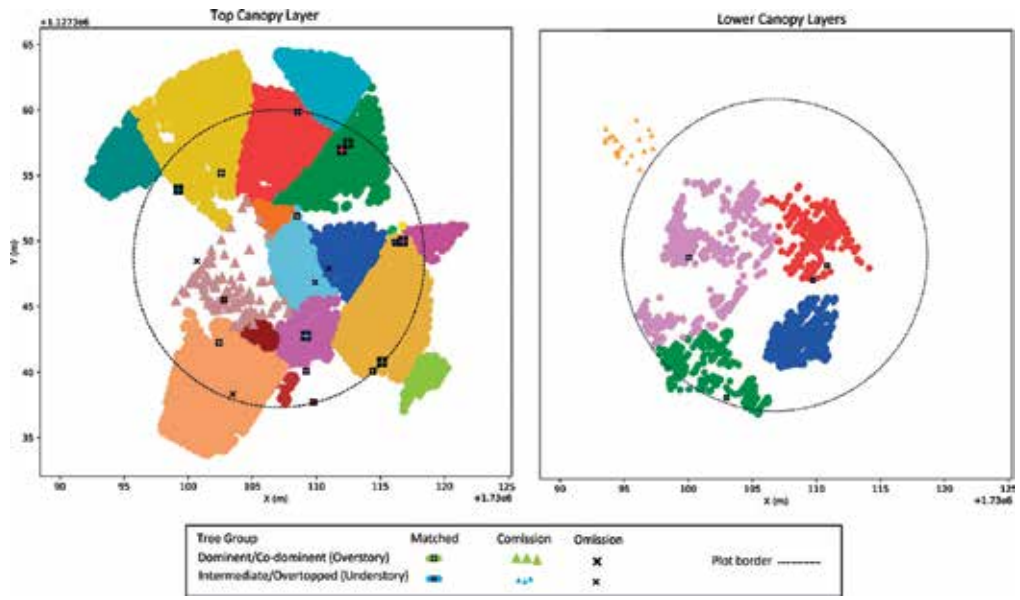

Figure 9. Aerial view of segmented trees within a dense plot that are matched with the ground referenced trunk locations (colors are for the purpose of distinguishing tree crowns and do not represent any semantic). Left panel shows tree segmentation result of the top canopy layer in which several understory trees were missed. Right panel shows tree segmentation result of the next canopy layers where the missed understory trees were detected, though a commission error at the understory level was introduced.

the F-score for overstory trees. When considering all crown classes, detection rate for dominant, co-dominant, intermediate, overtopped, and dead trees was 96, 93, 72, 53, and 30%, respectively. The improvements gained as a result of canopy stratification are mainly due to a strong increase in detection rate and a moderate decrease in correctness of the detected understory trees. This observation indicates an increased sensitivity to segment understory trees while not affecting the segmentation of overstory trees.

3.2. Stratified canopy layers

For most of the 270 plots, the canopy stratification procedure identified 3 (68.2%) or 4 (24.1%) canopy layers with an average number of canopy layers of 3.16 per plot. Any layer entirely located below 4 m was excluded because it likely represents ground level vegetation, although any of the remaining layers may extend below 4 m and even touch the ground. Starting height and thickness of a canopy layer are defined as the medians over all grid cells used to stratify the layer (**Figure 3**). The average starting height of a canopy layer ranged from 0.3 to 18.2 m and the average thickness of a layer ranged between 6.1 and 8.8 m. Also, the average point density ranged between 0.44 and 42.08 pt/m^2 (**Table 2**). The average starting height, thickness, and point density of the entire canopy (all layers aggregated) was 1.4 m, 24.8 m, and 47.5 pt/m^2, respectively. The average point density of the entire canopy agrees with the average point density of the initial LiDAR dataset of 50 pt/m^2 given that ground and ground level vegetation returns were removed.

Canopy layer	Plots (%)[1]	Starting height (m)		Thickness (m)		Point density (pt/m^2)	
		Avg.	S.D.	Avg.	S.D.	Avg.	S.D.
1	0.00	18.16	4.53	8.18	0.38	42.08	17.42
2	7.78	4.23	2.58	8.76	0.99	5.02	3.23
3	68.15	0.47	1.03	6.44	1.35	0.84	0.79
4	24.07	0.34	1.39	6.14	1.82	0.44	0.80
Aggregate	100.00	1.38	1.41	24.85	4.26	47.45	20.13

[1]Plots having as many number of canopy layers.

Table 2. Summary statistics of the canopy layers stripped over the 270 sample plots.

Thickness and point density generally decrease with lower canopy layers (**Table 2**). Specifically, the third and fourth top canopy layers, where the majority of understory trees are found, have an average density lower than 1 pt/m^2. Such low density is far less than the reported optimal point density in the literature of ~4 pt/m^2, where accuracies for segmenting individual trees plateau [11, 12]. This low density of understory canopy layers is the main reason for inferior tree segmentation accuracy of understory trees compared with overstory trees. As reported by Kükenbrink et al. [10], at least 25% of canopy volume remain uncovered even in small-footprint airborne LiDAR acquisition campaigns, which concurs with suboptimal point density of lower canopy layers for tree segmentation here.

3.3. LiDAR occlusion model

In order to estimate p_n in Eq. (7), we used the canopy stratification result of the 270 plot point clouds (**Table 2**). We recorded a sequence of five p_n values ($1 \le n \le 5$, zeros for missing layers) for each point cloud. We then fitted a logarithmic series distribution to all (n, p_n) pairs (N = 852, MSE = 0.0025—**Figure 10**):

$$p_n = \frac{0.266^n}{-ln(1-0.266) \times n} \qquad n \in \mathbb{N} \tag{12}$$

As mentioned, the reported optimal PCD for a reasonable segmentation of trees is about 4 pt/m^2 [11, 12], which is the value we adopt for PCD_{min}. Using Eq. (8) where p_n is calculated from Eq. (12), the minimum PCD required to reasonably segment trees in as deep as the third canopy layers would be 169.57 pt/m^2. Similarly, if we require having a reasonable segmentation for as deep as only two canopy layers, the minimum PCD becomes 30.1 pt/m^2.

3.4. Distributed processing

We implemented the distributed segmentation approach without canopy stratification using the message passing interface (MPI) and ran it on the University of Kentucky Lipscomb cluster. Using 192 processing cores, the distributed approach segmented a grand total of 1,994,970 trees in 2.5 hours. This time is actually ~167 times shorter than using only a single computer

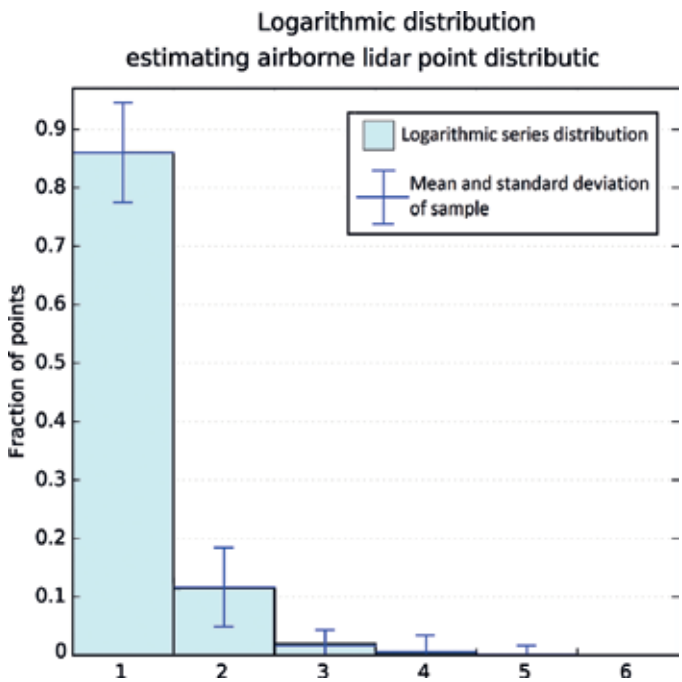

Figure 10. Logarithmic series distribution estimating observed fractions of LiDAR points recorded for different canopy layers. The distribution has a discrete domain supporting natural numbers.

assuming the computer has enough memory to load the entire LiDAR dataset (see [21] for a detailed analysis of the runtime). Implementation of the approach to run under the Hadoop MapReduce infrastructure [27] is also possible. Loading and segmentation of an individual tile is the map phase, where the non-boundary trees is output to the file system and each of the eight boundary data is assigned a unique key for the reduce phase. The unique key of each specific edge/corner data must be the same across all the map tasks that share the specific edge/corner. The reduce phase unifies all of the data it is given (edge/corner data portions having an identical unique key), re-segment the data, and output the result to the file system. There is no explicitly defined master process because the map-reduce infrastructure is responsible for coordination between the map and the reduce tasks, as well as scalability and fault tolerance.

As the distributed processing approach uses the tree segmentation method as a building block and does not require any knowledge on how the method functions, it may straightforwardly be used to adopt any other single-processor object identification/segmentation algorithm to scale up processing arbitrarily big spatial and geospatial datasets, such as remotely sensed buildings, cars, planets, etc. The only caveat is that the objects may not be greater than the tile size (they may not touch more than two adjacent edges of a tile). Also, generalization of the approach to process 3D spatial data in a similar manner is possible. Instead of tiles that are representing surfaces, cubes representing volumes form the data units for 3D analysis. Boundary data in this case would be surface (shared between two cubes), edge (shared among four cubes), and corner (shared among eight cubes).

3.5. Global parameters of Robinson Forest

Although in theory tile size does not affect the segmentation result of the distributed approach, a slight bias that was linearly correlated with the total length of the shared tile edges was introduced in practice. To quantify the bias, we created five 1.5 × 1.5 km square blocks of LiDAR point clouds (including ~3% of the entire RF data per block) and segmented each block using the tree segmentation method run on a single computer. We then partitioned each block into grids of 2 × 2, 3 × 3, …, 15 × 15 sub-blocks and segmented the partitioned blocks using the distributed approach. By comparing the number of trees segmented for different partitioning patterns, we discovered that an average of 96 additional trees (false positives) were segmented per 1 km of shared sub-block edge length (see [21]). Given the total length of the shared tile edges of the entire RF data is 446.23 km (**Figure 7b**), the estimated number of false positives became 42,833 (2.15% of the grand total number of trees). Subtracting these false positives resulted in a grand total of 1,952,137 segmented trees.

Due to the imperfectness of the segmentation method within each tile, a portion of the grand total number of segmented trees was over-segmented and a portion of existing trees in the forest was undetected. To account for the over-segmentations/undetected trees, we used the accuracy results of the segmentation method on the 270 plots of RF (**Figure 8**). The detailed accuracy result included the number of detected trees (bearing over-segmentations) and the number of existing trees (bearing undetected trees) by crown classes (dominant, co-dominant, intermediate, and overtopped). Within each of the 270 plots, we calculated by crown class a fraction of the existing trees in that crown class divided by the grand total (all crown classes) of detected trees. **Table 3** shows the mean and 95% confidence interval bounds of the fractions across the 270 plots. It also shows the adjusted estimates of number of existing trees, which were calculated by multiplying the grand total number of detected trees using the distributed approach to the corresponding fractions. Considering a 95% confidence interval, the total number of existing trees in the 7441.5-ha forested area is estimated to be 2,495,170 (±5.71%), which results in an average of 335.30 trees per ha.

Crown class	Fraction of existing to grand total detected		Estimated number of existing trees	
	Mean	95TCB (%)[1]	Entire forest	Per ha
Dominant	0.0785	±28.80	153,178	20.59
Co-dominant	0.3069	±7.84	599,106	80.50
Intermediate	0.5376	±8.18	1,049,446	141.32
Overtopped	0.2928	±10.94	571,522	76.80
Dead	0.0625	±18.63	121,917	16.38
All	1.2782	±5.71	2,495,170	335.30

[1]95% T-confidence bounds (DF = 269).

Table 3. Estimated number of trees categorized based on tree crown class.

For verification purposes, we compared the LiDAR-derived tree number estimates (**Table 3**) with equivalent estimates based on field measurements of the 270 plots from RF (**Figure 11**). The estimates for total number of trees per ha differ by about 3% (~342 LiDAR-derived compared with ~326 field estimated) and the estimates of number of dominant trees per ha differ by about 30% (~21 LiDAR-derived compared with ~15 field estimated). However, the large overlaps between the 95% confidence interval errors indicate no statistically significant differences. The height distribution of all segmented trees in RF shows a bimodal pattern (**Figure 12**), which can be attributed to the multi-story structure. A normal mixture model to the bimodal distribution was fitted, where the larger peak (associated with overstory trees) has a mean height of 26.9 m and a standard deviation of 6.6 m, and the smaller peak (associated with understory trees) has a mean height of 9.4 m and a standard deviation of 2.6 m. We compared the LiDAR-derived mean tree height estimates with those obtained from the 270 sample plots (371 overstory and 826 understory trees, **Table 1**). The sample mean height of overstory trees was 25.4 m with a standard deviation of 5.3 m, and the sample mean height of understory trees was 17.0 m with a standard deviation of 4.1 m. Considering that the LiDAR-detected tree heights are in fact biased by presence of falsely detected trees and absence of undetected trees, the field estimates are close to the LiDAR-detected estimates for overstory trees. However, field estimates for understory trees are remarkably larger than the LiDAR-detected estimates. The reason is likely that the only information used to fit the normal mixture model was the heights of the trees while height may not be sufficient for classification, that is, a moderately tall tree can be classified as an understory tree if it is surrounded by taller trees while the mixture model always classifies it as overstory according to its height, and vice versa.

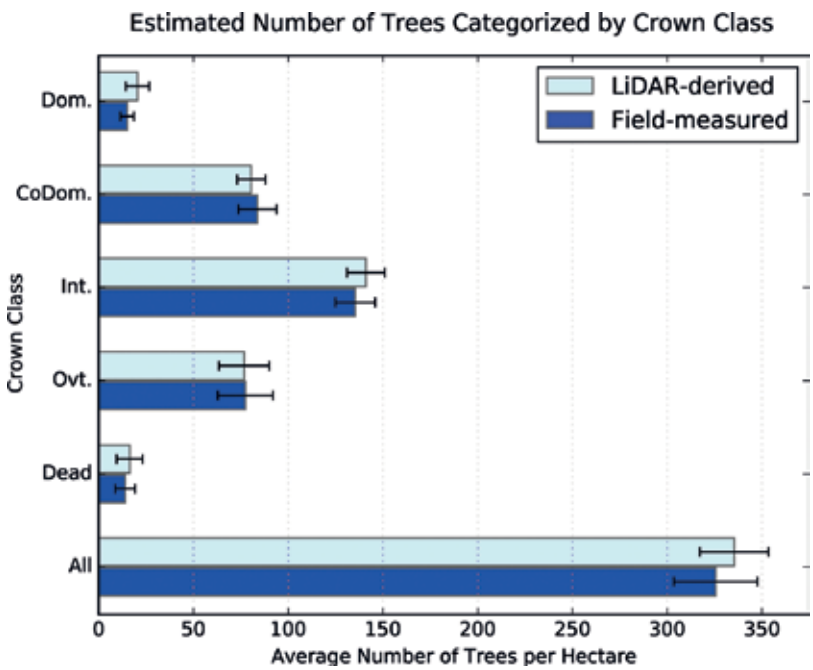

Figure 11. Estimated number of trees using LiDAR compared to field-collected along with the 95% confidence intervals.

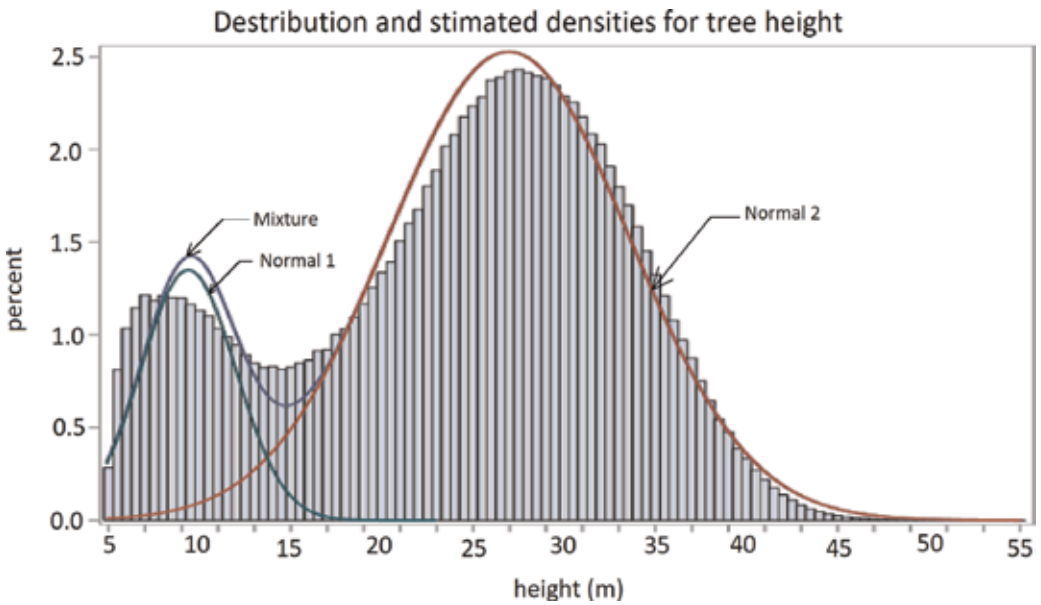

Figure 12. Height distribution of nearly two million trees segmented in Robinson Forest superimposed with estimated normal mixture model.

4. Conclusions

Airborne LiDAR point clouds covering forested areas contain a wealth of information about the horizontal and vertical structure of vegetation. This information can be used to segment individual trees and subsequently retrieve their morphological attributes. However, existing tree segmentation methods are forest type specific and are majorly focused on conifer stands and/or forests with open canopy. We presented a robust tree segmentation method that does not require prior assumptions about the crown shapes/sizes nor tree spacing. Applying the proposed approach to RF, a deciduous natural forest with complex vegetation and stand structures, we observed overall segmentation accuracies of ~87% for overstory trees and ~61% for understory trees. We also presented a canopy stratification procedure to separate the point cloud to an overstory and multiple understory canopy layers. We applied the tree segmentation method independently to each canopy layer, which improved the overall segmentation accuracy of understory trees from ~61 to ~73%. Using the canopy stratification, we developed a LiDAR pulse occlusion model in terms of point density and estimated that a density of about 170 pt/m^2 is required to segment understory trees found as deep as the third canopy layer as accurately as overstory trees. Lastly, we presented a distributed computing approach to scale up tree segmentation of the entire RF, which segmented about two million trees in 2.5 hours using 192 cores. The approach enabled locating individual tree and retrieving the point cloud segments representing tree crowns for large forested areas in a timely manner.

The presented work in this chapter provides methods for processing discrete return LiDAR point clouds of complex and large forested areas. Together with the advancements of the LiDAR sensor technology and platforms enabling acquisition of denser point clouds, accurate and remote quantification of forest resources at the individual tree level is expected to become feasible in near future, which in turn facilitates accurate monitoring, management, and conservation activities of these resources.

Acknowledgements

This work was supported by: (1) the Department of Forestry at the University of Kentucky and the McIntire-Stennis project KY009026 Accession 1001477, (ii) the Kentucky Science and Engineering Foundation under the grant KSEF-3405-RDE-018, and (iii) the University of Kentucky Center for Computational Sciences.

Author details

Hamid Hamraz[1]* and Marco A. Contreras[2]

*Address all correspondence to: hhamraz@cs.uky.edu

1 Department of Computer Science, University of Kentucky, Lexington, KY, USA

2 Department of Forestry, University of Kentucky, Lexington, KY, USA

References

[1] Pan Y, Birdsey RA, Phillips OL, Jackson RB. The structure, distribution, and biomass of the world's forests. Annual Review of Ecology, Evolution, and Systematics. 2013;**44**:593-622

[2] Shiver BD, Borders BE. Sampling Techniques for Forest Resource Inventory. New York, NJ, USA: John Wiley and Sons; 1996

[3] Haara A, Leskinen P. The assessment of the uncertainty of updated stand-level inventory data. Silva Fennica. 2009;**43**(1):87-112

[4] Maltamo M, Næsset E, Vauhkonen J. Forestry applications of airborne laser scanning: concepts and case studies. Managing Forest Ecosystems. Heidelburg, Germany: Springer Science and Business Media; 2014

[5] Latifi H. Characterizing forest structure by means of remote sensing: A review. In: Escalante B, editor. Remote Sensing—Advanced Techniques and Platforms. Rijeka, Croatia: INTECH Open Access Publisher; 2012

[6] Li Z, Zhu C, Gold C. Digital Terrain Modeling: Principles and Methodology. USA: CRC Press; 2010

[7] Goerndt ME, Monleon VJ, Temesgen H. A comparison of small-area estimation techniques to estimate selected stand attributes using LiDAR-derived auxiliary variables. Canadian Journal of Forest Research. 2011;**41**(6):1189-1201

[8] Koch B, Heyder U, Weinacker H. Detection of individual tree crowns in airborne LiDAR data. Photogrammetric Engineering & Remote Sensing. 2006;**72**(4):357-363

[9] Kaartinen H, Hyyppä J, Yu X, Vastaranta M, Hyyppä H, Kukko A, et al. An international comparison of individual tree detection and extraction using airborne laser scanning. Remote Sensing. 2012;**4**(4):950-974

[10] Kükenbrink D, Schneider FD, Leiterer R, Schaepman ME, Morsdorf F. Quantification of hidden canopy volume of airborne laser scanning data using a voxel traversal algorithm. Remote Sensing of Environment. 2016;**194**:424-436

[11] Jakubowski MK, Guo Q, Kelly M. Tradeoffs between lidar pulse density and forest measurement accuracy. Remote Sensing of Environment. 2013;**130**:245-253

[12] Evans JS, Hudak AT, Faux R, Smith A. Discrete return lidar in natural resources: Recommendations for project planning, data processing, and deliverables. Remote Sensing. 2009;**1**(4):776-794

[13] Thiemann F, Werder S, Globig T, Sester M, editors. Investigations into partitioning of generalization processes in a distributed processing framework. 26th International Cartographic Conference; Dresden, Germany; 2013

[14] Swatantran A, Tang H, Barrett T, DeCola P, Dubayah R. Rapid, high-resolution forest structure and terrain mapping over large areas using single photon lidar. Scientific Reports. 2016;**6**:28277

[15] Hamraz H, Contreras MA, Zhang J. A robust approach for tree segmentation in deciduous forests using small-footprint airborne LiDAR data. International Journal of Applied Earth Observation and Geoinformation. 2016;**52**:532-541

[16] Randolph KC. Equations relating compacted and uncompacted live crown ratio for common tree species in the South. Southern Journal of Applied Forestry. 2010;**34**(3): 118-123

[17] Hamraz H, Contreras MA, Zhang J. Vertical stratification of forest canopy for segmentation of understory trees within small-footprint airborne LiDAR point clouds. ISPRS Journal of Photogrammetry and Remote Sensing. 2017;**130**:385-392

[18] Hamraz H, Contreras MA, Zhang J. Forest understory trees can be segmented accurately within sufficiently dense airborne laser scanning point clouds. Scientific Reports. 2017; **7**(1):6770

[19] Laes D, Reutebuch S, McGaughey B, Maus P, Mellin T, Wilcox C, et al. Practical Lidar Acquisition Considerations for Forestry Applications. US Department of Agriculture, Forest Service RSAC; 2008. Report No.: RSAC-0111-BRIEF1

[20] Krishnamoorthy K. Handbook of Statistical Distributions with Applications. USA: CRC Press; 2016

[21] Hamraz H, Contreras MA, Zhang J. A scalable approach for tree segmentation within small-footprint airborne LiDAR data. Computers & Geosciences. 2017;**102**:139-147

[22] Aji A, Wang F, Vo H, Lee R, Liu Q, Zhang X, et al. Hadoop GIS: A high performance spatial data warehousing system over mapreduce. Proceedings of the VLDB Endowment. 2013;**6**(11):1009-1020

[23] Hongchao M, Wang Z. Distributed data organization and parallel data retrieval methods for huge laser scanner point clouds. Computers & Geosciences. 2011;**37**(2):193-201

[24] Carpenter SB, Rumsey RL. Trees and shrubs of Robinson Forest Breathitt County, Kentucky. Castanea. 1976:277-282

[25] Overstreet J. Robinson Forest Inventory. Department of Forestry: University of Kentucky, Lexington, Kentucky; 1984

[26] Manning CD, Raghavan P, Schütze H. Introduction to Information Retrieval. Cambridge: Cambridge University Press; 2008

[27] White T. Hadoop: The Definitive Guide. Boston, MA, USA: O'Reilly Media Inc.; 2012

Chapter 4

Remote Sensing in Land Applications by Using GNSS-Reflectometry

Yan Jia and Yuekun Pei

Additional information is available at the end of the chapter

http://dx.doi.org/10.5772/intechopen.72901

Abstract

Global navigation satellite system-reflectometry (GNSS-R) as an efficient tool for remote sensing has gained increasing interests in the last two decades, due to its unique characteristics. It uses GNSS signals as sources of opportunity, providing precise, continuous, all-weather, and 24 hours' detections, which play a key role in many land applications. The fundamental theoretical part of GNSS-R technique is examined at first. Then, GNSS-R methodologies applied in the soil moisture content, vegetation biomass sensing, and altimetry applications are also detailed. One retrieval method uses only RH (right-hand) reflected data. Another retrieval method for soil moisture content (SMC) aimed to calibrate the measurement by using water reflections, based on the bistatic equations with LH (left-hand) reflected and RH direct signals. The other method for SMC retrieval is related to the polarimetric ratio (PR), the ratio of LH/RH reflected signals can reveal the fluctuations of the SMC. Another vital parameter vegetation biomass was observed by using the variation of reflectivity of the LH and RH reflected components. Finally, the C/A code method was used for exploring the possibility to the altimetry estimation. The features of GNSS-R technique made it a promising remote sensing technique in hydrology, climatology carbon cycles, and other potential applications.

Keywords: GNSS-reflectometry (GNSS-R), soil moisture content, vegetation biomass, altimetry, polarimetric measurement

1. Introduction to GNSS

Global navigation satellite systems (GNSSs) are satellite constellations orbiting the Earth to provide continuous positioning and timing information for users on the globe. It mainly includes the United States' NAVSTAR global positioning system (GPS), European Union's Galileo, Russia's Glonass, China's BeiDou, and Japan's Quasi-Zenith satellite system (QZSS). For now,

such systems are used not only for navigation positioning but also for object detection in various disciplines, such as archeology (a 3-dimension map is generated using the combined signals of GPS, Glonass, and QZSS to detect each artifact), air traffic (the surveillance-broadcast system of air traffic control obtains aircraft positions by using GNSS signals), weather (forecast can be made through the atmospheric bending measurement of GNSS satellite signals), and others. The huge potential of GNSSs has led international governments and researchers made efforts on it [1]. Up to now, the United States' NAVSTAR GPS and the Russian GLONASS have begun providing global coverage for a long time. In December 2016, the European's Galileo formally announced to start its initial service to provide its full operational capability. China is in the process of expanding its regional BeiDou Navigation Satellite System into global compass navigation system in the very near 2020. India and Japan are also in the process of developing their regional navigation systems [2].

1.1. GPS system

GPS is the United States' global positioning system (GPS) developed since 1973. The number of satellites, the positions, and the relative inclinations was optimized to ensure an adequate global coverage. In 1978, the first operational prototype satellite was launched. In 1993, the initial capability and the full GPS system were declared [3]. As a universal positioning system, GPS provides an accurate, continuous, three-dimensional position and velocity information to the user with the appropriate receiver on Earth. Now, it is the most used navigation system in the world and fully operative both for military purpose and civilian aims [4].

The GPS signals are transmitted with right-hand circular polarization (RHCP) so that the ionosphere attenuation does not affect the signal reception. Each GPS satellite transmits

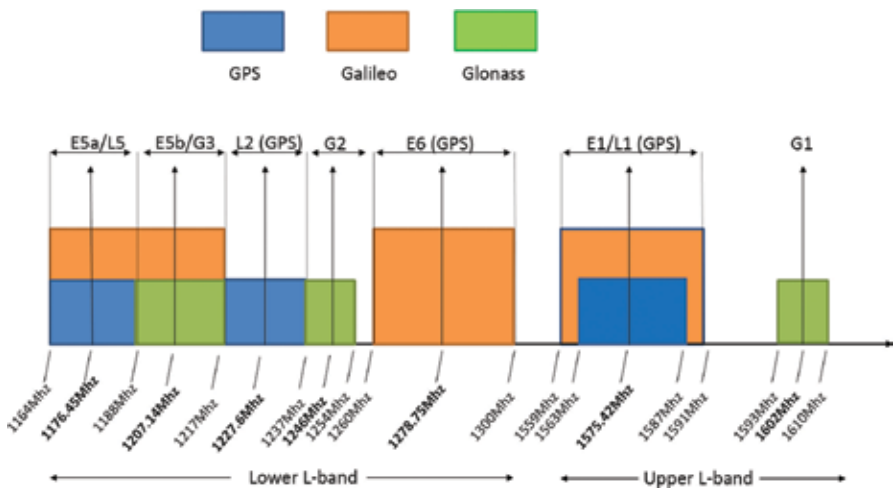

Figure 1. GNSS frequency bands.

microwave carrier signals at three bands: L1 (1575.42 MHz) carries the navigation message and the standard positioning services (SPS), L2 (1227.6 MHz) is used to measure the ionosphere delay by precise positioning services (PPS), and L5 (1176.45 MHz) was introduced to increase the accuracy for safety-of-life transportation applications [5]. The frequency plan and the band of GPS are shown in **Figure 1**, together with the information of Galileo and Glonass [6].

2. Theory of GNSS-reflectometry

GNSS-reflectometry is usually called for short as GNSS-R. Its main principle is to receive and further extract information from the GNSS signals which were reflected off the Earth surface. It works as a bistatic radar, in which the transmitter and the receiver are separated by a significant distance, comparable to the expected distance to the target. The concept can be expanded that the receiver receives multiple signals simultaneously from different transmitters, in which case, it is multistatic radar. Comparing with the other existing remote sensing tools, GNSS-R has following advantages: 1. The additional transmitter is not needed; 2. Many signal sources can be chosen, including GPS, Galileo, GLONASS, and BeiDou/Compass; 3. Use spread-spectrum communication technology for receivers to receive weak signals; 4. It provides a wide range of applications, for example, soil moisture retrieval, vegetation biomass detection, altimetry estimation, sea wind and wave height, and so on [1, 7–13].

2.1. GNSS-R geometry

In the case of GNSS-reflectometry, the transmitter and receiver are in the different locations, and the scattered signals can be originated from a variety of geometries, given a target that scatters sufficient power to the direction of the receiver. For the land surface, the typical bistatic geometry consists of a transmitter and receiver above the surface, with scattering taking place mainly from the region of the surface surrounding a specular reflection point. The specific geometry is depicted in **Figure 2**.

Figure 2 depicts signals transmitted from a GPS satellite (about 20,200 km height), scattered from the land surface along the specular direction, and received by a receiver equipped on an aircraft. The direct signal is received by the zenith antenna for processing positioning information or system calibration, and the reflected signal is received by the nadir antenna for remotely sensing the land surface. The incident RHCP GPS signal is predominantly left-hand circular polarization (LHCP) after specular scattering. The specular point is defined as a reflection point characterized that the incident and reflected angles are equal (Snell's Law). The strong coherent scattering component concentrated about a narrow area called the first Fresnel zone around the specular point. The size of this active region is usually considered to be the first Fresnel zone for which the differential phase change across the surface is constrained to $\lambda/2$ radians, where λ is the signal wavelength [14]. Surface roughness causes scattering from a

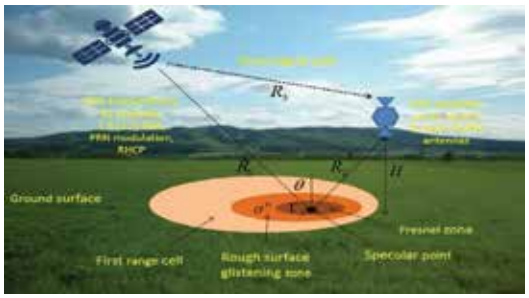

Figure 2. GNSS-R as a bistatic radar geometry.

glistening zone around the specular reflection point. The scattering component, also called incoherent or diffuse component, consists of power scattered randomly in all directions, with its magnitude smaller than coherent component.

When the distance from the surface to the transmitter is much larger than the distance from the surface to the receiver (or vice versa), the semi-major axis a and semi-minor axis b of the first Fresnel ellipse are dependent on the incidence angle θ, and minimum height of the transmitter or receiver H was given by [15]:

$$\alpha = \frac{\sqrt{2\delta H \cos(\vartheta)}}{(\cos(\theta))^2}, b = \frac{\sqrt{2\delta H \cos(\theta)}}{\cos(\theta)}, \tag{1}$$

where δ is the phase change measured in wavelengths ($\lambda/2$ for the first Fresnel zone) and θ is the incident angle.

As the signal scattering, the time delay and the frequency of the received signals change. The narrowly spaced iso-range ellipses (lines of equal delay across the surface) and iso-Doppler hyperbolas (lines of equal Doppler frequency across the surface) can be mapped across the Earth as shown in **Figure 3**. At each point in the glistening zone, the path delay and reflection angles are different. This results in a range of different path delays (between the transmitter and receiver) and Doppler frequencies at the receiver. Lines of constant delay or iso-range lines can be drawn as ellipses centered at the point of specular reflection. The lines with the same radial velocity are the cuts of the cone surfaces with the earth plane, i.e., parabola. At fixed radio frequency (RF), the radial velocity is proportional to the Doppler frequency. Therefore, the cone can also be called Doppler cone, and the cone cuts with the earth surface called iso-Doppler lines [16, 17].

In **Figure 3**, the red ellipses represent the first Fresnel zone. The uneven ring belts indicate equal-code delay lines (yellow lines). The black curves are the Equal-Doppler lines. GPS satellites are far from the Earth and thus the Fresnel belts are small. The surface property can be extracted through analyzing the reflected signal and the direct one.

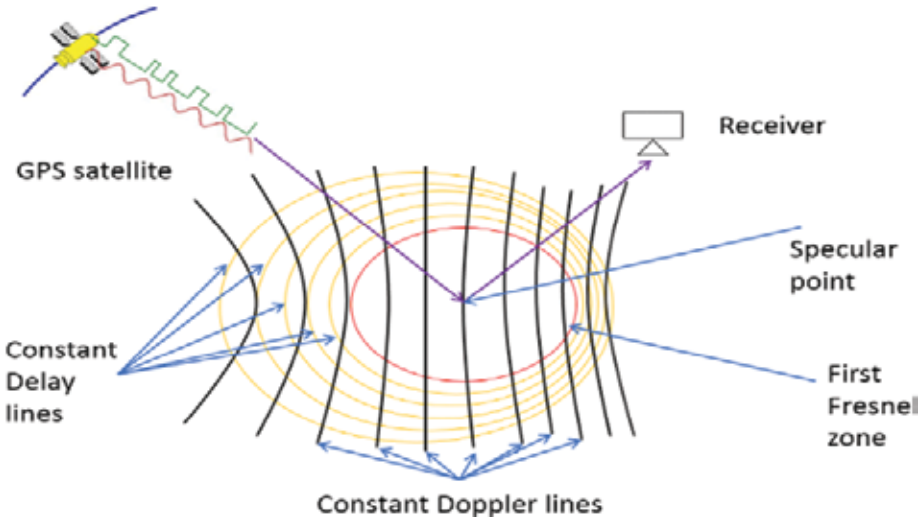

Figure 3. Iso range and iso-Doppler lines across the Earth's surface around the specular reflection point.

2.2. Bistatic radar equations

In general, the total scatter power p_{pq}^{r} measured by a bistatic radar can be expressed as [18]:

$$p_{pq}^{r} = p_{pq}^{c} + p_{pq}^{i}, \tag{2}$$

where subscripts q and p denote the incident and scattered polarizations. p_{pq}^{c} and p_{pq}^{i} are the coherent power and incoherent power, respectively.

2.2.1. Coherent component from smooth surface

For the coherent component in the case of like polarized GPS bistatic radar, the bistatic equation can be written as [18],

$$P_{lr}^{c} = \frac{P_{r}^{t} G^{t}}{4\pi (R_{st} + R_{rs})^{2}} \frac{G^{r} \lambda^{2}}{4\pi} \Gamma_{lr}. \tag{3}$$

Subscript lr represents the scattering when a satellite incident signal (right-hand polarized) is scattered by the surface and inverts the polarization to the left-hand, P_{r}^{t} is the transmitted RHCP signal power, G^{t} is the transmitter antenna gain, G^{r} is the receiver antenna gain, and λ is the wavelength (19.042 cm for GPS L1 signal). R_{rs} is the distance between the receiver and the specular point, R_{st} is the distance between the satellite and the specular point, and Γ_{lr} is the power reflectivity of the reflecting surface.

2.2.2. Coherent component from rough surface

As the smooth surface begins to transition to a rough surface, the coherent component of the reflected power is decreased. Therefore, the term Γ_{lr} in Eq. (3) decreased from that of the smooth surface case due to increasing roughness, which was described by [14].

$$\Gamma_{lr}(\theta) = |R_{lr}(\theta)|^2 \chi(z), \tag{4}$$

where R_{lr} is the Fresnel reflection coefficient and $\chi(z)$ is the probability density function of the surface height z.

The Fresnel reflection coefficient R_{lr} can be expressed as linearly polarization modes [7]:

$$R_{lr} = R_{rl=} \frac{1}{2}(R_{vv} - R_{hh}), \tag{5}$$

$$R_{rr} = R_{ll=} \frac{1}{2}(R_{vv} + R_{hh}), \tag{6}$$

where R_{vv} and R_{hh} are the Fresnel coefficients for horizontal and vertical polarization [19]:

$$R_{hh}(\theta) = \frac{\cos\theta - \sqrt{\varepsilon_r - \sin^2\theta}}{\cos\theta + \sqrt{\varepsilon_r - \sin^2\theta}}, \tag{7}$$

$$R_{vv}(\theta) = \frac{\varepsilon_r \cos\theta - \sqrt{\varepsilon_r - \sin^2\theta}}{\varepsilon_r \cos\theta + \sqrt{\varepsilon_r - \sin^2\theta}}, \tag{8}$$

$$\varepsilon_r = \varepsilon/\varepsilon_0 - j60\lambda\sigma, \tag{9}$$

where θ is the incident angle, in which ε is the dielectric constant of the surface, ε_0 is the dielectric constant of the air, λ is the wavelength of the signal, and σ is the electric conductivity.

Most of the natural surface can be modeled by a Gaussian height distribution. Thus, the reflectivity can be written as:

$$\Gamma_{lr}(\theta) = |R_{lr}(\theta)|^2 e^{-h(\cos\vartheta)^2}. \tag{10}$$

h was called roughness parameter, and it is defined as:

$$h = 4k^2\sigma^2, \tag{11}$$

where k is the wave number ($2\pi/\lambda$) and σ is the standard deviation of the surface. When it is a smooth surface ($h = 0$), the reflectivity R_{lr} is simply the square of the Fresnel reflection coefficient.

2.3. Coordinate reference systems

Latitude, longitude, and height are three coordinates used to characterize the user's position on Earth. A reference system with respect to the coordinates must be defined correspondingly.

In the beginning, the World Geodetic System 1984 ellipsoid (WGS84) in an Earth-centered, Earth-fixed (ECEF) coordinate system is defined for typical GPS measurements. The ECEF coordinates represent positions as (x, y, z). The x-axis points in the direction of $\mathbf{0}^{\circ}$ longitude (passing through the intersection of the Greenwich meridian with the equatorial plane), and the +y-axis points in the direction of $\mathbf{90}^{\circ}$ east longitude. The z-axis is chosen to be normal to the equatorial plane in the direction of the geographical north pole, thereby completing the right-handed coordinate system. The ECEF system enables users to know the positions with respect to the center of the Earth. The ellipsoid coordinate origin of WGS84 (latitude, longitude, and attitude) is meant to be located at the Earth's center of mass. It is a simplest geometric model, which best fits the entire Earth surface [20].

Since the Earth is not spherical and not uniform in density, the Earth Geoid Model 1996 (EGM96) was defined as the locus of all points with the same gravity potential (equipotential surface) best fitting with the mean sea level on the Earth [21]. When the height is indicated relevant to the mean sea level, it refers to the geoid model. The height of the geoid is denoted N with respect to the ellipsoid, which is shown in **Figure 4**. At each point, a geoidal height (N) is defined along the line perpendicular to the ellipsoid. It is measured from the ellipsoid to the geoid. Height h is the distance measured from the ellipsoid to the object. H indicates the height with respect to the geoid called orthometric height.

Georeferencing specular points on maps were done based on the ECEF coordinate system, by assuming the surface is locally flat and the surface height remains the same with that of the receiver projection position. However, a typical onboard GPS receiver and Google Earth software provide the ellipsoid height h based on the EGM96 model. Therefore, the EGM96 coordinates information was transferred in WGS84 and further converted to ECEF coordinates, in order to calculate the elevation angle with respect to the satellite position (x, y, z). On the other hand, the orthometric height H is useful, such as in the altimetry application. Hence, some computations are needed as Eq. 12 [3].

$$H \approx h - N. \tag{12}$$

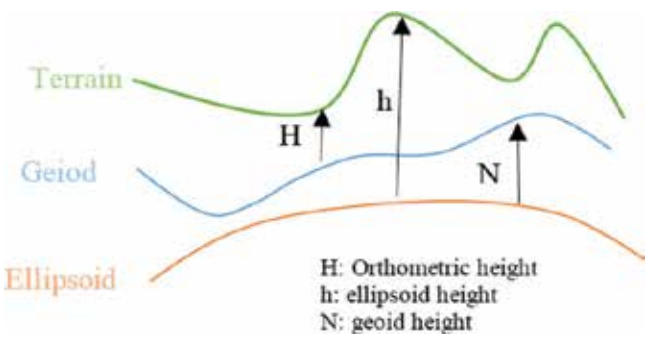

Figure 4. Relation of an ellipsoid, geoid, and terrain heights.

3. GNSS-R applications

3.1. Background and objective

After GNSS signals reflected off the Earth surface, the scattered signal received by the GNSS-R system contains the information of the surface. Hence, GNSS-R as an Earth's surface remote sensing tool has been widely studied for characterizing the reflecting surface. Several retrieval methods for soil moisture content (SMC), altimetry, and vegetation biomass estimation can be used to reveal the geographical and biological parameters of the Earth surface.

For altimetry application, the GPS Bistatic technique for altimetry application was first proposed by Martin-Neira [17]. The aim of the GNSS altimetry is to detect the height between the receiver and the reflecting surface. In principle, the altimetry techniques can be applied to any surface, but their performance will depend on the detecting environment [22–24].

For soil moisture application, frequencies in the range of 1–3 GHz have been shown to be ideally suited to sense soil moisture due to reduced atmospheric attenuation [25]. Njoku and O'Neill [26] showed that P-band (0.775 GHz) and L-band (1.4 GHz) frequencies are optimal for sensing soil moisture in the top 0–4 and 0–2 cm surface layers, respectively.

For biomass content sensing, a couple of papers mentioned that a retrieval method with very preliminary analysis is available. The one provided by Zavorotny et al. [27] proposed modeling GPS reflected signals having a different polarization state that can be used for sensing a homogeneous soil of rough land surface. The results were obtained by modeling the impact of soil moisture from the ratio between expected power levels in orthogonal polarizations (LR/RR, HR/VR), in function of the elevation angle. By varying the soil moisture level (x-axis) and different incident angles (the angle between the propagation path and the normal to the surface), the ratio of two orthogonal polarizations received power proved to be independent of the surface roughness factor and sensitive to the soil moisture. With this established theoretical hypothesis, the algorithm with respect to the orthogonal polarization was developed and presented as follows.

In the following, the retrieval methods for the SMC, vegetation sensing, and altimetry applications are applied and discussed in the framework of Italian SMAT-F2 (System of Advanced monitoring of the Territory—phase 2) project. First, the SMC retrieval and vegetation biomass sensing methods are detailed. With considering different kinds of measured signals, three kinds of retrieval methods based on the bistatic configuration are presented. Then, the C/A code altimetry method, which provides the possibility for altimetry estimation, will be discussed.

3.2. Methodologies

3.2.1. Overview of soil moisture retrieval methods

Soil dielectric constant and soil moisture retrieval play fundamental aspects in agriculture and water cycle attracting interests from many researchers and have started to produce some results. Three different methodologies were implemented mainly for this kind of applications:

1. Multipath effect and its relation to soil moisture: it uses a standard ground-based nearly hemispherical RHCP antenna to receive the direct signal (see **Figure 5(a)**). The reflected signal originated from ground creates multipath effects, since it interferes with the direct signal. The total received signal amplitude has a sinusoid behavior with the change of sine of elevation angle. By measuring the received SNR ratio, it is possible to retrieve soil moisture information [9, 27].

2. Interference pattern technique (IPT): usually a horizontal-pointing vertically polarized antenna is used (see **Figure 5(b)**). This technique consists of measuring the power fluctuations related to the signal resulting from the simultaneous reception (and interference) of the direct and the reflected GNSS signals. It is similar to a multipath effect. In this case, the two rays approach is adopted. Soil moisture retrieval is based on finding a specific 'notch' point from the interference pattern, versus satellite elevation [22, 28–30].

3. Bistatic method: this is based on the separate reception of direct and reflected signals using two different antennas and on the separate measurement of signal powers. Depending on the antenna configuration, three possible observing systems exploiting the bistatic geometry can be further identified:

   a. A down-looking LHCP antenna and an up-looking RHCP antenna: an LHCP antenna receives reflected GPS signal from the surface (see **Figure 5(c)**). The power reflectivity could be obtained either by using a bistatic radar equation [31] or from the power ratio between the reflected signal and the direct signal [32, 33]. The reflectivity is then a function of the dielectric constant of the soil, the elevation angle, and the surface roughness. By properly choosing the surface roughness parameter (elevation is known from the direct signal) for a certain scattering model (see for example [34]) such as the small perturbation method (SPM) and Kirchhoff approach (KA), the dielectric constant can be retrieved.

   b. One RHCP up-looking antenna and two down-looking antennas (or channels) with one RHCP polarized and the other LHCP polarized [7, 12, 35]. With this configuration (see **Figure 5(d)**), it is possible to measure both the co-polar component of the terrain reflectivity by using the LHCP signal and the cross-polar component by using the RHCP antenna. The ratio of these two reflectivities was in good correlation with SMC, and it was independent of the surface roughness.

   c. A similar configuration to the one described in (3.a) but with horizontally (H) and vertically (V) polarized antenna for both the up and down-looking directions (see **Figure 5(e)**): this configuration has been tested through some simulation studies [36]. The ratio between the reflected and the direct power on the horizontal polarization and the same ratio on the vertical polarization depend on the soil reflectivity and surface roughness. If the power ratio between the two channels with orthogonal polarization is considered, the influence of the surface roughness can be canceled. It was verified that the final expression holds under different scattering models, which means that it could be applied to a wide range of surface roughness. This dielectric constant retrieval approach is based on the use of the ratio of power densities scattered

at *HH* and *VV* polarizations along the specular direction for different incidence angles. Since the ratio is a function of both the elevation angle and the dielectric constant, a minimum least square technique was applied to better define the dielectric constant, by measuring at least two different elevation angles.

The retrieval of the soil moisture from the dielectric constant at microwave band (especially in L band) has been widely investigated, and several well-accepted theoretical and empirical models have been established, such as [25, 28, 37, 38]. The information of soil texture in terms

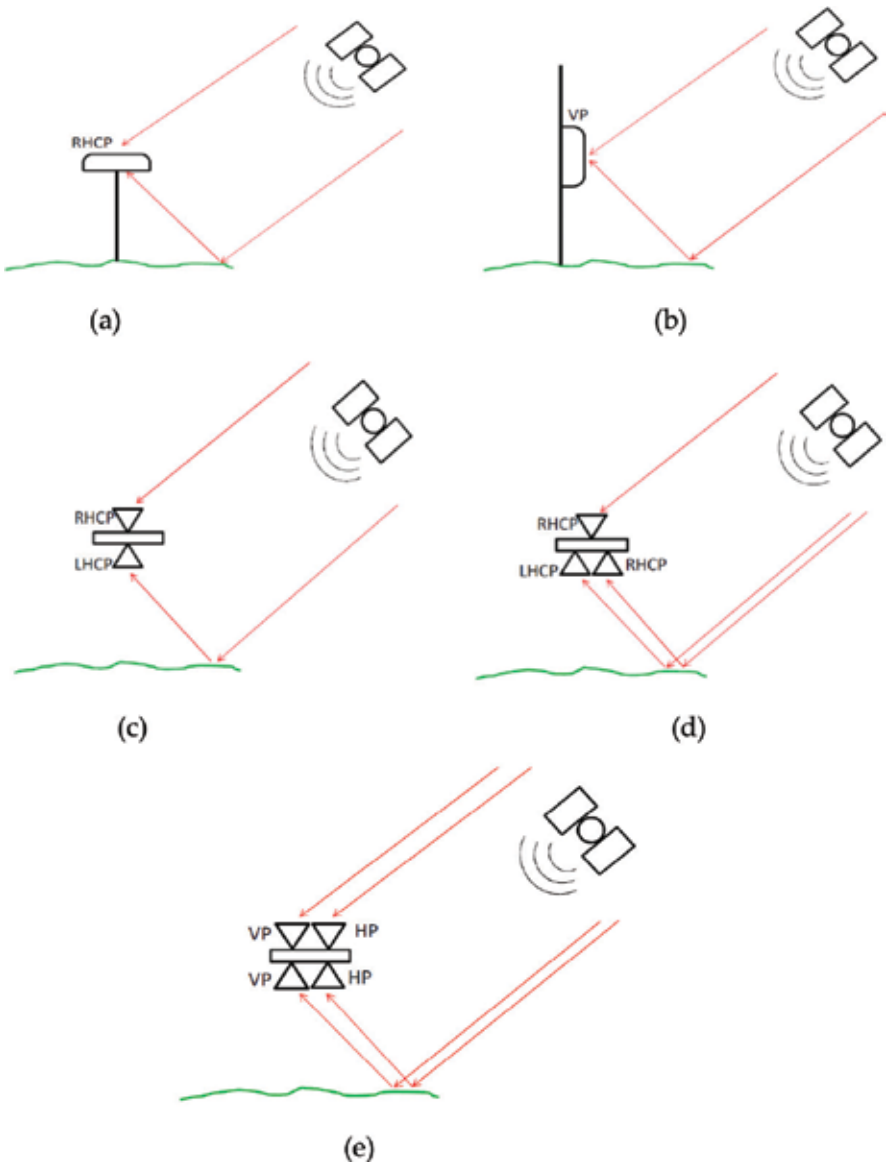

Figure 5. System schemes for different observing strategies.

of percentage of clay and sand should be known and provided in input to such models. A further model described by Topp et al. [39] does not depend on any input information, since it models the relative permittivity as a third-order polynomial function of soil moisture.

3.2.2. Bistatic methods for soil moisture retrieval

In this section, the algorithms used for SMC and vegetation sensing are applied based on the (5.a): bistatic method. The retrieval process aims to establish the link between received reflected signals and the dielectric constant of the soil. Moreover, the retrieval of dielectric constant is the key component to the retrieval of soil moisture, since there are several well-established models giving this relationship as introduced in the last section.

3.2.2.1. Only LH reflected GPS signals are measured

Assuming a perfectly smooth surface and regardless the surface roughness and incoherent components ($\Gamma_{lr} = (R_{lr}(\vartheta))^2$), the dielectric constant is retrieved from the LHCP-reflected SNR which can be processed by the open loop approach.

The expression of SNR is derived from bistatic radar equation:

$$SNR_{peak}^{reflect} = \frac{1}{4}\frac{P^t G^t}{4\pi(R_1+R_2)^2}\frac{G^r \lambda^2 G_D}{4\pi P_N}(R_{vv}-R_{hh})^2, \tag{13}$$

where P^t is transmitted signal power, G^t and G^r are antenna gains of transmitter and receiver, respectively. λ is signal wavelength (about 19 cm for GPS L1 signal). R_1 and R_2 represent the distances between specular point and transmitter or receiver. The superscript c denotes the coherent component, P_N is noise power, and G_D is the processing gain due to the de-spread of the GPS C/A code. The value of the correlation gain is determined by the chipping rate of the GPS L1 C/A code ($1.023e^6$ Hz) and 1 ms processing interval. It results:

$$G_{pr} = 10\log_{10}\left(\frac{1.023e^6}{1000}\right) = 30.1dB. \tag{14}$$

Fresnel reflection coefficients of *HH* and *VV* are given in Eqs. (7) and (8). The dielectric constant is then easy to be solved by combining the Eqs. (7), (8), and (13). Input parameters such as P^t, G^t, G^r, and G_D are usually seen to be constants. Since they are system parameters of GPS, P_N should be estimated or calculated properly. R_1, R_2, and θ are geographic information which can be calculated through receiver positions. SNR is the input parameter obtained from signal postprocessing. Knowing all the above input parameters, the dielectric constant can be solved numerically.

3.2.2.2. Both LH reflected and RH direct GPS signals are measured

In this case, both SNRs are obtained from RH direct signal and LH reflected signal. The dielectric constant can be retrieved from the power ratio of LHCP reflected SNR over direct

RHCP SNR, provided that direct RH signals are processed with the same open-loop approach to get SNR.

The SNR expression of the peak power for the direct RHCP signal is:

$$SNR_{peak}^{direct} = \frac{P^t G^t}{4\pi {R_3}^2} \frac{G^r \lambda^2 G_D}{4\pi P_N}, \tag{15}$$

where R_3 is the distance between the transmitter and receiver. It must be noted that receiver gain G^r and noise power P_N given in Eq. (15) are not equal to those given in Eq. (13) for the reflected signal path, and this is the reason why calibration is needed. By making the ratio of Eq. (13) to Eq. (15) canceling the same parameters and summarizing the uncertainties of G^r and P_N into a single calibration parameter C, we have:

$$\frac{SNR_{peak}^{reflect}}{SNR_{peak}^{direct}} = \frac{{R_3}^2}{4(R_1 + R_2)^2} (R_{vv} - R_{hh})^2 \cdot C. \tag{16}$$

Now, input parameters of R_1, R_2, θ and R_3 are only needed, and they are easy to obtain from positioning information. Calibration parameter C can be either ignored if there is no way to calibrate the system or calculated through over-water measurement. The dielectric constant can be obtained from Eq. (16), given all the input parameters defined.

3.2.2.3. Both LH reflected and RH reflected GPS signals are measured

The retrieval process has linked the measured reflected LHCP and RHCP power (or SNR) to the normalized bistatic radar cross section σ_{qp}^o, which has been widely studied and modeled for different surface roughness and scattering models, such as Kirchhoff Approximation in stationary-phase approximation (Kirchhoff Geometrical Optics, KGO), Kirchhoff approximation in physical optics approximation (KPO), and small perturbation method (SPM) [34].

Applying polarization scattering matrix [40] and combining some basic electromagnetic field theories, the cross-polarization power ratio of LHCP to RHCP has the relation with normalized bistatic radar cross section of linear polarizations:

$$\frac{\sqrt{P_{lr}^r}}{\sqrt{P_{rr}^r}} = \frac{\left|\sqrt{\sigma^o{}_{hh}} + \sqrt{\sigma^o{}_{vv}}\right|}{\left|\sqrt{\sigma^o{}_{hh}} - \sqrt{\sigma^o{}_{vv}}\right|}. \tag{17}$$

Note here that in Eq. (17), σ^o is approximated by the special case of $\sigma_{qp(spec)}^o$ in the specular direction for simplicity, and therefore, the cross polarization terms of $\sigma^o{}_{hv}$ and $\sigma^o{}_{vh}$ are computed to be zero for the models of KGO, KPO, and SPM in the specular direction case. Also, σ^o for hh and vv polarizations given by these three models are all products of a polarization sensitive parameter, usually the Fresnel reflection coefficient and other polarization independent surface roughness parameters (detailed expressions are given by [Ulaby, 1982]). Then, the expression shown in Eq. (17) can be simplified as:

$$\frac{\sqrt{P_{lr}}^{r}}{\sqrt{P_{rr}}^{r}} = \frac{||R_{hh}| + |R_{vv}||}{||R_{hh}| - |R_{vv}||}, \tag{18}$$

where R is the Fresnel reflection coefficient as given in Eqs. (7) and (8). This equation also holds the condition of specular reflection, and the result shows that the cross-polarization power ratio of LHCP to RHCP of reflected signals is independent with surface roughness and is only a function of dielectric constant and incident angle.

The received power for both *lr* and *rr* is obtained as input parameters after post-processing. The dielectric constant of the soil is solved after taking all the parameters.

3.2.3. Retrieval methods for vegetation biomass sensing

The GNSS signals in bistatic configuration were obtained by the cross-correlation between direct and reflected signals with the pseudo-random noise (PRN) code replica, respectively. The output of the cross-correlation is called Delay-Doppler map (DDM), and Delay Waveforms (DW) is a row from DDM with the Doppler frequency set to a constant value of where the peak is. The phase information of the signal is lost during the integration process, resulting in amplitude $< |Y_{pq}| >$ or power $< |Y_{pq}|^2 >$ waveforms for the incident q-polarized to p-polarized scattered signals. The observable polarimetric parameters Γ_{lr} and Γ_{rr} represent the cross and co-polar reflectivity can be defined as in [12]:

$$\Gamma_{pq} = \left| \left\langle \frac{Y^{peak}_{reflected,\, p(\Delta\tau, f)}}{Y^{peak}_{direct,\, q(0,f)}} \right\rangle \right|^2, \tag{19}$$

where $\Delta\tau$ is the delay difference between the direct and the reflected paths, and the f is assumed to be the Doppler frequency shift of the signal. With ground-based or low-altitude receivers, it also can be assumed to be the same, $f_d \approx f_r = f$. The above equation obtained both the coherent and incoherent component of the received direct and reflected signals. However, the unstable airborne platform, terrain variation, and fading phenomenon may impair the estimation of the coherent scattering component. By adding the time series, an averaging procedure can be used to remove the contribution of the incoherent component on the final observed reflectivity. It was written as:

$$\Gamma_{pq} = \left| < \frac{Y_{r,p(t)}}{Y_{d,q(t)}} > \right|^2 = < \left| \frac{Y_{r,p(t)}}{Y_{d,q(t)}} \right|^2 > - \delta^2_{\left| \frac{Y_{r,p(t)}}{Y_{d,q(t)}} \right|}. \tag{20}$$

After the reduction of the incoherent component from the received signal, the received signal is mainly composed of coherent components. Therefore, the spatial resolution can be roughly estimated from the first Fresnel zone [31]. For instance, the 600 m flight altitude and 40° incident angle lead to an elliptical active scattering area with a minor axis of 24 m and a major axis of 32 m. Finally, the reflectivities Γ_{lr} and Γ_{rr} and the ratio of Γ_{lr}/Γ_{rr}, which was called

polarimetric ratio (PR), are the three observable parameters used to investigate the SMC and the vegetation biomass of the terrain.

3.2.4. GPS C/A-code altimetry

The geometry of the reflecting surface with the receiver and transmitter is shown in **Figure 6** under the assumption of a flat Earth and ray optics. The path delay (δ) between the direct and the reflected signals can be taken as a delay difference ($N_{samples}$) in the DDM obtained from Eq. 21.

$$\delta = \frac{c}{f_s} N_{samples} = \frac{c}{f_s} \cdot \frac{N_{chip}}{1023/_1 ms} \cdot f_s, \tag{21}$$

where C is the light speed and f_s is the sampling frequency of the GNSS-reflectometer, and N_{chips} is the number of chips in one period.

Assuming that the signals are parallel as shown in **Figure 6**, it gives that $\theta = \alpha$ for the incoming signals. Height h is possible to be derived from the following equation [41, 42]:

$$h \approx \frac{\delta}{2 \sin \alpha}, \tag{22}$$

where δ is the excess path and θ is equal to the elevation angle α. Therefore, the estimated altitude of the receiver h depends on the measured delay between the two signals and the elevation of the satellite.

3.2.5. Data processing

The GNSS-R system used for the acquisition of the received power can measure both the direct GPS signal and the reflected one using two independent acquisition channels: one for the direct signal and the other for the reflected signal. The receiver consists of two commercial

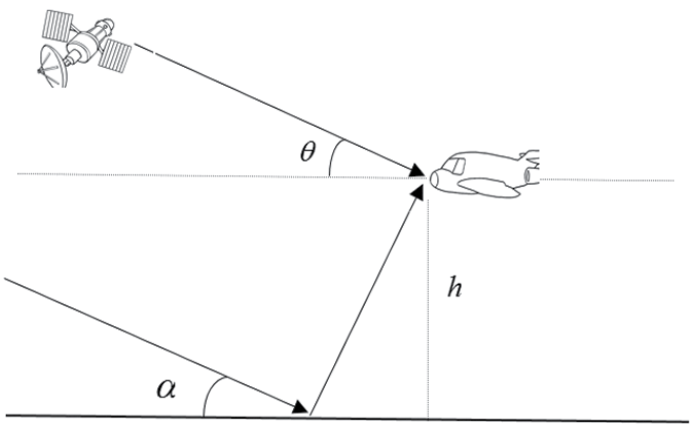

Figure 6. GNSS altimetry geometry with signals considered in a parallel condition.

front-ends (FEs) connected to two antennas: for instance, a traditional hemispherical GNSS L1 patch antenna pointed upward for the measurement of the direct signal. A high-gain LHCP antenna pointed downward for measuring the reflected signal as shown in **Figure 7**. Each FE is connected to a PC for data storage. The antennas and the FEs are mounted on a Kevlar bar. A typical tripod is used for more efficient adjustment of the orientation of the antennas.

The raw data of direct and reflected signals are collected and postprocessed with the software SOPRANO [43] for obtaining the peak power and SNR for each satellite. An open-loop approach is used for processing to obtain delay-Doppler maps (DDMs) and the corresponding delay waveforms. SNR time series were estimated from several noncoherently integrated delay waveforms generated by cross-correlation of the incoming data and local replica C/A codes.

Generally, increasing coherent integration time can help the low SNR to generate the DDM, but the performance may worsen when it exceeds a certain value. In this case, the coherent integration time was 1 ms because of the length of the GPS C/A code (1 ms). On the other hand, since the reflected signal power was attenuated by the surface as well as by the noise effects, it could not detect the real signal power. A noncoherent integration time technique (called averaging) was adopted during the postprocessing in order to mitigate the noise. Generally, it is in the range of 100-1000 ms. The noncoherent integration time, in this case is 500 ms. Moreover, the information of positions and altitude was recalculated, which was used to calculate the specular points on object areas. During the experiment, satellite positions (x, y, z) in an ECEF coordinate were collected by a GPS recorder. In the meanwhile, the receiver position (latitude, longitude, attitude) in geoid coordinate was collected in a file (.kml) which can be opened by the Google Earth software. The flowchart of obtaining the navigation message is shown in **Figure 8**.

The height coordinate z in the file (.kml) should be transferred into the WGS84 coordinate first, because the height z is in EGM96 coordinate system which already considered the sea surface altitude. The second step is to transfer the WGS84 coordinates (latitude, longitude, height) into the ECEF coordinate that can correlate with the satellite positions (x, y, z). With having receiver

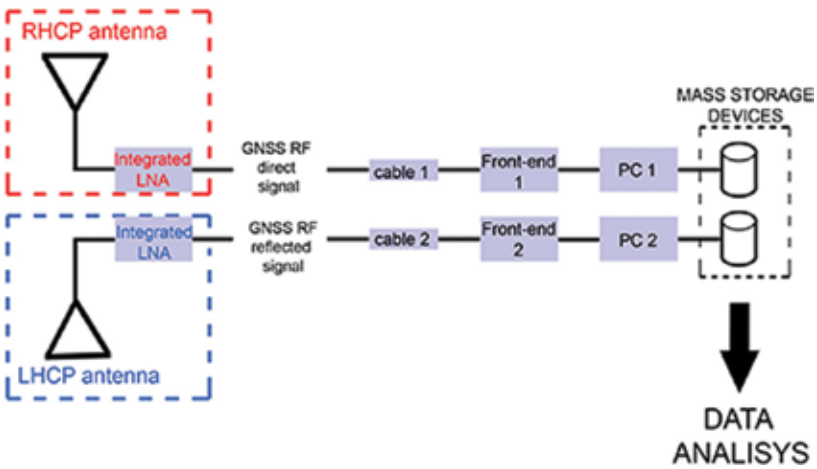

Figure 7. GNSS-R system block diagram: Antennas and front-end connections.

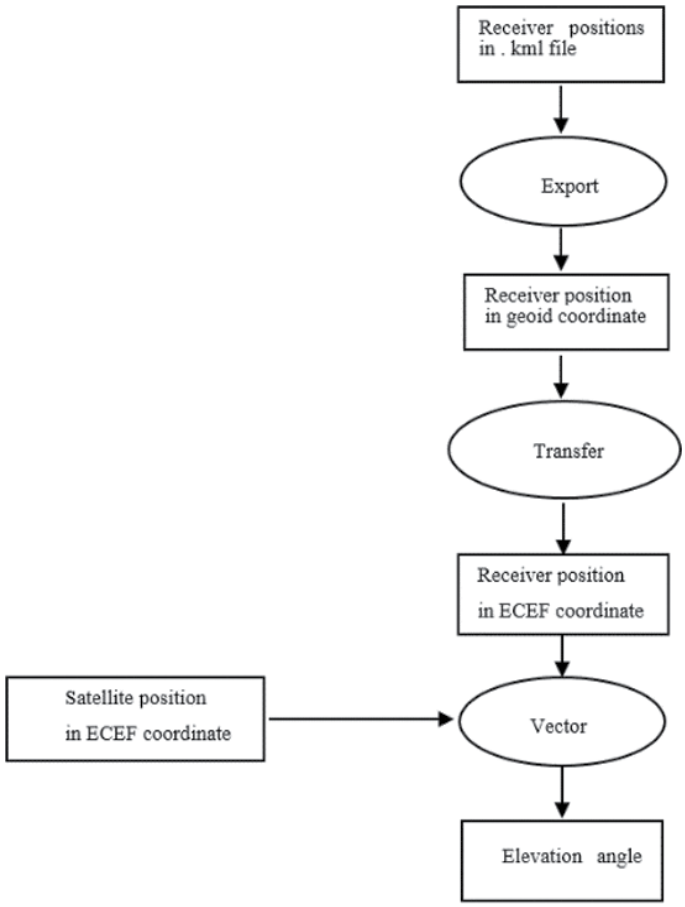

Figure 8. Flowchart of processing navigation message.

and satellite positions both in ECEF coordinates, elevation angle can be calculated with respect to the local tangent plane.

4. Results and discussions

A low-altitude airborne experiment was carried out by a P92 Digisky airplane over the Avigliana lake (45.099°N, 7.369°E) in Italy. An image of the experimental area from Google Map is shown in **Figure 9**.

In this area, there are two lakes, the size of the northern lake (bigger) is approximately 1 km x 1.3 km, while that of the southern lake (smaller) is 700 m × 1.1 km. The area was selected for the experiment because of the following reasons. First, the presence of two lakes of the experiment can provide the reflections and the known permittivity for calibration. Second, in the North and South directions of the two lakes, there are some grass areas which the flight

Figure 9. Avigliana area.

will go over, and in the West and East directions, the flight coverage areas are full of forest. This kind of geographical environment provides the possibility to investigate the roughness and vegetation biomass at the same time.

The elevation and azimuth angles were obtained, as shown in **Figure 8**. The sky plot of GPS satellites at the 1570th second of the flight is shown in **Figure 10**.

The reflected LHCP signal was collected through a high gain dual polarization antenna. With the direct RH signal obtained, the reflectivity was computed by the SNR of LH/RH signal

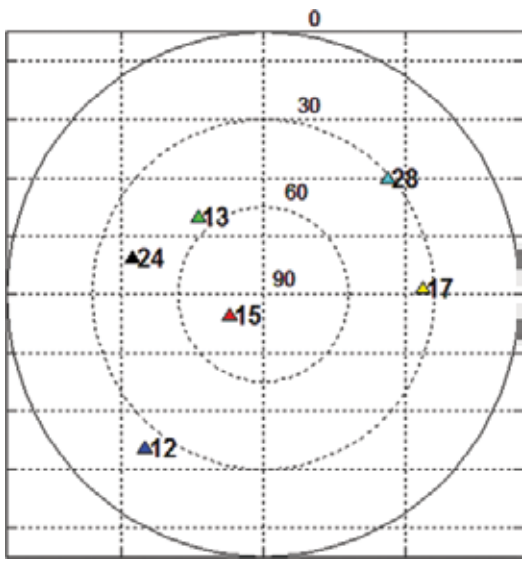

Figure 10. Sky plot of satellites on 18th June 2015.

component. The SMC was obtained by using the method introduced in Section 3.2.2. The SMC estimation result of PRN 15 with high elevation angle is shown in **Figure 11**, calibrated by the water reflectivity of 0.67. The color of the specular points is proportional to the estimated soil moisture (the red color denotes totally dry soil, and the green color represents humidity 100%).

The flight flew covered lake and two forest areas from east to west. The flight route was denoted by the yellow color in **Figure 12**. Since the reflection point begins from the forest in the east (mid-biomass) to big lake (flat) then stop with the forest in the west (big-biomass) as shown in **Figure 12**, it can be used to investigate the vegetation biomass sensing.

Based on the method introduced in Section 3.2.3, the reflectivities Γ_{lr} and Γ_{rr} and the ratio of the two polarization (*lr* and *rr*) PR can be calculated and shown in **Figure 13**. From 720 s, the big increment 6 dB of the average *lr* appears in the lake (L1) compared to the forest. The *lr* component is quite sensitive with SMC. The average *rr* in forests (F1 and F2) is 2–4 dB lower than the lake (L1). In addition, considering the average *lr* and *rr* in forests (F1 and F2), both

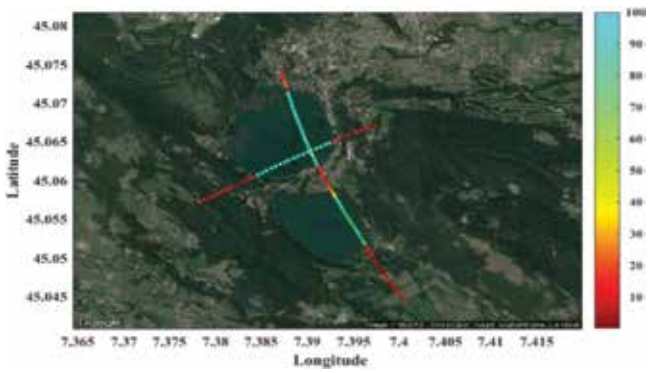

Figure 11. Soil moisture content estimation of PRN 15.

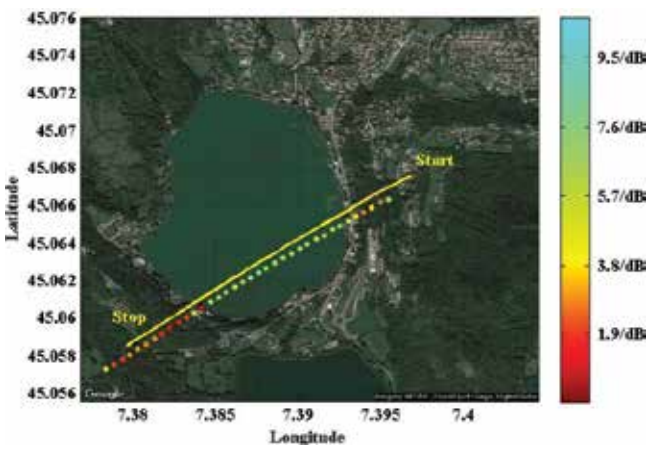

Figure 12. Flight route (yellow line) and PR level of reflection point georeferenced in Google Map.

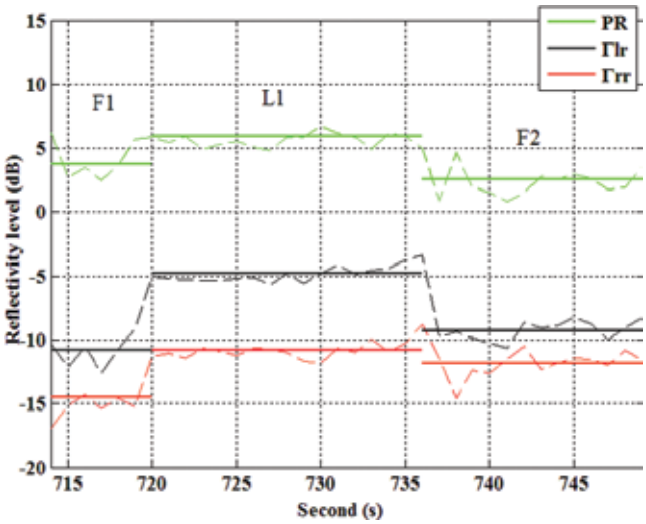

Figure 13. PR level, Γ_{lr} and Γ_{rr} level.

average in F2 are higher than F1. It could be considered that the vegetation biomass in F2 is lower than F1. It confirms the fact and further implies that both polarizations are sensitive to vegetation biomass. Moreover, the biggest PR level is the presence of the lake. Therefore, the PR can be taken as a good parameter for soil moisture estimation regardless of the vegetation biomass. The PR level is 5.6 dB in the lake, 3.9 dB in F1, and 2.3 in F2.

For the altimetry estimation, the C/A code method (see Section 3.2.4) was applied on the unsmooth surface to obtain the target height. Due to bandwidth and the equipment, the altimetry

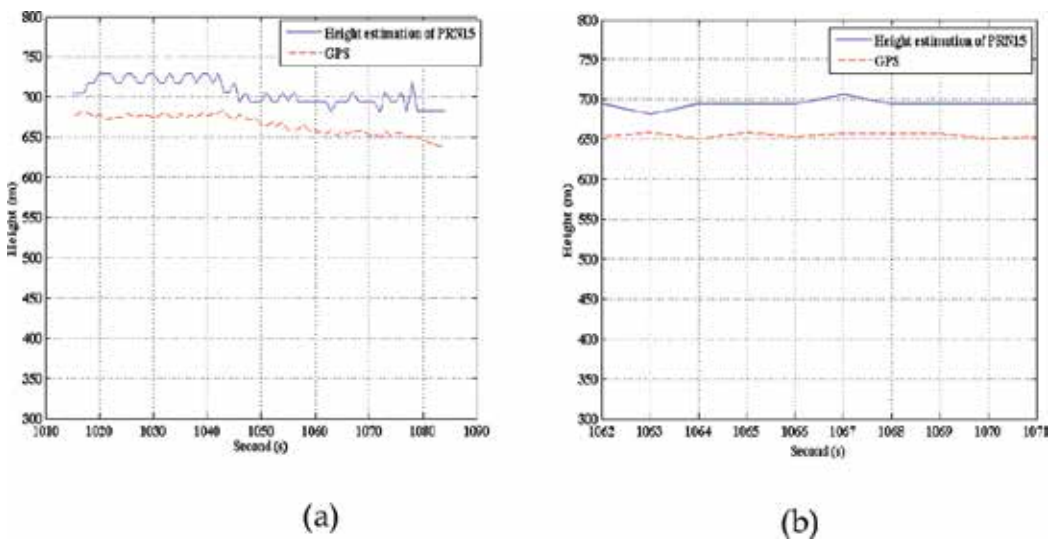

Figure 14. Altimetry estimation of PRN 15 from 1015s (a), 1062s (b).

resolution is limited, according to 1 sample 23.07 m. The altimetry estimation results of satellite PRN 15 with high elevation angle are presented in **Figure 14**.

Figure 14 shows two figures of height estimation of PRN 15 start from 1015s and 1062s. The elevation angle of PRN 15 is 76°. The estimation height is quite same with GPS recorder. The estimation deviation in **Figure 14 (a)** is bigger than **Figure 14 (b)**. It confirmed that the best condition for altimetry application is when using high elevation angle on the water surface, which can greatly avoid the interference of forest and cities. The accuracy of the altimetry estimation depends on the bandwidth, algorithm, and equipment, and it shows that it is quite affected by the environment as introduced in the beginning of Section 3.

5. Conclusion

In this chapter, the global navigation satellite system-reflectometry (GNSS-R) technique as a method of remote sensing that receives and processes microwave signals reflected from various surfaces to extract useful information is reported. GNSS-R technique has gained widespread attention in a variety of applications. This work assesses the capability of measuring soil moisture and vegetation biomass by means of reflected signals from global navigation satellites from a theoretical and experimental point of view.

The SMC was obtained and georeferenced in Google Maps. The type of terrain ranged from water (on the lakes) to terrain with small bushes to built-up areas. The results showed good correlation with the types of the underlying terrain. It was observed that the LH was rather more sensitive to SMC. The different SMC areas were detected with different PR values. The ratio of the two polarizations was independent of roughness, and it proved to be an optimum parameter for soil moisture estimation. Moreover, it was found that increasing the biomass quantity decreased the Γ_{lr} and Γ_{lr} polarization components, since the reflected signal components are attenuated from leaves, trunks, crowns, and so on. The altimetry estimation is based on the calculation of the delay differences between the two signals. In principle, the altimetry techniques can be applied to any surface, but their performance will depend on the scattering behavior. Therefore, GNSS-R altimetry has only been used on strongly reflecting surfaces and geometries, such as waters and smooth ice. The accuracy of the derived height is limited also due to the bandwidth and the sampling frequency of the equipment.

Acknowledgements

Some of the works illustrated in this chapter were developed by the authors and their collaborators at the University of Politecnico di Torino. The authors would like to thank the SMAT-F2 project, ISMB and all the researchers involved. Furthermore, this research is financed by National Science Foundation of China under projects No. 61601076 and sponsored by NUPTSF (Grant No. 217152).

Author details

Yan Jia[1] and Yuekun Pei[2*]

*Address all correspondence to: peiyuekun@dlu.edu.cn

1 Nanjing University of Posts and Telecommunications, Nanjing, China

2 Dalian University, Dalian, China

References

[1] Jin S, Feng G, Gleason S. Remote sensing using GNSS signals: Current status and future directions. Advances in Space Research. 2011;**47**(10)

[2] Dawoud S. GNSS Principles and Comparison. Potsdam: Potsdam University; n.d

[3] Groves P. Principles of GNSS, Inertial, and Multisensor Integrated Navigation Systems. London: Artech house; 2013

[4] Hofmann-Wellenhof B, Lichtenegger H, Wasle E. GNSS–Global Navigation Satellite Systems: GPS, GLONASS, Galileo, and More. New York: Springer Science & Business Media; 2007

[5] Parkinson B. Progress in Astronautics and Aeronautics: Global Positioning System: Theory and Applications. Reston: Aiaa; 1996

[6] Betz J. Signal structures for satellite-based navigation: Past, present, and future. Inside GNSS. 2013;**8**:34-42

[7] Zavorotny V, Voronovich A. Scattering of GPS signals from the ocean with wind remote sensing application. IEEE Transactions on Geoscience and Remote Sensing. 2000;**38**(2): 951-964

[8] Cardellach E, Fabra F, Nogués-Correig O, Oliveras S, Ribó S, Rius A. GNSS-R ground-based and airborne campaigns for ocean, land, ice, and snow techniques: Application to the GOLD-RTR data sets. Radio Science. 2011;**46**(6):1-16

[9] Larson K, Braun J, Small E, Zavorotny V, Gutmann E, Bilich A. GPS multipath and its relation to near- surface soil moisture content. IEEE Journal of Selected Topics in Applied Earth Observation and Remote Sensing. 2010;**3**(1):91-99

[10] Jia Y, Savi P. Sensing soil moisture and vegetation using GNSS-R polarimetric measurement. Advances in Space Research. 2017:858-869

[11] Jia Y, Savi P, Canone D, Notarpietro R. Estimation of surface characteristics using GNSS LH-reflected signals: Land versus water. IEEE Journal of Selected Topics in Applied Earth Observations and Remote Sensing. 2016;**9**(10):4752-4758

[12] Egido A, Caparrini M, Ruffini G, Paloscia S, Santi E, Guerriero L, et al. Global navigation satellite systems reflectometry as a remote sensing tool for agriculture. Remote Sensor. 2012;**4**(8):2356-2372

[13] Hugo C, Amèzaga A, Vidal D, Olivé R, Munoz J, Camps A. First polarimetric GNSS-R measurements from a stratospheric flight over boreal forests. Remote Sensing. 2015;**7**(10): 13120-13138

[14] Beckmann P, Spizzichino A. The Scattering of Electromagnetic Waves from Rough Surfaces. New York, USA: Artech House; 1987

[15] Katzberg S, Garrison J Jr. Utilizing GPS to determine ionospheric delay over the ocean. NASA T. R. TM-4750; 1996

[16] Willis NJ. Bistatic Radar, British Library. London: British Library; 1995

[17] Martin-Neira M. A passive reflectometry and interferometry system (PARIS): Application to ocean altimetry. ESA Journal. 1993;**17**:331-355

[18] De Roo R, Ulaby F. Bistatic specular scattering from rough dielectric surfaces. IEEE Transactions on Antennas and Propagation. 1994;**42**(2):220-231

[19] Stutzman W. Polarization in Electromagnetic Systems. London: Artech house; 1993

[20] Misra P, Enge P. Global Positioning System: Signals, Measurements and Performance. Lincoln, MA: Ganga-Jamuna Press; 2006

[21] Lemoine F, Kenyon S, Factor J, Trimmer R, Pavlis N, Chinn D, … Wang Y, Lemoine, Frank G, et al. The Development of the Joint NASA GSFC and the National Imagery and Mapping Agency (NIMA) Geopotential Model EGM96. NASA/TP-1998-206861; 1998

[22] Rodriguez-Alvarez N, Camps A, Vall-Llossera M, Bosch-Lluis X, Monerris A, Ramos-Perez I, et al. Land geophysical parameters retrieval using the interference pattern GNSS-R technique. IEEE Transactions on Geoscience and Remote Sensing. 2011;**49**(1):71-84

[23] Ruffini N, Soulat F, Caparrini M, Germain O, Martín-Neira M. The Eddy experiment: Accurate GNSS-R ocean altimetry from low altitude aircraft. Geophysical Research Letters. 2004;**31**(12):L12306

[24] Rius A, Cardellach E, Martin-Neira M. Altimetric analysis of the sea-surface GPS-reflected signals. IEEE Transactions on Geoscience and Remote Sensing. 2010;**48**(4–2):2119-2127

[25] Wang J, Schmugge T. An empirical model for the complex dielectric permittivity of soils as a function of water content. IEEE Transactions on Geoscience and Remote Sensing. 1980;**4**:288-295

[26] Njoku E, O'Neill P. Multifrequency microwave radiometer measurements of soil moisture. IEEE Transactions on Geoscience and Remote Sensing. 1982;**4**:468-475

[27] Zavorotny V, Larson K, Braun J, Small E, Gutmann E, Bilich A. A physical model for GPS multipath caused by land reflections: Towards bare soil moisture retrieval. IEEE Journal of Selected Topics in Applied Earth Observation and Remote Sensing. 2010;**3**(1):100-110

[28] Mironov V, Kosolapova L, Fomin S. Physically and mineralogically based spectroscopic dielectric model for moist soils. IEEE Transactions on Geoscience and Remote Sensing. 2009:2059-2070

[29] Mironov V, Muzalevskiy K. The new algorithm for retrieval of soil moisture and surface roughness from GNSS reflectometry. In: IEEE International Geoscience and Remote Sensing Symposium. Munich: IEEE; 2012. pp. 7530-7532

[30] Rodriguez-Alvarez N, Bosch-Lluis X, Camps A, Vall-Llossera M, Valencia E, Marchan-Hernandez J, Ramos-Perez I. Soil moisture retrieval using GNSS-R techniques: Experimental results over a bare soil field. IEEE Transactions on Geoscience and Remote Sensing. 2009; **47**(11):3616-3624

[31] Masters D, Axelrad P, Katzberg S. Initial results of land-reflected GPS bistatic radar measurements in SMEX02. Remote Sensing of Environment. 2004;**92**(4):507-520

[32] Gleason S, Hodgart S, Sun Y, Gommenginger C, Mackin S, Adjrad M, Unwin M. Detection and processing of bistatically reflected GPS signals from low earth orbit for the purpose of ocean remote sensing. IEEE Transactions on Geoscience and Remote Sensing. 2005;**43**(6):1229-1241

[33] Katzberg S, Torres O, Grant M, Masters D. Utilizing calibrated GPS reflected signals to estimate soil reflectivity and dielectric constant: Results from SMEX02. Remote Sensing of Environment. 2006;**100**(1):17-28

[34] Ulaby F, Moore R, Fung A. Microwave Remote Sensing Active and Passive-Volume II: Radar Remote Sensing and Surface Scattering and Enission Theory. New York, USA: Artech House; 1982

[35] Pierdicca N, Guerriero L, Giusto R, Brogioni M, Egido A, Floury N. GNSS reflections from bare and vegetated soils: Experimental validation of an end-to-end simulator. In: 2011 IEEE International Geoscience and Remote Sensing Symposium (IGARSS). Vancouver, BC, Canada: IEEE; 2011. pp. 4371-4374

[36] Ceraldi E, Franceschetti G, Iodice A, Riccio D, Ruello G. On the use of the specular direction copolarised ratio for the retrieval of soil dielectric constant. In: 2003 IEEE Geoscience and Remote Sensing Symposium. Vol. 7. Toulouse, France: IEEE; 2003. pp. 4144-4146

[37] Hallikainen M, Ulaby F, Dobson M, El-Rayes M, Wu L. Microwave dielectric behavior of wet soil-part 1: Empirical models and experimental observations. IEEE Transactions on Geoscience and Remote Sensing. 1985;**1**:25-34

[38] Dobson M, Ulaby F, Hallikainen M, El-Rayes M. Microwave dielectric behavior of wet soil—Part II: Dielectric mixing models. IEEE Transactions on Geoscience and Remote Sensing. 1985;**23**(1):35-46

[39] Topp G, Davis J, Annan A. Electromagnetic determination of soil water content: Measurements in coaxial transmission lines. Water Resources Research. 1980;**16**(3):574-582

[40] Knott E. Radar Cross Section Measurements. New York, U.S.A.: Springer Science & Business Media; 2012

[41] Martín-Neira M, Caparrini M, Font-Rosselló J, Lannelongue S, Vallmitjana C. The PARIS concept: An experimental demonstration of sea surface altimetry using GPS reflected signals. Remote Sensing. 2001;**39**:142-149

[42] Helm A. Ground-Based GPS Altimetry with the L1 OpenGPS Receiver Using Carrier Phase Delay Observations of Reflected GPS Signals. GFZ German Research Centre for Geosciences; 2008 Available: www.gfz-potsdam.de

[43] Falletti E, Margaria D, Nicola M, Povero G, Troglia Gamba M. N-FUELS and SOPRANO: Educational tools for simulation, analysis and processing of satellite navigation signals. In: IEEE International Conference on Frontiers in Education. Oklahoma, USA: IEEE; 2013. pp. 303-308

Chapter 5

Remote Sensing with Shipborne High-Frequency Surface-Wave Radar

Junhao Xie, Minglei Sun, Zhenyuan Ji and Guowei Yao

Additional information is available at the end of the chapter

http://dx.doi.org/10.5772/intechopen.72833

Abstract

High-frequency surface-wave radar (HFSWR) has been successfully applied for moving target detection and remote sensing of ocean surface dynamic parameters for decades. Compared with conventional instruments such as buoys, anemometers, and microwave radars, HFSWR can be employed to an all-weather and all-time surveillance far beyond the visible horizon. Moreover, based on agility and maneuverability, shipborne HFSWR can not only enhance the survivability in complex ocean environment but also enlarge the detection distance on open sea, which will gradually become a popular deployment situation. In this chapter, ocean surface cross sections for shipborne HFSWR with linear platform motion and sway motion are derived theoretically. Then, the methods for ocean surface wind direction, wind field, and current extraction are presented. The computer simulations and experimental results of the real data are given to verify the detection accuracy and the distance limit of the abovementioned methods.

Keywords: shipborne HFSWR (high-frequency surface-wave radar), ocean surface cross section, ocean surface wind field, ocean surface current

1. Introduction

High-frequency surface-wave radar (HFSWR) has been widely applied to early warning for decades, including the detection of airborne targets and surface targets. Its vertically polarized electromagnetic wave (3–30 MHz) follows the curvature of the Earth along the air-water interface and has a very low propagation loss on the ocean surface. In addition to early warning uses, HFSWR provides a unique ocean surface dynamics parameters remote-sensing

capability based on the Doppler spectrum characteristics of the sea echo backscattered from the ocean surface. Compared with conventional instruments such as buoys, anemometers, and line-of-sight radar, HFSWR can provide an all-time, all-weather, and cost-effective surveillance far beyond the visible horizon.

HFSWR can be classified into onshore and shipborne cases based on the platform where it is employed. Besides the advantages of onshore HFSWR, shipborne case has the agility and maneuverability, which can not only enhance the survivability in complex ocean environment but also enlarge the detection distance on open sea. Thus, ocean remote sensing with shipborne HFSWR is expected to receive increasing attentions.

The main objective of this chapter is to reveal the potential and experimental results of remote sensing of ocean surface wind field and current with shipborne HFSWR, which is organized into four sections. Section 1 describes the concept of operation for shipborne HFSWR, the general characteristics and nominal capabilities of such systems, as well as their potential roles in early warning uses and ocean remote-sensing applications. Section 2 represents the first- and second-order ocean surface cross sections derived for an omnidirectional receiving sensor in monostatic shipborne HFSWR, where the essential characteristics of the sea echo backscattered from the ocean surface are shown. Understanding the characteristics of sea echo is essential for further theoretical and experimental investigation in remote-sensing applications. Section 3 discusses the potential of remote sensing of ocean surface wind field with shipborne HFSWR. The wind field of the region covered by radar can be measured using a single receiving antenna, which is more beneficial for shipborne platform with limited deck space. Experimental results verify the detection accuracy and distance limit of the presented method. Section 4 discusses the feasibility of ocean surface current inversion in shipborne HFSWR.

2. Ocean surface cross sections for shipborne HFSWR

To investigate the potential of ocean remote sensing with shipborne HFSWR, ocean surface cross sections, which incorporates abundant ocean dynamic parameter information such as wind direction and speed, ocean surface current, and wave spectrum parameters, should be first studied. In this section, we discuss the first- and second-order ocean surface cross sections in shipborne HFSWR with a uniform linear motion [1, 2]. Moreover, we explore the effects of the radar platform motion and sea-state parameters on Doppler spectrum and present that the spreading characteristic of the first-order Doppler spectra can be utilized to resolve the wind direction ambiguity problem. Following this research, we develop the corresponding cross sections in shipborne HFSWR with both uniform linear motion and sway motion [3]. Furthermore, the effects of sway motion on Doppler spectra are discussed in detail.

2.1. First-order ocean surface cross section

2.1.1. First-order radar cross-section model

For a shipborne source, a small displacement from the origin, $\vec{\rho}_v$, is caused by the forward movement of the platform at a constant speed, as shown in **Figure 1**, ρ_1 and ρ_2 denote the

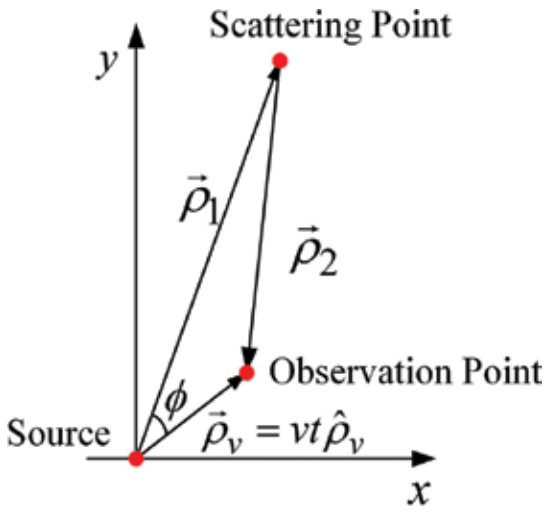

Figure 1. Geometry of the first-order scatter with platform-forward movement.

planar distances. Then, by analogy to the derivations in [4], the first-order cross section for shipborne HFSWR with a uniform linear motion is derived [1]

$$\sigma(\omega_d) = 2^6\pi^2 k_0^4 \sum_{m=\pm 1} S\left(2m\vec{k}_0\right)\delta\left(\omega_d + m\sqrt{2gk_0} - 2k_0 v\cos\phi\right) \tag{1}$$

where ω_d is the Doppler frequency, k_0 is the wavenumber of the transmitting signal, $m = \pm 1$ corresponds to the receding and approaching waves, respectively, $S(\cdot)$ is the directional wave height spectrum, $\delta(\cdot)$ is the Dirac delta function, g is the gravitational acceleration, v is the speed of shipborne platform, $S(\cdot)$ can be represented as a product of a P-M spectrum [5] and a modified cardioid directional factor $G(\cdot)$ [6]. The directional factor is shown in **Figure 2**, where θ is the incident direction of echo and α^* is the wind direction. When the shipborne platform is stationary (i.e., $v = 0$), it is readily checked that the results in Eq. (1) can be reduced onshore case.

2.1.2. Experimental and simulated results

2.1.2.1. Experimental result

The fundamental data-collecting experiment was conducted on the Yellow Sea of China [7], the radar carrier frequency $f_0 = 5.283$ MHz, $\alpha^* \approx 90^\circ$, the range resolution $\Delta\rho = 5$ km, $v = 10$ knots. The simulated result with Gaussian noise and experimental result are, respectively, displayed in **Figure 3a** and **b**.

The simulated result with Gaussian noise in **Figure 3a** indicates that the platform motion results in the spreading sea clutter spectrum, whose theoretical width is indicated by the long-dashed lines. Such a simulated spreading spectrum is confirmed by the experimental result in **Figure 3b** with the similar overall shape.

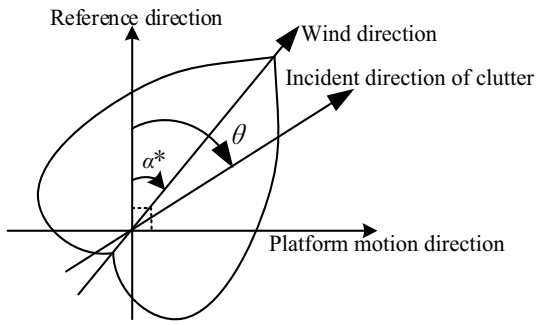

Figure 2. Wind distribution in relation to radar beam direction.

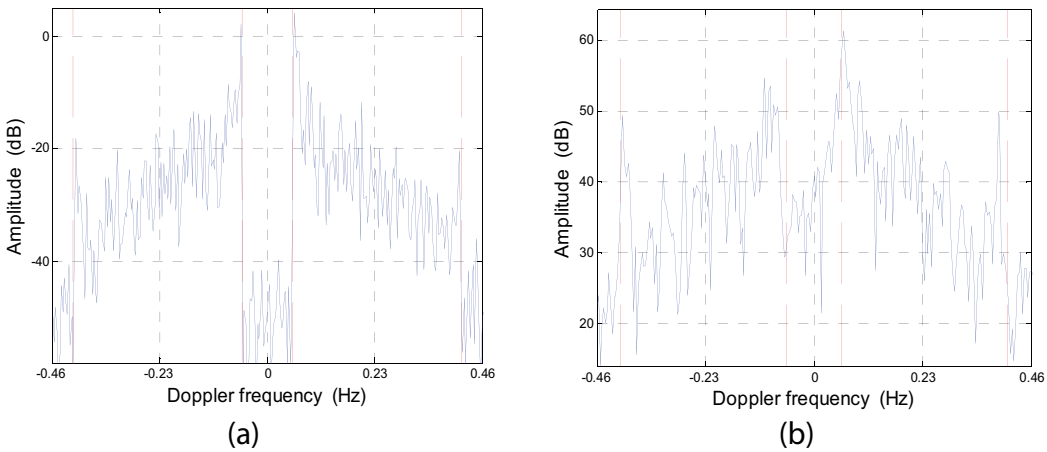

Figure 3. First-order ocean surface cross sections: (a) simulated result and (b) experimental result.

2.1.2.2. Simulated results

Effects of the wind direction on the first-order cross section are displayed. Simulation parameters include $f_0 = 5.283\,\text{MHz}$, $\Delta\rho = 5\,\text{km}$, and $\alpha^* = 45^\circ, 315^\circ$. Simulation results of shipborne HFSWR for $v = 10\,\text{knots}$ and onshore HFSWR for $v = 0\,\text{knots}$ are shown in **Figure 4**.

For onshore case, the results show that the wind direction ambiguity exists, where the first-order echo has the same characteristics for different wind directions. Moreover, the first-order Bragg peaks simultaneously contain the sea clutter returns from different directions. Studies on wind direction extraction have to be conducted based on the receiving array or the compact antenna system in Coastal Ocean Dynamics Applications Radar (CODAR) system, where the problem of wind direction ambiguity is still unavoidable.

For shipborne case, however, the simulated cross sections show that the ratios of the spreading first-order Bragg lines vary with the wind directions, which demonstrates that shipborne HFSWR has the potential of wind direction extraction. Meanwhile, the wind directions of the whole sea area covered by radar may be obtained based on the spreading mechanism of the

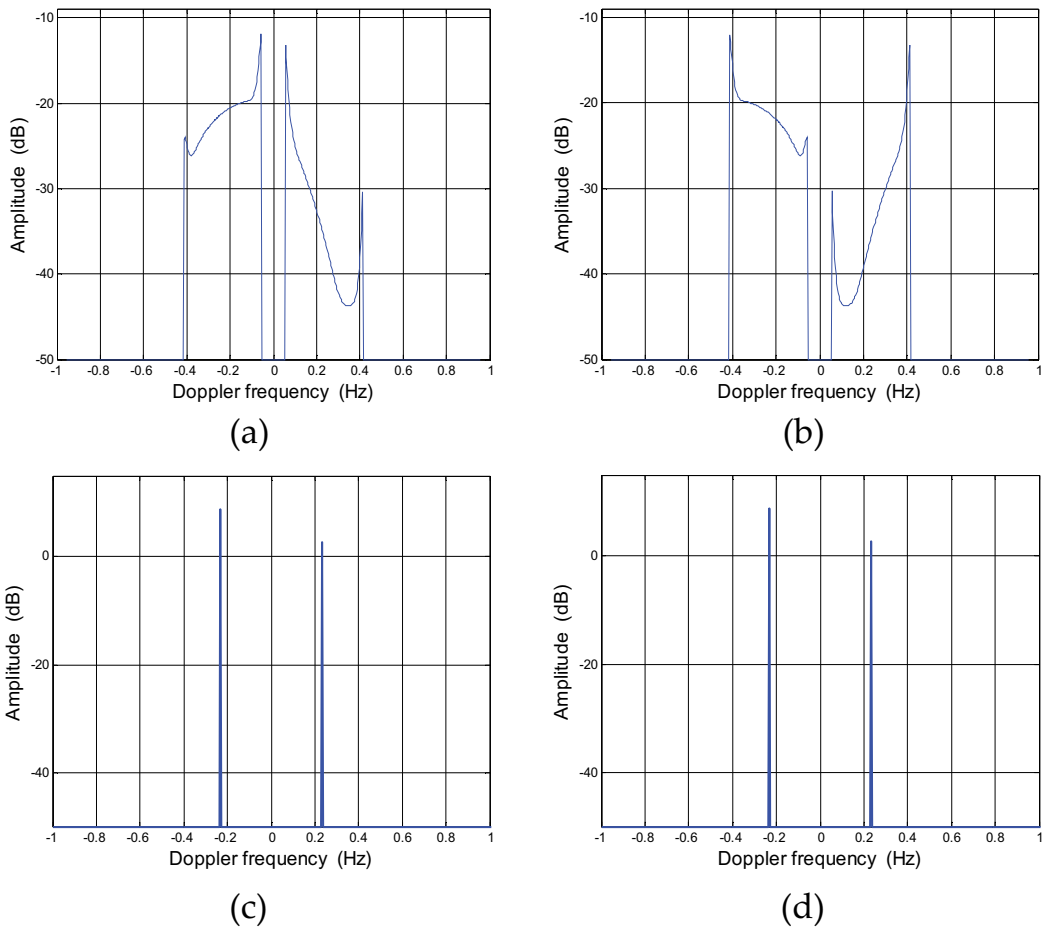

Figure 4. First-order cross section for (a) shipborne case with $\alpha^* = 45^\circ$. (b) Shipborne case with $\alpha^* = 315^\circ$. (c) Onshore case with $\alpha^* = 45^\circ$. (d) Onshore case with $\alpha^* = 315^\circ$.

first-order spectrum. Thus, compared with onshore method, it should be more easily realized in wind direction extraction by the use of a single receiving sensor instead of the receiving array.

2.2. Second-order ocean surface cross section

By analogy to the derivation in [8], the second-order cross section for shipborne HFSWR with a uniform linear motion is derived as the summation of the hydrodynamic and electromagnetic components.

2.2.1. Hydrodynamic component

The hydrodynamic component can be directly obtained by replacing the first-order ocean wave spectrum $S\left(\vec{K},\omega\right)$ in Eq. (1) with the second-order spectrum $S_2\left(\vec{K},\omega\right)$, which can be finally given by [2]

$$
\begin{aligned}
{}_1\sigma_2(\omega_d) = 2^6\pi^2 k_0^4 \sum_{m_1=\pm1}\sum_{m_2=\pm1}\int_{K_1}\int_{\theta_{\vec{K}_1}} |\Gamma_H|^2 S\left(m_1\vec{K}_1\right)S\left(m_2\vec{K}_2\right) \\
\cdot\delta\left(\omega_d - 2k_0 v\cos\phi + m_1\sqrt{gK_1} + m_2\sqrt{gK_2}\right)K_1 dK_1 d\theta_{\vec{K}_1}
\end{aligned} \tag{2}
$$

where $S_2\left(\vec{K},\omega\right) = 2\int_{\substack{\vec{K}_1+\vec{K}_2=\vec{K}\\ \omega_1+\omega_2=\omega}} S\left(\vec{K}_1,\omega_1\right)S\left(\vec{K}_2,\omega_2\right)|\Gamma_H|^2 d\vec{K}_1 d\omega_1$, and Γ_H denotes the hydrodynamic coupling coefficient. K_1 and $\theta_{\vec{K}_1}$ are the magnitude and direction of the wave vector $\vec{K}_1$, respectively. $\vec{K}_2$ is a wave vector with a magnitude of K_2. The frequencies ω_1 and ω_2 are related to $\vec{K}_1$ and $\vec{K}_2$, respectively.

2.2.2. Electromagnetic component

The second-order field equation in the time domain can be thus obtained by [2]

$$
\begin{aligned}
E_2(t) \approx & -j\eta_0\Delta l\Delta\rho I_0 k_0^2 \frac{F^2\left(\rho_0,\omega_0\right)}{\left(2\pi\rho_0\right)^{3/2}} e^{jk_0\Delta\rho} \\
& \cdot\sum_{\vec{K}_1}\sum_{\vec{K}_2}\sqrt{K}\Gamma_{EM}P_{\vec{K}_1}P_{\vec{K}_2}e^{-j\pi/4}e^{jK\rho_0}e^{jvtK\cos\phi}\mathrm{Sinc}\left[\frac{\Delta\rho}{2}(K-2k_0)\right]
\end{aligned} \tag{3}
$$

where η_0 is the intrinsic impedance, I_0 is the peak current for a dipole with length Δl, $k_0 = \omega_0/c$, ω_0 is the radian frequency, $\rho_0 = c(t-\tau_0/2)/2$, $\Delta\rho = c\tau_0/2$, c is the speed of light, and τ_0 is the length of the pulse. $\mathrm{Sinc}(\cdot)$ denotes the sinc function. $P_{\vec{K}_1}$ and $P_{\vec{K}_2}$ are random variables corresponding to the wave vectors $\vec{K}_1$ and $\vec{K}_2$, respectively. $\vec{K} = \vec{K}_1 + \vec{K}_2$, $F(\cdot)$ is the Sommerfeld attenuation function, and Γ_{EM} is the electromagnetic coupling coefficient.

The autocorrelation function with respect to the time shift τ is given by

$$
R(\tau) = \left\langle E_2(t+\tau)E_2^*(t)\right\rangle \cdot A_r/2\eta_0 \tag{4}
$$

where $(\cdot)^*$ and $\langle\cdot\rangle$ are the complex conjugate and statistical average, $A_r = \lambda_0^2 G_r/4\pi$, G_r is the antenna gain, and λ_0 is the wavelength.

Then, Eq. (4) can be finally simplified as

$$
\begin{aligned}
R(\tau) = & \frac{\lambda_0^2}{4\pi}\frac{G_r}{2\eta_0}\left\{\frac{\eta_0^2\Delta l^2\Delta\rho^2 I_0^2 k_0^4 F^4\left(\rho_0,\omega_0\right)}{\left(2\pi\rho_0\right)^3}\sum_{m_1=\pm1}\sum_{m_2=\pm1}\int_K\int_{\theta_{\vec{K}}}\int_{K_1}\int_{\theta_{\vec{K}_1}} K^2|\Gamma_{EM}|^2\right. \\
& \cdot\frac{1}{2}S\left(m_1\vec{K}_1\right)S\left(m_2\vec{K}_2\right)e^{jKv\tau\cos\phi}e^{-jm_1\sqrt{gK_1}\tau}e^{-jm_2\sqrt{gK_1}\tau} \\
& \left.\cdot\mathrm{Sinc}^2\left[\frac{\Delta\rho}{2}(K-2k_0)\right]\right\}K_1 dK_1 d\theta_{\vec{K}_1} d\theta_{\vec{K}}
\end{aligned} \tag{5}
$$

A Fourier transform of Eq. (5) yields the power density spectrum. Then, the second-order ocean surface cross section can be calculated by normalizing the power density spectrum per unit area, which is simplified by [2]

$$
\begin{aligned}
{}_2\sigma_2(\omega_d) = \; & 2^6\pi^2 k_0^4 \sum_{m_1=\pm1}\sum_{m_2=\pm1}\int_{K_1}\int_{\theta_{\vec{K}_1}} |\Gamma_{EM}|^2 S\left(m_1\vec{K}_1\right) S\left(m_2\vec{K}_2\right) \\
& \cdot\delta\left(\omega_d - 2k_0 v\cos\phi + m_1\sqrt{gK_1} + m_2\sqrt{gK_2}\right) K_1 dK_1 d\theta_{\vec{K}_1}
\end{aligned} \tag{6}
$$

2.2.3. Total second-order ocean surface cross section

Apart from the coupling coefficients, the hydrodynamic and electromagnetic cross sections in Eqs. (2) and (6) are identical. Thus, the total second-order ocean surface cross section in shipborne HFSWR can be written as [2]

$$
\begin{aligned}
\sigma_2(\omega_d) = \; & 2^6\pi^2 k_0^4 \sum_{m_1=\pm1}\sum_{m_2=\pm1}\int_{K_1}\int_{\theta_{\vec{K}_1}} |\Gamma|^2 S\left(m_1\vec{K}_1\right) S\left(m_2\vec{K}_2\right) \\
& \cdot\delta\left(\omega_d - 2k_0 v\cos\phi + m_1\sqrt{gK_1} + m_2\sqrt{gK_2}\right) K_1 dK_1 d\theta_{\vec{K}_1}
\end{aligned} \tag{7}
$$

where the total coupling coefficient $\Gamma = \Gamma_H + \Gamma_{EM}$.

2.2.4. Simulation results

2.2.4.1. Simulated cross sections for different platform speeds

Simulation parameters: $f_0 = 5.283\,\text{MHz}$, $\alpha^* = 90^\circ$, and wind speed $U = 15\,\text{knots}$. From **Figure 5a**, the Bragg peaks are located at $f_{B,M} = \pm 0.2344\,\text{Hz}$, and the $\sqrt{2}f_{B,M}$ peaks (the harmonic peaks) and $2^{3/4}f_{B,M}$ peaks (the electromagnetic "corner reflector" peaks) are also visible. From Eqs. (1) and (7), sea echoes at different incident directions correspond to different Doppler frequencies because an angle ϕ exists between echo incident direction and the direction of the platform-forward movement. That is, the radar Doppler spectra are spread, as

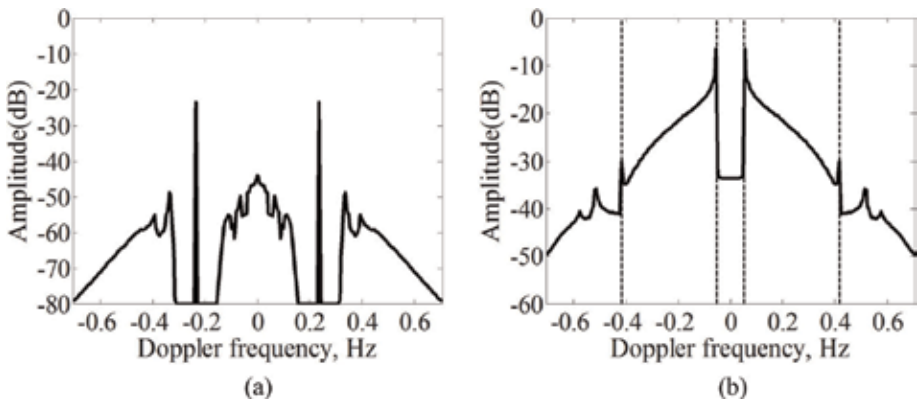

Figure 5. Simulated cross sections for (a) onshore case and (b) shipborne case with $v = 10$ knots.

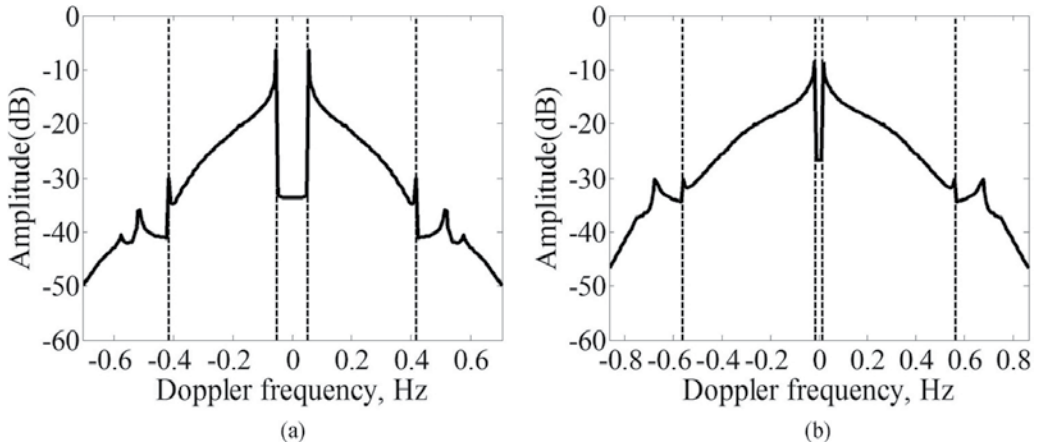

Figure 6. Simulated cross sections for (a) $f_0 = 5.283$ MHz and (b) $f_0 = 8$ MHz.

shown in **Figure 5b**. The dashed lines denote the theoretical spreading domains of the first-order sea clutter Doppler spectrum.

2.2.4.2. Simulated cross sections for different radar frequencies

Simulation parameters: $U = 15$ knots, $v = 10$ knots, and $\alpha^* = 90^\circ$. From **Figure 6**, the spreading domain increases and the energies of the second-order spectra increase with the increasing radar frequency. This shows that a high radar frequency may be negative for moving target detection and remote sensing.

2.2.4.3. Simulated cross sections for different wind speeds

Simulations parameters: $\alpha^* = 90^\circ$, $v = 10$ knots, and $f_0 = 5.283$ MHz. Simulation results show that the energies of the first- and second-order spectra increase as the wind speed increases, as

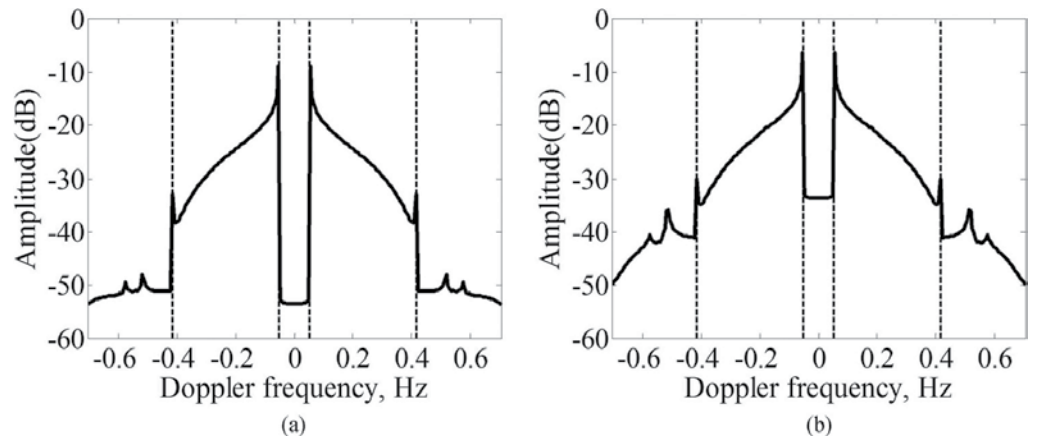

Figure 7. Simulated cross sections for (a) $U = 12$ knots and (b) $U = 15$ knots.

shown in **Figure 7**. The first- and second-order spectra may be overlapped when the wind speed is high, which may be unfavorable for remote sensing of ocean surface wind direction and speed. This is because the wind direction is extracted from the ratio of the positive and negative Bragg energies, and the wind speed relates to the energies of the second-order backscatter echo.

2.2.4.4. Simulated cross sections for different wind directions

Simulation parameters: $U = 15$ knots, $v = 10$ knots, and $f_0 = 5.283$ MHz. From **Figure 8**, it is apparent that the spreading first-order Bragg lines vary with wind direction. However, the Bragg line energies may be contaminated by the second-order contributions. Thus, the high sea state may influence wind direction extraction from the spreading Bragg lines in shipborne HFSWR.

2.3. Ocean surface cross sections for shipborne HFSWR with sway motion

In practice, the shipborne platform exists six-degree-of-freedom (DOF) motion due to the interaction between the platform and the complicated ocean environment. In this subsection, following the research in the previous subsection, we derive corresponding cross sections which incorporate both the uniform linear motion and the sway motion [3].

2.3.1. First-order cross section

For a shipborne source in **Figure 9**, the small displacement $\delta\vec{\rho}$ from the origin is induced by the uniform linear motion $\vec{\rho}_v = vt\hat{\rho}_v$ and the sway motion $\delta\vec{\rho}_0 = a\sin(\omega_p t)\hat{\rho}_p$. Following the above-mentioned research, the first-order cross section can be written as [3]

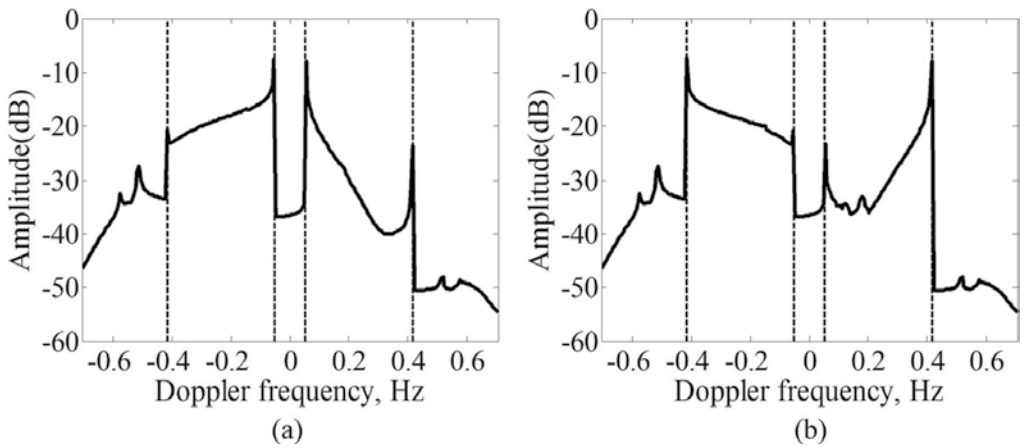

Figure 8. Simulated cross sections for (a) $\alpha^* = 45^\circ$ and (b) $\alpha^* = 315^\circ$.

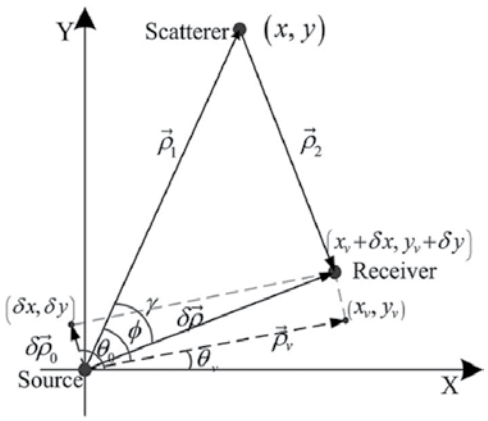

Figure 9. First-order scatter geometry in shipborne HFSWR with sway motion.

$$\begin{aligned}\sigma_1(\omega_d) = {} & 2^6\pi^2k_0^4\sum_{m=\pm1}S\left(2m\vec{k}_0\right)\left\{J_0^2[2ak_0\cos(\theta_k-\theta_0)]\right.\\ & \cdot\delta\left(\omega_d+m\sqrt{2gk_0}-2k_0v\cos\phi\right)+\sum_{n=1}^{\infty}J_n^2[2ak_0\cos(\theta_K-\theta_0)]\\ & \left.\cdot\left[\delta\left(\omega_d+m\sqrt{2gk_0}-2k_0v\cos\phi-n\omega_p\right)+\delta\left(\omega_d+m\sqrt{2gk_0}-2k_0v\cos\phi+n\omega_p\right)\right]\right\} \quad (8)\end{aligned}$$

where ω_p and a are the sway frequency and amplitude related to sea state, respectively. $\widehat{\rho}_p$ is the unit vector of $\delta\vec{\rho}_0$, $J_n(\cdot)$ represents the nth order Bessel function, and θ_K is the direction of the wave vector $\vec{K}$.

2.3.2. Second-order cross section

Similar to the derivation in Section 2.2, the second-order cross section for this new shipborne platform motion model can be derived as [3]

$$\begin{aligned}\sigma_2(\omega_d) = {} & 2^6\pi^2k_0^4\sum_{m_1=\pm1}\sum_{m_2=\pm1}\int_{K_1}\int_{\theta_{\vec{K}_1}}|\Gamma|^2S\left(m_1\vec{K}_1\right)S\left(m_2\vec{K}_2\right)\\ & \cdot\left\{J_0^2[2ak_0\cos(\theta_k-\theta_0)]\delta\left(\omega_d+m_1\sqrt{gK_1}+m_2\sqrt{gK_2}-2k_0v\cos\phi\right)\right.\\ & +\sum_{n=1}^{\infty}J_n^2[2ak_0\cos(\theta_K-\theta_0)]\delta\left(\omega_d+m_1\sqrt{gK_1}+m_2\sqrt{gK_2}-2k_0v\cos\phi-n\omega_p\right)\\ & \left.+\delta\left(\omega_d+m_1\sqrt{gK_1}+m_2\sqrt{gK_2}-2k_0v\cos\phi+n\omega_p\right)\right\}K_1dK_1d\theta_{\vec{K}_1} \quad (9)\end{aligned}$$

2.3.3. Simulation results

For convenience, the sea echo Doppler spectral cross section is decomposed as the sum of the first- and second-order scattering terms

$$\sigma(\omega_d) = \sigma_1(\omega_d) + \sigma_2(\omega_d) \tag{10}$$

It can be inferred from Eq. (10) that the derived cross sections could be reduced to the existing results. Specifically, in the case of no uniform linear motion (i.e., $v = 0$), it is readily checked that the derived expressions are consistent with Walsh's results for an antenna on a floating platform [4, 8]. For the platform without sway motion (i.e., $a = 0$), Eq. (10) agrees well with Xie's results [1, 2]. For $a = 0$ and $v = 0$, it is possible to reduce the derived results to the well-known cross sections derived by Barrick [5, 9] or Walsh [10] for onshore monostatic HF radar. This means that the derived cross section can be reasonably regarded as Xie's results in shipborne HFSWR are modulated by sway motion, or Walsh's results in HF radar on a floating platform are spread due to a uniform linear motion.

2.3.3.1. Cross sections for different platform speeds

Simulation parameters: $f_0 = 5.283\,\text{MHz}$, $\alpha^* = 90^\circ$, and $U = 15\,\text{knots}$. In **Figure 10**, A and A' indicate the Doppler frequencies of sea echo with $\phi = 0$, whereas B and B' represent the Doppler frequencies of sea echo with $\phi = \pi$. For a given radar-operating frequency in Eq. (10), it is evident that the broadening region of the first-order sea echo is proportional to v. Because such Doppler spreading can potentially mask the target echo of interest, a significant challenge in shipborne HFSWR is the detection of moving targets whose Doppler frequencies appear in the spreading region. When the platform moves at a high speed, the first-order sea echo spectrum will overlap. To avoid the effect of Doppler overlap on wind direction extraction with shipborne HFSWR, the platform speed should be limited by a theoretical maximum value $v_{\max} = \sqrt{g\lambda_0/(4\pi)}$. Additionally, it can be inferred that additional spectra induced by sway motion will repeatedly emerge and be located with uniform spacing of sway frequency, as shown in **Figure 10**.

2.3.3.2. Cross sections for different wind directions

Simulation parameters: $f_0 = 5.283\,\text{MHz}$, $U = 15\,\text{knots}$, and $v = 10\,\text{knots}$. From **Figure 11**, there exists obvious envelop distortion in the Doppler spectrum, which is indicated by the circles. Under this condition, the positive and negative Bragg line energies are contaminated by the second-order contributions [2], and the "corner reflector" peaks in the positive Doppler

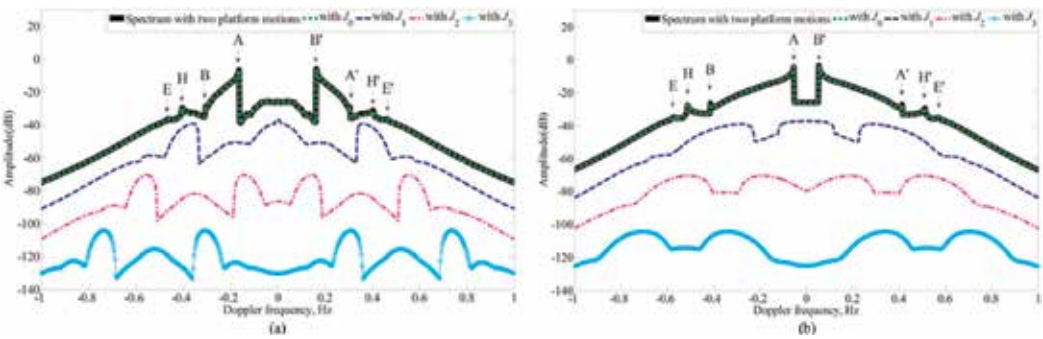

Figure 10. Simulated cross sections for (a) $v = 4$ knots and (b) $v = 10$ knots.

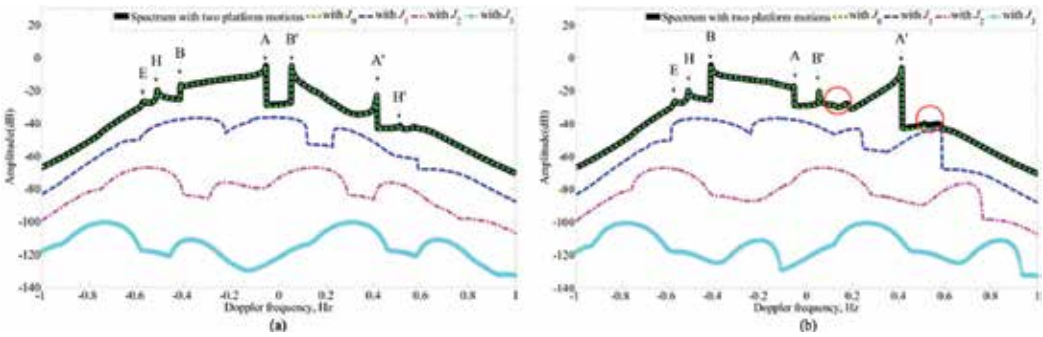

Figure 11. Simulated cross sections for different wind directions. (a) $\alpha^* = 45^\circ$ and (b) $\alpha^* = 315^\circ$.

spectrum are also masked by these sway-induced contributions. In remote-sensing applications, the sea echoes scattered from the ocean surface could be interpreted to extract the wave height spectrum, as well as to estimate the surface current and wind field. Therefore, the envelop distortions in the Doppler spectra may degrade the performance of ocean remote sensing. Specifically, this would be detrimental to the wind direction extraction from the ratio of the positive and negative Bragg line energies in shipborne HFSWR.

3. Remote sensing of ocean surface wind field with shipborne HFSWR

In this section, the potential of remote sensing of ocean surface wind direction and speed with shipborne HFSWR are presented [11, 12], respectively. Based on the spreading mechanism of the first-order Bragg lines, the unambiguous wind direction is extracted by the use of a single receiving sensor. Due to this single-side system consisting of a transmitter and a receiving sensor, it can be realized more easily and with less system cost, and it is more suitable for a shipborne platform with limited deck space.

3.1. Space: time distributions of first-order sea echo

From Eq. (1), it can be inferred that the locations of positive and negative Bragg lines are determined by the angle ϕ, which is consistent with the space-time distribution of the first-order sea clutter [7]

$$f_d = f_{dp} \cos\phi \pm f_B \tag{11}$$

where $f_d = \omega_d/2\pi$, $f_{dp} = 2v/\lambda$, $f_B = \sqrt{g/\pi\lambda}$ is the first-order Bragg frequency in monostatic onshore HFSWR. Different Doppler frequencies in Bragg region correspond to the sea echoes from different incident directions and vice versa; therefore, the first-order Doppler spectrum is

spread due to the forward movement of the platform. Then, the spreading domains of the first-order Doppler spectrum should be

$$\left[-f_B - 2v/\lambda, -f_B + 2v/\lambda\right], \quad \left[f_B - 2v/\lambda, f_B + 2v/\lambda\right] \tag{12}$$

Taking the differential of f_d in Eq. (11), the Doppler frequency resolution Δf_d can be expressed as a function of the azimuth resolution $\Delta\phi$, which can be expressed as

$$\Delta f_d = f_{dp} \sin\phi \cdot \Delta\phi \tag{13}$$

Analogously to Doppler beam sharpening (DBS), the azimuth resolution can be obtained by

$$\Delta\phi = \Delta f_d / \left(f_{dp} \sin\phi\right) \quad for\ \phi \neq 0 \tag{14}$$

Generally, HFSWR can provide a very high-frequency resolution with long coherent integration time (CIT). Therefore, the shipborne HFSWR may provide a higher transverse resolution than onshore HFSWR with a huge antenna array aperture.

3.2. Wind direction extraction in shipborne HFSWR

3.2.1. Mathematical model

For onshore HFSWR, wind directions are sensitive to the ratio of energies of positive and negative Bragg peaks, which can be used to measure the wind direction [13]. To extract the wind direction with shipborne HFSWR, analogously to onshore HFSWR case, the ratio R of the positive and negative Bragg lines energies, B^+ and B^-, is defined by

$$R = 10 \cdot \log_{10}(B^+/B^-) \tag{15}$$

where $\frac{B^+}{B^-} = \frac{\sigma(\omega_d)}{\sigma(-\omega_d)} = \frac{G(\theta+\pi-\alpha^*)}{G(\theta-\alpha^*)}$. The application prerequisite of Eq. (15) is that the two spreading domains of the first-order Doppler spectrum in Eq. (12) are not overlapped, which means the maximum permitted speed of shipborne platform $v_{\max} = \sqrt{g\lambda/(4\pi)}$.

Together with the modified cardioid directional factor in Eq. (1), the abovementioned ratio can be finally simplified as

$$R = 10\log_{10}\left(\frac{\xi + (1-\xi)\sin^4\left(\frac{\theta-\alpha^*}{2}\right)}{\xi + (1-\xi)\cos^4\left(\frac{\theta-\alpha^*}{2}\right)}\right) \tag{16}$$

where $\xi = 0.004$ is the strength ratio of upwind returns to downwind returns. For the convenience of description of Eq. (16), we can define y as

$$y = \sin^2\left(\frac{\theta-\alpha^*}{2}\right) \tag{17}$$

Therefore, once y is calculated from Eq. (16), possible wind directions can be deduced by

$$\alpha_p^* = \theta \pm 2\arcsin\left(\sqrt{y}\right) \tag{18}$$

where $\pm$ sign indicates the wind direction ambiguity.

3.2.2. Method for resolving wind direction ambiguity

For a fully developed sea area, wind directions are generally considered to be spatially uniform or slow-varying over adjacent ocean patch. That means the differences of wind directions in adjacent ocean patches should be zero or near zero. **Figure 12a** describes four adjacent ocean patches with corresponding incident directions. For ocean patch A with the incident direction ϕ_A, the energies of positive and negative Bragg lines can be derived, as shown in **Figure 12b**. Then, two possible wind directions α_{A1}^* and α_{A2}^* can be calculated by Eq. (18). Similarly, the possible wind directions α_{B1}^* and α_{B2}^* for ocean patch B can also be derived. We define

$$\Delta\alpha_{ij} = \left|\alpha_{Bi}^* - \alpha_{Aj}^*\right| \quad (i,j = 1,2) \tag{19}$$

The value of α_{Bi}^* that minimizes $\Delta\alpha_{ij}$ is considered as the real wind direction of ocean patch B. Therefore, the wind directions of the whole ocean area covered by radar can be measured by sequentially applying this method.

3.2.3. Simulation and discussion

3.2.3.1. Simulation for wind direction extraction

Simulation parameters:$f_0 = 5.283$ MHz, $v = 10$ knots. Consider that the input wind direction α^* slowly increasing from 135˚ to 180˚ is given for simulation. Due to the directional ambiguity, it is difficult to determine the unique wind direction from the two possible solutions with a single incident direction ϕ as shown in **Figure 13a**. However, the problem of wind direction

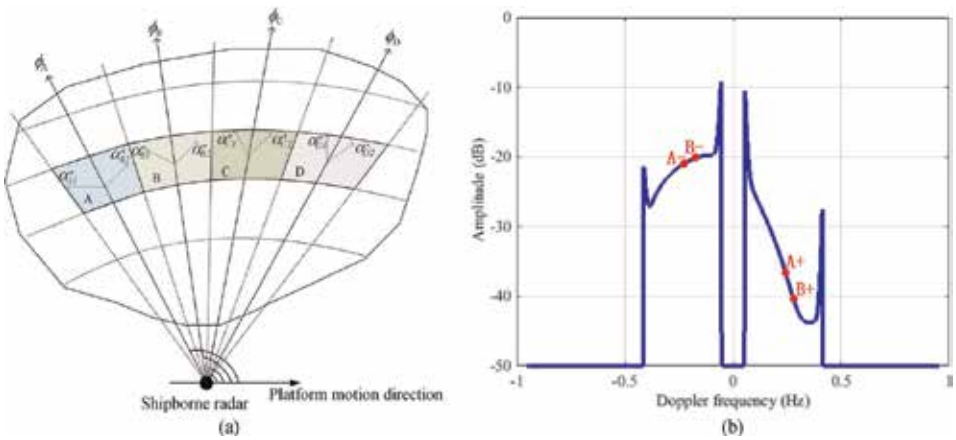

Figure 12. (a) Possible wind directions of four spatially adjacent ocean patches A, B, C, and D. (b) Doppler spectrum.

ambiguity can be effectively removed by comparing the possible results of adjacent sea cells, as shown in **Figure 13b**, where the circles denote the slow-varying wind directions for simulation. Simulation results visually illustrate the process of removing the directional ambiguity, and the good agreement between the derived wind direction and the simulation parameter shows the potential of unambiguity wind direction extraction with shipborne HFSWR.

3.2.3.2. Discussions of basic applications in shipborne HFSWR

In experiment, the effects of the coverage region shift due to platform motion, the real sailing conditions (fluctuations of platform speed and course) during CIT, and the external Gaussian noise on the wind direction extraction should be studied.

3.2.3.2.1. Effect of covered region shift due to platform motion

In order to investigate the effect of covered region shift, the ratio R_{shift} is defined as

$$R_{shift} = \frac{\Delta r}{\Delta R} \tag{20}$$

where $\Delta r = vT$ is the covered region shift during CIT T, $\Delta R = \Delta\phi \cdot \rho$ is the transverse resolution, $\Delta\phi$ is the azimuth resolution in Eq. (14), and ρ is the radar detection range.

Then, Eq. (20) can be rewritten as

$$R_{shift} = \frac{2v^2T^2 \sin\phi}{\lambda\rho} \leq \frac{2v^2T^2}{\lambda\rho} \tag{21}$$

Reviewing the typical radar parameters in [7]: $f_0 = 5.283\,\text{MHz}$, $v = 10\,\text{knots}$, $\rho = 100\,\text{km}$, and $T = 150\,\text{s}$, $R_{shift} < 0.21$ can be obtained. That means Δr is nearly one-fifth of ΔR during T. In addition, wind directions are considered to be uniform or slow-varying within adjacent ocean patches. As mentioned earlier, we consider that the covered region shift during T would not significantly influence the presented method.

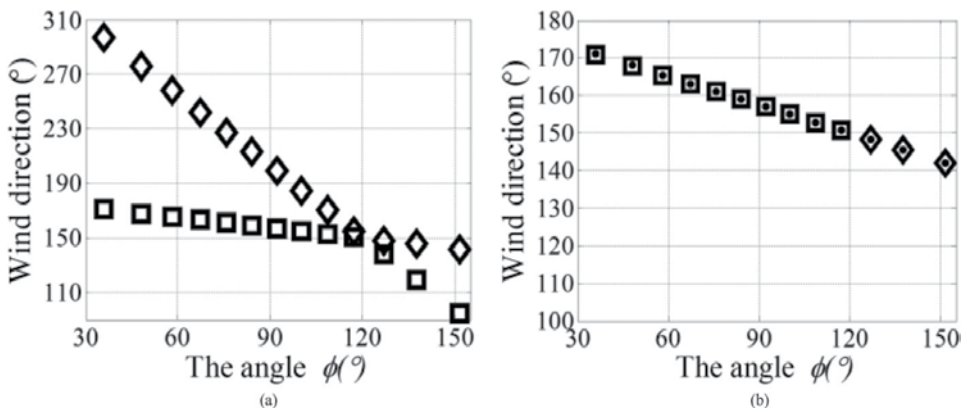

Figure 13. (a) Possible wind directions. (b) Determination of unique wind direction.

3.2.3.2.2. Effect of real sailing conditions

In order to explore the effect of real sailing conditions, the sailing data [7] are exploited to derive the synthetic Doppler spectra. For comparison, then, the ideal Doppler spectra also are derived. The simulation parameters are $f_0 = 5.283\,\text{MHz}$, $v = 10\,\text{knots}$, $\alpha^* = 90^\circ$, and $U = 25\,\text{knots}$.

A comparison of the ideal and synthetic spectra shows that the spreading regions of the latter are slightly more obvious, as shown in **Figure 14**. Although slight fluctuation exists in the speed and course, no apparent differences are found between the ideal and synthetic spectra except for the margin. In experiment, accordingly, the middle regions of the spreading spectra (e.g., $\phi \in [30^\circ, 150^\circ]$) should be exploited to measure the wind direction.

3.2.3.2.3. Effect of external Gaussian noise

To examine the performance of the proposed method in externally noise-limited environment, time series of the backscattered electric field is provided as follows:

$$(E_n)_1(\phi, t) = M \cdot \sum_{\vec{K},\,\omega} P_{\vec{K},\omega} \sqrt{K} e^{j\omega t} e^{j(\rho + vt\cos\phi)K} \Delta\rho \,\text{sinc}\left[(K - 2k_0)\Delta\rho/2\right] \tag{22}$$

where M is a constant, $P_{\vec{K},\omega}$ is Fourier coefficients of ocean surface components, K and ω are the wavenumber and radian angular frequency, respectively, $\Delta\rho$ is the range resolution, and $\text{Sinc}(\cdot)$ is the sinc function.

The spreading spectra with the Gaussian noise can be derived by a periodogram method [14, 15]. The simulated spectra from 150 s time series are shown in **Figure 15**, where $f_0 = 5.283\,\text{MHz}$, $\rho = 100\,\text{km}$, $v = 5.07\,\text{m/s}$, $\Delta\rho = 5\,\text{km}$, and α^* slowly increasing from 0° in the stern to 45° at the prow of shipborne platform. It is obvious that the noise floors decrease with the increasing signal-to-noise ratio (SNR). That means a high SNR can improve the performance of the wind direction estimation.

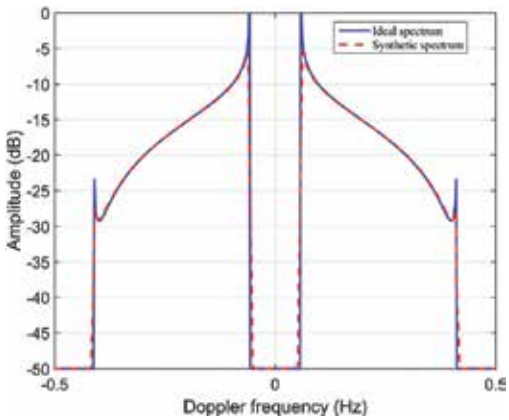

Figure 14. Ideal and the synthetic spreading Doppler spectra.

3.2.3.2.4. Effect of comprehensive factors

Together with the real sailing speed and heading data, the influence of external noise is shown in **Figure 16**. The performance is estimated via 100 independent Monte Carlo simulations for each SNR, where the simulation parameters are the same as those in **Figure 15**. It is apparent that the error of the wind direction estimation gradually decreases with the increasing SNR. There is no obvious deviation between the two error curves. Therefore, external Gaussian noise is the major factor affecting the performance of the wind direction estimation.

3.2.4. Experimental results

Shipborne HFSWR data were collected for moving target detection on 26 September 2016, in Taiwan Strait, China, by the Harbin Institute of Technology with a carrier frequency of

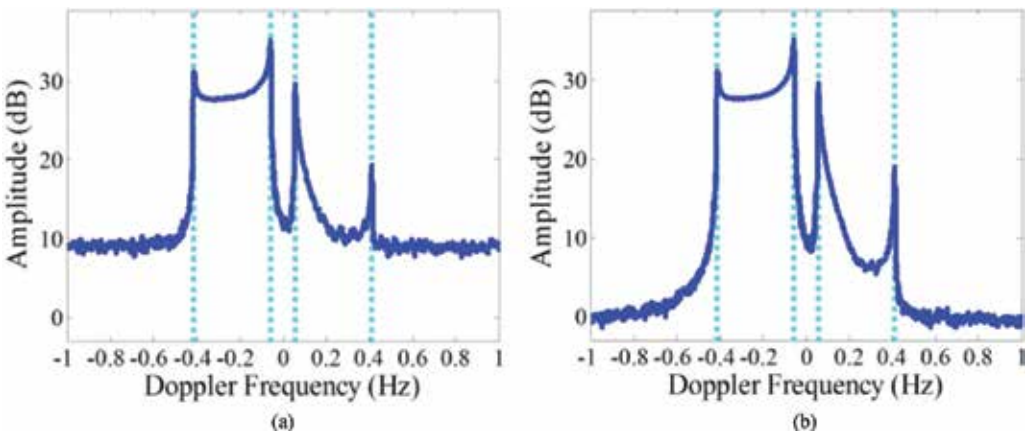

Figure 15. Simulated spreading spectra with Gaussian noise: (a) SNR = 10 dB and (b) SNR = 20 dB.

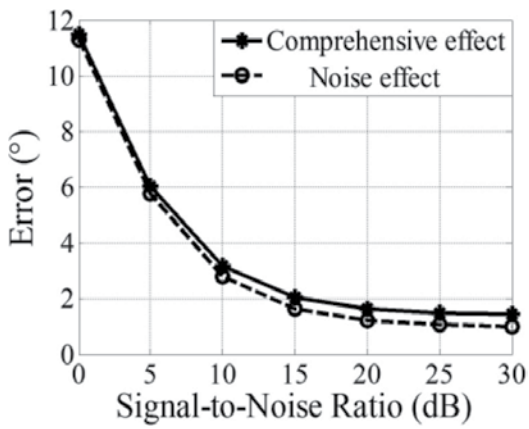

Figure 16. Wind direction error caused by external Gaussian noise and comprehensive factors.

6.45 MHz. Due to the directional ambiguity problem, partial data collected by shipborne HFSWR sailing along the coast with a suitable speed can be exploited to validate the proposed method.

In this experiment, the data collected by a single antenna during CIT from 08:47:37 to 08:49:46 were used for wind direction extraction. The average speed of the platform is 4.67 m/s. The CIT is 129 s and the number of pulse during CIT is 512. The signal bandwidth is 50 kHz. The detection limit and azimuth are 120 km and 53.4°–151.1° north, respectively. It should be noted that an integral shift method is used to alleviate the effect of ocean surface current.

The radar-measured wind direction results are shown in **Figure 17**. Forecast data supported by the FUJIAN MARINE FORECASTS (FJMF) are exploited to preliminarily validate the performance of the presented method because of the lacking of in situ data. A comparison of **Figures 17** and **18** shows that the radar-measured results agree well with the local wind direction forecasts over the same period. Given the data-observed time, **Figure 18a** is considered as the reference of the real wind field. That is, "real" wind directions are slow-varying from 27.5° to 10.6° northeast, and "real" wind speeds are slow-varying from 13.8 to 8 m/s in the detection region form north to south. A histogram of radar-measured wind direction results is shown in **Figure 19**. Only samples whose sampling number is greater than 10 are exploited to verify the performance of the wind direction measurement; 55.42% of the radar-measured results are located in the range of the "real" wind direction. The percentage can achieve 90.07% if the "real" wind direction range is extended to 0.6°–37.5° northeast. Meanwhile, the average value and the root-mean-square error (RMSE) of the radar-measured results are 14.56° northeast and 9.85°, respectively.

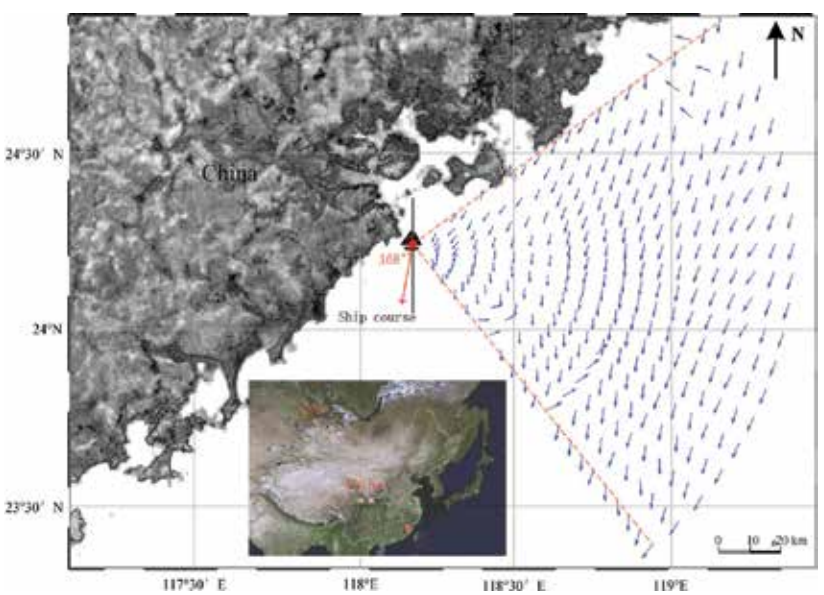

Figure 17. Wind direction map derived by shipborne HFSWR. Dot: Shipborne radar. Arrow: Ship course.

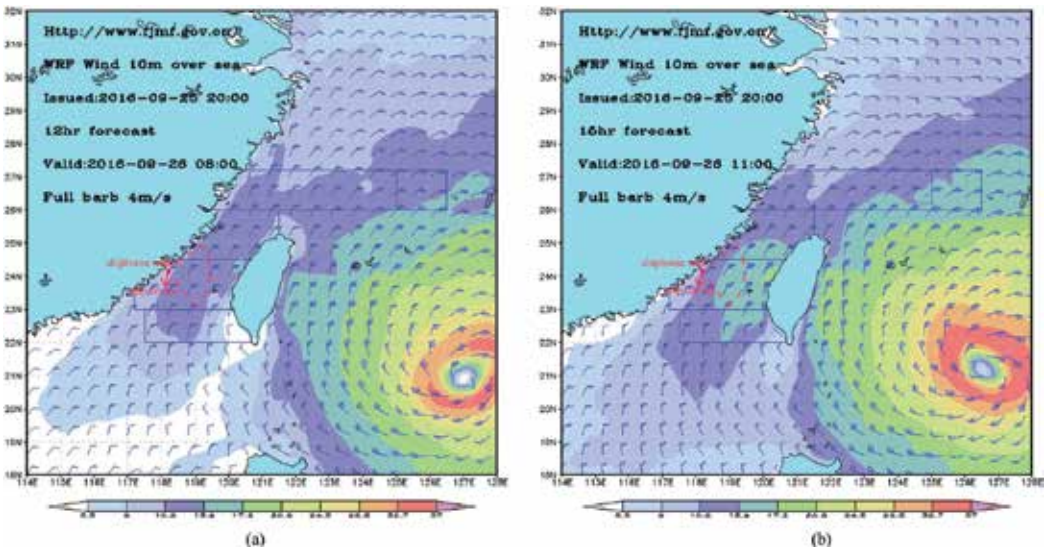

Figure 18. Wind field map at (a) 8:00 and (b) 11:00 on September 26, 2016. Dot: Shipborne radar.

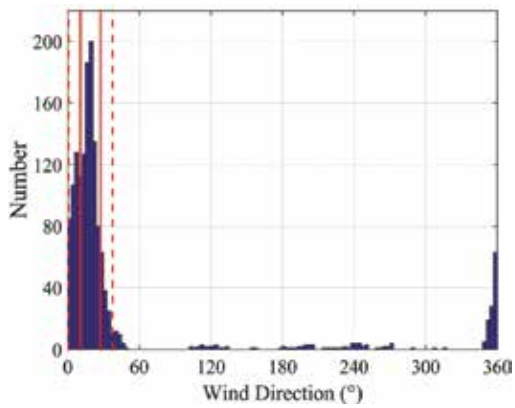

Figure 19. Histogram of derived wind directions for the degree interval of 3° each.

3.3. Wind field extraction in shipborne HFSWR

In Section 3.2, we proposed a method for extracting the unambiguous wind direction with an empirical spreading parameter value of 2. In view of [16, 17], the spreading parameter depends on the wind speed, which may be variable in the experiment. The optimum value for the spreading parameter should be estimated from the shipborne HFSWR experiment data itself. In this section, a method for simultaneously deriving the unambiguous wind direction and the unique spreading parameter will be presented. Then, a relationship between the wind speed and the spreading parameter will be developed by the drag coefficient. Therefore, the wind field can be measured by sequentially using the presented method.

3.3.1. Method for deriving unambiguous wind direction

Assuming that the spreading parameter s is a variable argument, analogously to Section 3.2.2, Eq. (15) can be rewritten as

$$R = 10\log_{10}\left(\frac{\xi + (1-\xi)y^s}{\xi + (1-\xi)(1-y)^s}\right) \tag{23}$$

where

$$y = \sin^2\left(\frac{\theta - \alpha^*}{2}\right) \tag{24}$$

Therefore, the possible wind directions can be deduced by

$$\alpha_p^* = \theta \pm 2\arcsin\left(\sqrt{y}\right) \tag{25}$$

where α_p^* varies with s, the $\pm$ sign indicates the ambiguity of wind direction.

For each incident direction of sea echoes, analogously to Section 3.2.3, the derived wind directions for different spreading parameters can be determined by Eq. (25), as shown in **Figure 20a**. Obviously, the intersection of these two curves should be the unique solution for the wind direction and the spreading parameter. **Figure 20b** shows a two-solution case, and then the sea echo at the third incident direction from the adjacent cell will be necessary to determine the unique solution.

3.3.2. Method for calculating wind speed

A relationship between s and the wind speed U is developed by a momentum transfer factor μ, which can be written as [18]

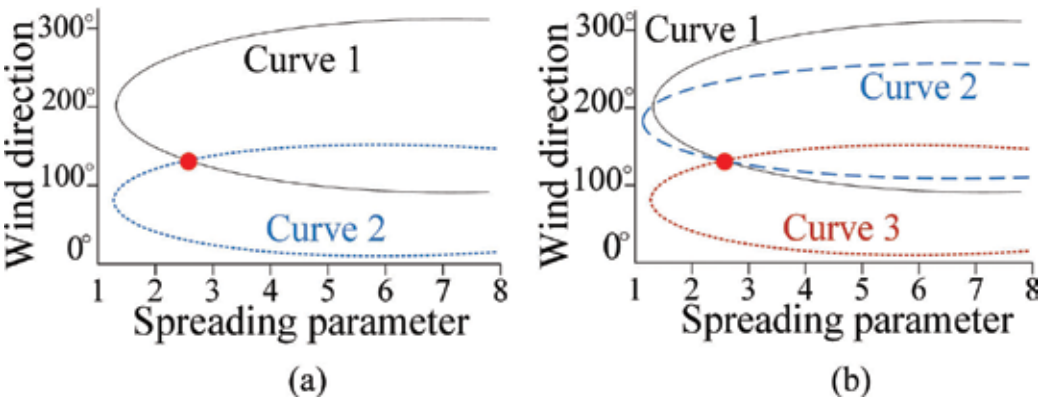

Figure 20. Relationship between the wind direction and the spreading parameter. (a) One-solution case. (b) Two-solution case.

$$s = \begin{cases} 0.2(\mu - 0.1)^{-1} & \mu > 0.1 \\ 2 & \mu < 0.1 \end{cases} \tag{26}$$

where $\mu = (C_D)^{1/2}(4\pi/g\lambda)^{1/2}U/\kappa$, $\kappa = 0.4$ is von Karman's constant and C_D is a drag coefficient proposed by Wu [19]

$$C_D = (0.8 + 0.065U) \times 10^{-3} \tag{27}$$

Substituting Eq. (27) into Eq. (26) and using the Cardano formula, we have

$$s = \begin{cases} 0.2\left(\frac{U}{\kappa}\sqrt{\frac{4\pi}{g\lambda}C_D} - 0.1\right)^{-1} & U > U^* \\ 2 & U < U^* \end{cases} \tag{28}$$

where U^* is related to the radar frequency.

When $U > U^*$, using the Cardano formula, we can derive the one-to-one correspondence relationship between U and s. Therefore, s can be considered as an indicator of U.

3.3.3. Simulation results

Simulation parameters: $f_0 = 5.283$ MHz, $v = 10$ knots, the true wind direction and speed are $\alpha_T^* = 90^\circ$ and $U_T = 25$ knots, respectively. The true spreading parameter is $s_T \approx 2.1$ calculated by Eq. (28).

The relationship between the derived wind directions α^* and s is shown in **Figure 21a**. The solid curve indicates α^* versus s for the incident direction of $\phi_1 = 100^\circ$, while the dashed curve represents the situation of the incident direction of $\phi_2 = 110^\circ$. The intersection of these two curves determines a solution for α^* and s. Therefore, the extracted wind direction and the

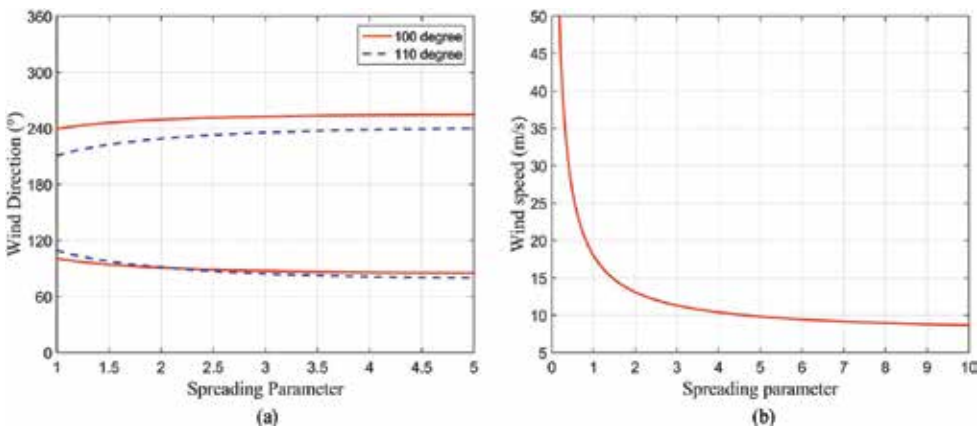

Figure 21. Deriving wind field. (a) Determination of α_E^* and s_E. (b) Determination of U.

spreading parameter are $\alpha_E^* \approx 90.02^\circ$ and $s_E = 2.10$, respectively. The corresponding wind speed is $U_E \approx 24.98$ knots calculated by Eq. (28), as shown in **Figure 21b**.

3.3.4. Experimental results

The experimental data and the "real" wind field have been described in Section 3.2.4. **Figure 22** intuitively shows the radar-measured wind field distribution. From **Figure 22**, the majority of wind directions are north-northeast and north. Meanwhile, wind speeds gradually decrease and wind directions are slow-varying from north-northeast to north in the detection region from north to south. Therefore, the radar-measured results are in good agreement with the local wind field forecast.

Experimental results in Sections 3.2.4 and 3.3.4 show that the wind direction and field estimation in shipborne HFSWR have derived very encouraging results. However, there are some "bad points" that appear over the edge of the detection area, as shown in **Figures 17** and **22**, where a larger deviation exists. This may be because the effect of directional ambiguity is not totally eliminated due to the complex coastline structures. In addition, the ocean surface current, six oscillating motions of shipborne platform, and swell may be have negative effects on the wind direction and field estimations. Note that the method for wind field estimation is

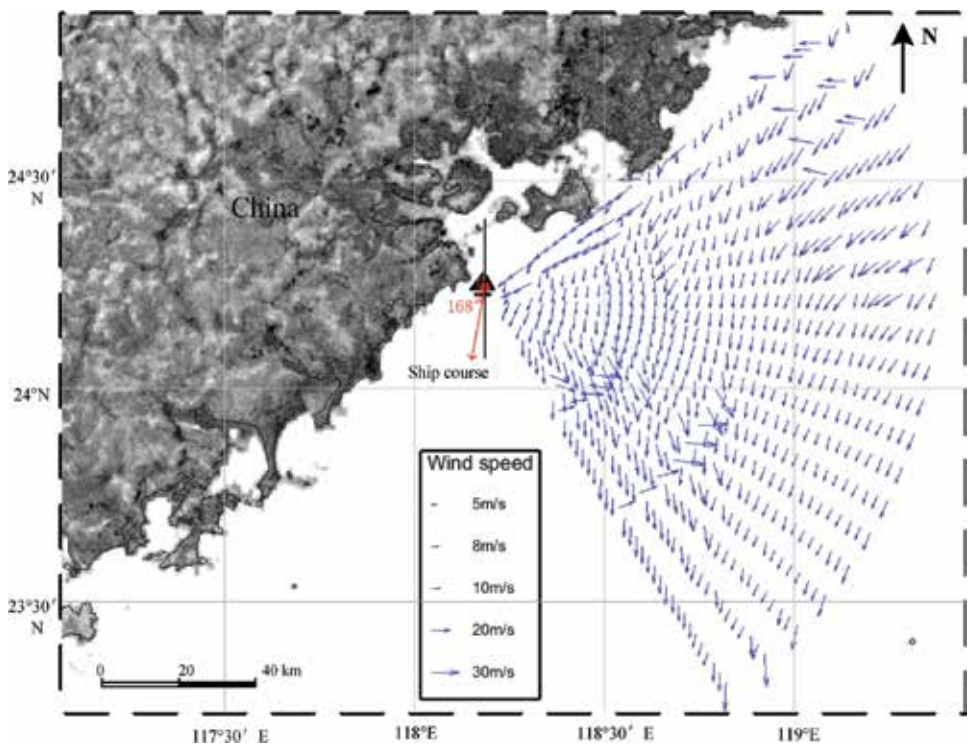

Figure 22. Wind direction map derived by shipborne HFSWR. The wind direction map is displayed with a range resolution interval each. Dot: Shipborne radar. Arrow: Ship course.

presented for a fully developed sea area and the wind speed inversion is conducted out only under the condition of $U > U^*$. Otherwise, the second-order spectra or other methods should be introduced. These are the subjects of ongoing investigations.

4. Remote sensing of ocean surface current with shipborne HFSWR

HFSWR system has been widely deployed for remote sensing of ocean surface current. With the development of signal-processing technology of HFSWR, shipborne HFSWR has gradually become a more potential deployment situation with its agility and maneuverability. Some experimental results and theoretical analyses have been conducted to explore the feasibility of remote sensing of ocean surface current in shipborne HFSWR [20–23]. In the previous works, however, the hull itself is either stationary or moving at a low speed without considering a high-speed case and effects of six DOFs motion on radar Doppler spectra. In this section, the potential of remote sensing of ocean surface radial current with shipborne HFSWR is presented [24]. Moreover, a stream function method is introduced to obtain current vector field using an improved music signal classification (MUSIC) algorithm and unitary transformation technique [25].

4.1. Remote sensing of ocean surface radial current

4.1.1. Received signal model

The shipborne platform exists six-DOF motion besides the forward movement owing to the effect of the complex ocean environment, which will introduce the superposed amplitude and phase modulations to the backscatter echoes [23], as shown in **Figure 23**. Considering antenna pattern, external noise, forward movement, and six-DOF motion, the time domain model of the received echo signal of the sea surface can be expressed as [25]

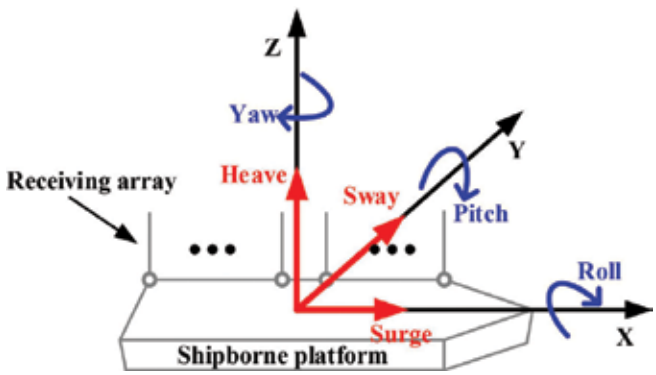

Figure 23. Diagram of six-DOF motion of shipborne platform.

$$x(R,t) = \sum_{r,s} \sigma(R_r, \theta_s, t) a(t) g(\theta_s, t) p(\theta_s, t) + e(t) \tag{29}$$

where $\sigma(R_r, \theta_s, t)$ is the first-order radar cross section of ocean surface, R_r and θ_s are the detection range and azimuth, respectively, $a(t)$ and $p(\theta_s, t)$ are the amplitude and phase of the array steering vector, respectively, $g(\theta_s, t)$ is the receiving antenna pattern, and $e(t)$ is the background noise.

4.1.2. Effect of six-DOF motion on ocean surface radial current estimation

In the previous section, a single antenna is used to estimate the directions of arrival (DOA) of sea echoes. In this case, however, the effects of ocean surface current are not considered. In order to estimate ocean surface radical current accurately, an antenna array with a high-resolution technique is necessary. Theoretical analyses [26] and experimental results [27] have demonstrated that MUSIC algorithm can achieve a good azimuthal resolution in ocean surface current estimation with short aperture. In this section, therefore, the MUSIC algorithm is employed to derive DOA.

From Section 2.1, the first-order Doppler spectra are spread due to the forward movement of shipborne HFSWR, and the spreading region increases with the increasing speed of the platform. That means the Bragg energies have been distributed into more peaks, and the spreading peaks exhibit many more Doppler sampling points which can be exploited to estimate DOA. From **Figure 24a**, the sampling points increase with the increasing platform speed. However, the performance of radial current estimation decreases. In particular, a higher RMSE appears when the ship is still, which may be because of lacking of sampling points. Meanwhile, the radial current RMSE is really high when the ship moves at a high speed, which may be caused by a low SNR. Therefore, the relationship between the RMSE and the platform speed would be a significant reference for the real sailing speed.

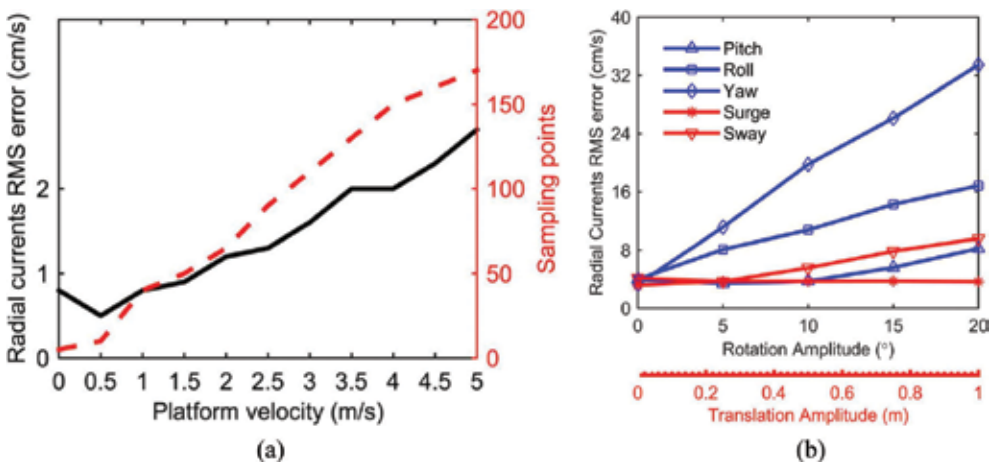

Figure 24. (a) Measurement errors of different platform speeds. (b) Effects of six-DOF motion.

From **Figure 24b**, the radial current RMSEs increase with the increasing amplitude of rotation (pitch, roll, and yaw) and sway. In particular, the surge has no severe influence on the measurement performance, which may be because the surge is generally in the direction of the platform-forward movement. Additionally, yaw plays the most important effect on the radial current estimation. Simulation results show the feasibility of remote sensing of ocean surface radial current in shipborne HFSWR. In addition, the performance of the current estimation is sensitive to the variation of amplitude of six-DOF motion besides surge, rather than the forward movement of the platform.

4.2. Remote sensing of ocean surface current vector field

4.2.1. Method for current vector measurement using RVSR-MUSIC

From Section 4.1, the estimate accuracy of DOA algorithm has significant influence on the performance of ocean surface current measurement. In order to take advantage of the limited radar data to improve the estimate accuracy of DOA, a real-valued MUSIC algorithm based on sparse-representing technique (RVSR-MUSIC) has been presented [25]. Once RVSR-MUSIC has been exploited to estimate DOA, the sea clutter spectra of shipborne HFSWR can be extracted with high resolution, and the Doppler frequency shift and the corresponding azimuth can be derived. Then, the radial velocity $\widehat{V}_r$ of ocean surface current at azimuth $\widehat{\phi}$ can be expressed as

$$\widehat{V}_r = \frac{\lambda}{2}\left(\frac{\widehat{f}_d \mp \sqrt{\frac{g}{\pi\lambda}} - 2v\cos\widehat{\phi}}{\lambda}\right) \tag{30}$$

where λ is the radiation wavelength, $\widehat{f}_d$ is the Doppler frequency shift, g is the gravitational acceleration, and $\widehat{\phi}$ is the corresponding azimuth.

As shown in **Figure 25**, the radial velocity of ocean surface current $V_r(x,y)$ in azimuth ϕ can be written as [25]

$$V_r(x,y) = \frac{xu(x,y) + yw(x,y)}{\sqrt{x^2+y^2}} \tag{31}$$

According to the introduction of stream function in [28], we have [25]

$$V(x,y) = \sqrt{u^2(x,y) + w^2(x,y)} \tag{32}$$

$$\gamma(x,y) = \begin{cases} \tan^{-1}[w(x,y)/u(x,y)] & \text{, if } u(x,y) \geq 0 \\ \pi + \tan^{-1}[w(x,y)/u(x,y)], & \text{else} \end{cases} \tag{33}$$

where $V(x,y)$ and $\gamma(x,y)$ are the amplitude and the direction of ocean surface current vector $\vec{V}(x,y)$, respectively.

4.2.2. Simulation results

Simulations are conducted under these conditions: the number of the receiving antenna is $M = 7$, the space between antennas is $d = \lambda/2$, the radar-operating frequency $f_0 = 7.5\,\text{MHz}$, the radar modulation period $T_r = 0.5\,\text{s}$, and the platform speed $v = 10\,\text{m/s}$ [25]. We assume a uniform ocean surface current field with a velocity of 0.5 m/s. Three different methods including spatial smoothing MUSIC (SS-MUSIC), complex-valued SR-MUSIC (CVSR-MUSIC), and RVSR-MUSIC are exploited to estimate ocean surface radial current by 50 independent Monte Carlo trials, as shown in **Figure 26**. It is obvious that RVSR-MUSIC is the most efficient algorithm for ocean surface radial current estimation.

Figure 27 shows the amplitude errors of the uniform current field using RVSR-MUSIC algorithm for radial current measurements and the second-order stream function for surface current vector measurements. It is apparent that a majority of amplitude errors are within 0.1 m/s. Simulation results demonstrate that the remote sensing of ocean surface current field using a single shipborne HFSWR is feasible. RVSR-MUSIC algorithm obtains the best estimation performance compared with other algorithms.

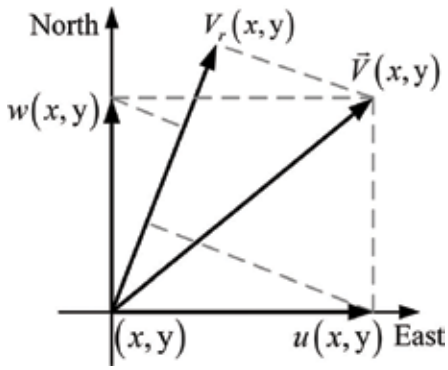

Figure 25. Geometrical relation between 2D surface current vector and radial current.

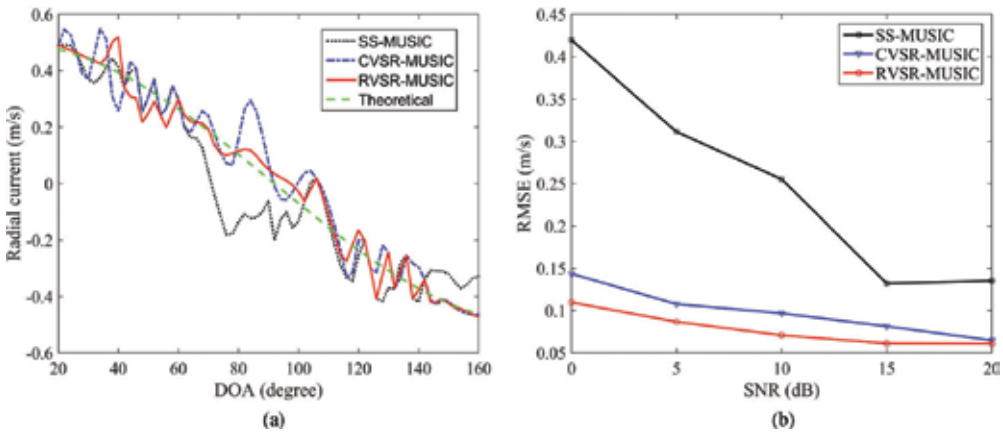

Figure 26. Performance estimation of ocean surface current. (a) Radial current profile. (b) RMSE of radial current versus SNR.

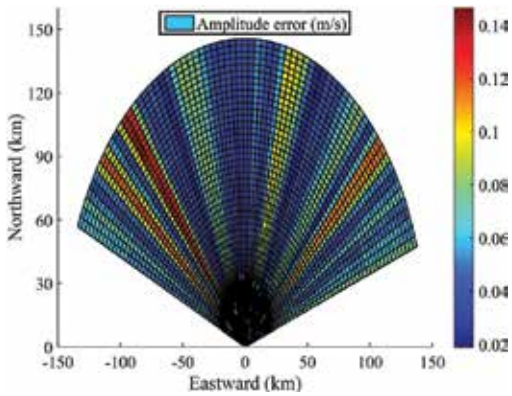

Figure 27. Estimated current field with RVSR-MUSIC.

Analyses of the simulation results show that the presented method here has derived very encouraging results. However, the effects of practical conditions in shipborne HFSWR should be considered. First, when HFSWR is mounted on a ship, the iron body distorts the electromagnetic field severely, which will lower azimuth resolution. Second, the nonideal motions will introduce a superposed amplitude and phase modulation to the backscatter echoes. Third, although RVSR-MUSIC algorithm can increase estimation accuracy and reduce the computational cost, unitary transformation is based on a centro-symmetrical array (CSA), which will severely limit the applications. In addition, the prerequisite of this method is that two-dimensional (2D) ocean surface current field is horizontally nondivergent (or incompressible). These are the subjects of ongoing investigations.

Author details

Junhao Xie[1]*, Minglei Sun[2], Zhenyuan Ji[1] and Guowei Yao[1]

*Address all correspondence to: xj@hit.edu.cn

1 Harbin Institute of Technology, Harbin, China

2 The 27th Research Institute of China Electronics Technology Group Corporation, Zhengzhou, China

References

[1] Xie J, Sun M, Ji Z. First-order ocean surface cross-section for shipborne HFSWR. Electronics Letters. 2013;**49**(16):1025-1026

[2] Sun M, Xie J, Ji Z, Cai W. Second-order ocean surface cross section for shipborne HFSWR. IEEE Antennas and Wireless Propagation Letters. 2015;**14**:823-826

[3] Sun M, Xie J, Ji Z, Yao G. Ocean surface cross sections for shipborne HFSWR with sway motion. Radio Science. 2016;**51**(11):1745-1757

[4] Walsh J, Huang W, Gill E. The first-order high frequency radar ocean surface cross section for an antenna on a floating platform. IEEE Transactions on Antennas and Propagation. 2010;**58**(9):2994-3003

[5] Lipa BJ, Barrick DE. Extraction of sea state from HF radar sea echo: Mathematical theory and modeling. Radio Science. 1986;**21**(1):81-100

[6] Shearman ED. HF ground-wave radar for sea-state and swell measurements: Theoretical studies, experiments and proposals. In: IEEE International Conference on Radar; London, United Kingdom. October 1982. pp. 101-106

[7] Xie J, Yuan Y, Liu Y. Experimental analysis of sea clutter in shipborne HFSWR. IEEE Proceedings-Radar, Sonar and Navigation. 2001;**148**(2):67-71

[8] Walsh J, Huang W, Gill E. The second-order high frequency radar ocean surface cross section for an antenna on a floating platform. IEEE Transactions on Antennas and Propagation. October 2012 **60**(10):4804-4813

[9] Barrick DE. First-order theory and analysis of MF/HF/VHF scatter from the sea. IEEE Transactions on Antennas and Propagation. 1972;**AP-20**(1):2-10

[10] Walsh J, Gill E. An analysis of the scattering of high-frequency electromagnetic radiation from rough surfaces with application to pulse radar operating in backscatter mode. Radio Science. 2000;**35**(6):1337-1359

[11] Sun M, Xie J, Ji Z, Cai W. Remote sensing of ocean surface wind direction with shipborne high frequency surface wave radar. In: IEEE Radar Conference on Radar; Arlington, VA, USA. May 2015. pp. 39-44

[12] Xie J, Yao G, Sun M, Ji Z, Li G, Geng J. Ocean surface wind direction inversion using shipborne high frequency surface wave radar. IEEE Geoscience and Remote Sensing Letters. 2017;**14**(8):1283-1287

[13] Huang W, Gill E, Wu S, Wen B, Yang Z, Hou J. Measuring surface wind direction by monostatic HF ground–wave radar at the eastern China Sea. IEEE Journal of Oceanic Engineering. October 2004;**29**(4):1032-1037

[14] Zhang J, Walsh J, Gill E. Inherent limitations in high-frequency radar remote sensing based on Bragg scattering from the ocean surface. IEEE Journal of Oceanic Engineering. July 2012;**37**(3):395-406

[15] Shen C, Gill E, Huang W. Extraction of swell parameters from simulated noisy HF radar signals. In: IEEE Radar Conference on Radar; Ottawa, Canada. April 2013. pp. 1-6

[16] Heron ML. Applying a unified directional wave spectrum to the remote sensing of wind wave directional spreading. Canadian Journal of Remote Sensing. 2002;**28**(3):246-353

[17] Heron ML, Prytz A. Wave height and wind direction from the HF coastal ocean surface radar. Canadian Journal of Remote Sensing. 2002;**28**(3):385-393

[18] Tayler GL, Teague CC, Stewart RH, Munk AM, Joy JW. Wave directional spectra from synthetic observations of radio scatter. Deep-Sea Research. 1974;**21**(12):989-1016

[19] Wu J. Wind-stress coefficients over sea surface from breeze to hurricane. Journal of Geophysical Research. 1982;**87**(C12):9704-9706

[20] Teague CC. Multifrequency HF radar observations of currents and current shears. IEEE Journal of Oceanic Engineering. April 1986;**OE-11**(2):258-269

[21] Lipa BJ, Barrick DE, Isaacson J, Lilleboe PM. CODAR wave measurements from a north sea semisubmersible. IEEE Journal of Oceanic Engineering. April 1990;**15**(2):119-125

[22] Gurgel KW. Experience with shipborne measurements of surface current fields by HF radar. Oceanography. 1997;**10**(2):82-84

[23] Gurgel KW, Essen H. On the performance of a shipborne current mapping HF radar. IEEE Journal of Oceanic Engineering. January 2000;**25**(1):183-191

[24] Chang G, Li M, Xie J, Zhang L, Yu C, Ji Y. Ocean surface current measurement using shipborne HF radar: Model and analysis. IEEE Journal of Oceanic Engineering. October 2016;**41**(4):970-981

[25] Wang Z, Xie J, Ji Z, Quan T. Remote sensing of surface currents with single shipborne high-frequency surface wave radar. Ocean Dynamics. 2016;**66**(1):27-39

[26] Laws KE, Fernandez DM, Paduan JD. Simulation-based evaluations of HF radar ocean current algorithms. IEEE Journal of Oceanic Engineering. October 2000;**25**(4):481-491

[27] Yang S, Ke H, Wu X, Tian J, Hou J. HF radar ocean current algorithm based on MUSIC and the validation experiments. IEEE Journal of Oceanic Engineering. July 2005;**30**(3): 601-618

[28] Liu L, Wu X, Cheng F, Yang S, Ke H. Algorithm for HF radar vector current measurements. Journal of Geophysical Research. 2007;**63**(1):47-66

Section 2

Applications of Remote Sensing

Chapter 6

Use of Historical Google Earth Images to Create Likelihood of Aquatic Plants along Segments of Ohio River

Yi-Hwa Wu, Ming-Chih Hung, Jeff Thomas and Maureen Gallagher

Additional information is available at the end of the chapter

http://dx.doi.org/10.5772/intechopen.77616

Abstract

Aquatic invasive plants are well known for causing severe impacts to local ecosystems, such as degrading water quality, decreasing biodiversity, consuming natural resources, among other impacts. Major water bodies in US had experienced such impacts. To mitigate such impacts, the U.S. Fish and Wildlife Service and the Ohio River Valley Water Sanitation Commission had put significant amounts of effort toward identifying and removing aquatic invasive plants along the Ohio River shorelines. Field work played a significant role in such identification and removal, but at great expense on labor and time. River systems are dynamic, coupled with similarities between spectral reflectance from submerged plants and background water bodies, limited success was reported from literature regarding the use of remote sensing with selected images on detecting aquatic plants. This study utilized Google Earth historical images between 2003 and 2015 along a section of Ohio River known as the Racine Pool and examined and recorded the appearances of aquatic plants. Visible aquatic plants or suspicious submerged objects were digitized and converted to ESRI shapefiles and grids. Spatial analyses and overlays were then performed between grids to derive a map showing frequency of appearance. Such frequency of appearance may serve the purposes of predicting future sighting and/or guides for directing field work in hopes to save labor and time.

Keywords: Google Earth, historical image, Ohio River, aquatic plants, prediction, frequency, remote sensing, GIS

1. Introduction

The proliferation of invasive plants in lakes, ponds, and inland wetlands is of increasing environmental concern; as such plants have the potential to degrade natural ecosystems by compromising water quality, decreasing the usable area of water bodies, and degrading aquatic habitats. Four invasive plant species (purple loosestrife (*Lythrum salicaria* L.), hydrilla (*Hydrilla verticillata*), water-milfoil (*Myriophyllum*), and curly pondweed (*Potamogeton crispus* L.)) have been identified as potential weed threats within the Ohio River Basin [1–4]. Ohio River Valley Water Sanitation Commission has the responsibility of educating people on the facts about the Ohio River, as well as monitor water quality and overall condition of the Ohio River [5]. Field surveys were conducted to survey lakes, ponds, and inland wetlands in this area to identify and monitor the extent of these invasive plants. An effective early detection and warning system utilizing remotely sensed images could greatly benefit the area and significantly reduce labor- and time-costs associated with field surveys.

Though remote sensing had been widely used in various environmental applications [6–8], there were only few studies using remote sensing on detecting submerged aquatic plants. The main difficulty in such a task is the similarity between spectral reflectance from submerged aquatic plants and their background water bodies. It becomes particularly challenging under circumstances where there are high amounts of sediment or suspected particles in the water. Use of remote sensing to identify or detect objects relies heavily on unique spectral reflectance from objects [9, 10]. When such unique spectral reflectance from objects is neither visible nor statistically significant, successful detection or identification of objects will be limited.

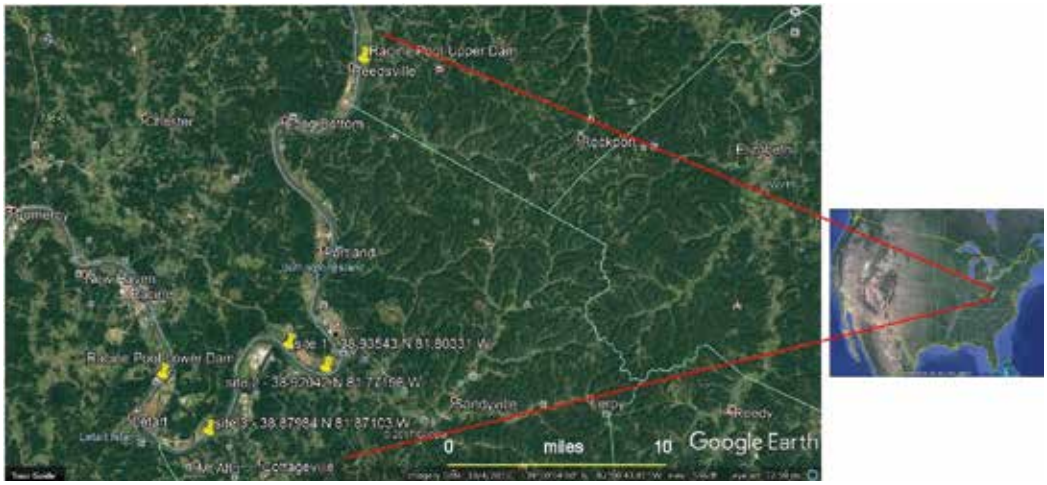

Figure 1. Study area: the Racine Pool section of Ohio River.

Site	Date	Lat/Long	UTM
Site 1	August 3, 2010	38.93543 N 81.80331 W	430376.315441 X 4309917.960553 Y
Site 2	August 3, 2010	38.92042 N 81.77196 W	433079.384833 X 4308228.797736 Y
Site 3	July 2, 2010	38.87984 N 81.87103 W	424447.956561 X 4303802.923941 Y

Table 1. Site locations in Racine Pool section.

1.1. Research objective

The research objective of this project is to use time series remote sensing images to derive a likelihood of sighting submerged aquatic plants along a section of Ohio River known as the Racine Pool.

1.2. Study area

The study area is the Racine Pool along the Ohio River. It is geographically defined as an upper boundary at 39.118468174 (39° 7′ 6″) N 81.740928386 (81° 44′ 27″) W and a lower boundary at 38.914896204 (38° 54′ 48″) N 81.91346283 (81° 54′ 54″) W as seen in **Figure 1** from a snapshot of Google Earth. The ground work confirmed the following aquatic invasive plants: site 1 on August 3, 2010 at 38.93543 N 81.80331 W; site 2 on August 3, 2010 at 38.92042 N 81.77196 W; and site 3 on July 2, 2010 at 38.87984 N 81.87103 W. **Table 1** summarizes sites of ground work and associated dates and coordinates, they are also shown in **Figure 1**.

2. Previous attempts to identify submerged aquatic invasive plants

2.1. Formosat-2 images

Formosat-2 images are unique in regard to their spatial and temporal resolution [11, 12]. Multispectral Formosat-2 images contain four bands (blue, green, red and near infrared) at an 8-m pixel size. Panchromatic Formosat-2 images contain one band at a 2-meter pixel size. Therefore, applying proper pan-sharpening processes will result in a multispectral image of four bands with 2-m pixel size. With such superior spatial resolution, these images are capable of monitoring heterogeneous areas, including urban areas. Most impressive is the ability to collect images daily. Due to the satellites' unique design and orbit, it is capable of collecting images of the same area every day, providing unparalleled capacity for monitoring rapid-change events, such as natural diseases.

Formosat-2 is managed by the Taiwan National Space Organization (NSPO). To facilitate world-wide applications, NSPO partnered with the Colorado, US-based Apollo Mapping to sell and distribute Formosat-2 images of the entire world. NSPO maintained the rights to sell and distribute Formosat-2 images of Taiwan. Two scenes of Formosat-2 images of the Racine Pool were acquired on October 28, 2010 (as shown in **Figure 2**) and November 1, 2010 (as

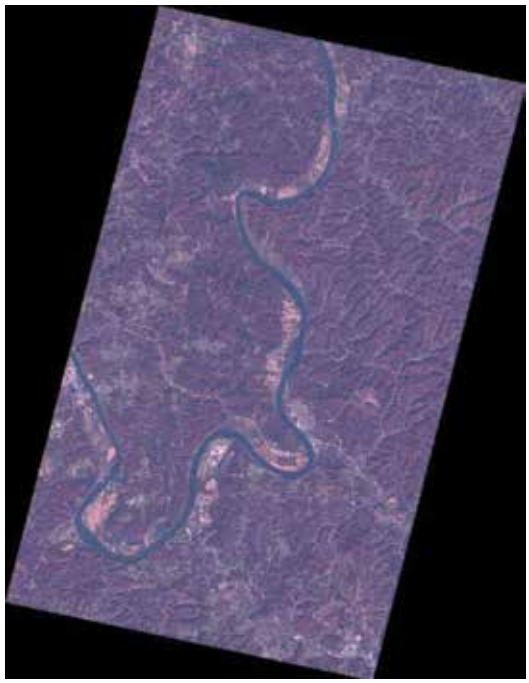

Figure 2. Formosat-2 image of Racine Pool section taken on October 28, 2010.

shown in **Figure 3**). **Table 2** summarizes sections of the Ohio River under study and Formosat-2 images acquired.

2.2. Image processing and results

According to **Table 2**, there were only 3 or 4 months between the site visit and Formosat-2 image. They were in close proximity in terms of temporal disparity. Upon close visual inspection of the Formosat-2 image, something unexpected drew our attention. As shown in **Figure 4**, site 3 was highlighted on Formosat-2 image with false color display (R,G,B/4,3,2). The Ohio River is a spectrally homogeneous water body, without any major visual spectral anomaly, except shadows from trees along the shoreline. With site visits and confirmed sightings, spectral anomaly was expected around site 3, where the crosshair is.

Several multispectral digital image processing (such as supervised classification, unsupervised classification, principal component analysis, band ratio, and others), regular image processing (such as RGB enhancement, HSV transformation, color clustering, and others), or even single band processing (such as threshold, density slicing classification, edge enhancement, and others) were applied on the Formosat-2 image trying to identify any spectral anomaly. Unfortunately, none of these techniques can identify spectral anomaly with confidence.

With such a disappointing result, the research team started over and reexamined data, ground truth, methodology, and the overall situation. It was soon discovered that river

http://dx.doi.org/10.5772/intechopen.77616

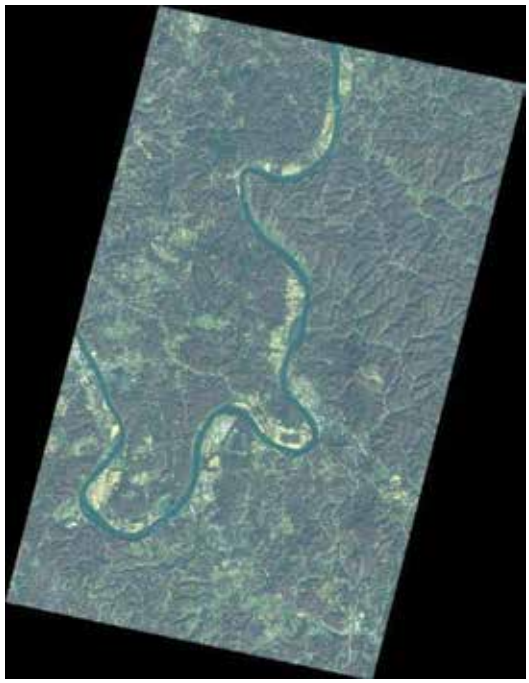

Figure 3. Formosat-2 image of Racine Pool section taken on November 1, 2010.

Name	Location	Formosat-2 image date	Ground work date m/d/y
Racine Pool	Upper: 39.11847 (39° 7′ 6″) N 81.74093 (81° 44′ 27″) W Lower: 38.91490 (38° 54′ 48″) N 81.91346 (81° 54′ 54″) W	10/28/2010 11/1/2010	#1: 8/3/2010 #2: 8/3/2010 #3: 7/2/2010

Table 2. Sections of Ohio River under study and images acquisition.

dynamics may be the cause for such disappointing results. River ecosystem is dynamic; it changes from time to time due to then-current local environments and weather conditions [13–15]. There are many factors that may affect a river ecosystem, especially how a river looks on satellite images. These factors may include water level, flow velocity, and sediment level, just to name a few.

With such dynamic conditions, working with a single satellite image is like taking a snapshot of a racing car. The satellite image captured the then-current condition, which may only be true to that particular moment but not even the moment before or after. These two Formosat-2 images truthfully recorded the conditions of the Ohio River on 10/28/2010 and 11/1/2010. However, aquatic plants were sighted on 7/2/2010, 4 months prior to the satellite image was taken. During these 4 months, many things may happen and change the overall appearance of a river, which in turn may affect the visibility of aquatic plants.

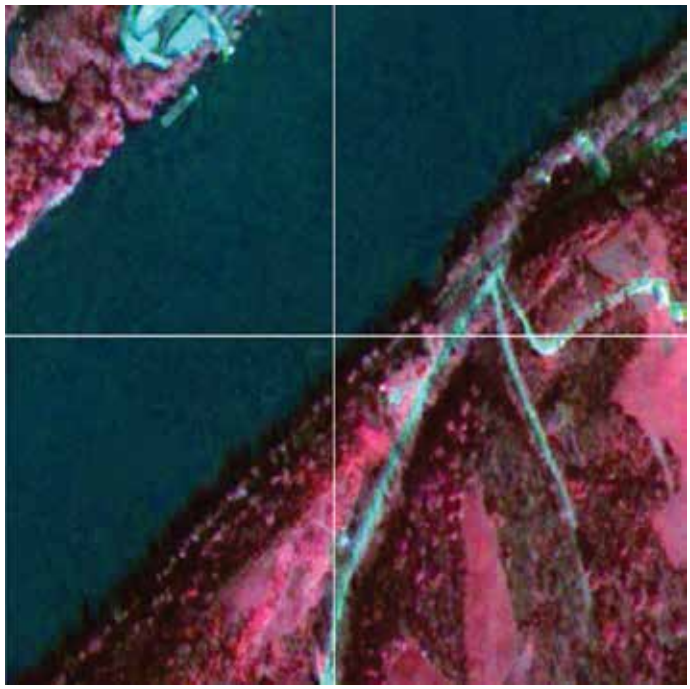

Figure 4. Site 3 on Formosat-2 satellite image with false color display (R,G,B/4,3,2).

3. Historical Google Earth images

To demonstrate the nature of river dynamics, historical images from Google Earth from 2003 to 2011 were taken and arranged side by side for comparison, as shown in **Figure 5**, with a close-up visual inspection of a particular pair of images (October 2011 in **Figure 5(j)** and November 2011 in **Figure 5(k)**) shown in **Figure 6**. As one may observe from **Figure 6(a)** and **(b)**, there clearly is a linear object appearing along shoreline on **Figure 6(b)**, but it is only faintly visible on **Figure 6(a)**. Just a month apart from each other, the appearance of this aquatic object dramatically changed, proving river ecosystem is dynamic, changing its appearance through time. Thus, the visibility of aquatic object is not consistent, depending on then-current conditions. Knowing this, it is not surprising that this particular aquatic object can be seen in some of the images shown in **Figure 5**, but not others. One may also notice that in **Figure 5(h)**, shadows from trees along the shorelines added confusions and challenges on identifying this aquatic object. These historical Google Earth images and their abilities to visually identify this particular aquatic object are summarized in **Table 3**. Note this: this particular site is site 3 with a confirmed sighting of aquatic plants on 7/2/2010 by field crews during their field work. It is only nature and logic to assume that this spectral anomaly or aquatic object is the reported aquatic plants. It is also safe to conclude that, even with confirmed sighting, the visibility of this particular aquatic plant is not consistent through time as demonstrated in **Figure 5**.

http://dx.doi.org/10.5772/intechopen.77616

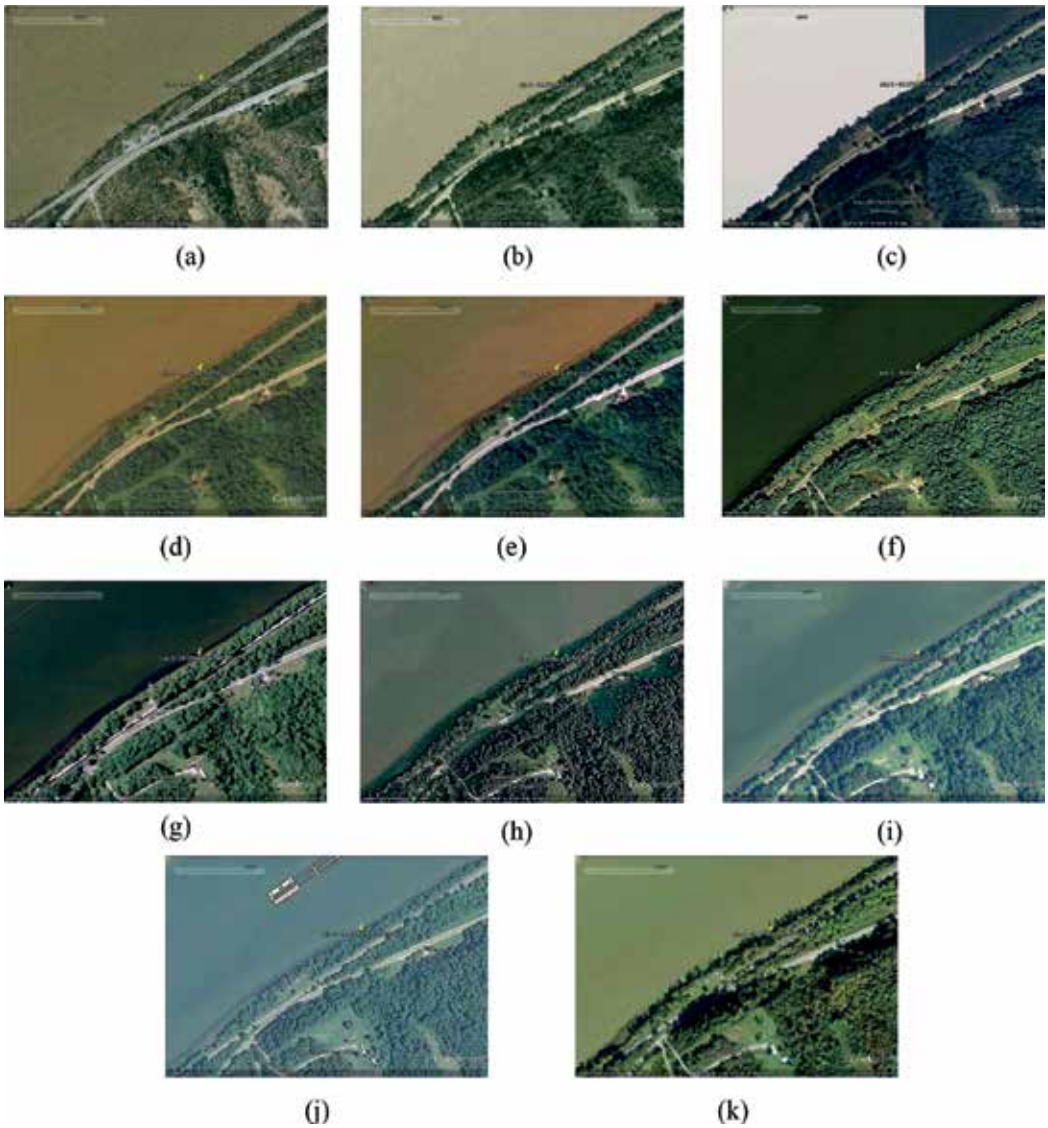

Figure 5. Historical Google Earth images of site 3. (a) Image of December 2003, (b) image of September 2004, (c) image of August 2005, (d) image of July 2006, (e) image of October 2006, (f) image of August 2007, (g) image of September 2009, (h) image of October 2009, (i) image of December 2010, (j) image of October 2011, (k) image of November 2011.

4. Development of a frequency of sighting map

4.1. Warning system and predictive model

Warning system or early warning system had been used in many conservation efforts trying to point out potential threats to a particular ecosystem [16–19]. In many cases, warning system is

Figure 6. A close-up visual inspection of (a) October 2011 and (b) November 2011 images.

Google Earth image date	**Sub** Figure 5	Spectral anomaly
December 2003	(a)	N
September 2004	(b)	N
August 2005	(c)	N
July 2006	(d)	Y
October 2006	(e)	Y
August 2007	(f)	Y
September 2009	(g)	Y
October 2009	(h)	Y
December 2010	(i)	Y
October 2011	(j)	Y
November 2011	(k)	Y

Table 3. Dates of historical Google Earth images of site 3.

a result of a predictive model, in which a particular ecosystem is simplified to or modeled by a combination of several factors with associated weights [16, 20, 21]. Success had been reported [18, 19, 22], particularly on solid land where changes are steady or reliable, comparing to aquatic environments.

A critical step in modeling is to identify key factors and their associated weights [23, 24]. These factors and/or weights can be derived from empirical work, literature search, or statistical analysis. In environmental modeling, factors should be something that can be clearly identified and observed in the real world. For example, elevation is to be between 1000 and 1500 m above sea level, slope is to be between 5 and 10°, aspect is to be facing south between southeast and southwest, and so on.

As demonstrated by historical Google Earth images in **Figure 5**, aquatic objects may be visible or not, depending on then-current river conditions. When it is not visible, it does not mean that the aquatic object (aquatic plants in this case) has been removed or is not present. It simply

indicates that the acquired images or photos cannot detect the existence of aquatic objects. They may be disguised. With such uncertainty in appearance, and subsequent ground truthing work, traditional modeling approach may not be suitable or even not workable in aquatic environments. A new approach which is realistic and suitable to aquatic environments is necessary.

Instead of using modeling approach, this study proposed an methodology to survey historical images and create a frequency of sighting map.

4.2. Temporal resolution of remote sensing images

Since the successful launch of Landsat-1 back in 1972, there had been a great wealth of satellite images monitoring our environments. With advances of modern technologies, satellite images are becoming of better quality with more resolution power, such as hyperspectral images with hundreds of spectral bands [25–27] or ultra-fine spatial resolution image with sub-meter pixel size [28–30].

In addition to spatial resolution and spectral resolution, another characteristic of remote sensing systems is temporal resolution or the repetitive coverage of the ground by the system itself. Though remotely sensed images have been widely used to identify vegetation in various conditions [31–33], majority of such projects focused on only selected images to identify objects under study, mainly utilizing spatial resolution or spectral resolution. Temporal resolution, on the other hand, had been overlooked in the mainstream remote sensing research. This study looks to survey historical images of the Racine Pool section of the Ohio River, and it requires a rich image history and a decent temporal resolution.

Google acquired Keyhole Inc., in 2004, and soon launched Google Earth in 2005 [34]. It became a huge hit in the broader geographic information system (GIS) community, as well as the general public. With Google Earth, everyone has free access to satellite images or aerial photos of the entire earth, not only recent images but also historical images. These historical images is an invaluable resource in many environmental projects requiring low cost (or even free) and historical images. Major drawbacks on these historical Google Earth images include inconsistent time interval between images (as short as a month or sometimes as far as years), inconsistent image quality (sun angle, image brightness, color/gray level, pixel size, etc.), lack of image metadata, and so on. Historical Google Earth images was a useful tool and resource to demonstrate the river dynamics earlier in this study. It is selected again as the image source for the new methodology.

4.3. Frequency of sighting from historical Google Earth images

Eleven sets of Google Earth images of the study area between 2003 and 2015 were selected for this project. Though Google provides images before 2003, many earlier images were excluded from this project due to image quality, such as pixel size, color detail, and so on. **Table 4** summarizes year and month of these historical Google Earth images.

Each historical Google Earth image was displayed on computer monitor and visually inspected. If a spectral anomaly is visible during visual inspection, such spectral anomaly was

Google Earth image year	Month
2003	December
2004	September
2005	August
2006	July
2007	August
2009	August
2010	December
2011	October
2012	March
2013	October
2015	October

Table 4. Historical Google Earth images selected for this project.

digitized as a KML polygon using available tools from Google Earth. **Figure 7** demonstrates this process. **Figure 7(a)** shows the 08/2007 Google Earth image of site 2, with visible spectral anomalies. Such spectral anomalies were then digitized as a KML polygon using available tools from Google Earth, as shown in **Figure 7(b)**. **Figure 7(c)** shows the 10/2009 Google Earth image of site 2, with no visible spectral anomaly. Therefore, no polygon was digitized for this area.

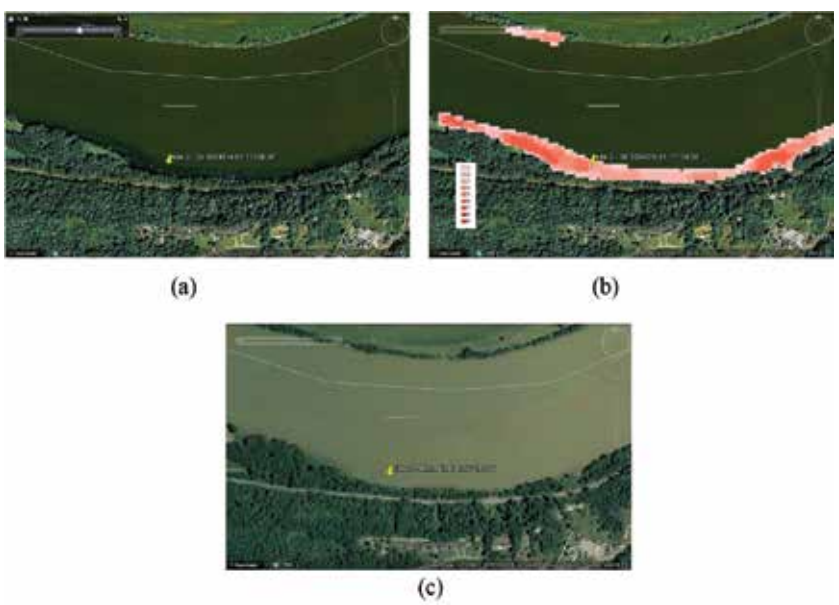

Figure 7. Example of digitizing spectral anomalies from Google Earth images. (a) 08/2007 Google Earth image of site 2 with visible spectral anomalies. (b) Digitizing this anomaly with a KML polygon. (c) 10/2009 Google Earth image of site 2 with no visible spectral anomaly. No KML polygon was digitized on 10/2009 Google Earth image.

http://dx.doi.org/10.5772/intechopen.77616

After all of the 11 historical Google Earth images were visually inspected and associated KML polygon digitized, a database of polygons showing potential aquatic plants in the study area, by image year, was created. These KML polygons were then converted to ArcGIS shapefile format for some clean-up work, and then converted to ArcGIS grids or raster format for further process. With grids or raster format, all of these spectral anomalies from all of these image years were then analyzed and overlaid through image algebra. The final result is a map or grid showing the frequency of visible spectral anomaly (referred to as frequency of sighting map) in the study area. **Figure 8** shows a portion of the frequency of sighting map, focusing on site 2. The frequency is color-coded, as shown in **Figure 8**. Different colors indicate different frequencies through the surveyed image years. For example, a frequency of 7 indicates that in the surveyed 12 image years, a spectral anomaly (potential aquatic plants) showed up in this particular area 7 times. In such a case, it is a high occurrence rate. Areas of higher frequency indicate more occurrences or sightings in the past. With more occurrences in the past, it is believed that it will lead to higher likelihood of occurrence in the future.

4.4. Discussions

The end results of this study are a frequency of sighting map of aquatic plants in the Racine Pool of the Ohio River. The frequency is obtained from surveying historical Google Earth images. Some of the consecutive Google Earth images are years apart from each other. In a dynamic environment, such long time interval is not ideal. A further study can acquire historical satellite images with reliable temporal resolution to obtain a higher quality of frequency of sighting map.

This frequency of sighting map can serve as a suggestive guide for field work. As budget difficulties rise, performing regular field work may become challenging. A suggestive guide may save time and money on field work. More resources may be directed to areas of higher

Figure 8. A portion of the frequency of sighting map showing site 2.

frequency, as they have higher potential of showing aquatic plants and therefore bigger threats to the river ecosystem.

Remote sensing had proven successful on developing a warning system for aquatic plants in the Racine Pool of the Ohio River. Though a warning system is in place, it is still critical to continuously monitor the environment and update the warning system. A future study with secured funding can schedule satellite images with reasonable temporal resolution to continuously monitor aquatic plants.

5. Conclusion

River is a dynamic ecosystem, with its appearance changing depending on then-current local environments. A snapshot of such dynamic environment can only truly represent a moment of truth when the snapshot was taken. Previous attempts trying to identify aquatic plants with remote sensing had results in unsatisfying results. Based on lessons learned from previous attempts, this study utilized historical Google Earth images from 2003 to 2015 to identify aquatic plants. Once aquatic plants were identified, they were digitized and overlaid to form a frequency of sighting map. This frequency of sighting map, which indicates the frequency of confirmed aquatic plants in the past 12 years, can serve as a suggestive guide for future field work should budget difficulties restrict or limit resources for field work. In some degrees, it serves the same function as a predictive model.

Acknowledgements

The research team would like to thank Northwest Missouri State University for providing financial support to this project through an undergraduate research funds (UGR) to Mr. Billy Crawford, who visually inspected Google Earth digitized KML polygons. The research team would also like to thank U.S. Fish and Wildlife Service to start this project with initial funding.

Author details

Yi-Hwa Wu[1], Ming-Chih Hung[1]*, Jeff Thomas[2,3] and Maureen Gallagher[4]

*Address all correspondence to: mhung@nwmissouri.edu

1 Northwest Missouri State University, United States

2 Ohio River Valley Water Sanitation Commission, United States

3 Electric Power Research Institute, United States

4 U.S. Fish and Wildlife Service, United States

References

[1] Ohio Environmental Council. Invasive Species. 2013. Available online from: http://www.theoec.org/campaign/invasive-species [Accessed: September 26, 2013]

[2] Appalachian Ohio Weed Control partnership. Help stop hydrilla from invading Ohio's inland bodies of water. 2013. Available online from: http://appalachianohioweeds.org/2013/06/03/help-stop-hydrilla-from-invading-ohios-inland-bodies-of-water [Accessed: September 26, 2013]

[3] Higgins Lake Property Owners Association. Eurasian Watermilfoil. 2013. Available online from: http://hlpoa.org/lakeinfo/watermilfoil [Accessed: September 26, 2013]

[4] US Environmental Protection Agency. Invasive Species. 2011. Available online from: http://www.epa.gov/glnpo/invasive [Accessed: September 26, 2013]

[5] Ohio River Valley Water Sanitation Commission. 2013, About Us, Available online from: http://www.orsanco.org/about [Accessed: September 26, 2013]

[6] Shalaby A, Tateishi R. Remote sensing and GIS for mapping and monitoring land cover and land-use changes in the Northwestern coastal zone of Egypt. Applied Geography. 2007;**27**(1):28-41

[7] Dewan AM, Yamaguchi Y. Using remote sensing and GIS to detect and monitor land use and land cover change in Dhaka Metropolitan of Bangladesh during 1960–2005. Environmental Monitoring and Assessment. 2009;**150**(1-4):237

[8] Geri F, Amici V, Rocchini D. Human activity impact on the heterogeneity of a Mediterranean landscape. Applied Geography. 2010;**30**(3):370-379

[9] Jensen JR. Introductory Digital Image Processing: A Remote Sensing Perspective. 3rd ed. Englewood Cliffs, NJ: Prentice-Hall, Inc.; 2005

[10] Jensen JR. Remote Sensing of the Environment: An Earth Resource Perspective. 2nd ed. Englewood Cliffs, NJ: Prentice-Hall, Inc.; 2007

[11] National Space Organization. Formosat-2. 2007. Available online from: http://www.nspo.narl.org.tw/2011/tw/F2_image/property.html [Accessed: September 26, 2013]

[12] Apollo Mapping. Formosat-2. 2017. Available online from: https://apollomapping.com/imagery/medium-resolution-satellite-imagery/formosat-2, [Accessed: December 8, 2017]

[13] Coleman JM. Dynamic changes and processes in the Mississippi River delta. Geological Society of America Bulletin. 1988;**100**(7):999-1015

[14] Friedman GM. Dynamic processes and statistical parameters compared for size frequency distribution of beach and river sands. Journal of Sedimentary Petrology. 1967;**37**(2):327-354

[15] Tockner K, Pennetzdorfer D, Reiner N, Schiemer F, Ward JV. Hydrological connectivity, and the exchange of organic matter and nutrients in a dynamic river–floodplain system (Danube, Austria). Freshwater Biology. 1999;**41**(3):521-535

[16] Zolghadri A, Monsion M, Henry D, Marchionini C, Petrique O. Development of an operational model-based warning system for tropospheric ozone concentrations in Bordeaux, France. Environmental Modelling & Software. 2004;**19**(4):369-382

[17] Gong LH, Han H. Research on meteorological early-warning system of geologic disaster in Dandong area. Journal of Meteorology and Environment. 2007;**1**:2

[18] Allen RM, Kanamori H. The potential for earthquake early warning in southern California. Science. 2003;**300**(5620):786-789

[19] Wu YM, Kanamori H. Experiment on an onsite early warning method for the Taiwan early warning system. Bulletin of the Seismological Society of America. 2005;**95**(1):347-353

[20] DeMers MN. GIS Modeling in Raster. New York, NY: Wiley; 2002

[21] Longley PA, Goodchild MF, Maguire DJ, Rhind DW. Geographic Information Systems and Science. New York, NY: John Wiley & Sons; 2005

[22] Lauver CL, Busby WH, Whistler JL. Testing a GIS model of habitat suitability for a declining grassland bird. Environmental Management. 2002;**30**(1):88-97

[23] McDermid GJ, Franklin SE, LeDrew EF. Remote sensing for large-area habitat mapping. Progress in Physical Geography. 2005;**29**(4):449-474

[24] Chen X, Tian S, Chen Y, Liu B. A modeling approach to identify optimal habitat and suitable fishing grounds for neon flying squid (Ommastrephes bartramii) in the Northwest Pacific Ocean. Fishery Bulletin. 2010;**108**(1):1-15

[25] Brando VE, Dekker AG. Satellite hyperspectral remote sensing for estimating estuarine and coastal water quality. IEEE Transactions on Geoscience and Remote Sensing. 2003; **41**(6):1378-1387

[26] Melgani F, Bruzzone L. Classification of hyperspectral remote sensing images with support vector machines. IEEE Transactions on Geoscience and Remote Sensing. 2004;**42**(8): 1778-1790

[27] Fauvel M, Tarabalka Y, Benediktsson JA, Chanussot J, Tilton JC. Advances in spectral-spatial classification of hyperspectral images. Proceedings of the IEEE. 2013;**101**(3):652-675

[28] Bruzzone L, Carlin L. A multilevel context-based system for classification of very high spatial resolution images. IEEE Transactions on Geoscience and Remote Sensing. 2006; **44**(9):2587-2600

[29] Laliberte AS, Rango A. Texture and scale in object-based analysis of subdecimeter resolution unmanned aerial vehicle (UAV) imagery. IEEE Transactions on Geoscience and Remote Sensing. 2009;**47**(3):761-770

[30] Yu Q, Gong P, Clinton N, Biging G, Kelly M, Schirokauer D. Object-based detailed vegetation classification with airborne high spatial resolution remote sensing imagery. Photogrammetric Engineering & Remote Sensing. 2006;**72**(7):799-811

[31] Hung M-C, Wu Y-H. Mapping and visualizing the Great Salt Lake landscape dynamics using multi-temporal satellite images, 1972-1996. International Journal of Remote Sensing. 2005;**26**(9):1815-1834

[32] Teillet PM, Staenz K, William DJ. Effects of spectral, spatial, and radiometric characteristics on remote sensing vegetation indices of forested regions. Remote Sensing of Environment. 1997;**61**(1):139-149

[33] Lee KS, Cohen WB, Kennedy RE, Maiersperger TK, Gower ST. Hyperspectral versus multispectral data for estimating leaf area index in four different biomes. Remote Sensing of Environment. 2004;**91**(3):508-520

[34] Mellen M. Google Earth A to Z: Keyhole and KML. 2012. Available online from: https://www.gearthblog.com/blog/archives/2012/07/google_earth_a_to_z_keyhole_and_kml.html [Accessed: December 14, 2017]

Chapter 7

Remote Sensing to Detect and Monitor Trees in Various Environments: Case Studies in Chile

Guido Staub

Additional information is available at the end of the chapter

http://dx.doi.org/10.5772/intechopen.72903

Abstract

Today, the presence of green areas in cities plays an important role for the well-being of its inhabitants and its sustainable development. Modern cities need green spaces for environmental, psychological, esthetic, economic, and social reasons. In this meaning, Chilean cities, although Chile is still considered by the United Nations[1] as a developing economy, are no exception. Given the importance of this common good, it is necessary to optimize its permanent care. An incident factor in the deterioration of vegetation in urban and rural areas is stress, which can be of biotic or abiotic origin. One way to systematize care of trees is by the application of multispectral sensors and modern digital image processing. Once plantations or trees are spectrally characterized, one can proceed to develop plant health mitigation programs. This article shows the potential of remote sensing for tree stress detection, in the central south of Chile. Focus is given on rural areas as forestry for the Chilean economy is of great importance. These approaches can easily be adapted to urban scenarios.

Keywords: trees, stress, remote sensing, image processing, rural, Chile

1. Introduction

Public open green spaces, urban and national parks, playgrounds, plazas, and even trees, grass, and shrubs on sidewalks or elsewhere, are important elements meant for recreation or to enhance the esthetic appeal of a neighborhood. So does vegetation planted or loosely installed on rooftops. A couple of particular benefits can be identified in this context. Not only green infrastructure helps to mitigate the urban heat island effect by filtering air and reducing runoff but also contribute to a couple of economical and environmental benefits. A study of low-income

[1]http://www.un.org/en/development/desa/policy/wesp/wesp_current/2014wesp_country_classification.pdf

Philadelphia neighborhoods published in [1] shows that newly planted trees boosted sale prices of nearby houses by 2%. Parks and green spaces, accessible by public, which include protected natural lands, ecological reserves, wetlands, and other green areas are critical to provide healthy habitats for humans, wildlife, and plants. The preservation of regional ecosystems is crucial for natural landscapes in a time cities tend to grow faster and faster.

Furthermore, some important health benefits such as better perceived general health, reduced stress levels, reduced depression, associated with access to public open space and parks, such as the Central Park in New York, USA (**Figure 1**), have been discovered. The World Health Organization (WHO) stated out that major public health risk is caused by physical inactivity during a prolonged period of time. In general, citizens or visitors of public green spaces prefer spaces that are highly attractive (e.g. due to high level of diversity), widely open, and in their nearby vicinity, see [2].

To grant access to green spaces and parks, for example, trail networks can be generated to link cities with parks or individual parks between each other. City parks can be made accessible through bikeways or even old rail tracks that can be transformed into greenways.

On the one hand and according to [3], in Chile, there are about 1.5 million hectares of plantations of *Pinus radiata* D. Don whose main use is commercial. Especially, the Chilean central south is considered as the most important region for the commercial forestry sector nationwide as climate conditions favor tree growth. The national forest institute INFOR indicates that only between the region Maule and Aysén, there are approximately 1.4 million hectares of *P. radiata*, both ponderosa as radiata, equivalent to 95% of the *P. radiata* trees planted across the country.

On the other hand, Chilean national parks and nature reserves play a fundamental role. In Chile, there are 36 national parks, 49 nature reserves, and 16 nature monuments. Fifty-eight (over 50%) of them are located in the central south. Flora and fauna are protected by law and its sustainable conservation is of public interest.

Figure 1. Urban public green space Central Park, New York, United States of America (https://de.wikipedia.org/wiki/Central_Park#/media/File:New_York_City-Manhattan-Central_Park_(gentry).Jpg).

In Chile, current pest and damage monitoring is mainly realized outdoors by specially trained personnel in order to detect symptoms and damages. The method used is based on polls or surveys that involve the visual inspection of trees in areas under threat and already affected areas, as described in [4]. It is necessary to have a tool or develop a methodology, that allows the detection of any disease in time and to take appropriate measures.

Our natural environment is changing constantly. It may be that these changes are natural (season of year, climate and weather, etc.), caused by human beings (construction, agriculture, etc.), or a combination of both. Today more than ever exists the necessity to understand natural processes and manage carefully the human activities. However, to carry out and establish a complex monitoring and analysis system of nature-human interaction, geospatial information is required. This information is generated based on observations that have been transformed into data, which finally is processed, thus achieving to extract what is particularly required, as for example, the physical state of nature. The observations can be acquired in different ways either through direct measurements, where the instrument must be in the same place where the object is located, or through remote measurements, the instrument is located at a considerable distance from the object and does not have physical contact with it.

According to [5], stress in nature can be defined as an external factor coming from any source that has a negative influence on a plant. It differs between biotic factors by the intervention of other living beings and abiotic, which are of a physical and/or chemical nature. The extent to which stress affects a plant is determined through measuring the survival of the plant, the crop yield, growth, or primary assimilation processes.

Detecting stress in plants is not a straightforward task. While on-site inspection by experienced professionals in the area can identify high-damaged trees or plants very accurately, the time required for inspecting larger areas is the most limiting factor for such a task. Through methods such as remote sensing, it is possible to study large surfaces in a much shorter time and with a high degree of reliability. Particularly, it is necessary to study certain plant characteristics such as visible symptoms of damage in the cup of trees and branches structure or properties associated with the reflection of electromagnetic energy coming from solar lighting.

2. Remote sensing

Remote sensing as defined by [6–8] and others, which includes a huge variety of procedures that allows to derive information about our environment, is based on the observation realized by a sensor located at a large distance (without having physical contact with the objects) of the reflected and/or emitted electromagnetic radiation. So, the goal is to capture the degree of interaction between electromagnetic energy and the objects with which it comes into contact. This way, it is possible to determine the degree of reflection and absorption of electromagnetic energy by any kind of object, whether it is natural or artificial.

One has to distinguish between two types of observing systems: active and passive sensor systems (**Figure 2**). The main difference between these systems is the source of the electromagnetic radiation emitted, which finally enters in contact with the objects.

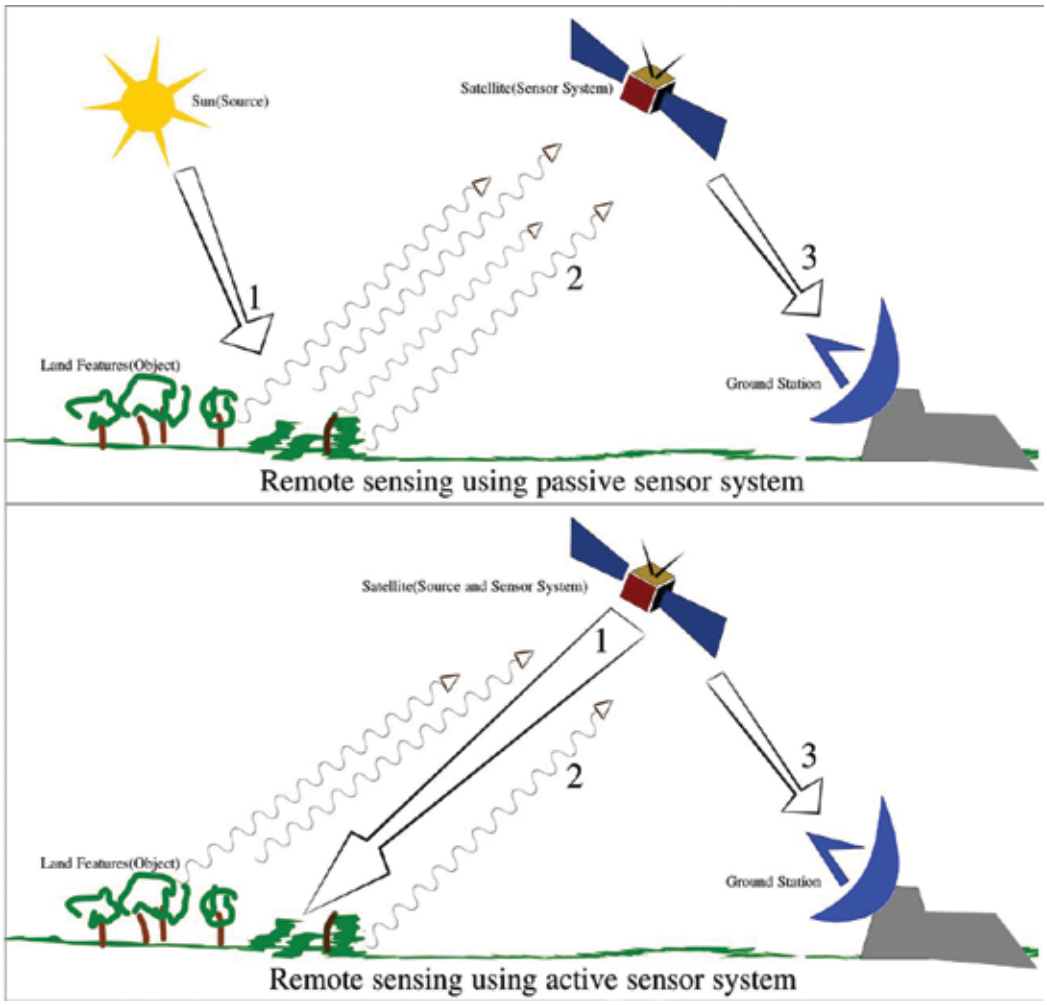

Figure 2. Principle of active and passive remote sensing sensors (adapted from https://en.wikipedia.org/wiki/Remote_sensing#/media/File:Remote_Sensing_Illustration.jpg).

The electromagnetic spectrum is formed by the energy distribution of the radiant energy according to its wave length λ and extends from gamma rays (shorter wavelength) until radio frequency (longer wavelength). However, remote sensing systems tend to make use of specific intervals within the electromagnetic spectrum, basically the visible, infrared, and microwave spectra **Figure 3**. This relies on the fact that within these spectra, atmospheric windows can be observed in which the transmission of the electromagnetic radiation is not altered by absorption and distortion.

The most relevant in the field of remote sensing are:

- Visible spectrum (λ = 0.38–0.78 μm).
- Near infrared (λ = 0.78–3.0 μm).

http://dx.doi.org/10.5772/intechopen.72903

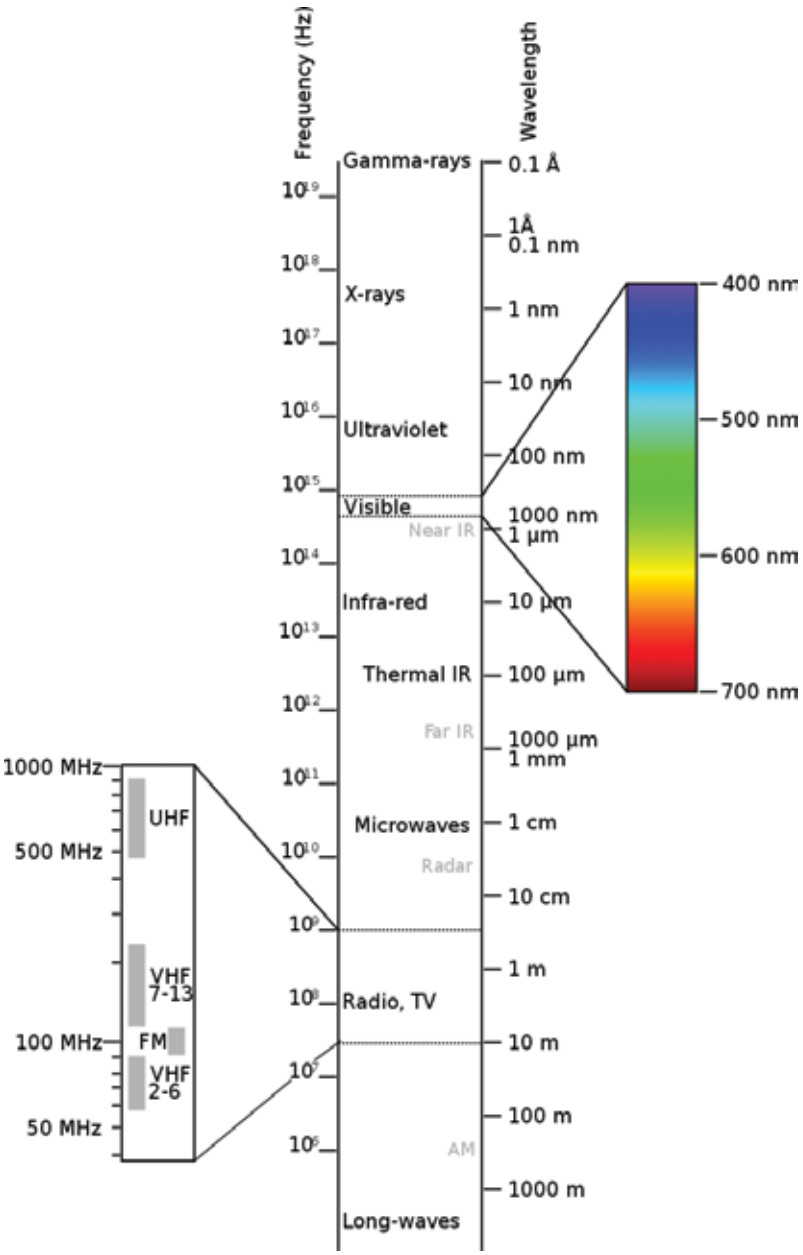

Figure 3. Electromagnetic spectrum (adapted from: https://en.wikipedia.org/wiki/Electromagnetic_spectrum#/media/File:Electromagnetic-Spectrum.svg).

- Short-wave infrared (λ = 3.0–50 μm).
- Thermal infrared (λ = 50–1 mm).
- Microwaves (λ = 1 mm–1 m).

2.1. Vegetation study based on remote sensing techniques

One of the most outstanding features of the majority of all remote sensing sensors is that they allow carrying out scientific studies on vegetation due to observations made not only in the visible but also in the infrared spectrum. This is where the magnitude of reflection is highly correlated with the amount of biomass, which is intact in the plants. In simple words, this phenomenon can be explained as the greater the degree of energy absorption in the near infrared, the lower the amount of active biomass and vice versa. More healthy vegetation shows less reflection in the visible spectrum.

The spectral plant characteristics relate to the photosynthetic activity of the pigments and the water stored in the leaves. The low degree of reflection in the visible spectrum is due to the absorbing effect of leaf pigments, mainly chlorophyll b, phycoerythrin, and phycocyanin, see **Figure 4**. However, there is a specific range in the spectrum in which absorption of electromagnetic energy is almost zero. Around 525 nm, which is located at the green band, the leaves have a high degree of reflection, which causes the human eyes to see the vegetation in this color.

Having knowledge of this theoretical background, it is possible to realize scientific studies on vegetation and their health. For example, through the normalized difference vegetation index (NDVI), it is possible to calculate the degree of active biomass in vegetation, considering the intensity of the reflection and emission of radiation in certain bands of the electromagnetic spectrum. This can be correlated to health and growth of a plant. The NDVI is calculated as follow:

$$NDVI = (NIR - R)/(NIR + R)$$

where NIR is the near infrared and R is the red band of a specific sensor.

An example is shown in **Figure 3**, which shows the result of calculating the NDVI for the Biobío region during second half of December 2014. Possible values for the NDVI range between −1.0 and +1.0. In this context, it was standardized so that a zero value indicates the absence of vegetation while values higher than 0.5 indicate little or sick vegetation. Values superior to 0.7 represent areas where vegetation is vigorous and healthy.

2.2. Systems for tree stress detection based on imagery

In countries like the USA, Canada, Australia, Germany, and Brazil described in [9–13], various techniques for forest monitoring were successfully implemented in the past. The possibility to derive the health of forest plantation through observations acquired by remote sensors has been demonstrated repeatedly, as in [14]. There are also examples of the proof of both the use of aerial photographs and satellite images. In Australia, aerial photographs were used for the detection of forest decline in native eucalyptus trees. Some of the most important aspects described by [15] considered during the planning and implementation of monitoring were that photographs should be acquired during a cloudy day to ensure a better view of the undergrowth and to avoid very likely pronounced reflectance, which could jeopardize the interpretation of the data. In addition, it requires a monitoring system available anytime that takes advantage of weather conditions, favorable for imaging. In China, since 1992, a

http://dx.doi.org/10.5772/intechopen.72903

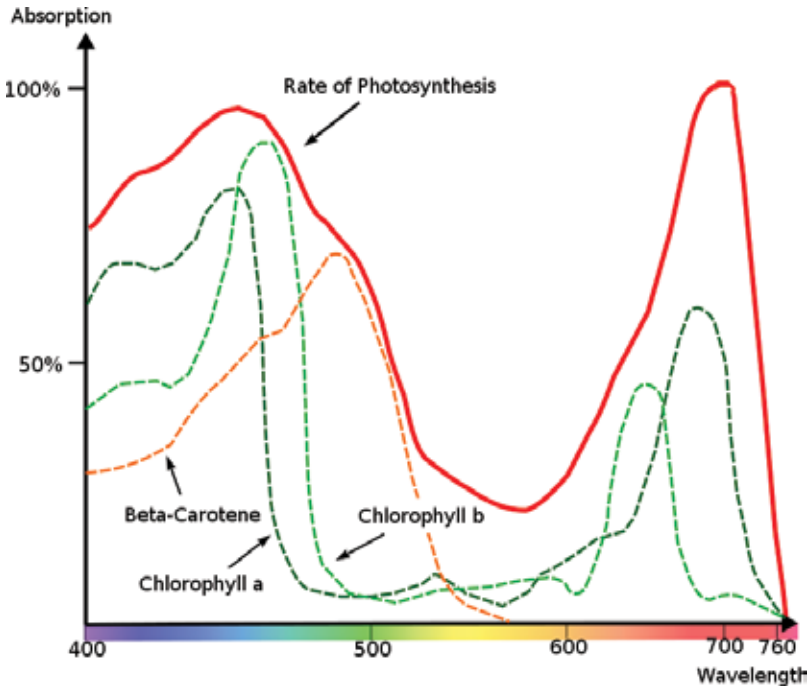

Figure 4. Leaves absorbing light at different wavelengths (adapted from https://de.wikipedia.org/wiki/Photosynthese#/media/File:Engelmannscher_Bakterienversuch.svg).

project funded by United Nations Development Program (UNDP) has been developed with the objective to establish a monitoring system consisting of an airborne video camera for sketchmapping, color infrared (CIR) digital camera, and a geographic information system, according to [14]. In Germany, and according to [12], it established a permanent monitoring program with archived observations since 1983 through satellite imagery (Landsat TM), CIR aerial images, and an airborne multispectral scanner. The image scale that was used in most cases was between 1:5000 and 1:6000, according to [16]. However, the tree classification and ground truthing was carried out in-situ.

For urban areas, it is possible to think of similar systems and solutions. Remote sensing systems, which in the past have already been successfully used in monitoring and detection of rural forest damage, can be adopted to monitor vegetation, and in particular trees, in cities although there is no coverage of large areas with a single species. For ornamental species, a higher ground sampling distance (GSD) needs to be considered beside a hyperspectral system. Therefore, a satellite-based approach should not be chosen, but rather opt for a different platform such as a drone equipped with an appropriate hyperspectral sensor. This way, it will be possible to study and detect individual trees and take appropriate measures that already have been checked and approved by the governmental authorities such as the Chilean Agricultural and Livestock Service Servicio Agricultura y Ganadero (SAG). Ref. [17] presented a review of latest advances made in recent years in both the technological part and with respect to the processing of hyperspectral observations in the field of urban forests. Typical applications

include mapping of surfaces covered with trees, transport network planning, studying urban heat islands, and measurement of vegetation stress, etc. However, since [18] published the need for continuous monitoring of the urban forest, few solutions were proposed. For example, [19] discuss different geospatial solutions and techniques, including GIS, remote sensing, and global positioning system (GPS). The combination of these tools allows collection of reliable forest information at different scales. [20] presented an approach based on hyperspectral imagery to classify urban tree species. In order to improve the reliability of the classification results, it is also proposed to use various techniques such as principal component analysis, indexes, and statistics. This way they managed to identify 91.4% of the species present in a sample consisting of a total of 500 urban trees. To date, there are very few operational systems. One of the most advanced systems is the one proposed by [21]. This work not only presents a discussion with respect to the platform but also with respect to the sensor. The conclusion indicates that the ideal system to detect and monitor stress in plants consists of a combination of an unmanned aerial platform, a hyperspectral sensor, and a couple of simulation tools.

The following five case studies, all related to tree stress, show the actual situation in the Chilean central south, see **Figure 5**. Stress caused by climate, insects, weeds, and even volcanic eruptions often affect trees in the Chilean central south. Satellite images help to detect them at almost real time and by the calculation of geospatial statistics and indices, which furthermore make it possible to quantify tree health.

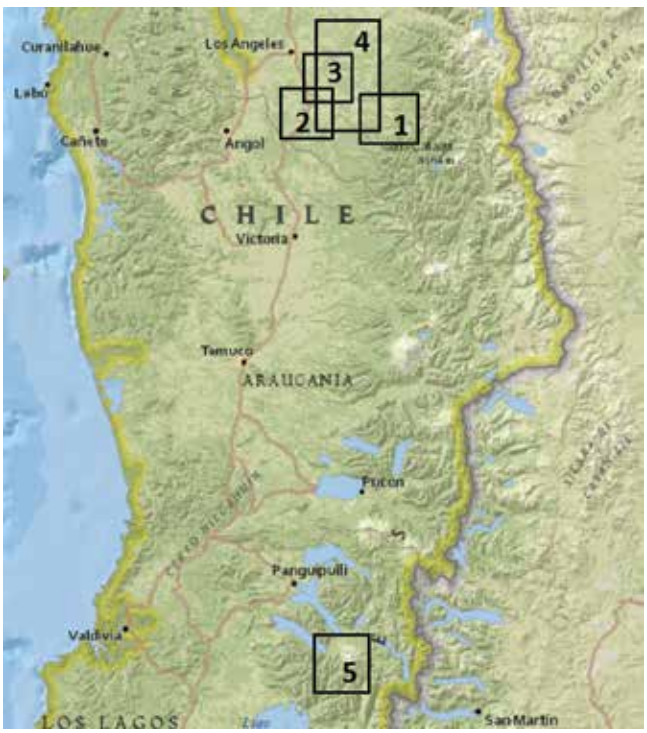

Figure 5. Case study locations in the central south of Chile (adapted from: http://www.geoportal.cl/Visor/).

http://dx.doi.org/10.5772/intechopen.72903

3. Pine plantations affected by Sirex woodwasp

3.1. Background

During the last decades *Sirex noctilio* Fabricius, 1773, a Hymenoptera of the Siricidae family, which is composed of more than 40 species of wasps, has produced extensive damage worldwide in forest plantations of *Pinus radiata* D. Don and its different subfamilies. This damage can lead to death of the infected tree, in almost 80% of the cases observed worldwide. Although, its origin is in Europe, Siberia, and Mongolia, due to exportation of wood, dispersion of the wood wasp was uncontrollable and today it is present in Australia, New Zealand, South Africa, and South America. In Chile, it is present since 2001. Several municipalities in the Maule, Biobío, La Araucanía, Los Ríos, Los Lagos, and Aysen region are under quarantine and the Agriculture and Livestock Service is forced permanently to establish new quarantine areas. Furthermore, in the Biobío and Maule region, the Agriculture and Livestock Service has established phytosanitary measures to get control over the plague. First, a biological control program against *S. Noctilio* was established. A complex of specific natural enemies is created in laboratory and released in the affected plantations. The second action consists in the control of wood transport from quarantined areas to other areas that might be endangered.

The main objective of this case study was to identify a suitable and reproducible methodology to timely detect *S. Noctilio* infections. Such a methodology can be very helpful when it comes to monitor large pine plantations, which are difficult to access.

3.2. Methodology

The study area is located in the commune of Quilaco, Biobío region (**Figure 6**) and comprises approximately 1800 km^2, and almost 70% is currently affected by *S. noctilio*. Therefore, it has been declared that quarantine area with a radius of 20 km for locations might be affected by *S. noctilio*.

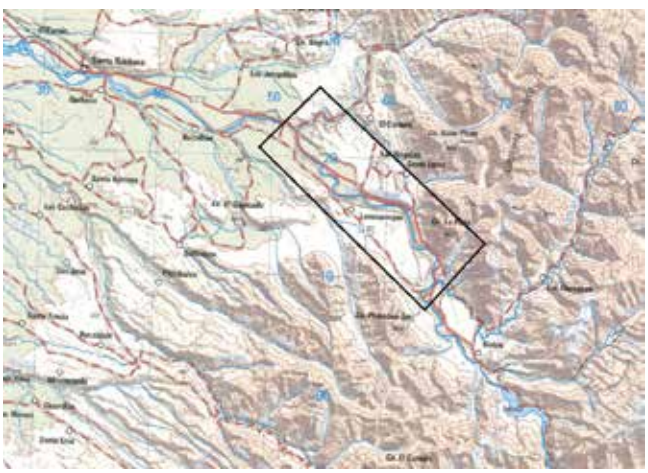

Figure 6. Study area where *S. Noctilio* has been detected (adapted from: http://www.geoportal.cl/Visor/).

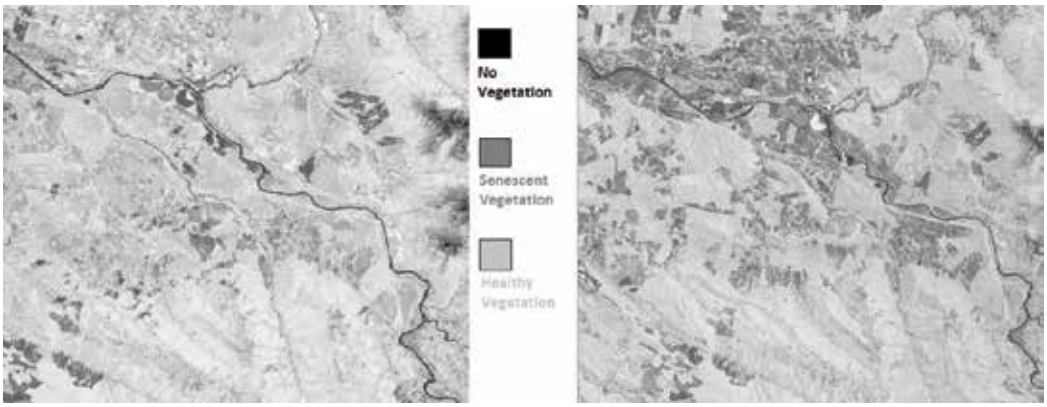

Figure 7. NDVI comparison 2010–2011.

Advanced Spaceborne Thermal Emission and Reflection Radiometer (ASTER) satellite images taken on November 2010 and February 2011 were used in this study. NDVI calculations were carried out to detect variations in time in photosynthetic activities of pine trees.

3.3. Results and conclusions

The results indicate that in the study area, certain sectors show a significant decline in photosynthetic activity during summer period of 2010 and 2011, a fact that was verified by both, calculating the NDVI, see **Figure 7**, and information provided by the Agricultural and Livestock Service. Based on an initial study of one of these specific sectors, identified by the Agriculture and Livestock Service in 2011 as a new outbreak of *S. noctilio*, it was possible to conclude that the photosynthetic activity decreased in the study area during a period of time of 4 months (November 2010–February 2011). In a second sector, photosynthetic activity also decreased during the same period, but it was not possible to clearly determine its cause because the Agricultural and Livestock Service had not declared this sector infested by *S. noctilio*. Nevertheless, it is important to highlight that an attack by *S. noctilio* was likely for two reasons. First, the index of normalized difference vegetation was 0.624 in 2011, which in comparison to the other sector is only 9% higher. And second, in the nearby area (within the range of natural displacement capability of *S. noctilio*), two outbreaks of *S. noctilio* already had been registered.

So, due to the rapid development of the forest pest, it was possible to detect changes in photosynthetic activity of the vegetation as well as areas of new infections.

4. Weed detection in eucalyptus plantations

4.1. Background

Early weed control for forest plantations is a recurrent, fundamental, and critical activity that has to be carried out by any forestry company. It must be conducted applying serious strategies, correct treatment times, and reasonable application of herbicide. This control must be

variable and flexible in time and magnitude, as on the one hand weed emerges in spring and summer months due to soil moisture left by the winter and on the other hand, weed growth augments with higher temperatures and daylight hours. Therefore, and due to the fact that in Chile approximately 500,000 ha are forest plantations, it is of great importance to count with a control system to manage lots of very complex geospatial information.

4.2. Methodology

In order to particularize the problem and transform it into local scale, Forestal Mininco S.A., a Chilean company dedicated to timber production, plants and seeds, is constantly working on automation processes and efficient management of huge volume of geoinformation generated during weed control activities. It is expected that financial and human resources can be optimized, by assigning certain levels of priority to plantations with high potentials to be damaged by weed during spring and summer period.

The main objective of this case study is to quantify the area affected by weed within the forest plantation denominated Fundo Porvenir, located between Mulchén and Collipulli in the Biobío region, see **Figure 8**. Almost 400 ha of different species of eucalyptus, such as *E. globulus* Labill., *E. nitens* H. Deane & Maiden, and *E. saligna* SM. can be found in the study area.

SPOT-6 high resolution satellite images, see **Figure 9**, were acquired because of their ground sampling distance and capacity to make observations in the infrared band of the electromagnetic spectrum. These two properties allow detecting small vegetation species, such as weed.

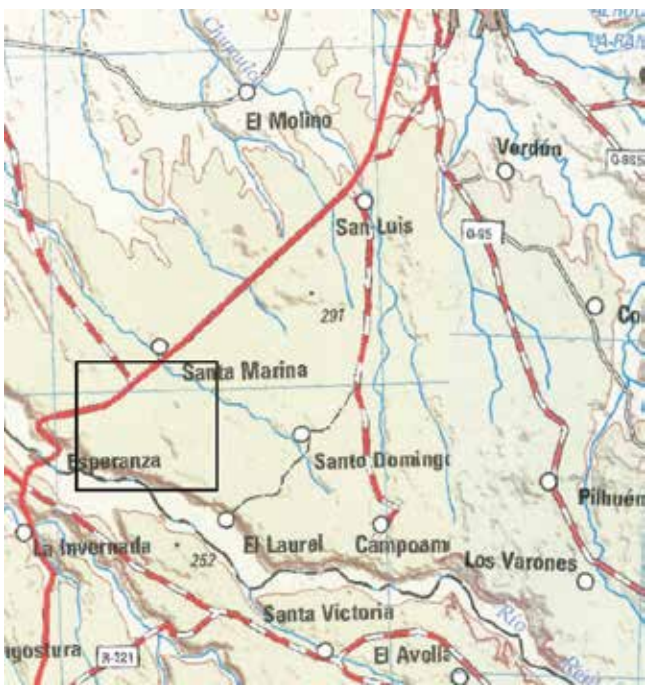

Figure 8. Study area with eucalyptus plantations (adapted from: http://www.geoportal.cl/Visor/).

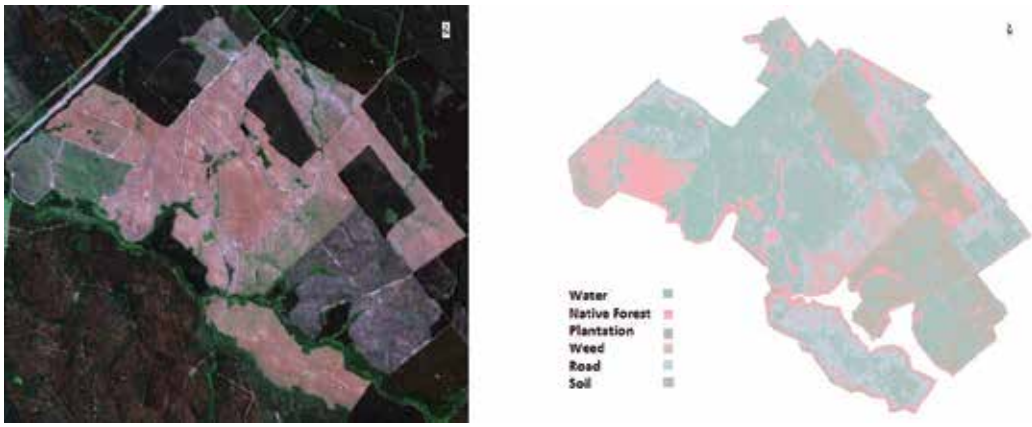

Figure 9. SPOT 6 image and result of supervised classification.

The most convenient date to select the image acquisition is closely coupled with the type of phenomenon that has to be studied according to [22]. So, image acquisition was during the last days of October.

First of all, a visible inspection of both, satellite image and terrain, for training site definition and subsequent ground truthing of the classification results, **Figure 9**, was carried out. Supervised classification was statistically analyzed using confusion matrix and Cohen's Kappa statistic.

4.3. Results and conclusions

Figure 9 shows the original SPOT 6 satellite image and the result of the supervised classification.

Table 1 summarizes information gathered regarding surface, species, area occupied by weeds, and the respective occupancy rate in the specific sectors (S1–S6), see **Figure 10**. Based on these percentages, control priority levels were established.

Name (Tree species)	Total [Ha]	Undergrowth [Ha]	Occupation %	Priority
S1 (*Eucalyptus nitens*)	46.2	28.7	62.1	1
S2 (*Eucalyptus nitens*)	35.9	18.6	51.8	2
S3 (*Eucalyptus nitens*)	48.3	15.7	32.5	3
S4 (*Eucalyptus nitens*)	66.2	19.3	29.2	4
S5 (*Eucalyptus globulos*)	193.7	26.4	13.6	5
S6 (Eucalyptus Smith)	24.3	2.1	8.6	6
Countryside Porvenir	414.6	110.8	26.7	

Table 1. Undergrowth in forest plantation.

http://dx.doi.org/10.5772/intechopen.72903

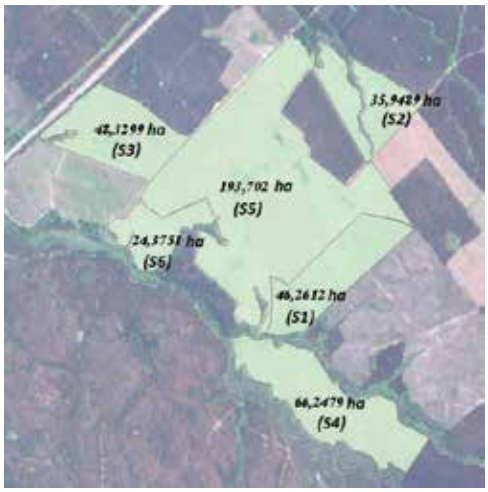

Figure 10. Specific sectors S1–S6.

Quality assessment based on field work, to compare classification results and vegetation found in the study area, provides the confusion matrix of the supervised classification. The result indicates that with 95% probability, the overall accuracy is 82%. The reliability to classify weed is about 90%. The results are shown in **Table 2**.

The Kappa statistic indicates that the classification is 76% better than expected to do so randomly. Field verification for 100% coverage was found.

As a direct conclusion, which can be drawn from the results, sector 1 (*Eucalyptus nitens* Sur 1) occupancy rate of 62% has to be treated first and with urgency. Sector 2 (*Eucalyptus nitens* Este)

	Water	**Native forest**	**Plantation**	**Weed**	**Road**	**Soil**	**Total**	**Consumer's accuracy (%)**
Water	20	0	0	0	0	5	25	80
Native forest	0	22	0	0	0	5	27	81
Plantation	0	0	35	0	0	1	36	97
Weed	0	0	2	37	0	0	39	94.9
Road	0	0	0	4	6	29	39	15.4
Soil	0	0	0	0	0	90	90	100
Total	20	22	37	41	6	130		
Producer's accuracy	100%	100%	94.6%	90.2%	100%	69.2%		
Overall accuracy: 82%								

Table 2. Confusion matrix of supervised classification.

with an occupancy rate of 52% also can be considered as critical. Occupation rate in all the other sectors is less alarming.

Nevertheless, it is recommendable to develop sustainable strategies, which allow weed control in order to guarantee tree growth and reduce tree death. As death of trees may imply considerable economic losses, it is even more important to count with relevant information. Satellite imagery and image processing can be used for trustworthy studies on weed growth and its extension.

5. Tree growth monitoring

5.1. Background

As mentioned by [23], in the Biobío region, forestry is one of the main economic activities. So, it has become necessary to perform serious analysis of growth in each plantation to have a record about its past and present development. In general, this task is poorly realized by a couple of experts employed by the forestry companies. Time and available financial resources are the two main limiting factors and therefore an alternative strategy, which allows reliable information generation that has to be envisaged in the near future.

5.2. Methodology

The area of interest corresponds to a part of the sector called Verdun of about 154.000 ha, owned by Forestal Mininco S.A., located south west of the city of Mulchén, see **Figure 11**. Plantations of *Eucalyptus globulus* Labill. and *Eucalyptus nitens* H. Deane & Maiden can be found there. The *E. nitens* plantation is under permanent treatment as an experiment for improvement of the species is carried out. It should also be noted that these types of plantations (Eucalyptus) around Mulchén have become the new landscape. For local residents, it is the main source of employment.

Red clay soil is dominant in the study area. Rainy weather during winter and dry during summer period are the main climate characteristics. Furthermore, the river Mulchén limits the area, what guarantees permanent water supply, and in consequence, better growth of the species. The study areas topography is almost plane with the exception of a small hill, which is located in the middle it.

The main objective of this case study was to demonstrate how remote sensing can help to carry out long-term studies on tree growth, in particular, using high resolution satellite imagery, which became more and more accessible during the last decade.

The images used for this study correspond to three aerial photographies with a spatial resolution of 30 cm (2009–2011), a SPOT 5 (2007), a QuickBird satellite image (2008) with spatial resolution of 5 m each, and an image taken from Google Earth, basically for visual image interpretation in 2007.

Beside the visual interpretation, a principal component analysis (PCA) and a RGB to HSV transformation were carried out.

http://dx.doi.org/10.5772/intechopen.72903

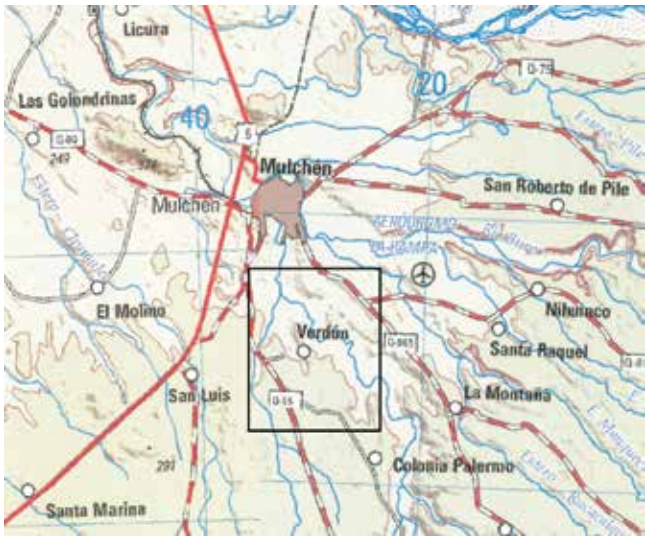

Figure 11. Tree growth monitoring study area (adapted from: http://www.geoportal.cl/Visor/).

5.3. Results and conclusions

With regard to the visual interpretation of the images, it was possible to clearly identify the transition phase between harvesting and reforesting. Horizontal growth of the vegetation cover and the newly planted eucalyptus species has augmented significantly.

The PCA method allows detecting vegetation cover that can be analyzed considering furthermore reflectance and in-situ gathered forest relevant information, such as the stand density. The resulting PCA components 1, 2, and 3 are shown in **Figure 12**. Tree growth can be observed in the first principal component as 98 and 65% of the information that can be found in the aerial photographies and the satellite image, respectively. The development of the eucalyptus plantations in the course of the years became detectable.

Figure 12. PCA components 1, 2, and 3 (left to right) for 2010 image of the study area.

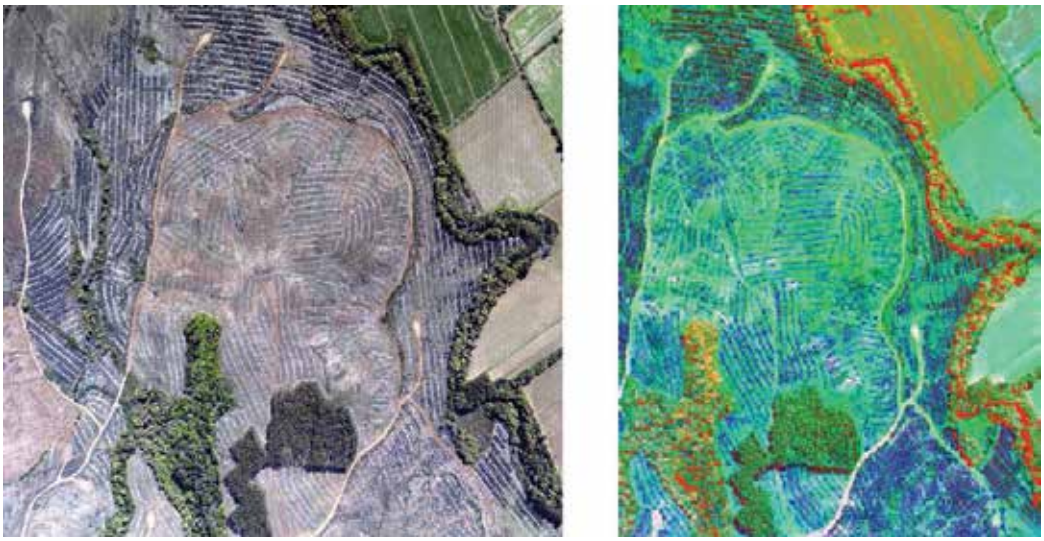

Figure 13. Original 2010 RGB image (left) and transformed IHS image (right).

In case of the RGB to IHS transformation, see **Figure 13**, mainly an estimation of tree growth through the comparison of soil covered by forest with soil covered by other type of vegetation was possible.

In particular, with this type of comparison, it was possible to highlight the importance of influencing factors such as water, soil, and temperature. They are fundamental characteristics for any plantation, which have to be studied. Nowadays, it is possible to make use of high resolution satellite imagery and determine surface characteristics in areas where tree plantations are planned.

6. Water stress detection and analysis in the Andean Precordillera

6.1. Background

The United Nations Organization (UNO) has recognized that desertification is a major problem of economic, social, and environmental concerns that affects many countries from all regions of the world. The United Nations Convention to Combat Desertification (UNCCD) defines desertification as: *land degradation in arid, semi-arid, and dry subhumid regions resulting from various factors, including climatic variations and human activities*. So, [24] indicate that desertification occurs as a result of long-term imbalance between manmade demand for ecosystem services and what ecosystems can provide. As a result of this degradation process, soil loses its fertility and in consequence, its production potential due to the destruction of vegetation cover and water shortages. Often, manmade interventions promote and enhance this process due to inappropriate and excessive activities such as cultivation, overgrazing, and deforestation.

In Chile, about two-thirds of the national territory is affected by soil degradation caused by desertification. The "Preliminary Map of desertification in Chile" prepared by the National

Forestry Corporation (CONAF) in 1999 and published in [25], is the only study of desertification in the country so far. The map, originally considered five principal indicators: erosion, poverty, xerophytism rate, length of the dry period, and a temporal trend indicator. It was concluded that of the 290 rural communes, 270 (93%) had some degree of desertification, of which 76 (27%) were severely affected and 108 (36%) were moderately affected by desertification.

In the central south of the Biobío region, the Biobío province limits the north with the Ñuble province, south to the Araucanía region, east to the Argentine border, and the west with the Arauco province. It is the only one of the four provinces within the Biobío region without coastline. Considering [26], it can be stated that the Biobío region has 353,315 inhabitants and covers an area of 16,226 km^2. According to the preliminary map, which was generated by CONAF in 1999 (the only study on desertification that covers the whole national territory), the Biobío province was classified as moderately affected by desertification.

The main objective of this case study is to quantify desertification process that took place during the last 15 years in the Andean Precordillera.

6.2. Methodology

Based on Landsat 5 and 7 satellite images, of the Andean Precordillera in the Biobio province, see **Figure 14**, preliminary identification of areas vulnerable to desertification were detected by moisture stress index (MSI) calculation. In general, MSI measures the water stress in plants and ranges from 0 to 3 (from excess to lack of water, as found in [27]). The satellite images were captured during March in 2000, 2005, 2010, and 2015. The results were statistically analyzed using the *Pearson* product–moment correlation coefficient, considering precipitation records of four climate observation stations within the study area.

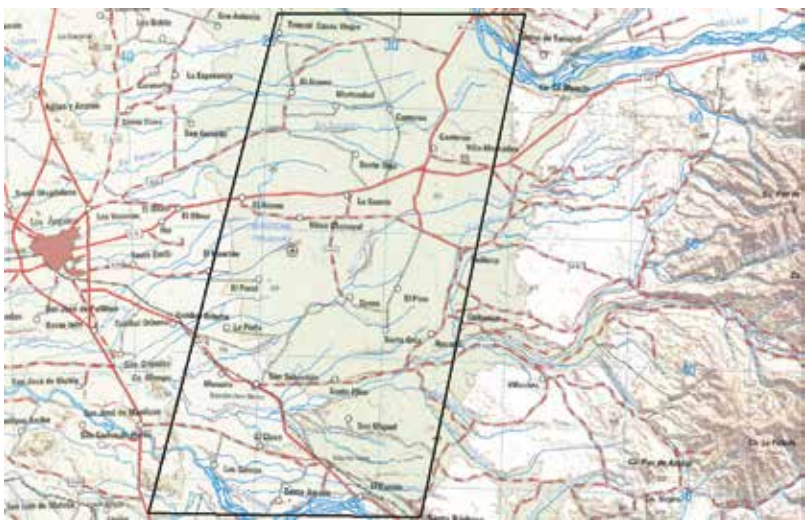

Figure 14. Andean Precordillera in the Biobío region (adapted from: http://www.geoportal.cl/Visor/).

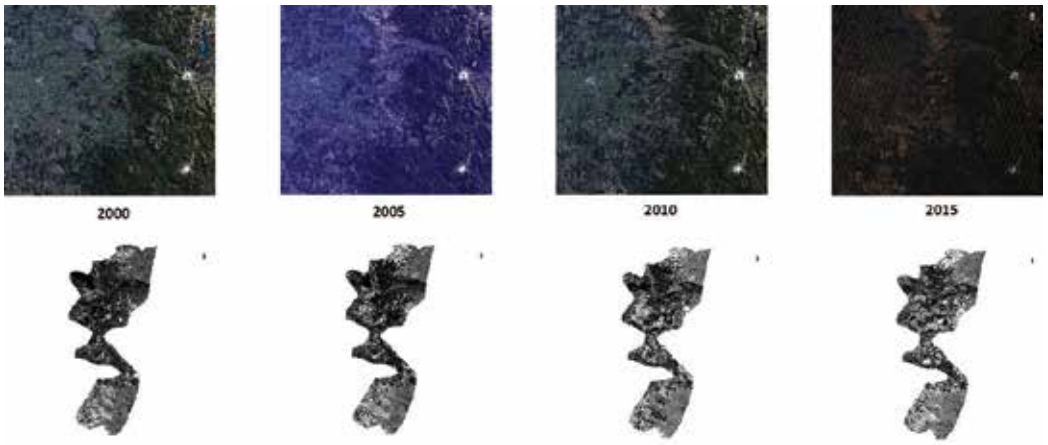

Figure 15. The original Landsat satellite images and the results of the MSI calculation are shown.

Year	Vulnerable surface (%)	Variation of vulnerable surface (compared to previous year) (%)	Precipitations (mm)
2000	28.50	-	1745.6
2005	36.02	7.52	1644.8
2010	49.36	13.34	1529.7
2015	16.19	−33.18	1792.3

Table 3. Vulnerable surface variation during the last 15 years.

6.3. Results and conclusions

In this particular study, areas vulnerable to desertification were identified where the MSI value did not reach a critical level (below 0.4 or above 2). The study reveals that these areas steadily increased every year except to 2015, due to an increase in rainfall during 2014, which temporally reduced the stress in the vegetation and in consequence led to a negative trend for possible desertification. The original satellite images and the results are shown in **Figure 15** and **Table 3**, respectively.

A negative correlation is observable between surface vulnerable to desertification and precipitation (−0.978). This means that a lack of precipitation leads to an augmentation of areas vulnerable to desertification processes.

At present, 16% of the Andean Precordillera of the Biobío province is vulnerable to desertification, a number that is significantly lower as in 1999 (28.5%). However, it is important to mention that this is something misleading because in the period from 2000 to 2010, a considerable increase of the area vulnerable to desertification can be detected. This means that in 2010, almost half of the Andean Precordillera was affected. The observed decrease in 2015 is due to the increased rainfall in 2014. The surface area vulnerable to desertification that is seen in 2015 decreased considerably in comparison to 2010, but still stays above 16% of the total study area surface.

It can be concluded that desertification is a long-term process, which has to be monitored. Short-term variations can be detected by the use of satellite imagery and image processing. Nevertheless, to identify trends in desertification, precipitation, and temperature records have to be considered within long-term studies.

7. Monitoring of vegetation recuperation after volcanic eruption event

7.1. Background

The emission of gas and ash during the eruption of the Volcanic Complex Puyehue–Cordón Caulle located 83 km northeast of the city of Osorno in the Los Lagos Region, **Figure 16**, in 2011 produced severe damage in the surrounding area of the volcano. For 10 days, an eruptive column with a height of approximately 9 km emerged and affected the Nahuel Huapi area with intense ash fall, at a distance of 100 km northeast of the crater. Furthermore, ash deposits affected flora and fauna in the southeast of the crater for a prolonged time period. Photosynthetic activity of vegetation decreased significantly as volcanic ash deposits affected old growth forest, which is predominant in the National Park Puyehue.

The objective of this case study was to monitor vegetation recovery after volcanic eruption. Of our particular interest, was the quantification of vegetation affected by ash deposits and to determine how and why it recovered.

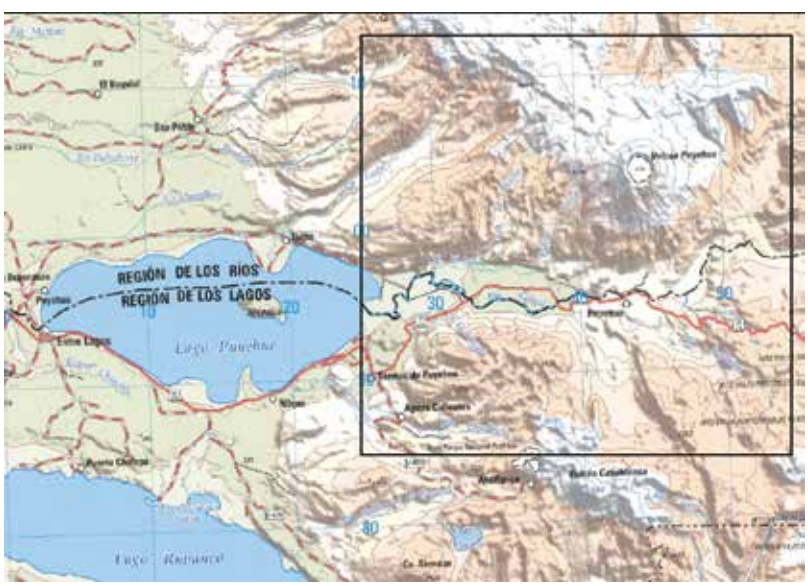

Figure 16. Volcanic complex Puyehue – Cordón Caulle and area affected by ash fall after 2011 eruption (adapted from: http://www.geoportal.cl/Visor/). And identification of three particular study sites.

7.2. Methodology

Satellite imagery and in-situ data collection are used to carry out a three-step methodology. At first, a visual image interpretation is carried out, based on a visual analysis of Landsat 7 ETM+ satellite imagery acquired in 2011 and 2012. Landsat 7 ETM+ typical band combinations for true and false color visualization (3, 2, 1, 4, 3, 2, 5, 4, 2), according to [28]. The natural color band combination (3, 2, 1), is considered to visualize the landscape as it appears in reality. With the help of band 3, it is possible to discriminate vegetation slopes, band 2 allows assessing vegetation vigor, and band 1 permits to distinguish soil from vegetation. False color combinations such as 4, 3, 2 and 5, 4, 2 are employed to highlight biomass content in plants (band 4) and moisture content in vegetation and soils (band 5).

Second, an analytical image analysis based on NDVI calculation is carried to determine vegetation health and photosynthetic activity potential.

The final step consists of ground truthing of the generated results. Therefore, between the months of January and February 2012, and during December 7 and 8 in 2012, field work was realized to obtain reliable first-hand information about, for example, the percentage of ash-covered/dead/sprouting vegetation within the area of interest.

Three specific sectors were identified inside the Puyehue National Park, where dominating forests are evergreen and different landforms can be observed. They were chosen because they were accessible for research and because reference data for comparison was facilitated by Corporación Nacional Forestal – National Forest Cooperation (CONAF). The first (1) corresponds to a small area near Aguas Calientes (southwest of the crater) in hilly country, the second (2) encompasses the border crossing complex Cardinal A. Samoré (south of the crater) in the Gol-Gol valley, and the third (3) includes an area near Route 215 next to the side of Laguna El Pato (southeast of the crater) in the high mountains of the Andes. All these sectors are of almost equal size and cover an area of approximately 43 ha. In 2011, experts of CONAF had already carried out intensive fieldwork and studies to detect vegetation affected by volcanic ash deposits.

7.3. Results and conclusions

Figure 17 shows the original Landsat 7 satellite images and the calculated NDVI values inside each study area (deliminated by a white rectangle).

A quantitative analysis of NDVI-related statistical measures (**Table 4**) indicates that in all three sectors, the potential of photosynthetic activity increased steadily. Nevertheless, only for sector 2 a significant change in vegetation recovery was detected. This is mainly due to wind-terrain interaction, as sector 2 is in a valley, strong winds that are typically there, helped to clean ash-covered foliage. For sectors 1 and 3, such recovery was not possible due to external factors like prolonged snow cover during observation period. Furthermore steepness of the terrain is also of great importance. Vegetation is not exposed to strong winds that might help to reduce ash cover. In consequence, only rainfall might help to do so.

The calculated NDVI values were compared with data collected during field trips and it was possible to prove that ash fall in vegetation caused dryness of the leaves in evergreen trees.

http://dx.doi.org/10.5772/intechopen.72903

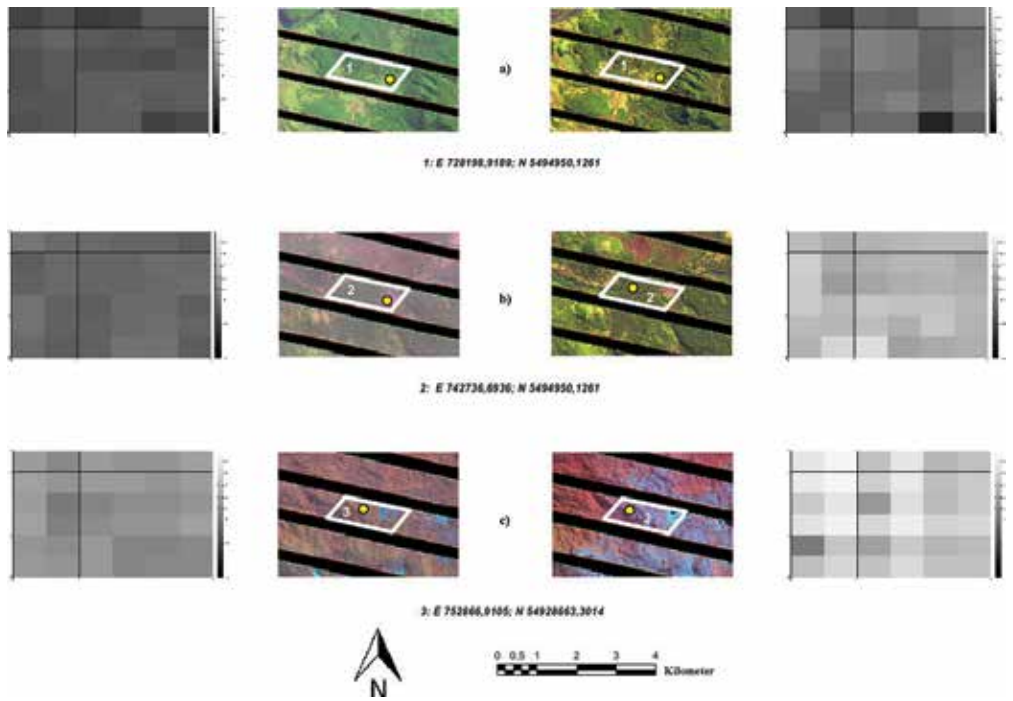

Figure 17. NDVI for each of the three study areas (middle) and for 2011 (left) and 2012 (right).

This led to a decrease in the potential of photosynthetic activity. Several reports published by CONAF allowed to proof the results and to identify the most affected vegetation during and after the eruption event.

Although the eruption of Cordón Caulle in 2011 did severe damage to Flora and Fauna, as indicated in [29, 30], a slow recuperation of the vegetation affected by ash deposits was observed. The decrease in contamination could be related to a combination of two phenomena: the cessation of volcanic activity and to climate (rainfall and prevailing winds in the study area). Recovery of photosynthetic activity started almost immediately after volcanic ash deposits were washed away by rain and wind.

	Mean	Variance	Year
Sector 1	0.236	0.002	2011
	0.486	0.011	2012
Sector 2	0.042	0.001	2011
	0.383	0.003	2012
Sector 3	−0.039	0.002	2011
	0.041	0.010	2012

Table 4. NDVI variations in the different sectors.

8. Conclusions

The use of geospatial tools for future management of trees is possible due to the characteristics of remote sensing and the ongoing development of image processing techniques. Nowadays, imagery is available on the Internet free of charge as well as some well-developed software suites for image processing. All over the world exists the necessity to carry out scientific studies on vegetation, migration processes, urban growth, and so on, to face climate change and to be aware of a changing world we live in. As shown, lots of investigation is ongoing at present and there is no limitation due to geographic location or data availability.

The five case studies presented in this chapter show that geospatial data, such as imagery and climate data is available, even in Chile. And that its study and analysis permit to develop strategies to monitor a wide range of natural phenomena. Desertification, weeds, forest plagues, and natural disasters are only some examples, which have to be studied in order to find answers on critical situations. As this works very well in rural sectors, it is possible to adapt them and to apply them in urban areas.

There is no doubt that once a suitable platform will be developed or established, for example, unmanned aerial vehicle (UAV) equipped with a multispectral camera, urban green areas can also be monitored. Its use will be vital for a number of strategic activities such as land use planning, installing green areas and urban parks, tree management plans, tree planning, fertilization, phytosanitary applications, removal, replacement, or gradual replacement tree in specific areas, among others.

Author details

Guido Staub

Address all correspondence to: gstaub@udec.cl

Department for Geodetic Sciences and Geomatics, University of Concepción, Los Ángeles, Chile

References

[1] Wachter SM, Bucchianeri WG. What is a tree worth? Green-City strategies, signaling and housing prices. Real Estate Economics. 2008;**36**(2):213-239

[2] Wolf KL. City trees, nature and physical activity: A research review. Arborist News. 2008;**17**(1):1-3

[3] Beéche M, Lanfranco D, Zapata M, Ruiz C. Surveillance and control of Sirex Woodwasp: The Chilean experience. In: Slippers, de Groot and Wingfield, eds. The Sirex Woodwasp and its Fungal Symbiont: Research and Management of a Worldwide Invasive Pest. The Netherlands: Springer; 2012

[4] Gomez C. Connotaciones en torno a la convivencia con *Sirex Noctilio*: Algunas consideraciones para su manejo. Patagonia Forestal. 2005;**11**(2):1-4

[5] Taiz L, Zeiger E. Plant Physiology. 4th ed. USA, Sunderland: Sinauer Associates, Inc.; 2006. 764 pp

[6] Campbell B, Wynne R. Introduction to Remote Sensing. 5th ed. New York: Guildford Press; 2011. 667 p

[7] Lillesand T, Kiefer R, Chipman J. Remote Sensing and Image Interpretation. 6th ed. Hoboken, New Jersey: John Wiley and Sons; 2008. 756 pp

[8] Purkis S, Klemas V. Remote Sensing and Global Environmental Change. Chichester, West Sussex, UK Hoboken, New Jersey: Wiley-Blackwell; 2011. 367 pp

[9] Francese JA, Zylstra KE, Mastro VC. U.S. Forest Service [Internet]. 2009. Available from: https://www.fs.usda.gov/treesearch-beta/pubs/34339 [Accessed: March, 2017]

[10] Ministry of Natural Resources and Forestry. 2016 [Updated: 2017]. Available from: https://www.ontario.ca/page/ministry-natural-resources-and-forestry [Accessed: June, 2017]

[11] Carnegie A, Eldridge R, Waterson D. History and management of Sirex wood wasp in pine plantations in new South Wales, Australia. New Zealand Journal of Forestry Science. 2005;**35**(1):3-24

[12] Ciesla WM, Hildebrand G. Forest Decline Survey Methods in West Germany: Opportunities for Application in North American Forest. USDA Forest Service, Forest Pest Management/Methods Application Group, Fort Collins, CO; 1986. 31 p

[13] Wylie R. Plague, pestilence and plantation. ITTO Tropical Forest Update. 2001;**11**(3):6-7

[14] Ciesla W. Remote Sensing in Forest Health Protection U.S. Dept. of Agriculture, Forest Service Forest Health Technology Enterprise Team, Remote Sensing Applications; 2000. 276 pp

[15] Bradshaw FJ. Low level aerial photography. In: Seminar on land use planning – recent advances, prospect 2000; May, 16-24, 1979; University of Western Australia, Nedlands. 1979

[16] Hildebrandt G, Kadro A. Aspects of countrywide inventory and monitoring of actual forest damages in Germany. Bildmessung und Luftbildwesen. 1984;**52**:201-216

[17] Hardin P, Hardin A. Hyperspectral remote sensing of urban area. Geography Compas. 2013

[18] McPherson E. Monitoring urban forest health. Environmental Monitoring and Assessment. 1992;**26**:165-174

[19] Ward K, Johnson G. Geospatial methods provide timely and comprehensive urban forest information. Urban Forestry & Urban Greening. 2007

[20] Jensen R, Hardin P, Hardin A. Classification of urban tree species using hyperspectral imagery. Geocarto International. 2012;**27**(5):443-458

[21] Garcia-Ruiz F, Sankaran S, Maja J, Lee W, Rasmussen J, Ehsani R. Comparison of two aerial imaging platforms for identification of Huanglongbing-infected citrus. Computers and Electronics in Agriculture. 2013;**91**:106-115

[22] Chuvieco E. Fundamentos de Teledetección Espacial. 3rd ed. 1996. 568 pp

[23] Instituto Forestal. Superficie de Plantaciones forestales; Regiones de Coquimbo a Aysén; e inventario plantaciones PYMP regiones Bío Bío y Araucaní – Actualización a Diciembre de 2008. **2009**:1-39

[24] GreenFacts - Facts on Health and the Environment [Internet]. 2001 [Updated: 2017]. Available from: https://www.greenfacts.org/en/index.htm [Accessed: January 2017]

[25] CEDOC- CIREN. Biblioteca digital CEDOC - CIREN [Internet]. 1999. Available from: http://bibliotecadigital.ciren.cl/handle/123456789/18039 [Accessed: August 2017]

[26] COMISION NACIONAL DEL XVII CENSO DE POBLACION Y DE VIVIENDA. CENSO 2002 - Síntesis de Resultados. 2003

[27] Harris Geospatial Solutions. Canopy Water Content [Internet]. 2017. Available from: https://www.harrisgeospatial.com/docs/CanopyWaterContent.html

[28] Quinn JW. Band Combinations [Internet]. 2001. Available from: http://web.pdx.edu/~emch/ip1/bandcombinations.html

[29] Fernández-Arhex V, Buteler M, Amadio ME, Enriquez A, Pietrantuono AL, Stadler T, Beckerand G, Bruzzone O. The effects of volcanic ash from Puyehue-Caulle range eruption on the survival of *Dichroplus vittigerum* (Orthoptera: Acrididae). Florida Entomologist. 2013;**96**(1):286-288

[30] Wilson T, Stewart C, Bickerton H, Baxter P, Outes V, Villarosa G, Rovere E. Impacts of the June 2011 Puyehue-Cordón Caulle volcanic complex eruption on urban infrastructure, agriculture and public health. GNS. Science. 2013;**20**:1-98

Chapter 8

Monitoring Land Surface Deformation with Satellite ScanSAR Images: Case Studies on Large Earthquakes in China

Tingchen Jiang, Xiuping Wang, Yuanzhi Zhang and Yu Li

Additional information is available at the end of the chapter

http://dx.doi.org/10.5772/intechopen.72834

Abstract

This chapter presents a new application of scanning interferometric synthetic aperture radar (ScanSAR) interferometry in monitoring land surface deformation caused by large earthquakes. To make better use of the ScanSAR data and obtain a wider deformation observation, this research studied and analyzed certain key elements of ScanSAR interferometry, including coherence, co-registering, methods of removing orbit errors, correction of atmosphere effects, and geoid undulation. The wide swath mode (WSM) is also known as the ScanSAR mode by which synthetic aperture time is shared by adjacent sub-swaths and azimuth resolution that is traded off for a wider coverage. So, it is possible to monitor a larger area of earthquake deformation. In this study, we obtained ScanSAR and Image Mode (IM) data and analyzed coherence, co-registering, methods of removing orbit errors, correction of atmosphere effects, and geoid undulation to monitor land surface deformation caused by large earthquakes in the 405 × 405 km field of the Wenchuan earthquake and Yutian earthquake, respectively, in China. The results obtained agree well with that of the investigations of the crustal motion in the study areas.

Keywords: deformation monitoring, ScanSAR interferometry, large earthquake

1. Introduction

Scanning synthetic aperture radar (ScanSAR) interferometry uses the wide swath synthetic aperture radar (SAR) mode to get geometrical information about the earth's surface [1, 2],

that is, all of the sub-swaths processed images were obtained to form a wider ScanSAR image. A wider swath can allow for multiple observations of an area in a single orbit cycle. In other words, the region in question can be observed by the sensors in several different orbit tracks [3–5]. Although resolution of the ScanSAR mode is relatively low, its many merits such as wider swaths and short intervals [6] for the deformation of a large area can contribute to effective imaging.

The ScanSAR concept was first introduced in the 1980s and the ScanSAR mode of Radarsat satellite was designed in 1988. Burst mode radar was first applied to the Magellan mission to map the Venus surface in order to reduce data volume and allow the use of other instruments in between radar bursts [5, 7, 8]. To our knowledge, the first ScanSAR amplitude image of the Earth was in 1996 [9]. The first ScanSAR interferogram was obtained by using ScanSAR data of Radarsat satellite in 1999 [10]. The ScanSAR mode was initially used on the National Aeronautics and Space Administration (NASA) Spaceborne Imaging Radar C-band (SIR-C) mission in 1994 [7, 10]. Many SAR sensors such as Envisat, Radarsat-2, Advanced Land Observing Satellite (ALOS), COSMO-SkyMed, and TerraSAR-X are capable of imaging in the ScanSAR mode. On Envisat, the ScanSAR mode was called as Wide Swath Mode (WSM) and has five sub-swaths. Unfortunately, communication with Envisat was lost on April 8, 2012 and, consequently, the mission officially ended on May 9, 2012. The Sentinel-1A satellite was launched in April 2014 and can operate the satellite SAR sensor that is capable of imaging in the ScanSAR mode. The ScanSAR mode is called as Interferometric Wide-swath mode (IW).

With many of the current SAR satellites carrying advanced imaging capabilities, ScanSAR mode acquisitions are replacing the conventional strip-map mode acquisitions for portions of a SAR mission [11]. In light of future SAR missions and modifications of existing SAR mission imaging strategies, a detailed study of ScanSAR interferometry for ground motion monitoring of large earthquakes will provide significant input for mission planning and InSAR applications [6].

To use ScanSAR data for deformation monitoring, same as Image Mode (IM) data, many studies have been focused on the following three points: (1) imaging algorithms [12–15]; (2) removing coherence of spaceborne ScanSAR interferometry [3–5]; and (3) developing new algorithms of ScanSAR interferometry [12, 13].

With regard to ScanSAR interferometry, scholars have studied how to form the interference [4–6, 12, 13], but the effects of errors are yet to be studied systematically. For example, ScanSAR interferometry was applied in Wenchuan earthquake [16, 17]; however, in the study of monitoring the surface deformation, they only considered the influence of the atmosphere on the results using Medium Resolution Imaging Spectrometer (MERIS) data. In fact, to obtain a high accuracy ScanSAR interferogram, some key techniques such as geoid undulation, correction of atmosphere effects, and reducing orbit error besides removing coherence and mosaicking of wide swath SAR data were studied. In this chapter, we applied these key techniques to the wider deformation fields of ENVISAT ScanSAR images to monitor the land deformation caused by large earthquakes such as Wenchuan (2008) and Yutian (2008), respectively, in China.

http://dx.doi.org/10.5772/intechopen.72834

2. Settings and data processing

The ScanSAR mode is able to image multiple strips of land called sub-swaths from a single satellite pass. This can be achieved by electronically steering the radar beam through a set of elevation or look angles. Each sub-swath is collected in the burst mode, wherein the inter-burst gap time corresponds to the time when the sensor is imaging the remaining sub-swaths [5]. The raw data from each sub-swath are processed to burst mode images and merged into a composite ScanSAR image. In the ScanSAR mode, the satellite electronically steers the beam between sub-swaths, while in the strip-map mode, the beam is maintained within a single sub-swath. The elevation angle is often cycled enough during ScanSAR operation to maintain contiguous ground coverage. The process of ScanSAR interferometry is shown in **Figure 1**, which includes mosaicking bursts, image co-registration, common band filtering, and so on. In addition to mosaicking bursts to sub Single Look Complex (SLC) and sub-interferograms, the other is the same as the IM interferometry.

The principle of ScanSAR interferometry in the burst is the same as that of IM [5, 6, 12, 13]. If the SAR satellite at certain time intervals orbits (typically tens to 100 m) and scans on a region repeatedly, the spatial positions are S1 and S2, respectively, during the two different flight processes. The spatial interferometric baseline vector is B and named baseline length. The

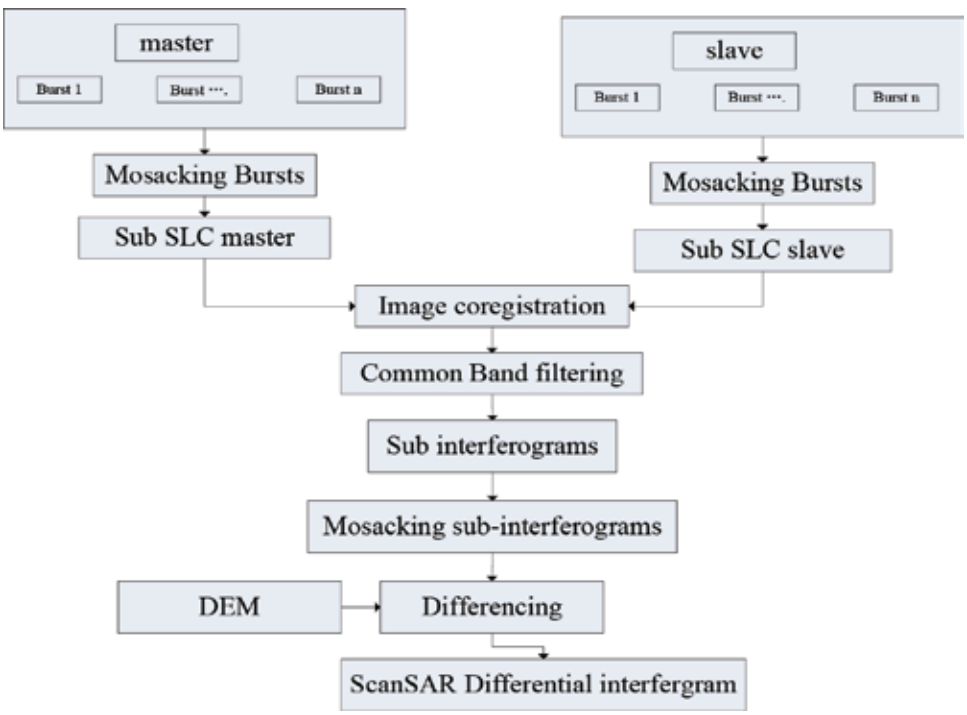

Figure 1. The data processing of ScanSAR interferometry.

angle between the baseline vector B and horizontal vector is baseline obliquity, and θ is the incident angle. In addition, two spatial positions, S1 and S2 to ground point P are r and r+Δr. At the same time, the interferometric baseline is divided into a parallel baseline component $B_{\parallel}$ ($B_{\parallel} = B\sin(\theta - a)$ which is parallel to the line-of-sight direction and vertical baseline component $B_{\perp}$ ($B_{\perp} = B\cos(\theta - a)$ (perpendicular to the view direction). According to the principle of conventional Differential Interferometric Synthetic Aperture Radar (DInSAR), the interferometric phase of the ScanSAR interferogram can be expressed as:

$$\phi = \frac{4\pi}{\lambda}(B_{\parallel} + \frac{B_{\perp}}{r\sin\theta}h - \Delta p) \tag{1}$$

where ϕ is the total phase after unwrapping and Δp is surface deformation of the line of sight. If surface deformation is obtained using two pass methods, surface deformation of the line of sight, *i*, can be written as:

$$\Delta p = B_{\parallel} + \frac{B_{\perp}}{r\sin\theta}h - \frac{\lambda}{4\pi}\phi \tag{2}$$

From Eq. (2), it can be seen that surface deformation of the line of sight is closely related to the ground phase $\frac{4\pi}{\lambda}B_{\parallel}$ and Digital Elevation Model (DEM)error. If Eq. (2) is transformed as the derivation of B, h, and a, the results are as follows:

$$\begin{aligned}
&\frac{d\Delta p}{dB} = \sin(\theta - a) + \frac{B_{\perp}h}{r\sin\theta} \\
&\frac{d\Delta p}{da} = -B\cos(\theta - a) + \frac{B\sin(\theta - a)}{r\sin\theta} - \frac{B\cos(\theta - a)\cos\theta}{r\sin^2\theta} \\
&\frac{d\Delta p}{dh} = \frac{B_{\perp}}{r\sin\theta}
\end{aligned} \tag{3}$$

That is,

$$\begin{aligned}
&\sigma_{\Delta p} = (\sin(\theta - a) + \frac{B_{\perp}h}{r\sin\theta})\sigma_B \\
&\sigma_{\Delta p} = (-B\cos(\theta - a) + \frac{B\sin(\theta - a)}{r\sin\theta} - \frac{B\cos(\theta - a)\cos\theta}{r\sin^2\theta})\sigma_a \\
&\sigma_{\Delta p} = \frac{B_{\perp}}{r\sin\theta}\sigma_h
\end{aligned} \tag{4}$$

where σ_B is the error of baseline, σ_a is the error of baseline obliquity, and σ_h is DEM error. According to the abovementioned equation, regardless of baseline length error, baseline obliquity errors will affect the results of ScanSAR interferometry, and the influence degree is related to the slant range. However, DEM error is related to both the oblique distance, angle of incidence, and the vertical baseline length. In addition to these errors, the atmospheric refraction phase is also an influencing factor. Undoubtedly, in order to obtain deformation data of

large earthquakes with ScanSAR interferometry, the following techniques and methods were applied to eliminate these errors in the monitoring of land deformation.

2.1. Removing influence of geoid difference

In order to obtain deformation data of the region in question through DInSAR, it is necessary to use two or more scenes of SAR data to form a differential interferogram. Since the SAR data are not sufficient and an outlay of the research project is not relatively scarce, there is only one way to use DEM to get a differential interferogram. Currently, DEM such as Shuttle Radar Topography Mission (SRTM) and Advanced Spaceborne Thermal Emission and Reflection Radiometer Global Digital Elevation Model (ASTER GDEM) are referenced to the Earth Gravitational Model 1996 (EGM96) geoid datum, while in interferometry SAR (InSAR), data processing is established on the ellipsoidal height (e.g., WGS84); therefore, both data are inconsistent.

In this study, geodetic height was obtained based on the EGM96 gravity field model. To convert EGM96 height into geodetic height, geoid gap N can be calculated using the following formula [18]:

$$N(\theta,\lambda) = \varsigma_Z + \frac{GM}{r_p \gamma_p} \sum_{n=2}^{N} C_{nm} Y_{nm}(\theta,\lambda) + \frac{\Delta g_B(\theta,\lambda)}{\bar{\gamma}} H(\theta,\lambda) \tag{5}$$

According to Eq. (5), the elevation of SRTM or GDEM data is converted into geodetic height.

2.2. Correction of atmosphere effects

Atmospheric refraction is an important source of error for interferometric synthetic aperture radar, the reason is that the radar signal propagation in atmosphere by tropospheric and ionospheric refraction is delayed, or it gets ahead of its phase. With other similar mode interference, atmospheric effects with other errors (such as DEM and baseline error) also seriously affect the final deformation monitoring results for ScanSAR interferometry; however, unlike other laws of error influence, atmospheric effects are not affected by radar imaging geometry but are only related to the atmospheric relative states of the two ground observations. The ionosphere at about 60–2000 km height has inhomogeneous bodies from several kilometers to hundreds of thousands of meters. SAR satellites are inclined cone when exposed to the ground; at the same time, the scanning area of the ground is less than a few hundred kilometers, so it has less influence. In general, it is basically eliminated by the difference in the spatial domain. Tropospheric delay can be divided into two parts, the dry and wet delay. Dry delay is generated by no water vapor atmospheric delay and accounts for about 90% of the total delay, and the model accuracy can reach submillimeter range. In addition, the time domain is relatively stable and has the characteristics of large-scale changes in the airspace, while dry delay is negligible after double difference. The wet delay is caused by the water vapor in the atmosphere, which accounts for about 10% of the total delay. However, it is difficult to establish a real-time and accurate model due to the uneven distribution of water vapor in the atmosphere and the rapid change. Therefore, the main error of troposphere delay is caused by wet delay.

In order to reduce or remove the wet delay of ScanSAR interferometry [5, 6, 12, 13], the atmospheric effects of corrections were analyzed based on medium-resolution imaging spectrometer (MERIS) data. When compared with the correction method of atmospheric effects using external data such as Moderate Resolution Imaging Spectroradiometer (MODIS), making use of MERIS, correct atmospheric effects of advanced synthetic aperture radar (ASAR) interferogram have great superiority, for the imaging time of ASAR and MERIS are synchronous, and the resolution of ScanSAR is close to the resolution of MERIS data.

The reason of correction of atmospheric effects based on MERIS data is that atmosphere delay information is first obtained using two MERIS data corresponding to two SAR data to be converted into path delay by using function mode. In the end, this path delay will be removed so that atmospheric effects in the ScanSAR interferogram is corrected. The process of correcting atmospheric effects is shown in **Figure 2**. When using MERIS data to correct atmosphere effects, it involves removing cloud, difference, and co-registration. As the water vapor algorithm of MERIS is very sensitive to the cloud, it is necessary to use Cloud product categories to obtain cloud pollution and then to interpolate relevant data. To reduce interpolation errors, MERIS data will only be calibrated without the removal of the mask method.

2.3. Reducing orbit error

Orbit error is another key factor in ScanSAR interferometry because it influences baseline estimation precision. Baseline estimation is required for a number of operations, including

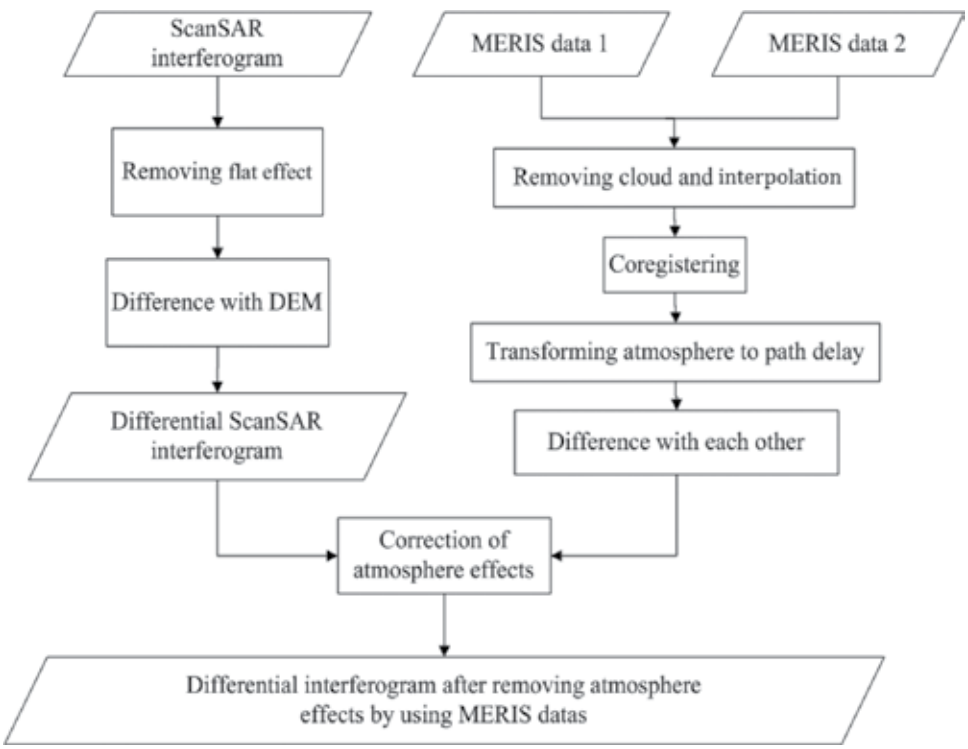

Figure 2. The process of basic idea of the correction of atmospheric effects using MERIS data.

http://dx.doi.org/10.5772/intechopen.72834

common band filtering, flattening of the interferogram, phase unwrapping, and derivation of interferometric heights from the unwrapped phase [5, 6].

The baseline can be estimated using (1) orbital information, (2) fringe rate of the interferogram, and (3) ground control points (after unwrapping). It is clear that the method based on state vectors works well when accurate state vectors are available. In the absence of reliable state vector information, the local fringe rate at the center of the interferogram can be used to obtain an estimated perpendicular baseline. The third method is the most effective because its coverage is very wide and the fringe rate is not always constant. Moreover, the size and influence of the baseline error can be seen more clearly in the ScanSAR interferogram.

3. Case study: Wenchuan earthquake

3.1. Background

Wenchuan earthquake struck on May 12, 2008 with M8.0 of the high strength of a large earthquake, which resulted in a large number of collapsed houses, about 80,000 casualties, tens of thousands of geological hazards, such as landslide and collapse, and debris flow. The earthquake led to a large number of rupture and regional ground deformation on the surface, including the gaining of much of the information of the earth's dynamics [16, 19] (**Figure 3**).

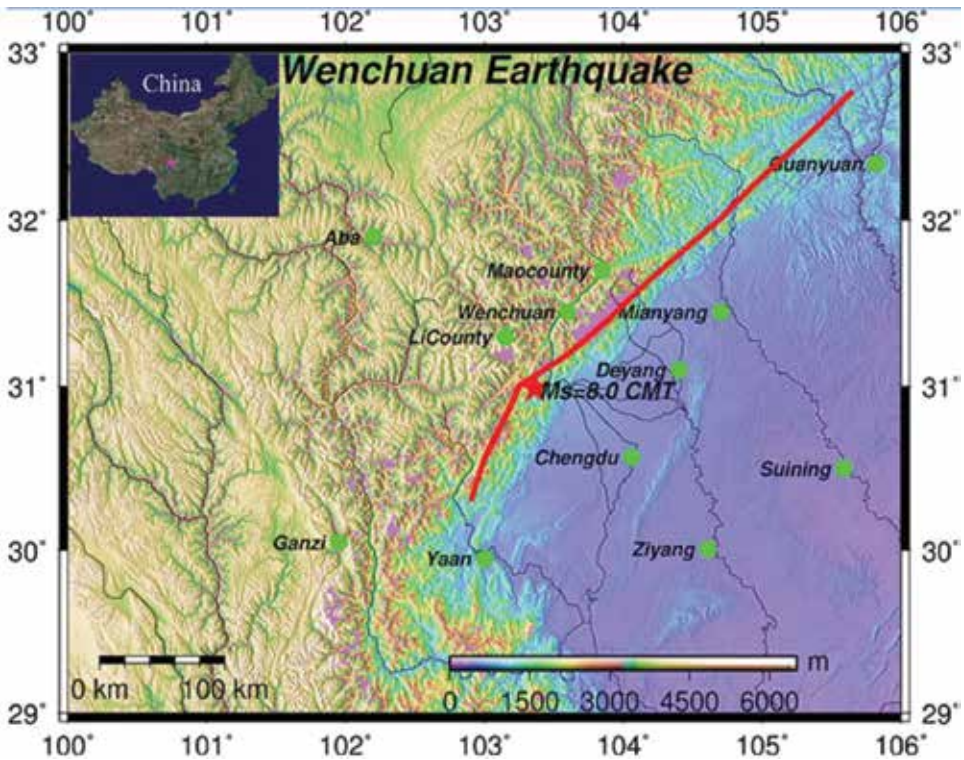

Figure 3. Location of Wenchuan earthquake (★is center of Wenchuan earthquake).

After the Wenchuan earthquake, many studies were conducted to simulate the seismogenic structure and seismic characteristics [16, 19–22], such as tectonic activities, intensity, and focal mechanism, by which the research methods including field survey, gravity survey, GPS, and the conventional interferometric SAR were applied, and there were some valuable achievements [19–22]. However, since the approaches applied have their own limitations and shortcomings (i.e., low precision, large discreteness, narrow scopes, influences of natural factors, etc.), results on the fracture zone length, direction of rupture, and rupture surface size for Wenchuan earthquake are different [23–25]. The co-seismic deformation field of the Wenchuan earthquake by ScanSAR interferometry was studied because of the defects of the abovementioned methods [17]. However, there were a lot of errors which had not been removed and considered in the processing of interferometry such as geoid undulation and orbit error. In addition, when atmospheric effects had been considered for removal, Moderate Resolution Imaging Spectroradiometer (MODIS) data was only used to reduce the influence of atmosphere. In fact, MERIS is better than MODIS because the MERIS and ScanSAR data used were derived from the ENVIronmental SATellite (ENVISAT) satellite, so as to maintain synchronization. Therefore, these factors were considered in this chapter.

3.2. Data and processing

The Wenchuan earthquake was so strong and its rupture zone was about 300 km. In order to mantle the overall earthquake deformation field, two scenes of ENVISAT ScanSAR data were selected to cover the deformation field, with the imaging times of January 25, 2008 (before the earthquake) and June 13, 2008 (after earthquake), respectively.

Before interferometry processing, the geoid difference of the GDEM of Wenchuan was computed based on EGM96. The regional level of the contour line is presented in **Figure 4**, from which the maximum and minimum value of the regional level is −28.78 and − 42.98 m, respectively, with a difference of 14.2 m.

The deformation zone of Wenchuan earthquake is located in the Western Sichuan province. In addition, the imaging time of both ASAR image and MERIS vapor products were consistent with the similar spatial resolution of both ScanSAR interferogram and MERIS, so that the atmospheric effects can be reduced using MERIS data. **Figure 5** shows the result that is absolute wet delay of January 25, 2008 (**Figure 5a**) and June 23, 2008 (**Figure 5b**) in the Wenchuan earthquake area. **Figure 6** shows the corresponding relative atmospheric wet delay after difference. As shown in **Figure 5**, the weather of two periods were in good condition, and the regional atmospheric wet delays of the two periods were about 3 mm. Therefore, it is necessary for the ScanSAR differential interferogram to correct atmosphere effects based on the relative wet delay.

Image co-registration of ScanSAR with the same IM mode can determine the final result quality. In order to form a robust and reliable interferogram and to make the co-registration precision to remain less than 0.2-pixel, it is applied with the co-registration method based on DORIS precise orbit and the external DEM. After co-registration and differential interferometry, it is possible to obtain the sub-swath interferogram and sub-swath interferograms are mosaicked to the total ScanSAR interferogram. At the end, flat and topographic phases are removed from

http://dx.doi.org/10.5772/intechopen.72834

the interferogram to obtain the differential interferogram as shown in **Figure 7a** and **b** after phase unwrapping which is the result where the baseline is mended using the ground control point (GCP) method.

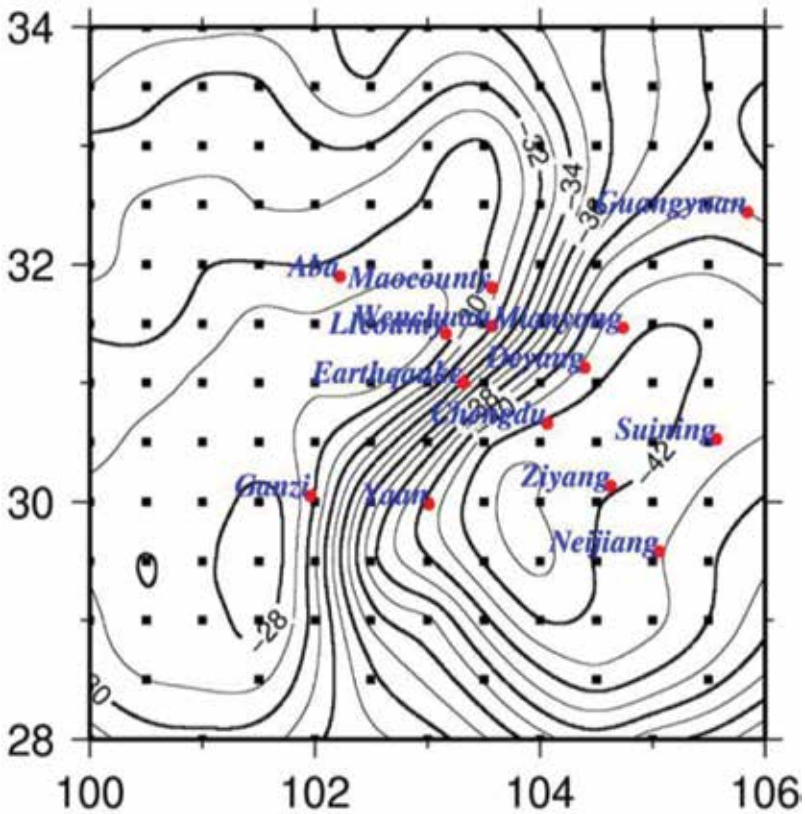

Figure 4. Wenchuan regional level of contour lines.

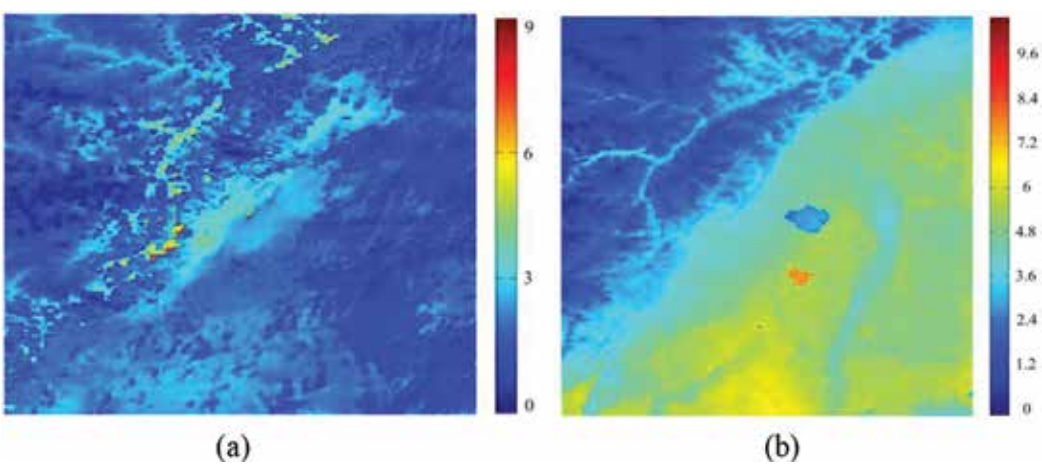

Figure 5. Wenchuan area of absolute wet delay of January 25, 2008 (a) and June 23, 2008 (b) (unit mm).

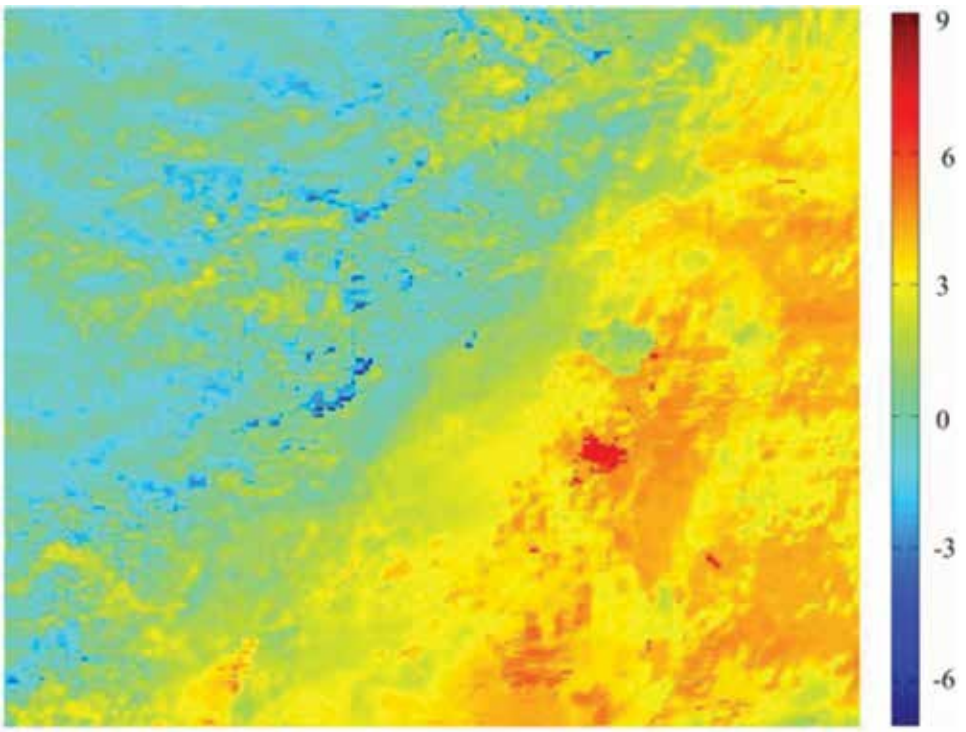

Figure 6. Relative atmospheric wet delay after difference (unit mm).

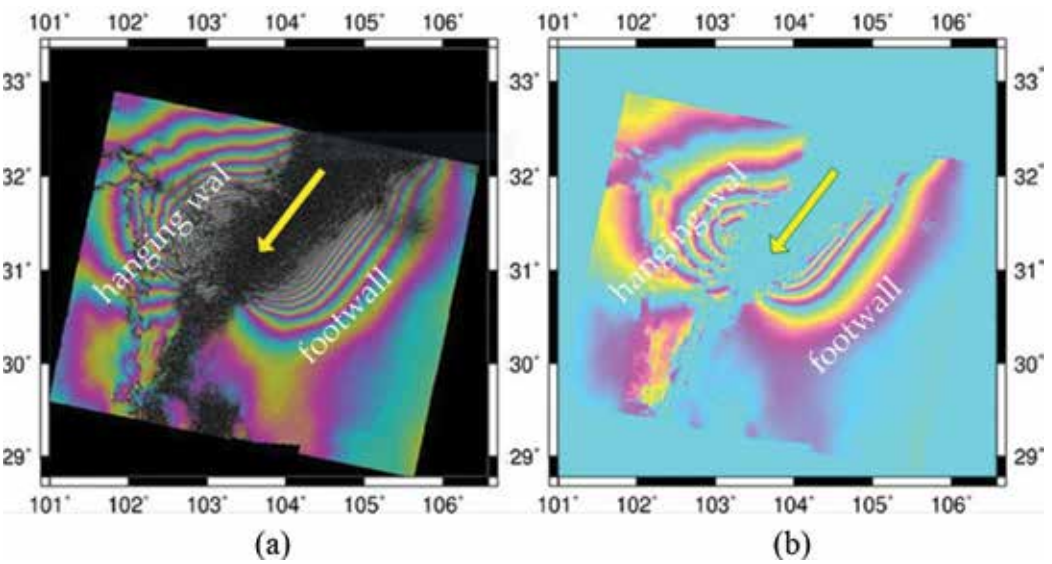

Figure 7. Differential interferogram of Wenchuan earthquake. (a) before phase unwrapping (b) after phase unwrapping.

http://dx.doi.org/10.5772/intechopen.72834

3.3. Results and discussions

Figure 7 shows that the size of the whole area that the ScanSAR interferogram covered is about 405 × 405 km, which is sufficient to reflect the total seismic deformation field and seismogenic fault location of the Wenchuan earthquake. The deformation region can be roughly divided into three areas, while the middle one is a noncoherent region where the Wenchuan seismic belt is located. The noncoherent field results from the fact that the deformation gradient in the region exceeds the C-band monitoring ability of ASAR images. This means that if the deformation of two adjacent pixels exceeds π radian, the coherence is pure noise. Consequently, landslides and the destruction of vegetation investigated in the field caused by the earthquake led to the loss of coherence. The other two regions of the interference fringes with increasing distance away from the fault and is more and more sparse, but the right side of the noncoherent area is the footwall (i.e., Chengdu Plain), while the wrapped phase image shows nearly parallel extension. On the other side of the noncoherent zone is the hanging wall of fault which is the concentric circular interference fringe area.

According to the phase in **Figure 7**, considering relative atmospheric wet delay in **Figure 6** and its space imaging geometric relationship, ScanSAR interferometry value is transformed into the deformation of line of sight (LOS) as shown in **Figure 8**. To further analyze deformation, as

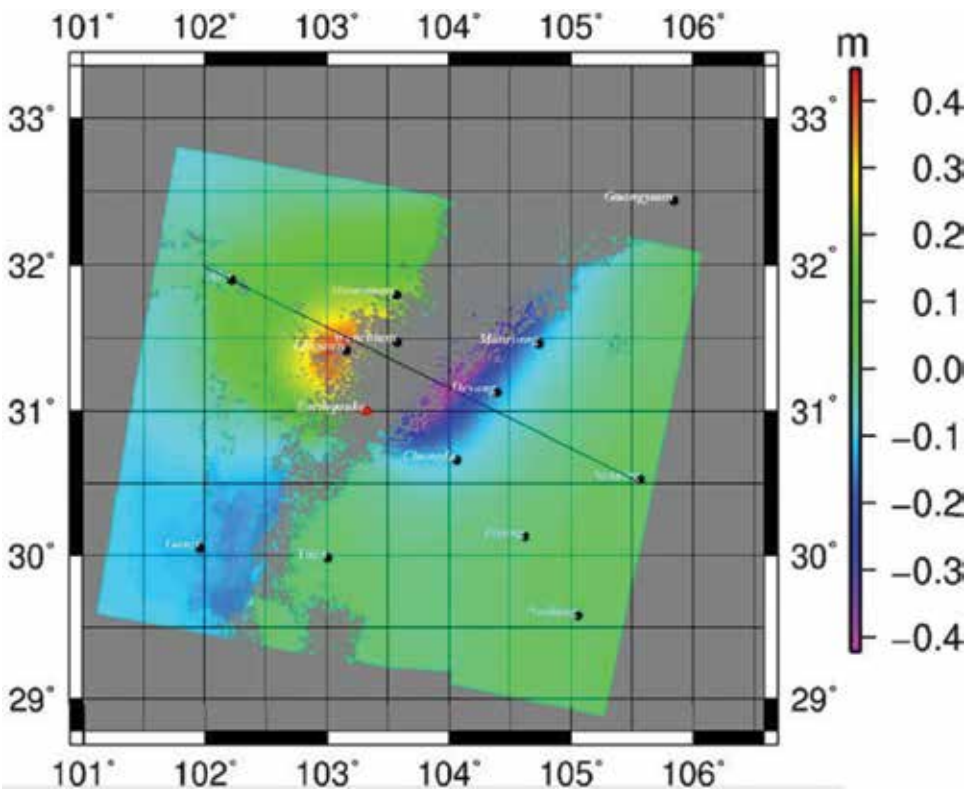

Figure 8. Wenchuan earthquake deformation field by ScanSAR interferometry.

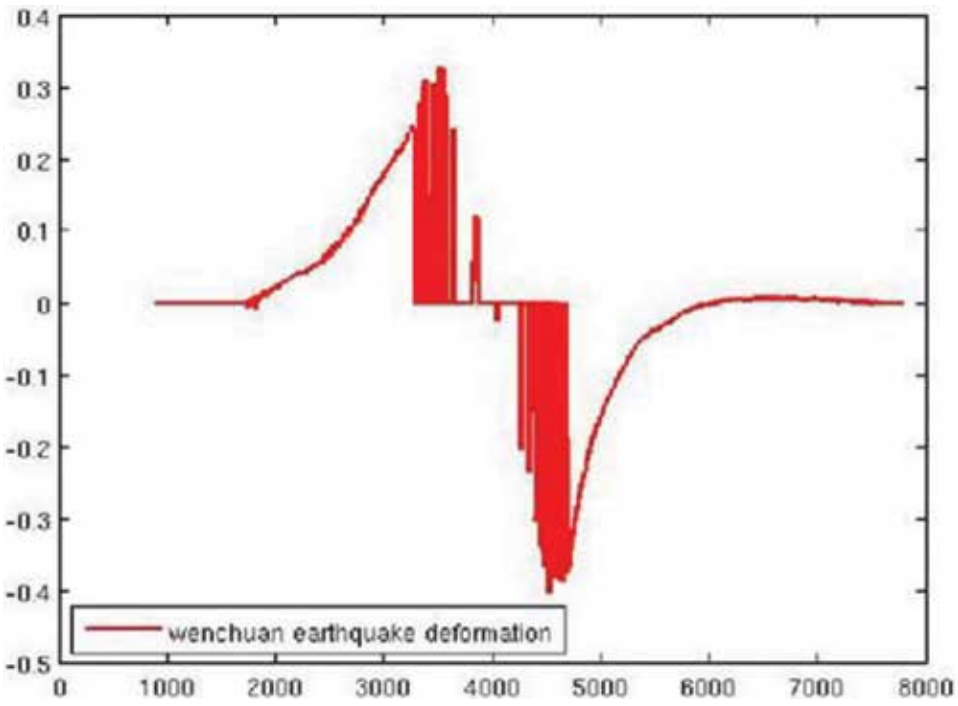

Figure 9. Deformation profile of Wenchuan earthquake along the black line in **Figure 8** (unit: M).

the center of interferogram is a noncoherent district, the interferogram is unwrapped, respectively, at different points of the upper west and lower east image as the reference point, so that it is possible to gain two deformation results. **Figure 8** is the deformation field taken at the lower east corner as reference point, which shows that the deformation scope of the Wenchuan earthquake is very great, even the A'ba region recorded deformation. In addition, deformation of the Chengdu region is about 0.10 m. To analyze the deformation, its profile is mapped as shown in **Figure 9**. Based on profile of the two points, the max deformation value of the left part of the fault is 0.48 m, while that of the right part is −0.42 m. When compared with the west part, the deformation scope of the east part is narrow, while the deformation grades are very high, especially near the fault.

4. Case study: Yutian earthquake

4.1. Background

There was an M7.3 earthquake at the boundary of Yutian County in Hotan Prefecture, Xinjiang, China, on March 21, 2008, and the epicenter of earthquake (Latitude: 35.6, Longitude: 81.6) was 225 km from the Hetian city and about 120 km from the Yutian county, as presented in **Figure 10**. Yutian earthquake was considerably destructive. This is again an earthquake higher than M7.0 in the western edge of the Qinghai Tibet Block that occurred after Kunlun

http://dx.doi.org/10.5772/intechopen.72834

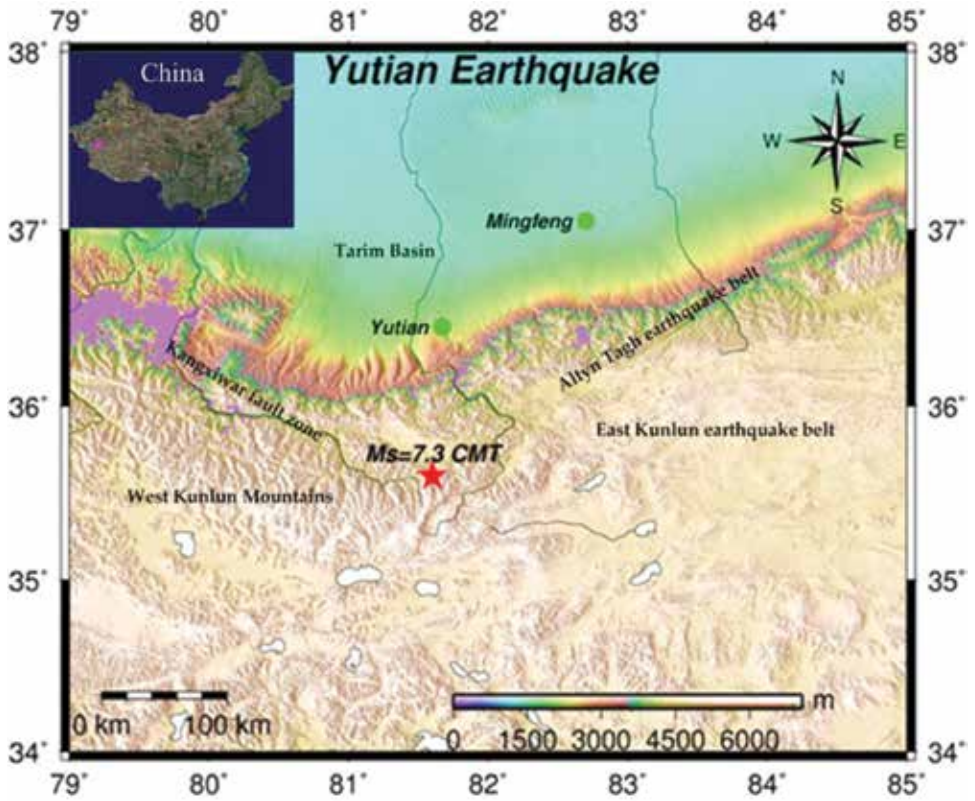

Figure 10. Location of Yutian earthquake (★ is center of Wenchuan earthquake).

Mountain earthquake of magnitude 8.1 in 2001, and a M6.2 earthquake was in this region in 2012. According to statistics, there were 33 above M3.0 earthquakes in this region from January 2012 to November 2013. Thus, this is an earthquake-prone area and as a research hotspot [26].

Yutian earthquake occurred in the intersection of the East Kunlun earthquake belt, Kangxiwar fault zone and Altyn Tagh earthquake belt, which is near the edge of the West Kunlun Mountains, located in the southern part of Tarim Basin, belonging to Tibet and two big western active plots. Although the Yutian earthquake in the basin limits the distribution range of aftershocks, the earthquake deformation range still reflects the motion state of the active block [26]. The activities of Arkin fracture zone are the main causes of the Yutian earthquake. Strong earthquake activities of Arkin fault are often accompanied by earthquake activity in the Qinghai Tibet Plateau and its surrounding main fault zone. For example, Wenchuan M8.0 earthquake took place more than 1 month after the Yutian earthquake, and 2 years later, the M7.1 Yushu earthquake occurred.

4.2. Data and processing

To monitor the total deformation field of Yutian earthquake, ASAR data of ScanSAR and two IM models of the ESA ENVISAT satellite were selected to study seismic deformation as shown

in **Table 1**. Using Global Digital Elevation Model (GDEM) to get differential interferogram and the geoid difference of the GDEM of Yutian was computed based on EGM96. The regional level of the contour line is shown in **Figure 11**, in which the maximum and minimum value of the regional level is 62.3 and −19.8 m, respectively, and the difference between them is 42.5 m.

After co-registering and differential interferometry, sub-swath interferogram was acquired and then sub-swath interferograms were mosaicked to the total ScanSAR interferogram. At the end, the flat and topographic phase were removed from the interferogram to obtain a differential interferogram as seen in **Figure 12a**, while **Figure 12b** is the differential interferogram obtained after phase unwrapping, and its perpendicular baseline is 75.6 m, in both cases the data of November 29, 2007 and April 17, 2008 were applied.

4.3. Results and discussions

As shown in **Figure 12**, the ScanSAR differential interferogram mantle scope is about 405 × 405 km, almost reflecting the deformation field and fault place of the Yutian earthquake. At the same time, it also shows that the surface deformation influence on the scope of Yutian earthquake was enormous. In addition, the earthquake isoseismal is oval, and the differential interferogram is roughly divided into two areas, namely, the coherent and noncoherent regions. Yutian earthquake center is located in the noncoherent region (shown in **Figure 12**).

The noncoherent area on the left is the hanging wall of the earthquake, while the right side is the footwall of the earthquake. Moreover, interference fringes in these regions with increasing distance away from the fault are more and more sparse, but when compared with the hanging wall of the earthquake, footwall deformation decays earlier.

As shown on the upper right corner area in **Figure 12b**, even far away from the fault, the case still remained strips. To verify whether the interference fringes is caused by the seismic deformation, another four landscape ScanSAR data before and after the earthquake were processed and the results are shown in **Figure 13**. **Figure 13a** is the interferometry result using two data of pre-earthquake and **Figure 13a** shows the interferometry result using two data between pre-earthquake and post-earthquake.

Track number	Imaging time (YY-MM-DD)	Ascending or Descending	Imaging mode	Polarization mode	Orbit number
434	2007-05-03	Descending	WSS	HH	30,862
	2007-06-07	Descending	WSS	HH	31,363
	2007–2011-29	Descending	WSS	HH	28,085
	2008-04-17	Descending	WSS	HH	33,095
	2008-05-22	Descending	WSS	HH	33,196
477	2008-04-20	Descending	IM	HH	33,093
	2008-04-01	Descending	IM	HH	33,083

Table 1. SAR data to obtain deformation of Yutian earthquake.

http://dx.doi.org/10.5772/intechopen.72834

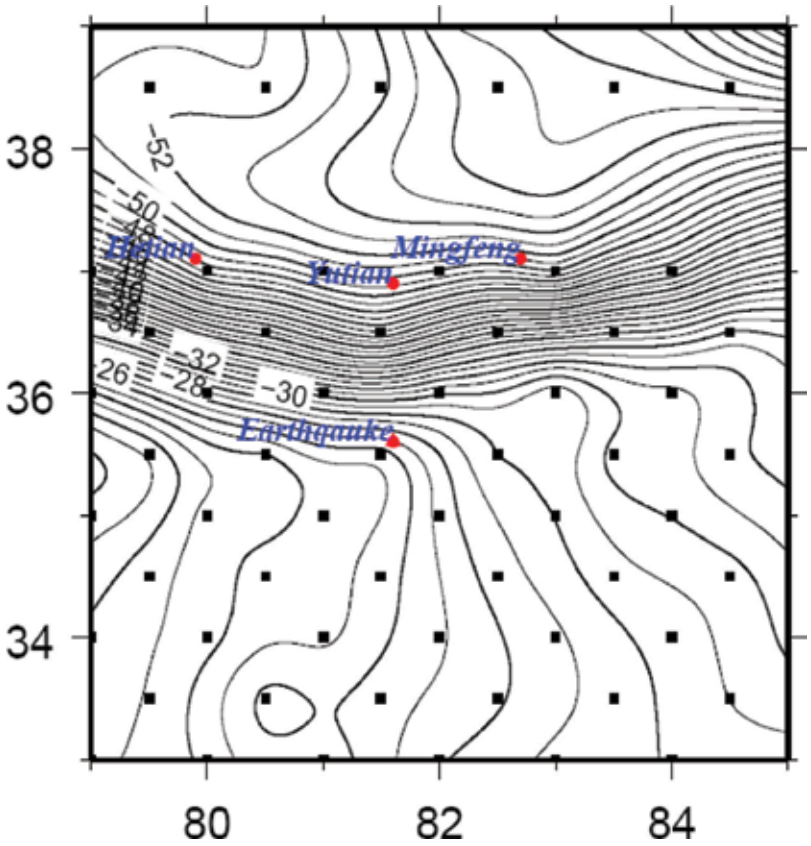

Figure 11. Geoid isolines of Yutian region.

From **Figure 13a**, it is clear that the upper right corner areas of the interferogram remain as interference fringes even when the vertical baseline is 2.87 m; however, **Figure 13b** has no interference fringes. Undoubtedly, this proved that these stripes are not caused by a DEM error or other factors but Yutian earthquake. Although the region from the earthquake center is about 170 km and located in east Kunlun and Arkin faults, it is found that transition part between the region and earthquake deformation field has no interference fringes, which may be related to the Bayan Kara block geological structure.

Based on the spatial geometry and differential interferogram, ScanSAR interferometry observations are transformed into the deformation value of the line of sight. As shown in **Figure 14**, the rupture strip of Yutian earthquake is about 80 km. The maximum deformation of hanging wall for the fault is 0.41 m and the maximum of the footwall deformation value is 0.32 m. When compared with the footwall, the hanging wall deformation range is narrow, but the deformation gradient near the fault is great. In addition, ASAR image mode data are used to form the interferometry and deformation results as shown in **Figure 15**. It is clear that the differential interferometry results of the image mode reflect almost fault and deformation distribution of the Yutian earthquake. The maximum deformation of the hanging wall is 0.60 m

and the maximum deformation of the footwall is 0.63 m. The noncoherent region of the IM interferometry is in a certain range in comparison with results from the ScanSAR mode interference. Furthermore, the non-coherent region is small and the deformation results reflected is not the same, which is mainly due to the higher resolution induced by IM.

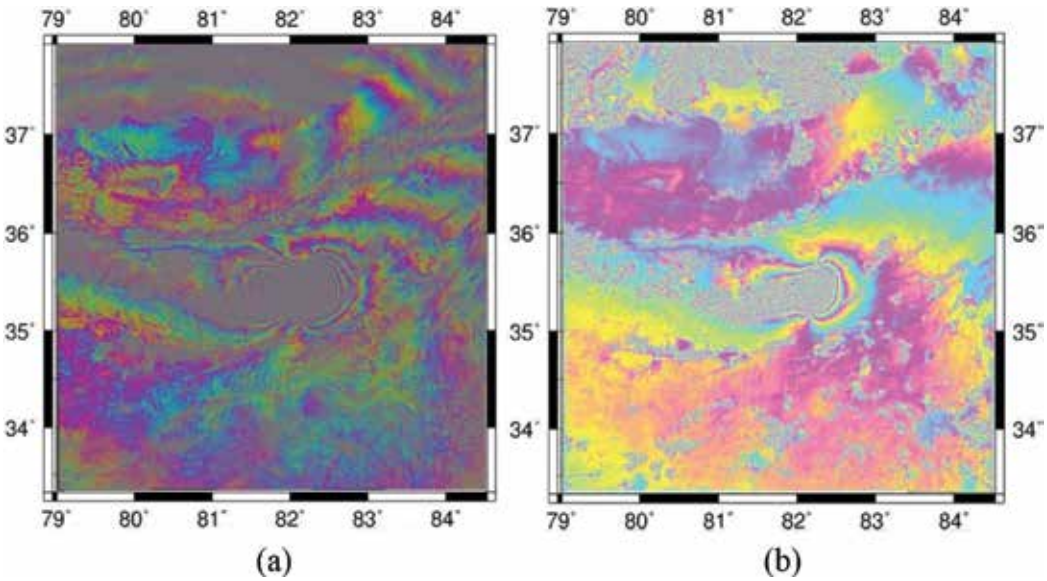

Figure 12. Differential interferogram of Yutian earthquake. (a) wrapped interferometric phase and (b) unwrapped interferometric phase.

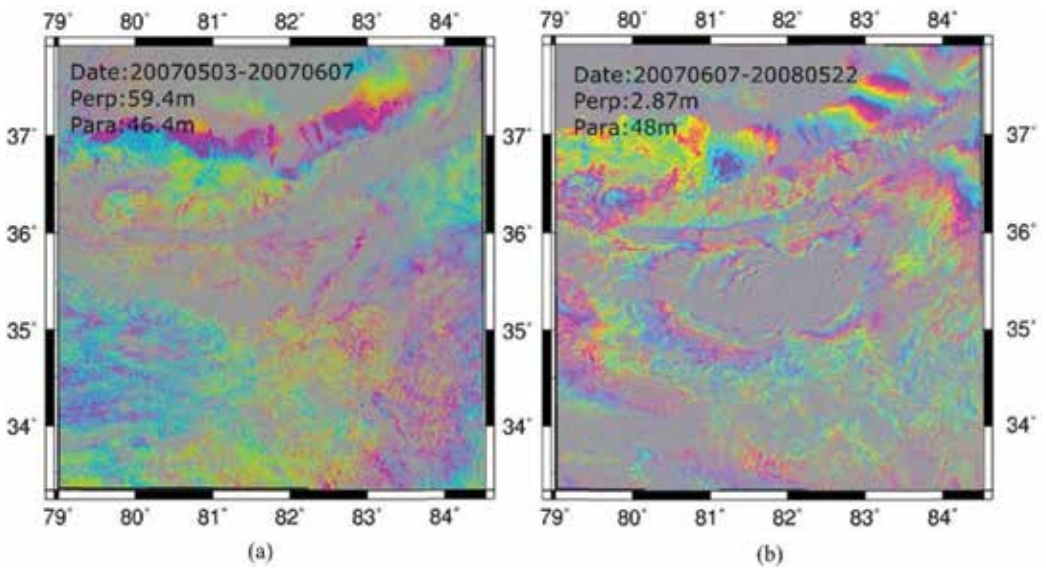

Figure 13. Other differential interferogram of Yutian earthquake (wrapped). (a) Before earthquake. (b) After earthquake.

http://dx.doi.org/10.5772/intechopen.72834

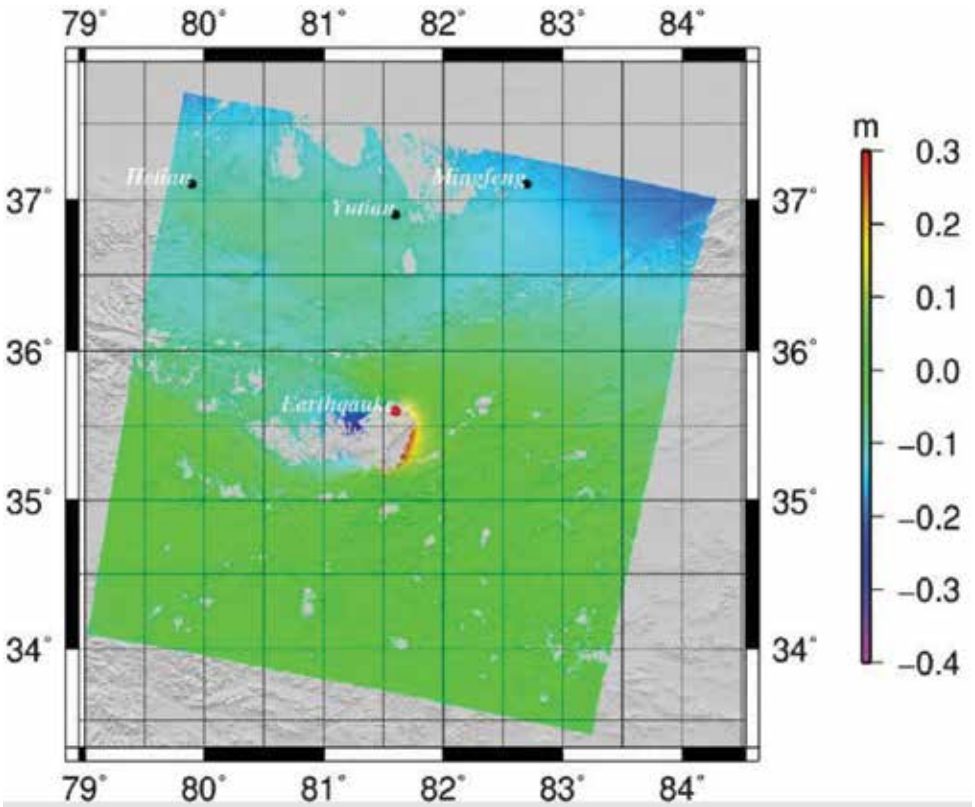

Figure 14. Wide deformation field of Yutian earthquake.

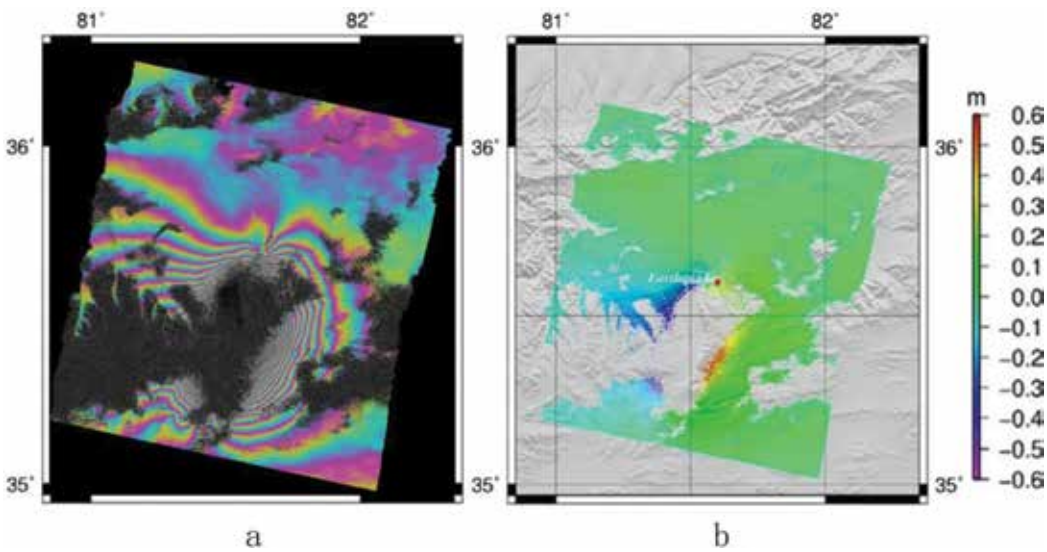

Figure 15. Result of IM mode for Yutian earthquake. (a) Interferogram. (b) Deformation result.

5. Conclusions

In this chapter, we studied several key techniques of monitoring large area deformation caused by earthquakes. The wider deformation fields of ScanSAR interferometry data were employed to monitor the land deformation after Wenchuan earthquake (2008) and Yutian earthquake (2008), respectively, in China. The results show that in the deformation field of Yutian earthquake, the maximum deformation of hanging wall for the fault is 0.41 m and the maximum of the footwall deformation value is 0.32 m. But in Wenchuan earthquake, its deformation field is greater than that of Yutian earthquake, which can preferably reflect the land deformation, especially for the deformation information of far fields. The max deformation value of the hanging wall part of the fault is 0.48 m, while that of the foot wall part is −0.42 m. These results agree well with our field investigations after the two earthquakes.

The result also indicates that ScanSAR mode can fully reflect the deformation field and the corresponding seismic geological structure characteristics. Although the conventional SAR interferometry method is relatively effective because of its narrow covering area, it is very important to explore the mechanism and the dynamics of earthquakes using wider deformation fields of ScanSAR images to monitor the land deformation caused by large earthquakes such as Wenchuan 2008 and Yutian 2008 earthquakes.

Acknowledgements

Data from the European Space Agency (ESA) and the ESA Earth Observation Missions Helpdesk Team are highly appreciated. This research is jointly supported by the Natural Science Foundation of China and Jangsu province (41004003, BE2016701, SH1506, SH1608, JC1604, Z2015013), the National Key Research and Development Program of China (Project Ref. No. 2016YFB0501501), the Priority Academic Program Development of Jiangsu Higher Education Institutions, and Qing Lan Project Sponsored by Overseas Training Plan of Outstanding Young and Middle-aged Teachers of Colleges and Universities in Jiangsu Province.

Conflicts of interest

The authors declare no conflict of interest. The founding sponsors had no role in the design of the study; in the collection, analyses, or interpretation of data; in the writing of the manuscript; and in the decision to publish the results.

Author contributions

Tinhchen Jiang and Yuanzhi Zhang conceived and designed the experiments; Xiuping Wang performed the experiments; TingchenJiang, Yu Li, and Yuanzhi Zhang analyzed the data and wrote the chapter.

Author details

Tingchen Jiang[1], Xiuping Wang[1], Yuanzhi Zhang[2,3]* and Yu Li[4]

*Address all correspondence to: yuanzhizhang@hotmail.com

1 School of Surveying and Mapping, Huaihai Institute Technology, Lianyungang, China

2 Chinese Academy of Sciences, Key Lab of Lunar Science and Deep-space Exploration, Beijing, China

3 Center for Housing Innovations, Chinese University of Hong Kong, Hong Kong

4 Faculty of Information Technology, Beijing University of Technology, Beijing, China

References

[1] Cumming IG, Guo Y, Wong FH. A comparison of phase-preserving algorithms for burst-mode SAR data processing. IEEE Geoscience and Remote Sensing Society'97. 1997; **2**:731-733

[2] Cumming IG, Wong FH. Digital Processing of Synthetic Aperture Radar Data: Algorithms and Implemention; 2005

[3] Ferretti A, Monti-Guarnieri A, Prati C, Rocca F. InSAR Principles: Guidelines for SAR Interferometry Processing and Interpretation. Netherlands: ESA Publications; 2007

[4] Guccione P. Interferometry with ENVISAT wide swath ScanSAR data. IEEE Geoscience and Remote Sensing Letters. 2006;**3**(3):377-382

[5] Ortiz AB, Zebker HA. ScanSAR-to-Stripmap mode interferometry processing using ENVISAT/ASAR data. IEEE Transactions on Geoscience and Remote Sensing. 2007; **45**(11):3468-3480

[6] Gudipati KV. Deformation monitoring using scanning synthetic aperture radar interferometry [PhD dissertation]. The University of Texas; 2009

[7] Johnson W. Magellan imaging radar mission to Venus. Proceedings of the IEEE. 1991; **79**:777-790

[8] Lemoine FG, Kenyon et al. The development of the joint NASA GSFC and the national imagery and mapping agency (NIMA) geopotential model EGM 96. NASA no.19980218814; 1998

[9] Chang CY, Jin MY, Lou Y-L, Holt B. First SIR-C scansar results. IEEE Transactions on Geoscience and Remote Sensing. 1996;**34**(5):1278-1281

[10] Bamler R, Geudtner D, Schattler B, Vachon PW. RADARSAT ScanSARInterferometry. In: Proceedings of the International Geoscience and Remote Sensing Symposium, IGARSS'99. Vol. 3. 1999. pp 1517-1521

[11] Guarnieri AM. ScanSAR interferometric monitoring using the PS technique. In: Proceedings of the ERS/ENVISAT Symposium; 2000

[12] Bamler R. Adapting precision standard SAR processors to ScanSAR. IGARSS. 1995;**3**: 2051-2053

[13] Guarnieri AM, Guccione P. Optimal "focusing" for low resolution ScanSAR. IEEE Transactions on GARS. 2001;**39**(3):479-491

[14] Guarnieri AM, Prati C. ScanSAR focusing and Intexferometry. IEEE Transactions on Geosclence and Remote Sensing. 1996;**34**(4):1029-1039

[15] Guarnieri AM, Rocca F. Combination of low- and high-resolution SAR images for differential interferometry. IEEE Transactions on Geoscience and Remote Sensing. 1999; **37**(4):2035-2049

[16] Shen ZK, Sun JB, Zhang PZ. Slip maxima at fault junctions and rupturing of barriers during the 2008 Wenchuan earthquake. Nature Geoscience. 2009;**2**:717-724

[17] Xu CJ, Wang H, Jiang GY. Study on crustal deformation of Wenchuan Ms8. 0 earthquake usingwide-swath ScanSAR and MODIS. Geodesy and Geodynamics. 2011;**2**(2):1-6

[18] Lemoine FG, Kenyon SC, Factor JK. The development of the joint NASA GSFC and NIMA geopotential model EGM96, NASA technical paper, Nasa/TP-1998-206861; 1998

[19] Shi C, Lou Y, Zhang H, Zhao Q, Geng J, Wang R, Fang R, Liu J. Seismic deformation of the mw 8.0 Wenchuan earthquake from high-rate GPS observations. Advances in Space Research. 2010;**46**(2):228-235. DOI: 10.1016/j.asr.2010.03.006

[20] Burchfiel BC. A geological and geophysical context for the Wenchuan earthquake of 12 May 2008. GSA. 2008;**18**:4-11

[21] Hashimoto M, Enomoto M, Fukushima Y. Coseismic deformation from the 2008 Wenchuan, China, Earthquake derived from ALOS/PALSAR images. Tectonophysics. 2009, 2010; **491**(1-4):59-71

[22] Wang W-M, Zhao L-F, Li J, Yao Z-X. Rupture process of the Ms 8.0 Wenchuan earthquake of Sichuan¸ China. Chinese Journal of Geophysics. 2008;**51**:1403-1410

[23] Wei M, Sandwell D, Smith-Konter B. Optimal combination of InSAR and GPS for measuring interseismic crustal deformation. Advances in Space Research. 2010;**46**(2):236-249. DOI: 10.1016/j.asr.2010.03.006

[24] Song XG, Shan X, Qu C, Zhang G, Guo L, Zhang G. Coseismic surface deformation casused by the Wenchuan M8 earthquake from InSAR data analysis. IGARSS2009, III: pp. 69-73; 2009

[25] Zhang Y, Feng WP, Xu LS, Zhou CH. Spatio-temporal rupture process of the 2008 great Wenchuan earthquake. Science in China Series D: Earth Sciences. 2009;**52**(2):145-154

[26] Wu L, Xiao AC, Wang LQ. EW-trending uplifts along the southern side of the central segment of the AltynTagh fault, NW China: Insight into the rising mechanism of the Altyn Mountain during the Cenozoic. Science China Earth Sciences. 2012;**55**:926-939. DOI: 10.1007/s11430-012-4402-7

Chapter 9

Applications of Remote Sensing in Geoscience

Hakim Saibi, Mohand Bersi,
Mohamed Bodruddoza Mia,
Nureddin Mohamed Saadi,
Khalid Mohamed Saleh Al Bloushi and
Robert W. Avakian

Additional information is available at the end of the chapter

http://dx.doi.org/10.5772/intechopen.75995

Abstract

Remote sensing is becoming an important and useful tool in mapping large, remote areas and has many applications in geosciences such as geologic and geo-structural mapping, mineral and water exploration, hydrocarbon exploration, natural hazards analysis, and geomorphology. The recent advances in remote-sensing imaging acquisition and availability of images can help geoscientists to explore and prepare maps quickly and evaluate the geo-potential of any specific area on the globe. Advances in remote-sensing data analysis techniques have improved the capacity to map the geological structures and regional characteristics and can serve in mineral exploration in complex and poorly understood regions. In this chapter, geophysical remotely sensed data (airborne geophysics) are integrated with other sources of remotely sensed data to analyze three separate areas, one each for geological structure, lineament presence and orientation, and geothermal potential. Three case studies are discussed in this chapter from three countries—Afghanistan, United Arab Emirates, and Algeria—to show the effectiveness of remote sensing in mapping and detecting geo-structural, geomorphological, and geothermal characteristics of ground surfaces.

Keywords: remote sensing, geological structures, geothermal exploration, remote areas

1. Introduction

Airborne remote sensing could be said to have started in 1858 when French balloonist Gaspard-Felix Tournachon took a photo of Paris from above. Sensors have ridden over time on balloons, to kites, to various aircraft, rockets, and finally on satellites. Sensor technology has come a long way from cameras and film, and we can now detect the entire useful electromagnetic spectrum, as well as gravity and magnetics themselves.

There are a number of advantages in using remote sensing. These include large existing databases such as Landsat and Satellite Pour l'Observation de la Terre (SPOT21); the ability to get regional views of large areas; ease of combining information from multiple sensors; no difficulty or danger in covering remote areas; availability of sophisticated computer analysis programs; a wide selection of energy bands (e.g., Infrared, ultraviolet, etc.) and of vital importance, low cost, and high speed.

Today's wide assortment of sensors allows interpreters to overlay, combine, or even subtract sensors in the search of meaningful maps. Spectral signatures of various plants and common rocks and minerals are well established, allowing remote reconnaissance to identify areas favorable for energy and mineral exploration or expand such areas through sensing techniques. This chapter shows only a small sample of what can be done with remote sensing, and the capabilities of these methods will only increase with time.

2. Application of remote sensing and remote geophysics to geological structural investigations in Aynak-Logar valley, Afghanistan

2.1. Introduction

The Aynak-Logar valley (ALV) is located around 30 km south of the capital city of Afghanistan (Kabul) (**Figure 1**). ALV is an area rich in cobalt, chromium, and copper, and other minerals (**Figure 2**). To detect the geo-structural features and understand their relationship with mineralization in this study area, remote-sensing and geophysical techniques were used.

Integrating remote-sensing and geophysical data has the potential to define the quantitative details of hitherto unknown areas and reduce the ambiguity of geological interpretation [1–5]. The results from remote-sensing and geophysical interpretation will support future mining exploration and development studies.

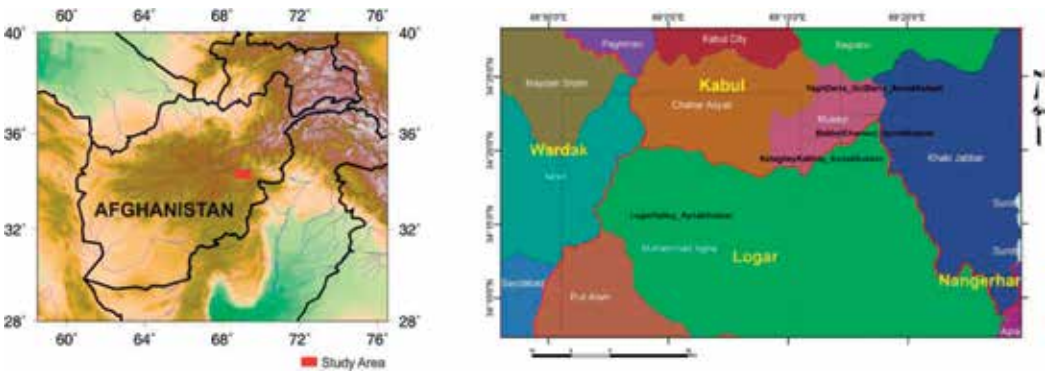

Figure 1. (left) Location of ALV study area in Afghanistan. (Right) ALV study area, red line shows the province boundary and the different districts as color coded.

http://dx.doi.org/10.5772/intechopen.75995

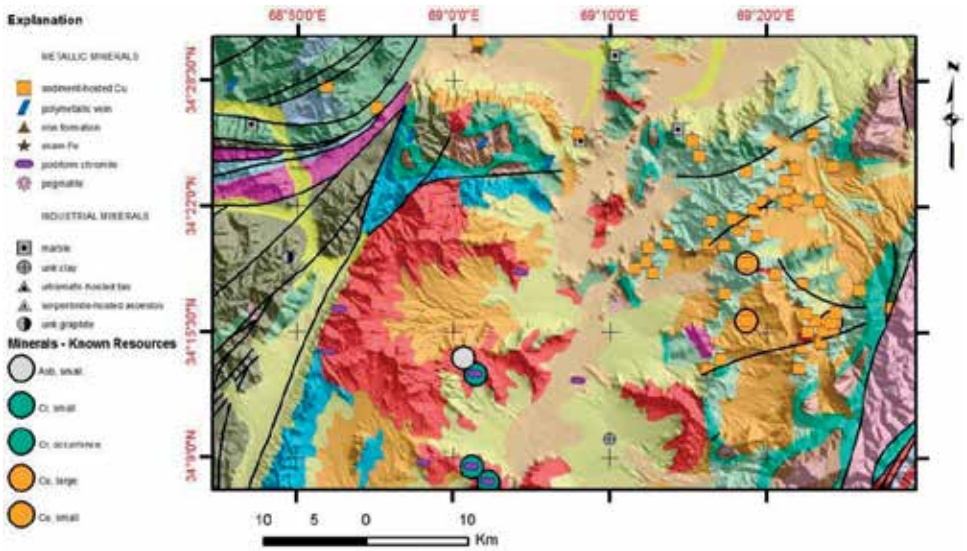

Figure 2. Map showing the mineral and structural information of the study area.

Geophysical data consist of aeromagnetic data obtained from the US Geological Survey (USGS) and processed using Geosoft Oasis Montaj Ver. 8. A magnetic survey is a powerful method to study the location of faults and other geological structures (dykes, intrusions) and is routinely applied in mining exploration surveys [6]. The remote-sensing data were processed using Earth Resource (ER) Mapper Ver. 7.

The Euler deconvolution (ED) method was applied to the aeromagnetic data with the objective of making geological features such as faults, contacts, and dykes more visible and of estimating their depth where possible.

Geologically, the exposed rocks in the core of anticline in ALV are metamorphic, mainly amphibolites, and gneiss, and belong to Welayati Formation (Fm). The Loy Khwar Formation overlies the Welayati Fm and is composed of metasedimentary sequences and hosts the copper mineralization in ALV.

Structurally, the Aynak-Logar Valley region is a pull-apart, post-orogenic basin resulting from the transpressive phase of two major sinistral shear faults, likely of Triassic age, trending in the NNE-SSW direction, while the main stress is in the NW-SE direction. The NW-SE compression causes on echelon folds in the NE-SW direction, with Triassic centers, sigmoidal in shape, and parallel to the edge of the major shear faults of NNE-SSW direction. This is due to the intensity of the deformation near the shear zone. The extension is represented by a NW-SE-oriented horst and graben structure that is the origin of the intrusion of ultramafic rocks into this region. The presence of normal faults at the boundaries of the horst and graben structures and their role in the intrusion of such rocks explain the presence of copper at the edges of these faults. The NE-SW faults are synthetic, with the major sinistral fault in the NNE-SSW direction. N-S faults are also synthetic to the major faults. During the Eocene,

NE-SW folds were created and present evidence of another deformational stage at that time but with NW-SE compression. The Pliocene-Oligocene forms an unconformity with Paleozoic and Triassic formations.

2.2. Materials and methods

2.2.1. Remote-sensing data

2.2.1.1. Landsat-enhanced thematic mapper plus (ETM+)

Landsat-7 was launched on April 15, 1999, from the Western Test Range aboard a Delta-II expendable launch vehicle. At launch, the satellite weighed approximately 2200 km. The spacecraft is about 4.3 m long and 2.8 m in diameter [7]. The Enhanced Thematic Mapper Plus (ETM+) instrument on board this spacecraft is an eight-band multispectral scanning radiometer (**Table 1**) capable of providing high-resolution imaging information of the earth's surface. It detects spectrally filtered radiation at visible, near-infrared, mid-infrared, and thermal infrared frequency bands from the sunlit earth in a 183 km-wide swath when orbiting at an altitude of 705 km ([7]). Nominal ground sample distances or "pixel" sizes are 15 m in the panchromatic band; 30 m in the 6 visible, near and mid-infrared bands; and 60 m in the thermal infrared band [7]. The satellite orbits the earth at an altitude of approximately 705 km with a sun-synchronous 98-degree inclination and a descending equatorial crossing time of 10 in the morning, with a repeat coverage interval of 16 days (233 orbits).

2.2.1.2. Shuttle radar topography mission

The Shuttle Radar Topography Mission (SRTM) obtained elevation data on a near-global scale to generate the most complete high-resolution digital topographic database of the Earth [8]. SRTM consisted of a specially modified radar system that flew onboard the Space Shuttle Endeavour during a 11-day mission in February of 2000. SRTM is an international project spearheaded by the National Geospatial-Intelligence Agency (NGA), National Aeronautics and Space Administration (NASA), the Italian Space Agency (ASI), and the German Aerospace Center (DLR). There are three resolution outputs available, including 1-km and 90-m spatial

	Wavelength (μm)	EM region	Spatial resolution
1	0.45–0.52	Blue	30 m
2	0.52–0.60	Green	30 m
3	0.63–0.69	Red	30 m
4	0.76–0.90	Near-infrared	30 m
5	1.55–1.75	Middle-infrared	30 m
6	10.40–12.50	Thermal infrared	60 m
7	2.08–2.35	Middle-infrared	30 m
8	0.52–0.90	Panchromatic	15 m

Table 1. Radiometric characteristics of ETM+ sensors.

resolutions for the world and a 30-m spatial resolution for the US. The Global Land Cover Facility (GLCF) serves the main USGS editions and has "enhanced" editions. It also provides editions in WRS-2 tiles to approximate Landsat scenes. In this study, the 90-m resolution SRTM (WRS-2) data (**Table 2**) were used to derive the topographic features of the study areas.

2.2.2. Aeromagnetic data

The aeromagnetic data for the Aynak region were acquired in 2006 and 2008 by the USGS and the Naval Research Laboratory (NRL) [9, 10]. Lines were spaced 4 km apart and were flown at heights of 5 km or more, which is higher than ideal. The aeromagnetic data were reduced to the pole (RTP) using a magnetic inclination of 48.74 and a declination of 2.01 degrees.

2.2.3. Data analysis and data integration

Two Landsat-Enhanced Thematic Mapper Plus (ETM+) images were used for analysis **(Figure 3**). Three types of contrast stretching were tested by using a mathematical function to map the pixel values to new, enhanced values: linear stretch, histogram stretch, and special stretch [11]. These methods were used to enhance the contrast between lithological units in the study area and enhance the printed geological map. The transformation technique Hue-Intensity-Saturation (HIS) was applied to differentiate rock units in ALV. The HIS components (blue, red, and green) were allocated, respectively, using ETM bands: 631, 743, and 763 [12]. The variance of the bands was calculated by the optimum index factor (OIF) method [13].

Edge enhancement was applied to the ETM+ image to detect edges, and then these enhancements were added back into the original images to increase contrast in the vicinity of an edge [14]. Individual panchromatic band (15 m) applications of the edge detection filter (Laplacian of Gaussian filter) were tested for lineament identification. Principal component analysis (PCA) was also applied to the ETM+ image to reduce the number of variables in the dataset, while retaining most of the original variability in the data.

PCA transforms the data into a set of uncorrelated random variables that capture all of the variance of the original dataset and assign as much variance as possible to the fewest number of variables. PCA is a very effective method for analyzing multispectral satellite imagery. PCA transforms the original image bands into uncorrelated output bands. PCA is often used

Satellite	Sensor	Capture resolution	Pixel resolution
Space Shuttle Endeavor	C-band and X-band	1 arc second	30 m
		3 arc second	90 m
		30 arc second	1 km
Scene Type	Scene Size		Projection
Degree	1 degree latitude × 1 degree longitude		Geographic
WRS-2	185 km × 185 km		UTM
Mosaic	Global		Geographic

Table 2. Sensor and product characteristics of SRTM data.

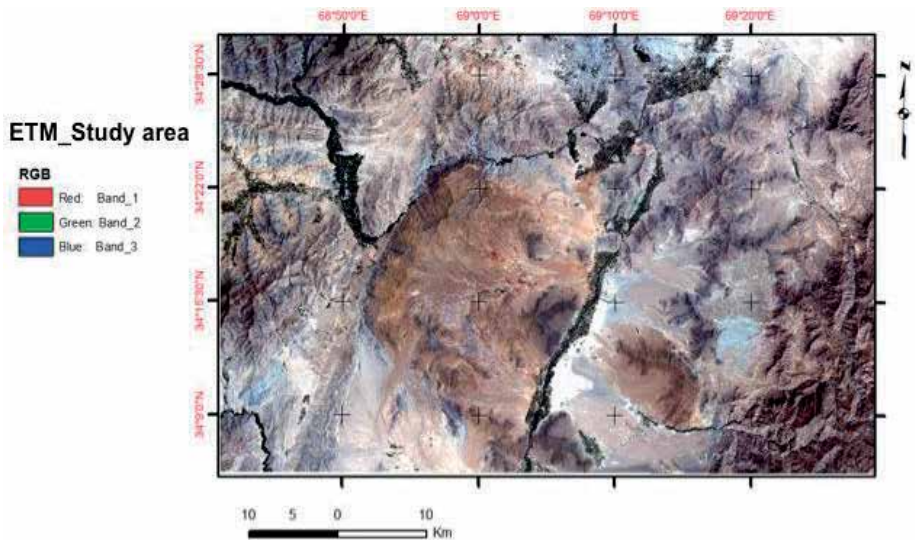

Figure 3. ETM map of the study area.

for dimensionality reduction and for creating color composite images with maximum information content. **Figure 4** shows the PCA map of the study area.

The Landsat ETM+ band combinations RGB-742 (red, green, blue) (SWIR-VNIR composite), RGB-543 (SWIR-NIR-VIR composite), and RGB-748 (SWIR-NIR-Panchromatic composite) were overlain on shaded relief maps to improve the possibility of lineament extraction [15]. The selected combinations have the advantage of preserving morphological features as well

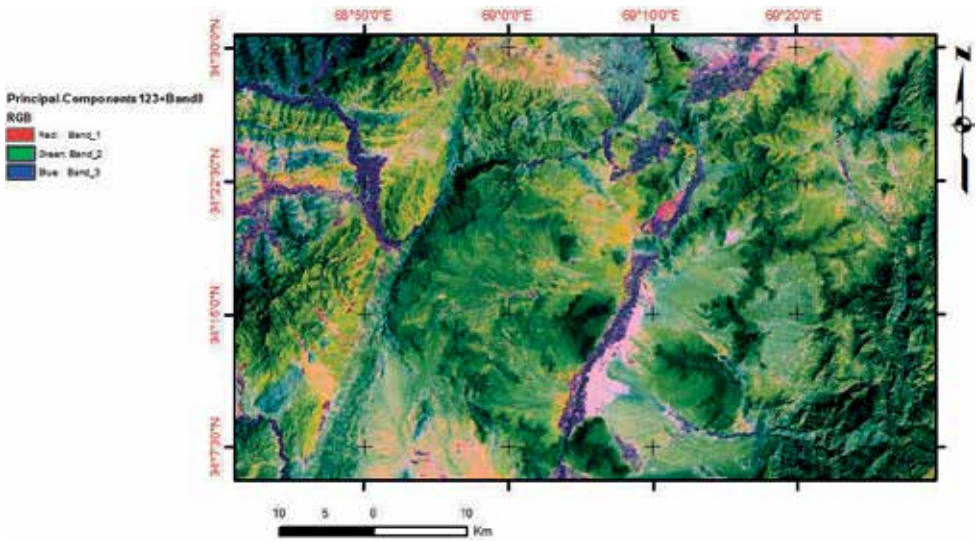

Figure 4. PCA map of the study area.

as displaying different lithological units in various colors because bands within the very near-infrared (VNIR) and shortwave infrared (SWIR) portions of the electromagnetic spectrum were used [16].

The shaded relief maps were used to simulate shading effects that were caused by the sun azimuth and elevation [17]. In this study, we experimented with an evaluation using an incoming illumination that is perpendicular to the prevailing trend of lineaments in the study area. Lineament identification has become increasingly valuable to structural recognition [18, 19].

Shaded relief maps were constructed from the SRTM Digital Elevation Model (DEM) by varying the azimuth and elevation of simulated sun illumination [20]. ETM+ VNIR color composites were overlaid on SRTM map to enhance lineaments identified in the ALV.

Lineaments were manually extracted based on photographic characteristics, such as shape (size, pattern, shadow, tone and texture) and geomorphologic features (fault-scarp, straight valley and drainage patterns).

The extracted lineaments were statistically analyzed to create rose diagrams and to evaluate differences in lineament direction and density. The analysis and interpretation of the extracted lineament lengths and trends, based on the age of the geological formations, provided useful information about the tectonic evolution of the study area.

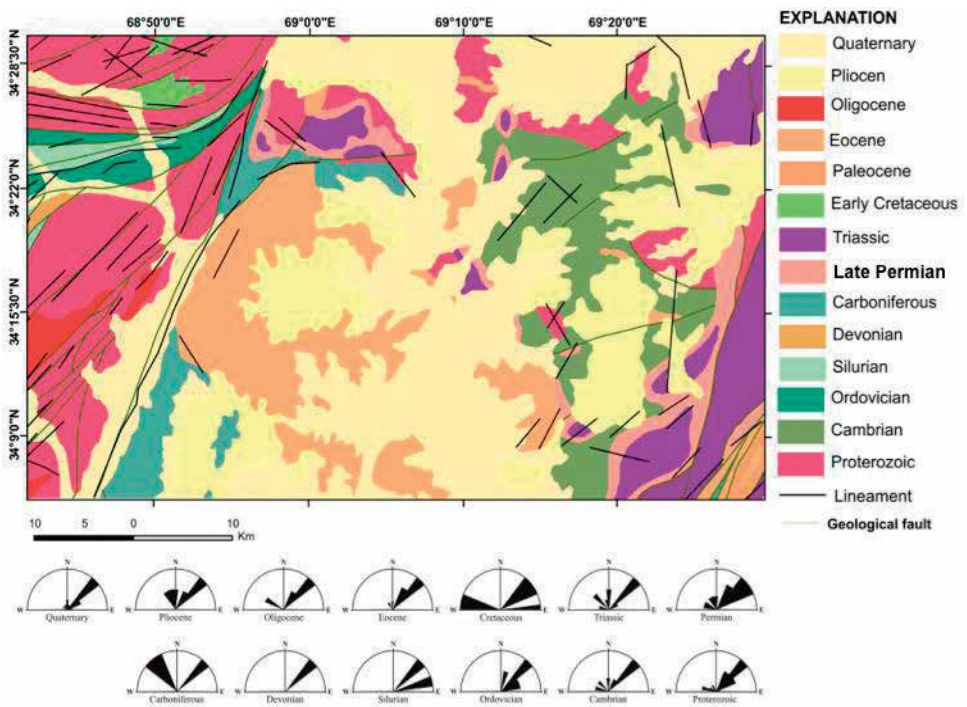

Figure 5. Geological map of the study area including the locations of geological faults [24–26] and interpreted lineaments from the remote-sensing data for the different geological ages from Proterozoic to Quaternary. The NE-SW geological-structural trend is present and the extracted lineaments run dominantly in the NE direction.

The aeromagnetic data were interpreted using Euler Deconvolution in order to determine the depth of geo-structural features (faults, contacts, dykes) and their location. The method was developed by [21, 22].

2.3. Results and discussions

Extracted lineaments were divided into 13 groups based on the age of the geological formations. The rocks of each geological age were classified as one unit and presented in one color group (**Figure 5**). The geological formations were cut by the extracted lineaments—Proterozoic, Cambrian, Ordovician, Silurian, Devonian, Carboniferous, Permian, Triassic, Cretaceous, Eocene, Oligocene, Pliocene, and Quaternary. Interpretation of these lineaments was based on the principle of crosscutting relationships [23]. The lineaments of each geological age were individually statistically analyzed to create rose diagrams. **Figure 6** presents the density map showing the location of lineaments from remote sensing. The interpreted faults from remote sensing are trending in the NE direction, which is in agreement with the trend of geological faults (**Figure 7**).

Figures 8 and **9** show the Euler solutions for a structural index (SI) of 0 and 1, respectively. The depths to the faults are ranging from 250 m to 2.5 km. The detected faults are located at borders of high magnetic anomalies and in agreement with the observed geological faults and interpreted remote-sensing geo-structural features.

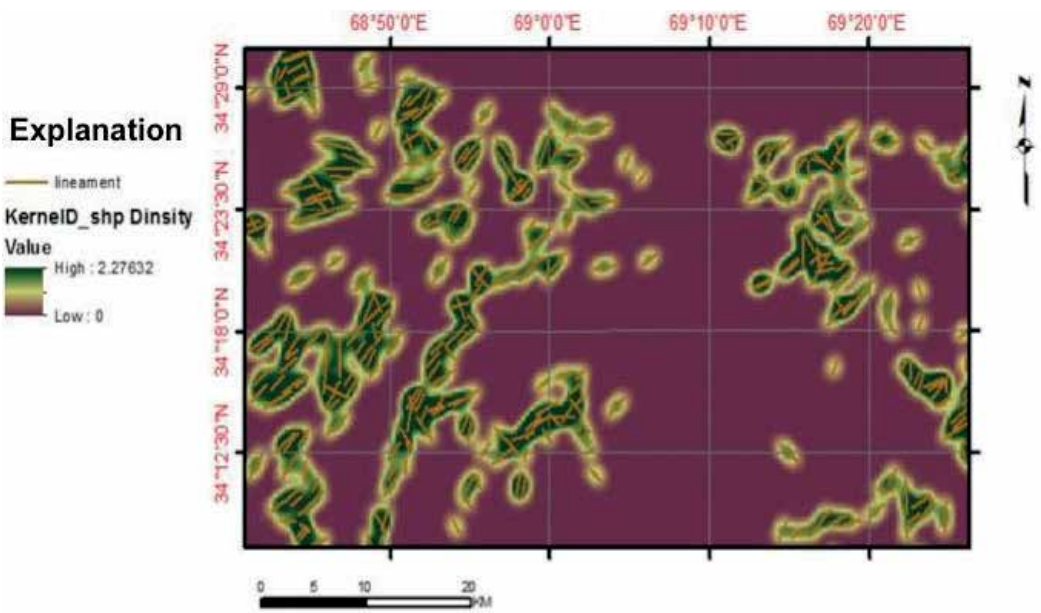

Figure 6. Lineament density map extracted from the shaded maps based on 30-m DEM data and natural-color Landsat imagery in the study area.

http://dx.doi.org/10.5772/intechopen.75995

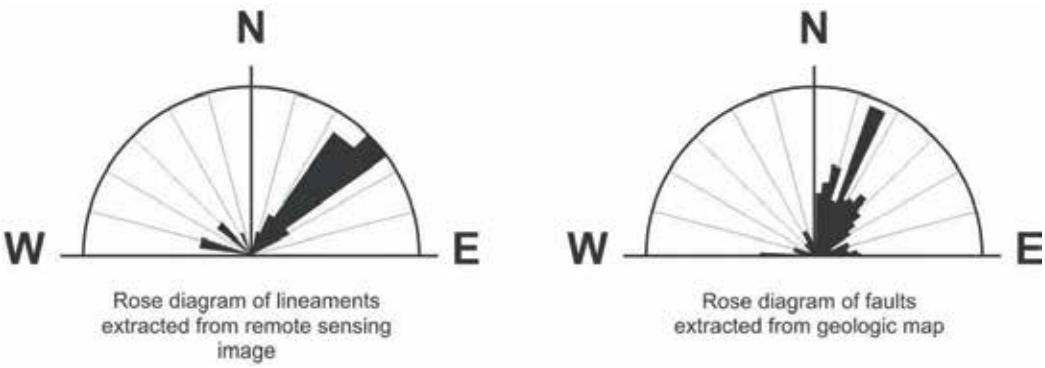

Figure 7. Rose diagrams extracted from geological map and shaded maps of the study area.

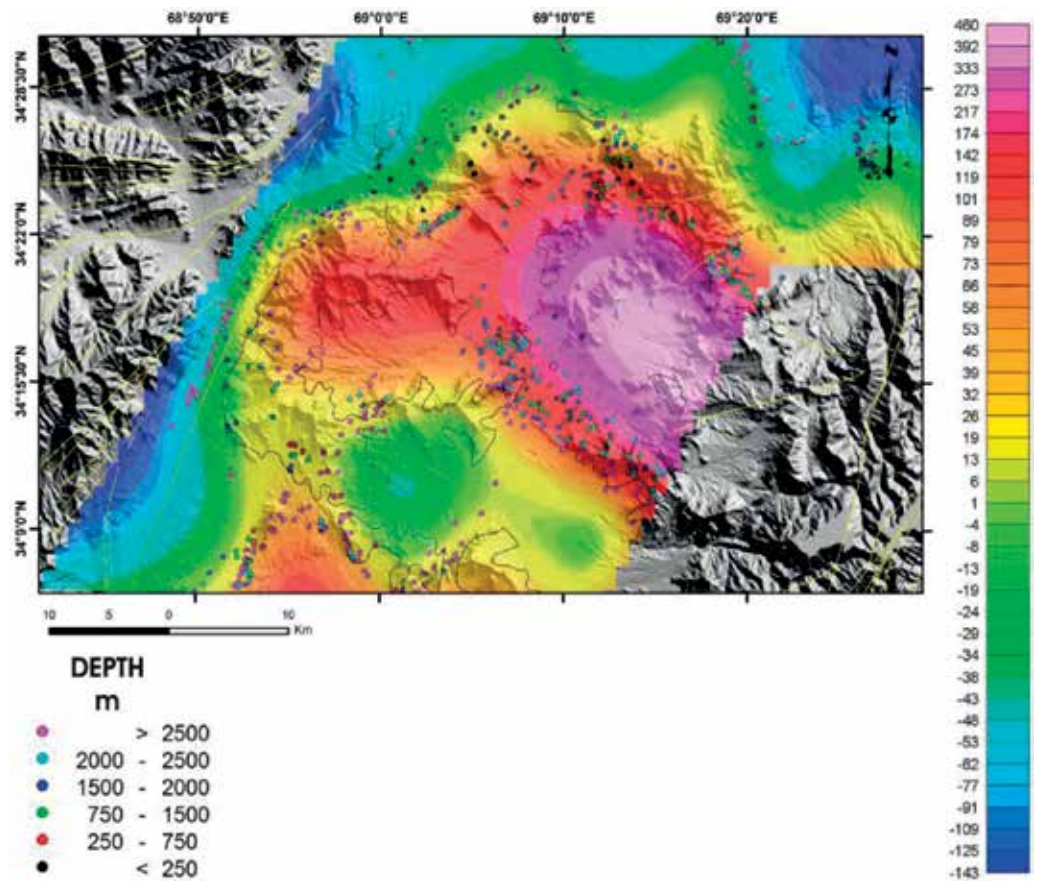

Figure 8. Euler deconvolution map of the study area with SI = 0. The background represents the RTP aeromagnetic map in nT overlaid on the SRTM map. Yellow lines represent geological faults.

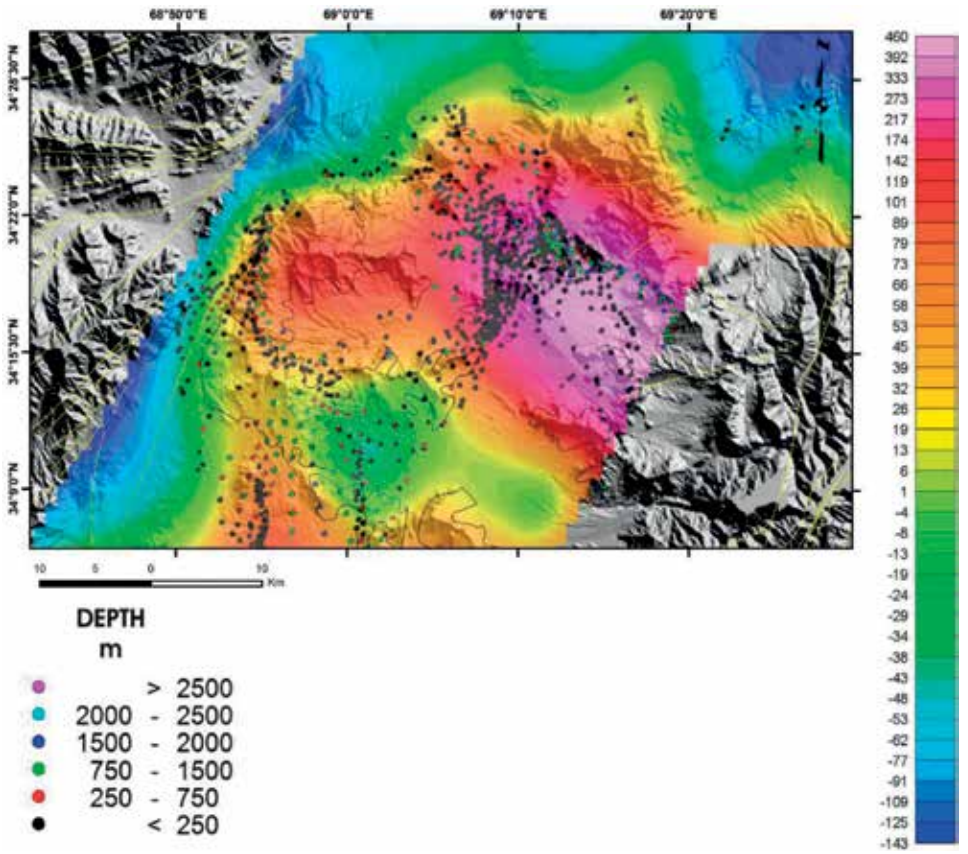

Figure 9. Euler deconvolution map of the study area with SI = 1. The background represents the RTP aeromagnetic map in nT overlaid on the SRTM map. Yellow lines represent geological faults.

3. Application of remote sensing in geothermal exploration: a case study at Mubazzarah Green Park hot spring area, Al-Ain city, United Arab Emirates

3.1. Introduction

Remote sensing is an essential technique for investigating geothermal ground, volcanic, or hot spring areas considering the unstable ground, and in this case, poor accessibility due to a national park. In addition, spatial analysis and repetitive monitoring of the thermal status can be done at lower cost than ground techniques. Satellite remote sensing offers the possibility to map land surface and vegetation variables in a thermal ground, volcanic, or hot spring areas such as hydrothermal altered minerals, land surface temperature (LST), emissivity, radiative heat flux (RHF) and land cover, and so on. [27]. Landsat satellite images (TM/ETM+) have a long history of use in volcano monitoring, considering hydrothermal alteration, heat flux, and thermal anomaly mapping over the whole world [28–35].

To provide a continuous monitoring of our environments, Landsat program launched a new satellite on February 11, 2013, that is, Landsat 8 with Operational Land Imager/Thermal Infrared Sensor (OLI/TIRS) sensors providing a total of 11 spectral bands: 9 OLIs and 2 TIRS bands. Landsat 8 sensors acquire images of both day and nighttime with a revisit time of 16 days for the same region. The OLI sensor collects data at 30-m resolution in visible, near-infrared, and shortwave infrared as well as a 15-m resolution panchromatic band. In addition, this sensor has a 30-m coastal aerosol band and 30-m cirrus band for cloud detection [36–38].

3.2. Materials and methods

In this case study, we applied the Landsat 8 Operational Land Imager (OLI)/thermal Infrared Sensor (TIRS) image to investigate the land use—land cover, emissivity, land surface temperature, and radiative heat flux of the Mubazzarah Green park hot spring area in Al-Ain city, United Arab Emirates (UAE) (**Figure 10**). The Landsat 8 OLI/TIRS image was acquired on December 1, 2016, and obtained from United States Geological Survey (USGS) archives free of cost. It has nine OLI bands of 30-m spatial resolution and two TIRS bands of 100-m spatial resolution. Land use-land cover (LULC) of the study area was mapped using Normalized Directional Vegetation Index (NDVI) value using the equation of NDVI = ρ_{nir}-ρ_r/ρ_{nir} + ρ_r; where ρ_{nir} is the reflectance of near-infrared band and ρ_r is the reflectance of the red band [27]. The NDVI value is a unitless ratio and ranges from +1 to −1. It is divided into four land cover classes: water body (NDVI <0), bared land/desert (NDVI = 0–0.2), mixed land (NDVI = 0.2–0.5) and vegetated (NDVI >0.5) [27]. The emissivity values in this region were calculated using the NDVI threshold method [39]. The Landsat 8 TIRS sensor has two thermal bands of 100 m in spatial resolution. We used band 10 of the sensor for land surface temperature estimation using the Mono-window algorithm [35, 39]. Radiative heat flux (RHF) was estimated by

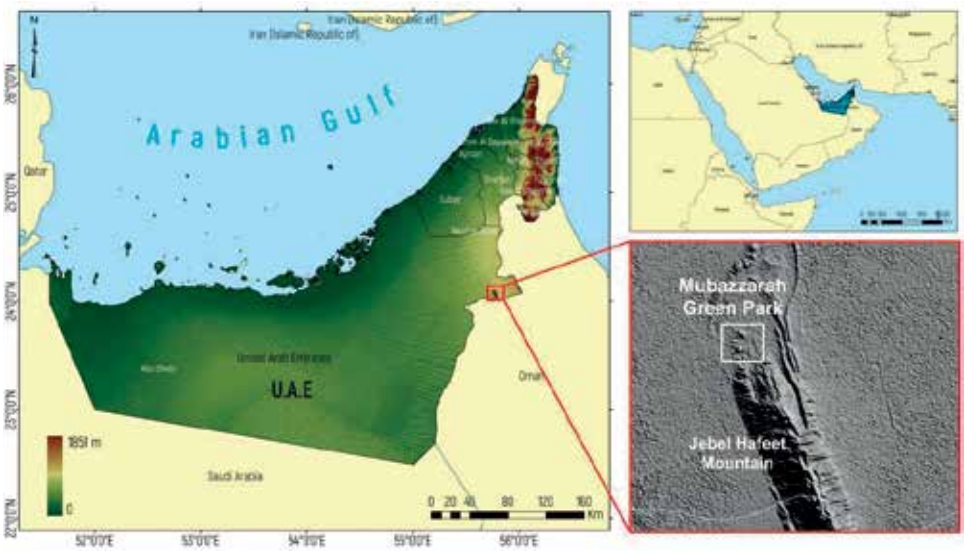

Figure 10. Location of study area.

using the Stefan-Boltzmann equation, that is, $Q_r = \tau\ \varepsilon\ A\ (T_s^4 - T_a^4)$, where Q_r = radiative heat flux (W/m^2), τ = atmospheric transmissivity, σ = Stefan-Boltzmann constant, ε = emissivity, A = area (m^2), Ts = land surface temperature (k), and Ta = ambient temperature (k) [27]. Meteorological data were collected from local meteorological station in the UAE including relative humidity (42%), ambient temperature (27°C), and so on. The atmospheric transmissivity during image acquisition was calculated using the NASA calculator. We obtained an atmospheric transmissivity of about 0.78 during the image acquisition of the study area.

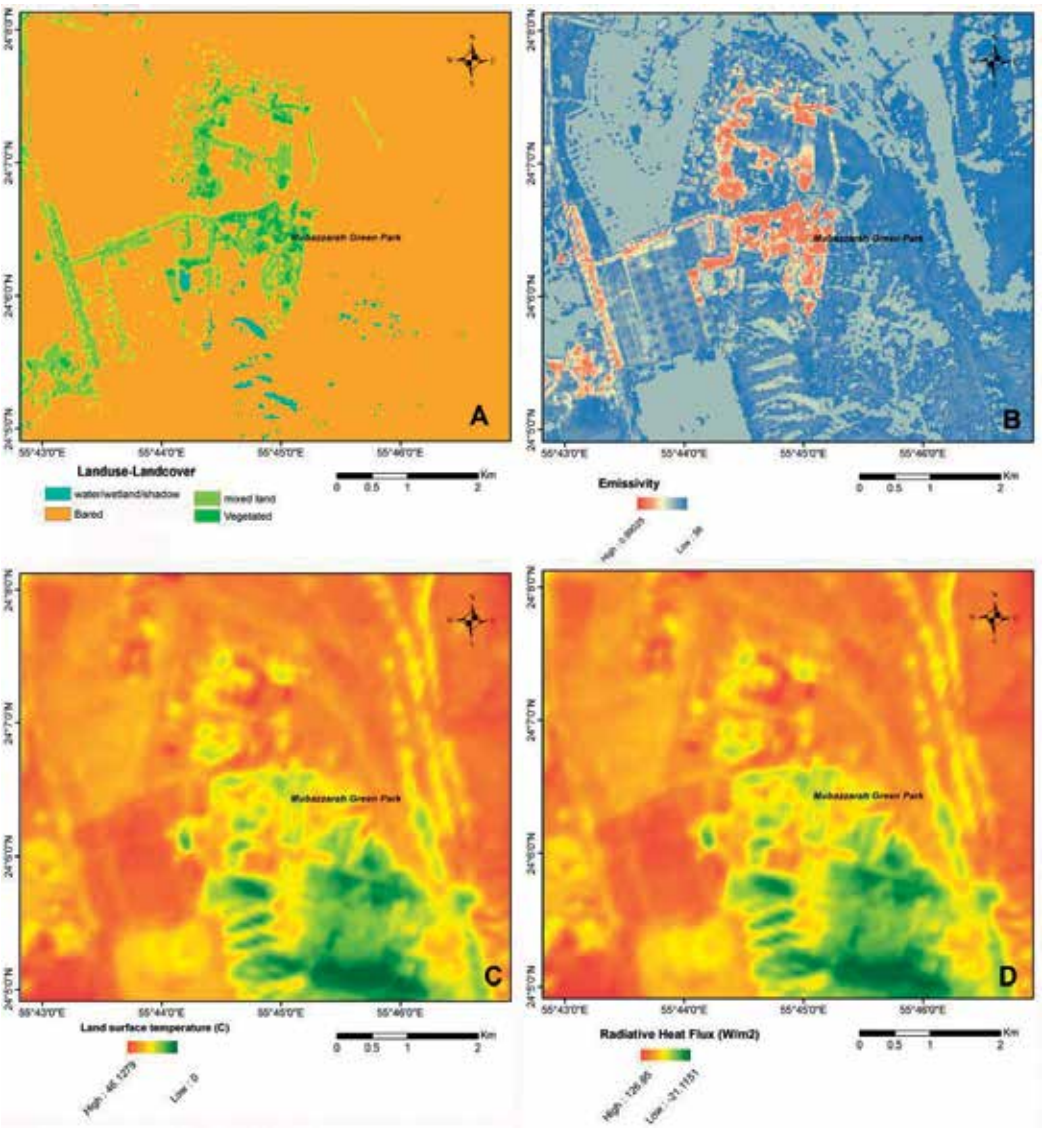

Figure 11. Remote-sensing application in the green Mubazzarah Park area in Al-Ain city, UAE. (A) LULC, (B) emissivity, (C) LST, (D) RHF.

3.3. Results and discussions

Total study area is the 43km^2 in and around the green Mubazzarah park area in Al-Ain City, UAE. The LULC result shows that the water bodies cover about 112 hectares, that is, 2.63% of the study area (**Figure 11A**). The largest LULC is the bare or desert land covering about 3721 hectares or 87.42% of the study area. The smallest LULC is the healthy vegetated region, which covers an area of about 59.4 hectares or 1.4% of the total study area. The mixed land, that is, the pixel area (30 × 30 m), contains some vegetation or some bare land or water, is present over about 364.14 hectares or 8.55% of the total study region (**Figure 11A**).

The calculated emissivity value ranges from 0.98 to 0.99025 for the land covers of this study area (**Figure 11B**). The highest land surface temperature (LST) obtained was about 46°C in the hot spring region of the green Mubazzarah Park shown as bright red color in the **Figure 11C**. The lowest LST was about 23.44°C shown as green color in the figure. We obtained the highest and lowest RHF of the study area, respectively, which was about 127 and − 21 W/m^2 using the Stefan-Boltzmann equation (**Figure 11D**). The calculated total radiative heat loss was about 1927 MW. The total heat discharge rate after multiplying the total RHL using the relationship coefficient (6.49) was about 12,507 MW. In conclusion, the study confirmed that the applied methods and images are adequate to explore and monitor (if possible) the thermal status of any geothermal area like this hot spring region with less time and low cost.

This is an ongoing experimental project. Ground truth data is not available at the time of writing. Ground truthing or accuracy assessment is an important part of remote-sensing applications; it may be added as part of further studies or developments.

4. Application of remote sensing in mining and geological investigations, case study: southern part of Algeria

This case study shows an example of the application of remote sensing to geological and mineralogical mapping of the Central Atlantic Magmatic Province (CAMP) formations in southern Algeria. Remote-sensing techniques such as principal component analysis (PCA), band ratios, band math, and target detection wizard can detect different mineral resources and interesting geological structures [40]. In this section, we present applications of different remote-sensing methods to map the mineral resources of the CAMP formations in southern Algeria using Landsat 8 OLI multispectral images. The remote-sensing analysis allows us to create a photo-lithological map of the study area presenting sills and dykes. The CAMP formations are associated to these large doleritic sills and long dikes.

4.1. General location and objectives of the study

The study area is located in the southwestern part of Algeria on the north flank of Tindouf basin (**Figure 12**). The north flank of the Tindouf basin contains two distinct regions. There is a high elevation region, which corresponds to the Hamada of Dra and a low elevation region situated in the Zemoul depression. The Zemoul depression is characterized by a steep relief, so a remote-sensing approach is the best way to map the CAMP outcrops in that region.

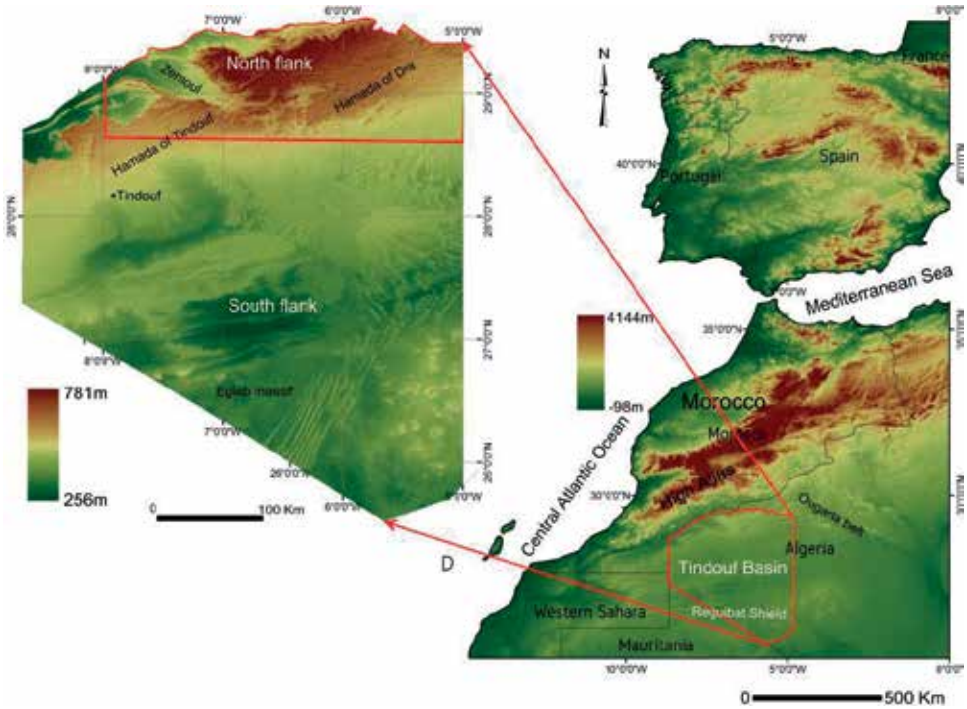

Figure 12. General location map of the study area.

4.2. Geological setting

The stratigraphic sequence in the study area consists of Paleozoic rocks [41, 42]. The main ages of the outcropping formations are Carboniferous and Devonian. The Carboniferous formations are mainly sandstone, while the Devonian formations are primarily clay sediments. The CAMP formation is in the form of doleritic sills and dykes, the most important mass of dolerites outcrop in the Devonian (**Figure 13**).

4.3. Remote-sensing analysis

The Operational Land Imager (OLI) multispectral images were used to enhance and highlight the geological and structural features in the study area. The image processing techniques such as band ratios, principal components analysis (PCA), target detection wizard, and band math have proved to be a strong tools for mapping geological features for mineral exploration purposes [40, 44].

4.3.1. Band ratios

Ratio is a powerful image processing technique, in that it allows discrimination between different lithological features. It is based on the division of the radiometric value of one band by the radiometric value of the same pixel of another band. The 7/1, 5/3, and 4/2 ratios have been selected to display in RGB mode (**Figure 14**).

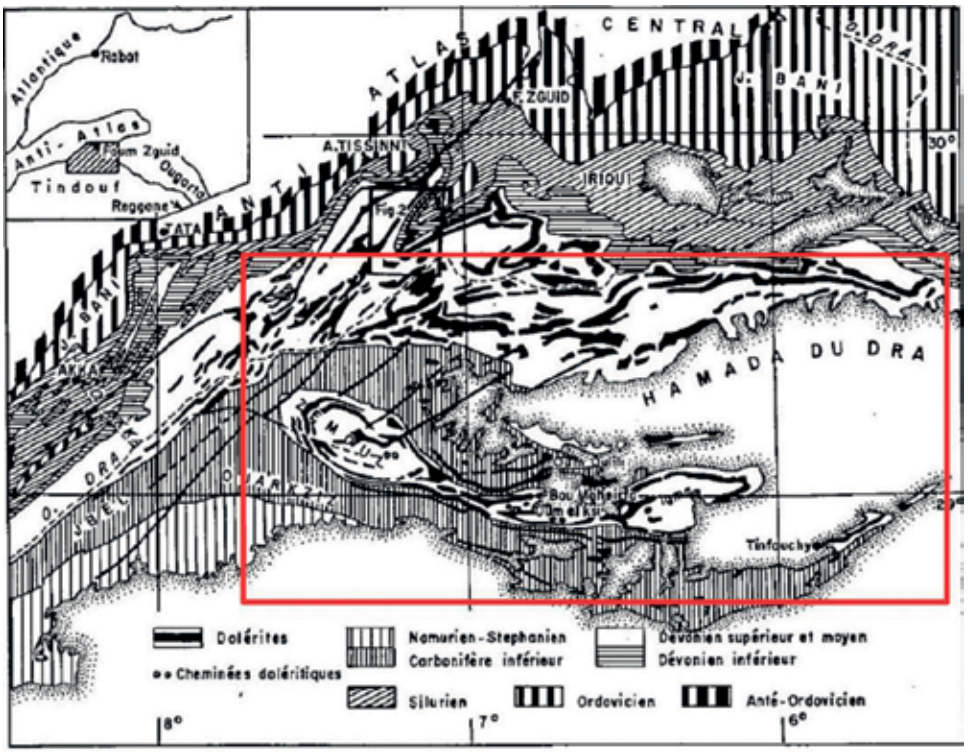

Figure 13. Geological map of the northern part of the Tindouf basin [43].

The ratio process highlighted the dolerites with dark green color; they are in the form of sills and long dykes. The Paleozoic are in shades of light green.

4.3.2. Principal components analysis (PCA)

The PCA technique is widely used in remote-sensing studies. The land cover reflectance in the OLI multispectral bands may present data redundancies, which can be avoided by using PCA analysis. It transforms an original correlated dataset into a substantially smaller set of uncorrelated variables that represents most of the information present in the original dataset [45]. The three first components, containing a large amount of information, were selected for RGB display (**Figure 15**).

The principal component analysis allows us to distinguish between different terrain aspects; the dolerites are in light yellow to white shades. The Paleozoic rocks appear in shades of magenta. This analysis shows that the intersection of the NE trending dykes with the center of the Zemoul antiform creates circular forms, which may correspond to the mineralization area.

4.3.3. Target detection wizard

The target detection wizard process allowed the detection of mineral targets by using specific algorithms such as adaptive coherence estimator (ACE) and spectral angle mapper (SAM).

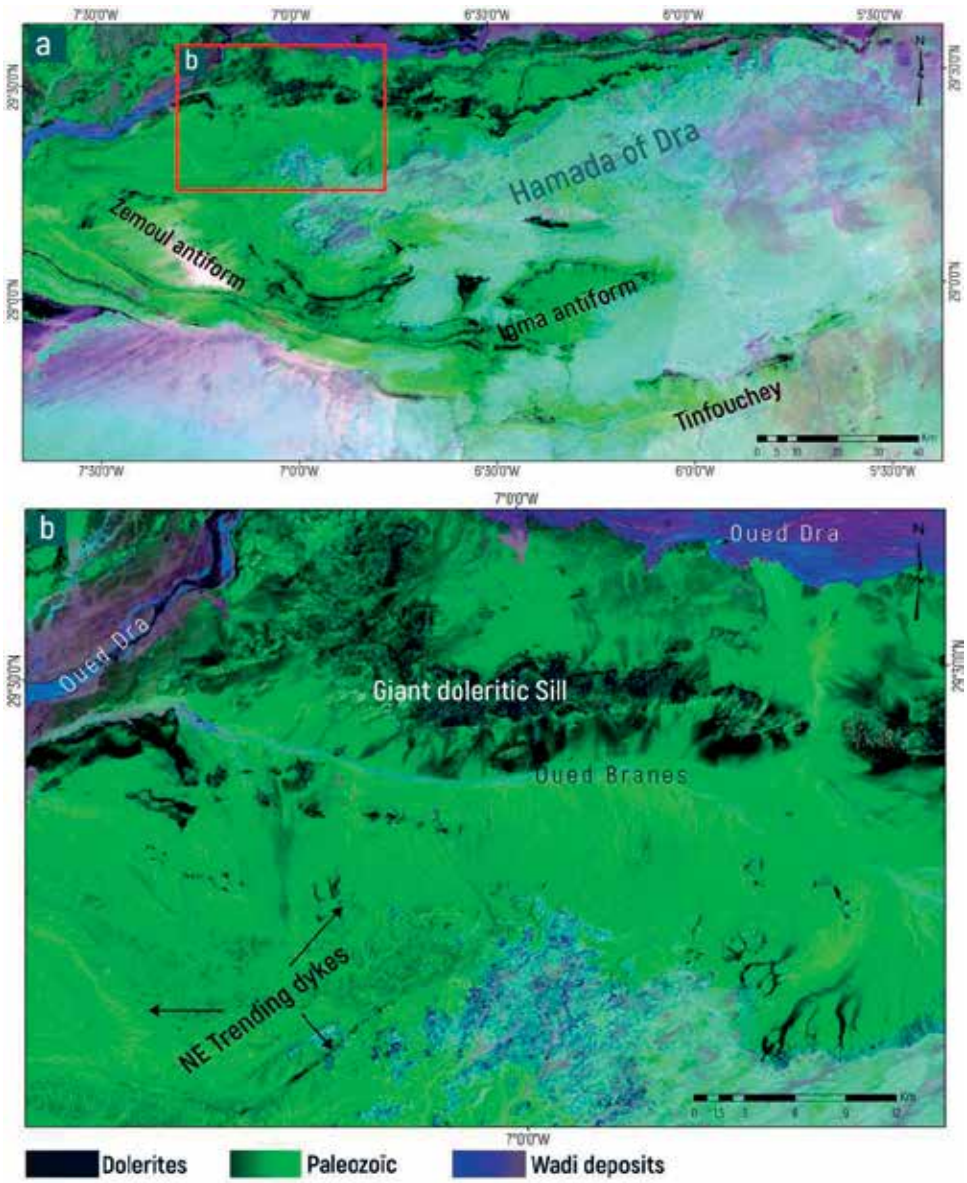

Figure 14. RGB display of 7/1, 5/3 and 4/2 ratios. (a) Regional area, (b) Focus area.

These methods have been proven able in geological target detection [46–50]. They are based on the spectral signature of rock-forming minerals, and they try to match image spectra to reference target spectra. The Anorthite was selected as a target lithology. The resulting image shows the distribution of non-altered sills. The target detection wizard analysis shows the high clinopyroxene dolerites, which are less altered than others, and may show good fracturation and structural indexes (**Figure 16**).

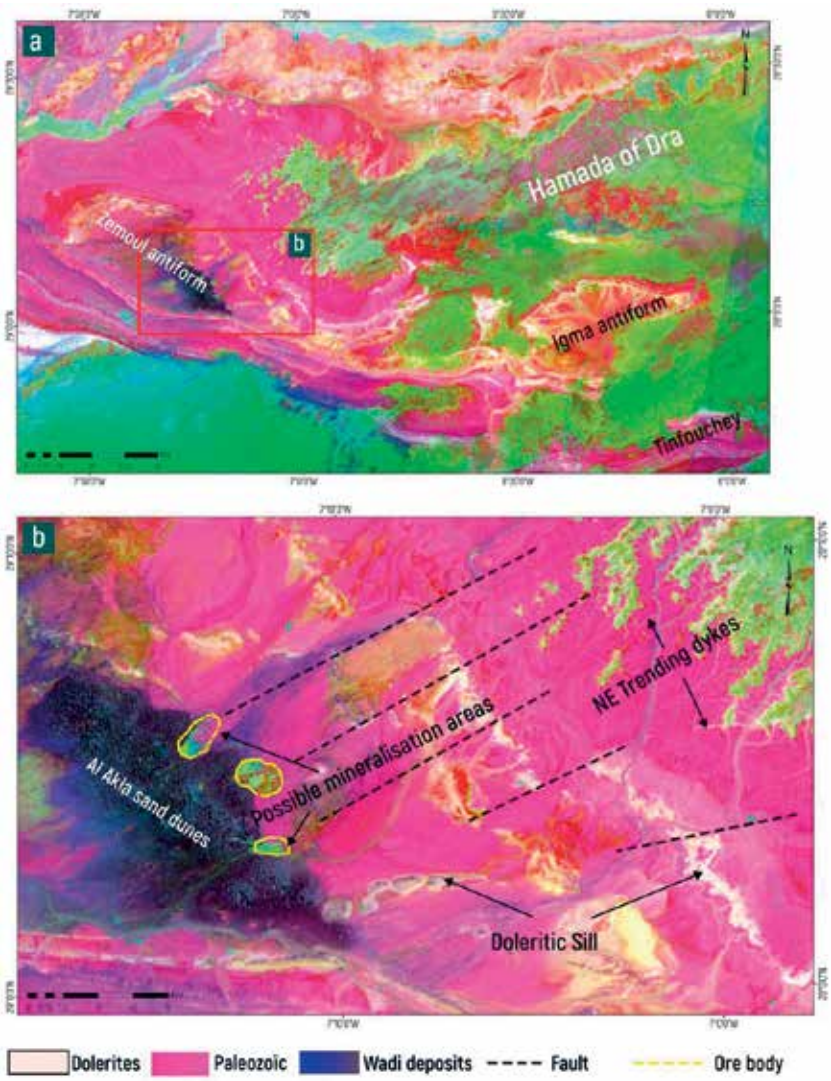

Figure 15. Three first components (PC3, PC2, and PC1) displayed in RGB mode, respectively.

4.4. Conclusions

Remote sensing in arid area such as the Tindouf basin has been proven to be a good tool for geological and mineralogical mapping. The use of advanced remote-sensing analysis allowed us to map dolerite outcrops, estimate their alteration and fracturation level, and then, extract the ore indexes and potentials. The results show that all dykes concentrate around Al Akla area, where some circular dolerite bodies have been detected. These circular bodies may correspond to a mineralized area. A lithostructural map of the study area has been created (**Figure 17**). This map can be used as a base map for the field validation mission.

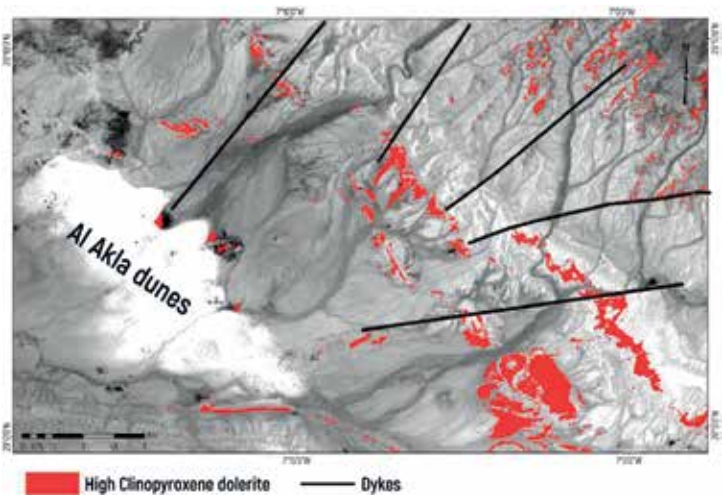

Figure 16. The target detection wizard results showing the high Anorthite content dolerites.

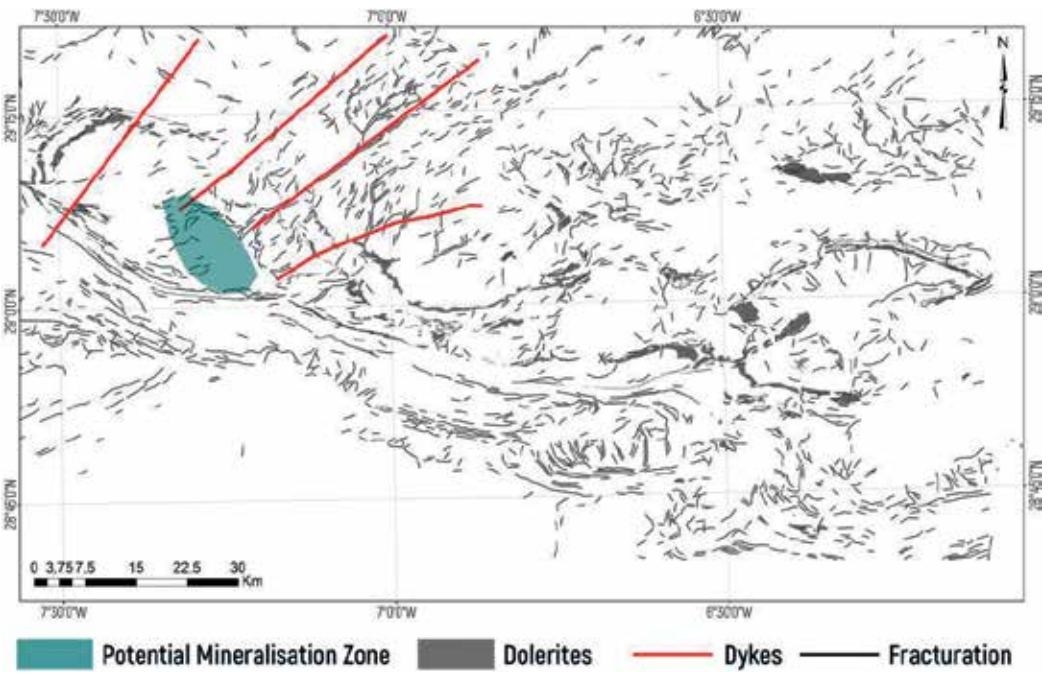

Figure 17. Photo-lithological map of the study area.

5. Conclusion

Here, we see a small bit of what can be done using remote sensing. As new sensors, such as Light Detection and Ranging (LIDAR) and new techniques like artificial intelligence (AI), come upon the scene, the potential for remote sensing will only grow. The modern interpreter will no

longer be hampered by maps of questionable quality in remote areas. They will be able to routinely assess the resources of vast, otherwise inaccessible areas quickly and effectively through the use of remote sensing.

Acknowledgements

The first author HS acknowledges the financial support of United Arab Emirates University (UAEU) by Research Start-Up Grant No. 8, Fund 31S264 (2016).

Author details

Hakim Saibi[1]*, Mohand Bersi[2], Mohamed Bodruddoza Mia[3,4], Nureddin Mohamed Saadi[3], Khalid Mohamed Saleh Al Bloushi[1] and Robert W. Avakian[5]

*Address all correspondence to: saibi.hakim@gmail.com

1 Department of Geology, College of Science, United Arab Emirates University, Al-Ain, United Arab Emirates

2 Department of Earth Sciences, Ferhat Abbas University, Setif, Algeria

3 Faculty of Engineering, Department of Earth Resources Engineering, Kyushu University, Fukuoka, Japan

4 Faculty of Earth and Environmental Science, Department of Geology, University of Dhaka, Bangladesh

5 Oklahoma State University Institute of Technology, USA

References

[1] Saadi NM, Aboud E, Saibi H, Watanabe K. Integrating data from remote sensing, geology and gravity for geological investigation in the Tarhunah area, Northwest Libya. International Journal of Digital Earth. 2008;**1**(4):347-366

[2] Saadi NM, Watanabe K, Imai A, Saibi H. Integrating potential fields with remote sensing data for geological investigations in the Eljufra area of Libya. Earth, Planets and Space. 2008;**60**:539-547

[3] Thurmond AK, Abdelsalam MG, Thurmond JB. Optical-radar-DEM remote sensing data integration for geological mapping in the afar depression, Ethiopia. Journal of African Earth Sciences. 2006;**44**:119-134

[4] Saibi H, Azizi M, Mogren S. Structural investigations of Afghanistan deduced from remote sensing and potential field data. Acta Geophysica. 2016;**64**(4):978-1003

[5] Mogren S, Saibi H, Mukhopadhyay M, Gottsmann J, Ibrahim EH. Analyze the spatial distribution of lava flows in Al-Ays Volcanic Area, Saudi Arabia, using remote sensing. Arabian Journal of Geosciences. 2017;**10**:133. DOI: 10.1007/s12517-017-2889-0

[6] Azizi M, Saibi H, Cooper GRJ. Mineral and structural mapping of the Aynak-Logar Valley (eastern Afghanistan) from hyperspectral remote sensing data and aeromagnetic data. Arabian Journal of Geosciences. 2015;**8**(12):10911-10918

[7] U.S. Geological Survey. Landsat 7, National Aeronautics and Space Administration. 1999. p. 32

[8] NASA. Available from: http://www2.jpl.nasa.gov/srtm/

[9] Ashan S, Hussain S, Kohistany AH, Shenwary GS, Mutty AS, Daud MA, Abraham JD, Anderson ED, Drenth BJ, Finn CA, Kucks RP, Lindsay CR, Phillips JD, Sweeney RE, Brozena JM, Ball DC, Childers VA, Gardner JM, Jarvis JL, Liang RT. Aeromagnetic survey in Afghanistan: U.S. Geological Survey Open-File Report 2007-1247. 2007

[10] Shenwary GS, Kohistany AH, Hussain S, Ashan S, Mutty AS, Daud MA, Wussow MD, Sweeney RE, Phillips JD, Lindsay CR, Kucks RP, Finn CA, Drenth BJ, Anderson ED, Abraham JD, Liang RT, Jarvis JL, Gardner JM, Childers VA, Ball DC, Brozena JM. Aeromagnetic surveys in Afghanistan: An updated website for distribution of data: U.S. Geological Survey Open-File Report 2011-1055. 2011. p. 8

[11] Mather PM. Computer Processing of Remotely-Sensed Images. 3rd ed. Chichester: Wiley; 2004

[12] Navulur K. Multispectral Image Analysis Using the Object-Oriented Paradigm. Boca Raton, CRC Press/Taylor & Francis; 2007

[13] Chavez PS, Berlin GL, Sowers LB. Statistical Methods for Selecting Landsat MSS. Florida, USA: CRC Press/Taylor and Frances Group; 1982

[14] Richards JA. Remote Sensing Digital Image Analysis, An Introduction. 2nd ed. Berlin: Springer; 1993

[15] Smith MJ, Clark CD. Methods for the visualization of digital elevation models for landform mapping. Earth Surface Processes and Landforms. 2005;**30**(7):885-900

[16] Sabins F. Remote Sensing Principles and Interpretation. New York: W.H. Freeman Company; 1997. p. 494

[17] Schowengerdt RA. Remote Sensing: Models and Methods for Image Processing. 3rd ed. London: Academic Press; 2007

[18] Yassaghi A. Integration of Landsat imagery interpretation and geomagnetic data on verification of deep-seated transverse fault lineaments in SE Zagros, Iran. International Journal of Remote Sensing. 2006;**27**:4529-4544

[19] Gloaguen R, Marpu PR, Niemeyer I. Automatic extraction of faults and fractal analysis from remote sensing data. Nonlinear Processes in Geophysics. 2007;**14**(2):131-138

[20] Singh AK, Parkash B, Choudhury PR. Integrated use of SRM, Landsat ETM+ data and 3D perspective views to identify the tectonic geomorphology of Dehradun valley, India. International Journal of Remote Sensing. 2007;**28**:2403-2414

[21] Thompson DT. EULDPH: A new technique for making computer assisted depth estimates from magnetic data. Geophysics. 1982;**47**(1):31-37. DOI: 10.1190/1.1441278

[22] Reid AB, Allsop JM, Granser H, Millett AJ, Somerton IW. Magnetic interpretation in three dimensions using Euler deconvolution. Geophysics. 1990;**55**(1):80-91. DOI: 10.1190/1.1442774

[23] Rowland SM, Duebendorfer EM. Structural Analysis and Synthesis. 2nd ed. Palo Alto: Blackwell Scientific Publications; 1994

[24] Abdullah S, Chmyriov VM. Geological Map of Afghanistan. Kabul/Afghanistan: Ministry of Mining and Industry of Democratic Republic of Afghanistan; 1977 scale 1:500,000

[25] Doebrich JL, Wahl RR, Ludington SD, Chirico PG, Wandrey CJ, Bohannon RG, Orris GL, Bliss JD. Geologic and mineral resource map of Afghanistan, U.S. Geological Survey Open-File Report 2006-1038. 2006

[26] USGS. Aeromagnetic and gravity surveys in Afghanistan: A website for distribution of data, U.S. Geological Survey Open-File Report, 2006-1204. 2006

[27] Mia MB, Bromley CJ, Fujimitsu Y. Monitoring heat flux using Landsat TM/ETM + thermal infrared data – A case study at Karapiti ('Crater of the Moon') thermal area, New Zealand. Journal of Volcanology and Geothermal Research. 2012;**235-236**:1-10

[28] Abdelsalam MG, Stern RJ, Berhane WG. Mapping gossans in arid regions with Landsat TM and SIR-C images: The Beddaho alteration zone in northern Eritrea. Journal of African Earth Sciences. 2000;**30**(4):903-916

[29] Madani A, Abdel Rahman EM, Fawzy KM, Emam A. Mapping of the hydrothermal alteration zones at Haimur Gold Mine Area, South Eastern Desert, Egypt using remote sensing techniques. Egyptian Journal of Remote Sensing and Space Science. 2003;**6**:47-60

[30] Yetkin E. Alteration mapping by remote sensing: application to hasanda-melendiz volcanic complex [MSc thesis]. Ankara, Turkey 97: Middle East Technical University; 2003

[31] Ramadan TM, Kontny A. Mineralogical and structural characterization of alteration zones detected by orbital remote sensing at Shalatein District, SE Desert, Egypt. Journal of African Earth Sciences. 2004;**40**:89-99

[32] Harris AJL, Lodato L, Dehn J, Spampinato L. Thermal characterization of the Vulcano field. Bulletin of Volcanology. 2009;**71**:441-458

[33] Mia MB, Fujimitsu Y. Mapping hydrothermal altered deposits using Landsat 7 ETM+ image in and around Kuju volcano, Kyushu, Japan. Journal of Earth System Science. 2012;**121**(4):1049-1057

[34] Mia MB, Bromley CJ, Fujimitsu Y. Monitoring heat losses using Landsat ETM + thermal infrared data: A case study in Unzen geothermal field, Kyushu, Japan. Pure and Applied Geophysics. 2013;**170**(12):2263-2271

[35] Mia MB, Nishijima J, Fujimitsu Y. Exploration and monitoring geothermal activity using Landsat ETM + images-a case study at Aso volcanic area in Japan. Journal of Volcanology and Geothermal Research. 2014;**275**:14-21

[36] Roy DP, Wulder MA, Loveland TR, Woodcock CE, Allen RG, Anderson MC, Helder D, Irons JR, Johnson DM, Kennedy R, Scambos TA, Schaaf CB, Schott JR, Sheng Y, Vermote EF, Belward AS, Bindschadler R, Cohen WB, Gao F, Hipple JD, Hostert P, Huntington J, Justice CO, Kilic A, Kovalskyy V, Lee ZP, Lymburner L, Masek JG, McCorkel J, Shuai Y, Trezza R, Vogelmann J, Wynne RH, Zhu Z. Landsat-8: Science and product vision for terrestrial global change research. Remote Sensing of Environment. 2014;**145**:154-172

[37] Mishra N, Helder D, Barsi J, Markham B. Continuous calibration improvement in solar reflective bands: Landsat 5 through Landsat 8. Remote Sensing of Environment. 2016;**185**:7-15

[38] Loveland TR, Irons JR. Landsat 8: The plans, the reality, and the legacy. Remote Sensing of Environment. 2016;**185**:1-6

[39] Qin Z, Karnieli A, Berliner P. A mono-window algorithm for retrieving land surface temperature fromLandsat TM data and its application to the Israel–Egypt border region. International Journal of Remote Sensing. 2001;**22**(18):3719-3746

[40] Bersi M, Saibi H, Chabou MC. Aerogravity and remote sensing observations of an iron deposit in Gara Djebilet, southwestern Algeria. Journal of African Earth Sciences. 2016;**116**:134-150

[41] Fabre J. Géologie du Sahara occidental et central. Tervuren: Musée Royal de l'Afrique Centrale; 2005

[42] Chabou MC, Sebaï A, Feraud G, Bertrand H. Datation 40Ar/39Ar de la Province Magmatique de l'Atlantique Central dans le Sud-Ouest algerien. Comptes Rendus Geoscience. 2007;**339**:970-978

[43] Hollard H, Schaer JP. Southeastern Atlantic Canada, northwestern Africa, and continental drift: Discussion. Canadian Journal of Earth Sciences. 1973;**10**(4):584-586

[44] Sabins FF. Remote sensing for mineral exploration. Ore Geology Reviews. 1999;**14**(3): 157-183

[45] Jensen JR, Lulla K. Introductory digital image processing: A remote sensing perspective. New Jersey, USA: Prentice-Hall, Englewood Cliffs; 1987

[46] Drake NA, Mackin S, Settle JJ. Mapping vegetation, soils, and geology in semiarid shrublands using spectral matching and mixture modeling of SWIR AVIRIS imagery. Remote Sensing of Environment. 1999;**68**(1):12-25

[47] Girouard G, Bannari A, El Harti A, Desrochers A. Validated spectral angle mapper algorithm for geological mapping: comparative study between QuickBird and Landsat-TM. Paper presented at the XXth ISPRS Congress, Geo-Imagery Bridging Continents; Istanbul, Turkey; 2004

[48] Khan S. Hyperspectral remote sensing for detection of natural hydrocarbon seeps. Asian Journal of Multidisciplinary Studies. 2016;**4**(2):1-10

[49] Li Q, Wei X, Zhang B, Yan S, Liu X. The spectral analysis and information extraction for small geological target detection using hyperion image. Paper presented at the International Conference on Earth Observation Data Processing and Analysis. Wuhan, China. 2008

[50] Li Q, Zhang B, Gao L, Lu L, Jiao Q. The identification of altered rock in vegetation-covered area using hyperspectral remote sensing. Paper presented at the 2014 IEEE International Geoscience and Remote Sensing Symposium (IGARSS). 2014

Edited by Ming-Chih Hung and Yi-Hwa Wu

Remote sensing was the primary data source since the launch of the first environmental monitoring satellite back in 1972. In the past five decades, remote sensing technology has come a long way and evolved into a mature science. Even so, new technologies, new theories, new methodologies, and new applications continue to emerge. With the rapid pace of technological advancement, it is essential to share experiences especially between different disciplines, either on breakthroughs in new theory or understanding, or applications of remote sensing on real world issues.

Disciplines or fields covered in this book include geography, geology, agriculture, forestry, botany, and oceanography. Though remote sensing may be used differently in various disciplines, the principles are similar, if not the same. This book will be valuable to scientists, scholars, working professionals, or students who use remote sensing in their work, and are interested in learning how others use remote sensing in different ways.

Published in London, UK

IntechOpen

ISBN 978-1-83881-271-3